Fluorescence Resonance Energy Transfer between multiple chromophores studied by single-molecule spectroscopy

Thesis

Department of Mathematics and Natural Sciences

Heinrich-Heine University Düsseldorf

Alessandro Valeri

from Rome

February 2009

Institute of Molecular Physical Chemistry,

Heirich-Heine University Düsseldorf

Printed with the permission of
Department of Mathematics and Natural Sciences
Heinrich-Heine-University Düsseldorf

1. Referee: Prof. Dr. Claus A.M. Seidel

2. Referee: Prof. Dr. Filipp Oesterhelt

Date of the oral examination: 06.05.2009

This thesis is based on the following papers:

Filtered FCS and Species Cross Correlation Function.

Felekyan, S., Kalinin, S., Valeri, A., Seidel, C. A. M, *Proceedings of SPIE*, 2009, *accepted.*

Characterizing Multiple Molecular States in Single-molecule Multi-parameter Fluorescence Detection by Probability Distribution Analysis.

Kalinin, S., Felekyan, S., Valeri, A., Seidel, C. A. M, *Journal of Physical Chemistry B*, 2008, 112 (28), p. 8361-8374.

Probability Distribution Analysis of a Two-State Interconverting FRET System.

Kalinin, S., Valeri, A., Antonik, M., Felekyan, S., Seidel, C. A. M, *manuscript.*

Nucleosome disassembly intermediates characterized by single-molecule FRET.

Gansen, A., Valeri, A., Hauger, F., Felekyan, S., Kalinin, S., Tóth, K., Langowski, J., Seidel, C.A.M., *manuscript.*

Posters at international conferences:

Molecular Ångström Optics: A dynamical view of biomolecular structure.

Seidel, C. A. M., Felekyan, S., Kalinin, S., Oesterhelt, F., Valeri, A., Woźniak, A. K.

Biophysical Society 52nd Annual Meeting and 16th International Biophysics Congress, Long Beach, February 02-06, 2008, Long Beach, USA.

Dynamics of individual nucleosomes analysed with single molecule.

Gansen, A., Hauger, F., Toth, K., Valeri, A., Felakyan, S., Seidel, C. A. M., Langowski, J.

Biophysical Society 52nd Annual Meeting and 16th International Biophysics Congress, Long Beach, February 02-06, 2008, Long Beach, USA.

Multiparameter Fluorescence Detection, theory and application to Two-Step FRET.

Valeri, A., Tojira, O., Felekyan, S., Kudryavtsev, V., Antonik, M., Muller, P.A., Seidel, C. A. M.

9th Conference on Methods and Applications of Fluorescence (MAF-9), September 04 – 07, 2005, Lisbon, Portugal.

Conformational dynamics of special nucleic acid structures studied by single molecule FRET.

AlessandroValeri, Enno Schweinberger, Volodymyr Kudryavtsev, Marcelle König, Pierre-Alain Muller, Rüdiger Dede, Suren Felekyan, Claus A. M. Seidel

9th International Workshop on "Single Molecule Detection and Ultra Sensitive Analysis in the Life Sciences" September 24-26, 2003, Berlin, Germany.

Conformational Dynamics of special Nucleic Acid Structures Studied by Single Molecule FRET.

E. Schweinberger, A. Valeri, M. König, V. Kudryavtsev, P. A. Muller, R. Dede, S. Felekyan, C. A. M. Seidel

8th Conference on Methods and Applications of Fluorescence (MAF-8), August 24-27, 2003, Prague, Czech Republic.

CONTENTS

1 Introduction

In all biological processes that rely on molecular interactions there is a precise link between structure and function. Biomolecules, however, do not have static structures, they rather fluctuate between conformations and their functions "are governed ultimately by their dynamic character (or *personality*)" (Henzler-Wildman and Kern 2007). It has been shown, for example, that it is the dynamic nature of an enzyme that characterises its activity (Eisenmesser, Millet et al. 2005), and that in a broad class of proteins, folding takes place only upon binding to a substrate, intrinsically disordered proteins (Dyson and Wright 2005).

Thus, to understand those processes that are at the base of life, one has to study not only the static molecular structures but also the conformational changes each molecule undergoes prior and during interaction with its partners.

Since the first observations of single molecules with optical detection methods (Hirschfeld 1976; Moerner and Kador 1989) fluorescence spectroscopy has become an important tool in the study of the dynamic and conformational properties of biomolecules (Moerner and Fromm 2003). In single-molecule experiments, in fact, ensemble averaging is avoided and the information on the heterogeneities and dynamic properties of a system is directly accessible (Kühnemuth and Seidel 2001).

Fluorescence emission is highly sensitive to the chromophore's environment therefore conformational changes in the immediate surrounding of the fluorescent probe can be easily detected. However, when molecular interactions induce long-range conformational changes, one chromophore may not be enough to obtain detailed information. This problem is overcome by labelling the molecule (or the molecular assembly) with multiple dyes so that Fluorescence Resonance Energy Transfer (FRET) (Förster 1948) can occur. In FRET, energy is transferred non-radiatively from an excited donor to an acceptor chromophore. The efficiency of the transfer is strongly dependent on the distance and mutual orientation of the dyes, thus intra- and inter-molecular distances, and their fluctuations, can be assessed with high accuracy. The distances that can be probed are comparable to the size of the molecules, 10-100Å, and for this reason FRET has been used as a *molecular ruler* (Stryer and Haugland 1967).

A chromophore possesses multiple fluorescence *dimensions* (intrinsic properties): the spectral properties of absorption and emission, fluorescence brightness and quantum yield, Φ_F, fluorescence lifetime, τ, and fluorescence anisotropy, r. With the use of multiple chromophores even more *dimensions* are available (intrinsic properties of donor and acceptor

and donor-acceptor distances via FRET). Multi-parameter fluorescence detection (MFD) (Eggeling, Berger et al. 2001) is a single-molecule technique that allows one to record simultaneously all these fluorescence parameters and thus, give access to a wealth of information which can be used to successfully investigate and characterise complex systems. Moreover MFD is a time-resolved technique, making the time evolution of the system another available parameter.
In this work it is shown how to combine MFD with other techniques, Fluorescence Correlation Spectroscopy and Probability Distribution Analysis, to enhance their capabilities.

Fluorescence Correlation Spectroscopy.

Fluorescence Correlation Spectroscopy (FCS) is a powerful technique used to study all those processes that induce a fluctuation of the fluorescence signal (Magde, Elson et al. 1972; Magde, Elson et al. 1974). The characteristic relaxation times that describe the kinetic properties of each process are obtained in FCS by fitting the correlation function of the fluorescence signal. A wide range of processes, spanning over several order of correlation times, are accessible to FCS: translational and rotational diffusion (Mets and Rigler 1994), chemical reactions (Elson and Magde 1974; Palmer III and Thompson 1987) and conformational changes (Widengren and Mets 2002). The limits in single-molecule FCS are represented by the possibility to separate the different correlation contributions when multiple species are present and to obtain the correct molecular fractions. In this thesis, is presented a method that uses the lifetime and polarisation information from MFD to obtain simultaneously the correlation curves of all species in solution and the relative concentrations. Moreover here is explored the possibility to selectively cross-correlate different species

Probability Distribution Analysis.

The emission of a photon from an excited fluorophore is a stochastic process, therefore the signals recorded with MFD result distributed due to shot noise. Shot noise distributions represent the minimal dispersion around the average recorded signal and any process inducing a change in the state of the chromophore causes a broadening of these distributions. By analysing the signal distributions it is in principle possible to extract structural information. With Probability Distribution Analysis (PDA) (Antonik, Felekyan et al. 2006; Kalinin, Felekyan et al. 2007), it is possible to predict, in FRET and polarisation experiments, the theoretical distributions of histogrammed fluorescence parameters and thus assess the presence of additional broadening. In this thesis it is presented how static heterogeneities due

to brightness effects and multi-molecular events can be resolved. Moreover, PDA theory is extended to encompass the simple dynamic case of a two-state interconverting system. The mathematical model proposed is here used to analyse distributions arising from the dynamical mixing of FRET states and to obtain the interconversion rate constants with high accuracy.

The latest developments of MFD, FCS and PDA are applied, in this thesis, to the study of DNA model systems of increasing complexity; (i) static DNA, (ii) dynamic DNA; (iii) DNA-interacting with proteins.

Static DNA – Multi-chromophore labelled DNA.

The requirement for multi-labelled molecules is born from the necessity to extend FRET measurements to multi-domain systems or multi-component assemblies. The use of multiple chromophore allows for a first qualitatively assessment of the simultaneous presence and proximity of the domains/components and for the possibility to triangulate distances within the same experiment (Kapanidis, Lee et al. 2004; Lee, Kapanidis et al. 2007).

Here DNA is chosen because; (i) being a fairly rigid structure any complexity deriving from dynamic properties of the system is avoided (ii) the correlation between basepair distance and absolute distance is well characterised (Wozniak, Schröder et al. 2008) allowing for an easy individuation of any underlying process, other than FRET, that could arise from the simultaneous presence of more than two fluorophores. In this thesis, the goal is to assess if good separation of the dyes signals can be achieved and under which conditions distances can be calculated.

Dynamic DNA – Holliday junctions.

Holliday junctions are four-way DNA junctions formed during the genetic recombination of homologous double stranded DNA molecules (Holliday 1964). When the region of homology extends further from the branching point, sequential exchange of basepairing is observed and the Holliday junction effectively migrates along the DNA sequence (Lilley 2000) until complete strand exchange is achieved or enzymatic cleavage takes place. In presence of divalent metal ions, the cruciform structure folds into a more compact conformation in which two consecutive arms stack together. Two folded conformers are possible depending on the stacking pairs. These conformers interconvert into each other with rates decreasing with increasing salt concentration. Branch migration shows similar dependency on metal ions

concentration, suggesting that in both dynamical processes the junction has to have access to the same intermediate structure.

In this thesis, conformer interconversion is studied as a function of Mg^{2+} concentration. Different Holliday junctions are investigated with bulk and single-molecule techniques to obtain relaxation rate constants and to gather information about the intermediate species in the dynamic processes. The ultimate goal of this work is to individuate any common trait in the dynamic properties of the different junctions and to assess if statements of general principle can be done.

DNA interacting with proteins – Nucleosomes.

Nucleosomes are the basic units of genomic DNA compaction (Kornberg 1974; Olins and Olins 1974). Nucleosomes are molecular assemblies constituted of an octamer of histone proteins around which about two turns of double-stranded DNA are wound. Even though chromosomal DNA is tightly packed to fit into the cell nucleus, it is readily available for transcription and repair, meaning that the nucleosome is a dynamic structure that can easily associate/dissociate.

In this work, NaCl-induced dissociation of nucleosomes is studied with single-molecule FRET to elucidate the disassembly mechanism and possibly individuate the intermediate structures in the dissociation pathway.

2 Fluorescence

When a molecule, or a group of atoms in a molecule, absorbs a photon, one electron is promoted from the ground state to a higher energy excited state. Once the chromophore (this is the general name of light-absorbing groups) is in an excited electronic state it can follow several pathways to relax to the ground state. These deactivation processes can be divided in two categories, those that involve the emission of light (luminescence) and those that do not. The emission of light from an excited electronic state is also referred to as fluorescence or phosphorescence depending on whether the transition to the ground state is spin-allowed or spin-forbidden, respectively. A chromophore that emits light is also called a fluorophore or more commonly a fluorescent dye.

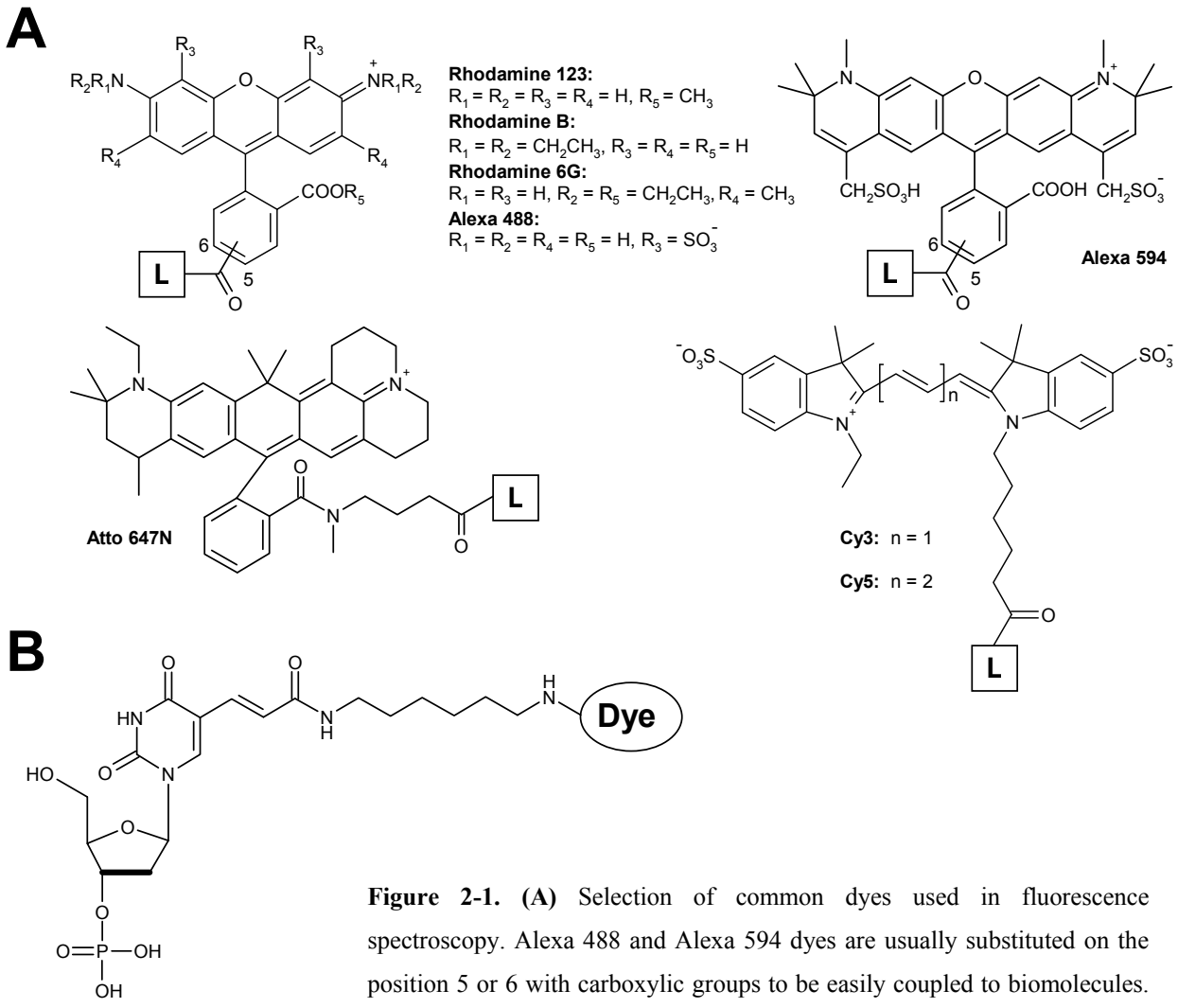

Figure 2-1. (A) Selection of common dyes used in fluorescence spectroscopy. Alexa 488 and Alexa 594 dyes are usually substituted on the position 5 or 6 with carboxylic groups to be easily coupled to biomolecules. **(B)** Structure of a fluorescently labelled Deoxythymidine. The linker, L, used to couple the base and the dye is the commercially available C6-Aminolinker.

Usually, as shown in figure 2-1, fluorophores are constituted of conjugated aromatic systems and, therefore, they have a singlet ground state. A schematic representation of the intra-molecular processes following absorption is given by the Jablonski diagram (Lakowicz 1999), (see figure 2-2). This omits any photochemical pathways.

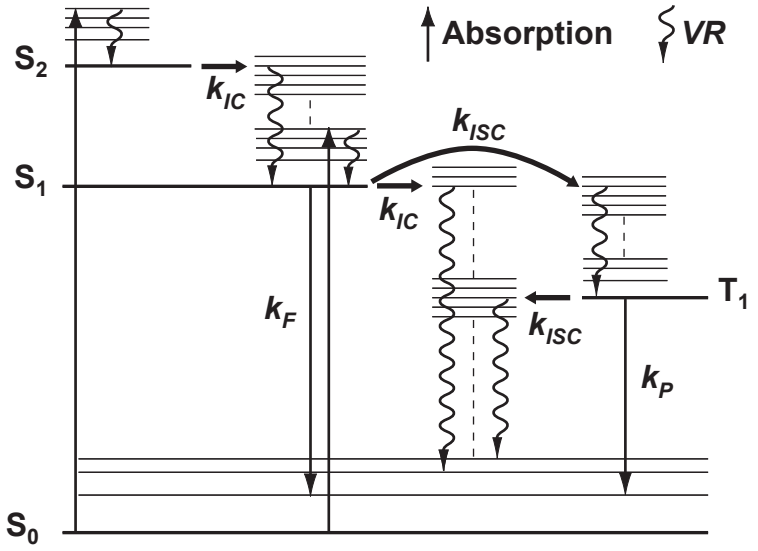

Figure 2-2. Jablonski diagram, S_0, S_1, S_2 and T_1 refer to the singlet and triplet states of the dye, respectively. $k_{F,}$ $k_{IC,}$ $k_{ISC,}$ k_P, are the rate constants of Fluorescence, Internal Conversion, Inter-System Crossing and Phosphorescence, respectively, Vibrational Relaxaton, *VR*, is indicated by wavy arrows. *IC, ISC* and *VR* are all non-radiative processes.

In solution, the radiationless relaxation to the lowest vibrational level of the S_1 state through vibrational relaxation (*VR*) or through internal conversion (*IC*) from higher excited states followed by *VR* is generally a very efficient deactivation pathway. As a consequence fluorescence is observed only from the S_1 state and emission is independent from the excitation wavelength, Kasha's rule (Kasha 1950).

The average time a fluorophore spends in the excited state before a fluorescence photon is emitted defines the fluorescence lifetime, τ_0. If the fluorophore relaxes only through intra-molecular processes, fluorescence lifetime can be calculated by solving the differential equation

$$\frac{dF(t)}{dt} = -\left(k_f + k_{IC} + k_{ISC}\right)F(t) \qquad \text{(Eq. 2-1)}$$

where k_f, k_{IC} and k_{ISC} are the fluorescence, internal conversion and inter system crossing rate constant, respectively, for simplicity $k_f + k_{IC} + k_{ISC} = k_0$. The solution of equation 2-1 is a first order exponential decay

$$F(t) = F(0)\exp[-k_0 t] = F(0)\exp\left[-\frac{t}{\tau_0}\right] \qquad \text{with} \qquad \tau_0 = \frac{1}{k_0} \qquad \text{(Eq. 2-2)}$$

The efficiency of fluorescence as a relaxation pathway is quantified by the fluorescence quantum yield, $\Phi_{F(0)}$, defined as

$$\Phi_{F(0)} = \frac{Emitted\ \ photons}{Absorbed\ \ photons} = \frac{k_f}{k_0} \qquad \text{(Eq. 2-3)}$$

The rate constants of each process illustrated in the Jablonski diagram vary from molecule to molecule, making the fluorescence lifetime and quantum yield distinctive signatures of a fluorophore.

2.1 Fluorescence anisotropy

Fluorophores absorb preferably the component of light with polarisation parallel to their absorption dipole moment, a process known as photoselection, and emit with polarisation parallel to their emission dipole moment. Fluorescence anisotropy, r, is a measure of the polarisation of the emitted light. The angle between the transition dipole moments, β, defines the fundamental anisotropy, r_0

$$r_0 = \frac{3\cos^2(\beta) - 1}{5} \qquad \text{(Eq. 2.1-1)}$$

r_0 depends only on β, and, therefore, is characteristic for each fluorophore. For fluorophores freely diffusing in solution, r_0, is obviously the limiting value of anisotropy. In fact given enough time to rotate, due to the randomisation of the emission dipole, the anisotropy will be gradually lost. Anisotropy's time dependence is expressed by the Perrin equation (Lakowicz 1999)

$$r = \frac{r_0}{1 + \frac{\tau}{\rho}} \qquad \text{(Eq. 2.1-2)}$$

In equation 2.1-3 r_0 is the fundamental anisotropy, τ is the fluorescence lifetime and ρ the rotational correlation time.

In practice, fluorescence anisotropy is calculated as

$$r = \frac{gF_{//} - F_{\perp}}{gF_{//} + F_{\perp}} \qquad \text{(Eq. 2.1-3)}$$

where $F_{//}$ and $F_{\perp}$ are the fluorescence signals parallel and perpendicular to the linearly polarised excitation light, respectively, and g is the factor that takes into account the different detection sensitivities of the setup for parallel and perpendicularly polarised light.

2.2 Fluorescence Resonance Energy Transfer (FRET)

In fluorescence resonance energy transfer an excited fluorophore, the donor, transfers its energy to a second fluorophore, the acceptor. The transfer does not involve emission and absorption of a photon but is a dipole-dipole interaction between the emission dipole moment of the donor and the absorption dipole moment of the acceptor. Therefore, the FRET rate constant, k_{FRET}, depends, among other parameters, on the distance and mutual orientation of the transition moments of the fluorophores (Lakowicz 1999)

$$k_{FRET} = \frac{9000 \ln(10) \Phi_{FD(0)} \kappa^2 J}{128 \pi^5 N n^4 \tau_{D(0)} R_{DA}^6} \qquad \text{(Eq. 2.2-1)}$$

where $\Phi_{FD(0)}$ is the quantum yield of the donor in absence of the acceptor, $\tau_{D(0)}$ is the lifetime of the donor in absence of the acceptor, N is Avogadro's number, n is the refractive index of the medium, R_{DA} is the distance between donor and acceptor, J is the overlapping integral and κ^2 is the term taking into account the orientations of the transition dipoles.

The overlapping integral, J, expresses the overlap between the emission spectrum of the donor, $F_D(\lambda)$, and the absorption spectrum of the acceptor, $\varepsilon_A(\lambda)$, and is a measure of the matching of the energy levels of the two fluorophores. J can be calculated as

$$J = \int_0^\infty F_D(\lambda)\varepsilon_A(\lambda)\lambda^4 d\lambda \qquad \text{(Eq. 2.2-2)}$$

In equation 2.2-2 λ is the wavelength and $F_D(\lambda)$ is normalised to unity.
The κ^2 term accounts for the angular dependence of the dipole-dipole interaction and is defined as

$$\kappa^2 = (\cos\theta_T - 3\cdot\cos\theta_D\cdot\cos\theta_A)^2 = (\sin\theta_D\cdot\sin\theta_A\cdot\cos\phi - 2\cdot\cos\theta_D\cdot\cos\theta_A)^2 \qquad \text{(Eq. 2.2-3)}$$

where θ_T is the angle between the donor emission dipole and the acceptor absorption dipole, θ_D and θ_A are the angles between the dipoles and the vector connecting the donor and acceptor, $\vec{R}_{DA}$, and ϕ is the angle between the donor-$\vec{R}_{DA}$ and acceptor-$\vec{R}_{DA}$ planes.

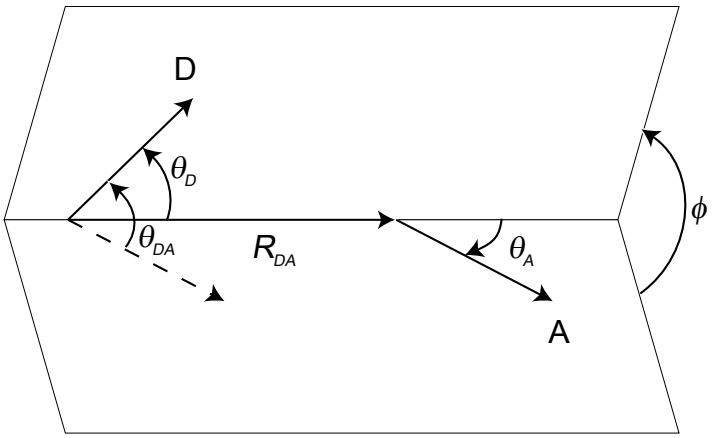

Figure 2.2-1. Schematic representation of the angular dependence of the dipole-dipole interaction between donor and acceptor dye.

Equation 2.2-1 can be written in a more compact way as

$$k_{FRET} = \frac{R_0^6}{\tau_{D(0)}R_{DA}^6} \qquad \text{(Eq. 2.2-4)}$$

where R_0 ($R_0 = 9000\ln(10)\Phi_{FD(0)}\,\kappa^2 J/128\pi^5 N n^4$) is called Förster radius after Theodor Förster who first investigated FRET in 1948 (Förster 1948).
In common practice, energy transfer is quantified by the FRET efficiency, E_{FRET}, defined as

$$E_{FRET} = \frac{k_{FRET}}{k_0 + k_{FRET}} \qquad \text{(Eq. 2.2-5a)}$$

Combining equations 2.2-4 and 2.2-5a, E_{FRET} can be expressed as a function of the inter-dye distance

$$E_{FRET} = \frac{k_{FRET}}{k_0 + k_{FRET}} = \frac{1}{\frac{k_0}{k_{FRET}} + 1} = \frac{1}{\left(\frac{R_{DA}}{R_0}\right)^6 + 1} = \frac{R_0^6}{R_0^6 + R_{DA}^6} \qquad \text{(Eq. 2.2-5b)}$$

It is clear from equation 2.2-5b that the Förster radius is the distance at which there is a 50% chance that an excited donor will transfer its energy to the acceptor. Moreover, if we plot E_{FRET} as a function of distance, figure 2.2-1, we can see that small variations of distance in the region of $R_{DA} = R_0$ lead to significant changes in FRET efficiency, making this the most sensitive range of donor-acceptor distances for FRET experiments.

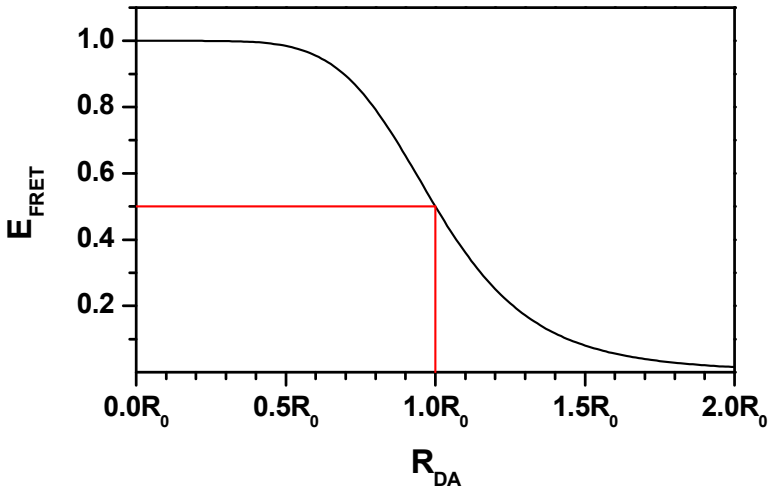

Figure 2.2-2. FRET efficiency as a function of donor-acceptor distance, R_{DA}. The distance is expressed in Förster radius units.

FRET is an additional deactivation pathway available for the excited donor dye. To account for this process the Jablonski diagram can be modified as described in (van der Meer, Cooker et al. 1994).

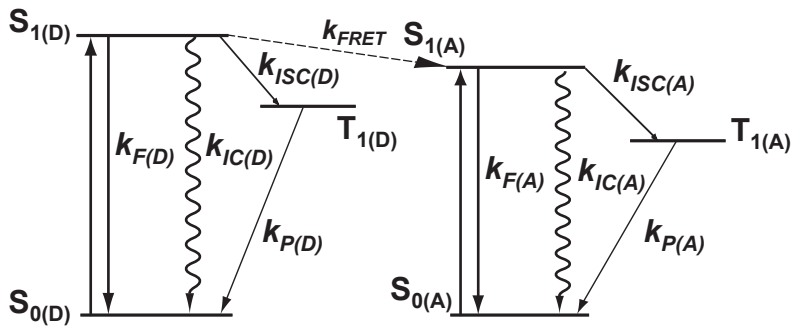

Figure 2.2-3. Simplified energy–level diagram of resonance energy transfer (adopted from (van der Meer et al., 1994)) $S_{1(D)}$, $S_{0(D)}$, $T_{1(D)}$ refer to the singlet and triplet states of donor, and $S_{1(A)}$, $S_{0(A)}$, $T_{1(A)}$, to the singlet and triplet states of acceptor; $k_{IC(D)}$, $k_{ISC(D)}$, $k_{P(D)}$, $k_{F(D)}$, $k_{IC(A)}$, $k_{ISC(A)}$, $k_{P(A)}$, $k_{F(A)}$, and k_{FRET} are rate constants: $k_{IC(D)}$, $k_{IC(A)}$ for internal conversion of donor and acceptor, $k_{ISC(D)}$, $k_{ISC(A)}$ for intersystem-crossing of donor and acceptor, and $k_{P(D)}$, $k_{P(A)}$ for phosphorescence and intersystem-crossing from the triplet to singlet state, S_0, k_{FRET} for energy transfer, and $k_{F(D)}$, $k_{F(A)}$ for fluorescence of donor and acceptor.

Taking into account the presence of FRET, fluorescence lifetime and quantum yield of the donor in presence of the acceptor, $\tau_{D(A)}$ and $\Phi_{FD(A)}$, are

$$\tau_{D(A)} = \frac{1}{k_f + k_{IC} + k_{ISC} + k_{FRET}} = \frac{1}{k_0 + k_{FRET}} \qquad \text{(Eq. 2.2-6)}$$

$$\Phi_{FD(A)} = \frac{k_f}{k_f + k_{IC} + k_{ISC} + k_{FRET}} = \frac{k_f}{k_0 + k_{FRET}} \qquad \text{(Eq. 2.2-7)}$$

In practice E_{FRET} is calculated through lifetime or intensity experiments

$$E_{FRET} = \frac{k_{FRET}}{k_0 + k_{FRET}} = 1 - \frac{k_0}{k_0 + k_{FRET}} = 1 - \frac{\tau_{D(A)}}{\tau_{D(0)}} \qquad \text{(Eq. 2.2-8a)}$$

$$E_{FRET} = \frac{k_{FRET}}{k_0 + k_{FRET}} = 1 - \frac{k_0}{k_0 + k_{FRET}} = 1 - \frac{\Phi_{FD(A)}}{\Phi_{FD(0)}} \qquad \text{(Eq. 2.2-8b)}$$

3 Instrumentation

3.1 UV-VIS spectrophotometer

Absorption spectra were recorded with a UV-Vis spectrophotometer Cary 300-Bio from Varian. The absorption of light was measured in Absorbance, *Abs*, defined by the Lambert-Beer equation

$$Abs = -\log\frac{I_{Trans}}{I_0} = \varepsilon\, c\, d \qquad \text{(Eq. 3.1-1)}$$

where I_0 is the intensity of the incident light, I_{Trans} the intensity of the transmitted light, ε the extinction coefficient, c the concentration of the sample and d the optical path length of the cell.

The spectra were collected in double beam mode, meaning that the excitation light was divided into two parts, one directed to the sample cell and the other to a reference cell to record simultaneously the intensity of the light transmitted through the sample and the intensity of the incident light.

3.2 Steady state fluorometers

Fluorescence spectra were recorded with Fluoromax-3 and Fluorolog-3 fluorometers from HORIBA Jobin Yvon, SPEX. According to the definition of quantum yield, (Eq. 2-3), the recorded fluorescence intensity, *F*, can be expressed as

$$F = \Phi_F\, I_{Abs} \qquad \text{(Eq. 3.2-1a)}$$

where I_{Abs} is the intensity of the absorbed light. Keeping in mind that $I_{Abs} = I_0 - I_{Trans}$, equation 3.2-1a can be rewritten as

$$F = \Phi_F\, I_0\left(1 - 10^{-\varepsilon c d}\right) \qquad \text{(Eq. 3.2-1b)}$$

3.3 Time Correlated Single Photon Counting (TCSPC)

Fluorescence lifetime decays were recorded through a Data Station Hub from HORIBA Jobin Yvon, IBH. Data acquisition was performed in reversed start-stop mode, meaning that the decay histograms were built from the delay times between a fluorescence photon and the following excitation pulse. The time between two consecutive laser pulses, TAC time, was divided in 4096 channels, TAC or TCSPC channels. Fluorescence decays were computed by deconvolution of the instrument response function, IRF, obtained from a concentrated solution of a highly scattering compound, Ludox. Lifetimes were modelled and fit as a sum of exponential decay terms

$$F(t) = \sum_i A_i \exp\left[-\frac{t}{\tau_i}\right] \qquad \text{(Eq. 3.3-1)}$$

with A_i and τ_i the amplitude and lifetime of the i-th species, respectively.

3.4 Confocal microscope setup

Single-molecule experiments were performed with a custom built confocal microscope setup as the one described in figure 3.4-1.

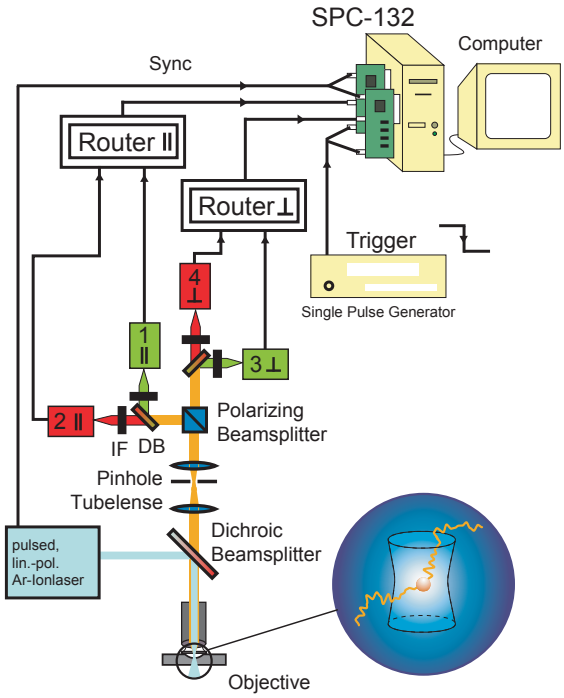

Figure 3.4-1. Sketch of the confocal microscope setup for two-colour single-molecule experiments.

The technical characteristics of the setup have already been described in detail in (Eggeling, Berger et al. 2001) and (Widengren, Kudryavtsev et al. 2006) therefore for the purposes of this thesis it will suffice to note that:

- the emitted light is first split into two polarisation components: parallel and perpendicular to the linearly polarised excitation light,
- each polarisation component is further divided in two spectral ranges (or *colours*), relative to the donor's and the acceptor's emission,
- the different polarisations are registered by two different single photon counting cards,
- each card registers the time between the detection of two consecutive photons as well as the arrival time of each photon after the excitation pulse.

The outlined features enable to:

- calculate the fluorescence correlation curve over the complete correlation time range (see chapter 4),
- record the fluorescence intensity, lifetime and anisotropy for donor and acceptor dye simultaneously (see chapter 5).

In some particular cases (see chapter 7), the setup was extended to record a third spectral range, as shown in figure 3.4-2.

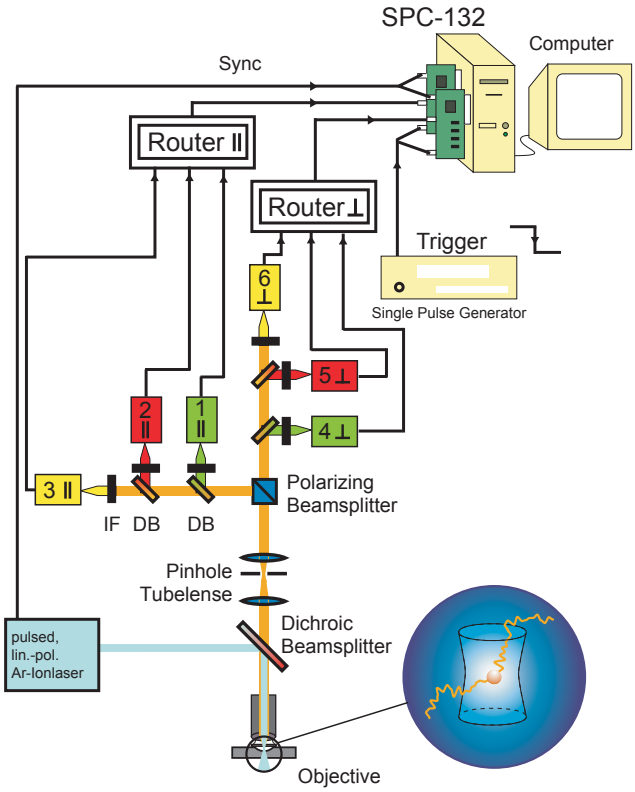

Figure 3.4-2. Sketch of the confocal microscope setup for three-colour single-molecule experiments.

3.4.1 Fluorescence signals

The total signal recorded by the detectors of the SMD setup is indicated by the letter S with the subscripts G and R to indicate the signal registered by the green and red detectors, respectively. If not differently stated, S_G and S_R refer to the sum of both, the parallel and perpendicular components. The signal S is not constituted of fluorescence signal only but includes background and dark count photons. Pure fluorescence signal is indicated by the letter F and for the two spectral ranges is defined as

$$F_G = S_G - B_G \qquad \text{(Eq. 3.4.1-1)}$$

$$F_{RT} = S_R - B_R \qquad \text{(Eq. 3.4.1-2)}$$

where B_G and B_R represent the sum of background and dark count signals recorded in the green and red channels, respectively. F_{RT} is the total fluorescence signal recorded by the red detectors and as such is comprised not only by the signal of the acceptor dye but also by the bleed-through of the donor dye in the acceptor channel, crosstalk. The recorded fluorescence signal of the acceptor dye only is indicated by F_R and defined as

$$F_R = S_R - \alpha F_G - B_R \qquad \text{(Eq. 3.4.1-3)}$$

The crosstalk is indicated by α and is expressed as the fraction of donor florescence recorded by the red detectors divided by the fraction of donor fluorescence recorded by the green detectors.

However, the signals F_G and F_R do not represent the total photons emitted by the donor or the acceptor but only the fraction that is transmitted through the optical components of the setup, i.e. dichroic mirrors, fluorescence filters, and successfully detected. To correct for this the detection efficiencies g_G and g_R are introduced. The total fluorescence signal emitted by the donor, F_D, and acceptor dye, F_A, are therefore calculated as

$$F_D = \frac{F_G}{g_G} = \frac{S_G - B_G}{g_G} \qquad \text{(Eq. 3.4.1-4)}$$

$$F_A = \frac{F_R}{g_R} = \frac{S_R - \alpha F_G - B_R}{g_R} \qquad \text{(Eq. 3.4.1-5)}$$

The detection efficiencies g_G and g_R are defined as

$$g_G = \int g_G(\lambda) F_D(\lambda) d\lambda \qquad \text{(Eq. 3.4.1-6)}$$

$$g_R = \int g_R(\lambda) F_A(\lambda) d\lambda \qquad \text{(Eq. 3.4.1-7)}$$

where $F_D(\lambda)$ and $F_A(\lambda)$ are the fluorescence spectra normalised to unity of donor and acceptor, respectively, and $g_G(\lambda)$ and $g_R(\lambda)$ the shape functions of the detection efficiency of the green and red channels, respectively. The shape functions $g_G(\lambda)$ and $g_R(\lambda)$ take into account not only the properties of the mirrors and filters of the setup but also the different sensitivities of the detectors at the different wavelengths. As an example, the effects of the shape functions on the emission spectrum of Alexa 488 in a three-colour setup are reported in figure 3.4.1-1 (only $g_G(\lambda)$ and $g_Y(\lambda)$ are taken into account).

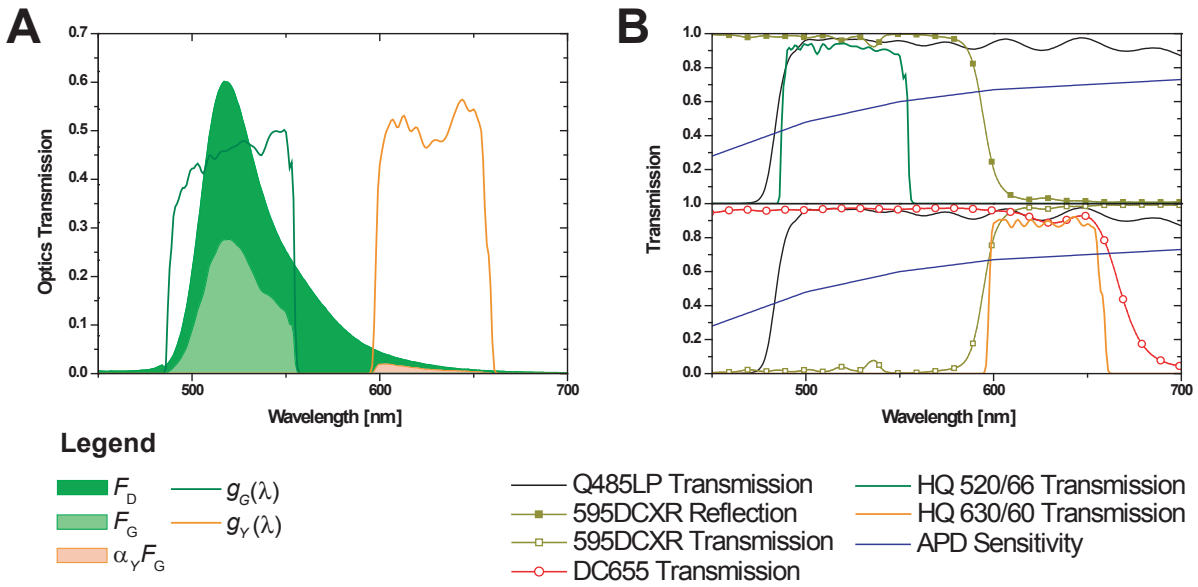

Figure 3.4.1-1. Graphical representation of the effect of the detection efficiencies on the emission spectrum of Alexa488 in a three-colour single-molecule experiment. A) The darker green area represents the total fluorescence emitted by the dye, F_D, while the light green and orange areas represent the Alexa 488 photons effectively detected in the green and yellow channel, respectively, F_G and $\alpha_Y F_G$. Here α_Y is the crosstalk of Alexa 488 in the yellow channel. The shapes of $g_G(\lambda)$ and $g_Y(\lambda)$ are obtained for the filter-set reported in the legend. B) Contribution of each detection component to the shape functions of the green channel (top panel) and yellow channel (bottom panel). The contributions are indicated as the fraction of light that is transmitted in the

appropriate detector direction by each component. The shape functions $g_G(\lambda)$ and $g_Y(\lambda)$, are obtained by multiplying the different spectra.

3.4.2 Anisotropy

As described in (Koshioka, Saski et al. 1995), the fluorescence signal recorded with a confocal microscope results depolarised by the objective. Therefore, to calculate properly fluorescence anisotropy, r, equation 2.1-3 is modified by introducing the correction factors l_1 and l_2 (Koshioka, Saski et al. 1995)

$$r_S = \frac{gF_{//} - F_{\perp}}{(1-3l_2)gF_{//} + (2-3l_1)F_{\perp}} \qquad \text{(Eq. 3.4.2-1)}$$

where the r_S indicates that signals were corrected for scatter (or, in other words, that pure fluorescence signals were used to calculate anisotropy). Sometimes, to calculate anisotropy, the signal S is used. In these cases anisotropy is called experimental anisotropy, r_{exp}

$$r_{exp} = \frac{gS_{//} - S_{\perp}}{(1-3l_2)gS_{//} + (2-3l_1)S_{\perp}} \qquad \text{(Eq. 3.4.2-2)}$$

3.4.3 Colours

The distinction between donor/acceptor and green/red is important. The terms donor/acceptor refer exclusively to the photons emitted by the dyes while the terms green/red are descriptive terms and indicate in which channel the photons are detected. As such, green/red can be associated to different signals, i.e. fluorescence, scatter, crosstalk, and, by analogy, to the detection components of the SMD setup, i.e. filters, detectors.

4 Fluorescence Correlation Spectroscopy (FCS)

Any dynamic process that produces a change in the brightness of a fluorophore, at time *t*, will induce a fluctuation of the fluorescence intensity, $\delta F(t)$, around the average signal, $\langle F \rangle$. By calculating the second order correlation function, $G^2(t_C)$, of the fluorescence signal, $F(t)$, it is possible to assess the characteristic time of each process responsible for fluorescence intensity fluctuations

$$G^2(t_C) = \frac{\langle F(t) \cdot F(t+t_C) \rangle}{\langle F \rangle^2} = 1 + \frac{\langle \delta F(t) \cdot \delta F(t+t_C) \rangle}{\langle F \rangle^2} \qquad \text{(Eq. 4-1)}$$

For DNA freely diffusing in an open volume, the correlation curve ranges from nanoseconds, the timescale of fluorescence emission (antibunching), to milliseconds, the timescale of translational diffusion. Figure 4-1 shows a model correlation curve where the occurring processes are emission, rotational diffusion, triplet formation and translational diffusion.

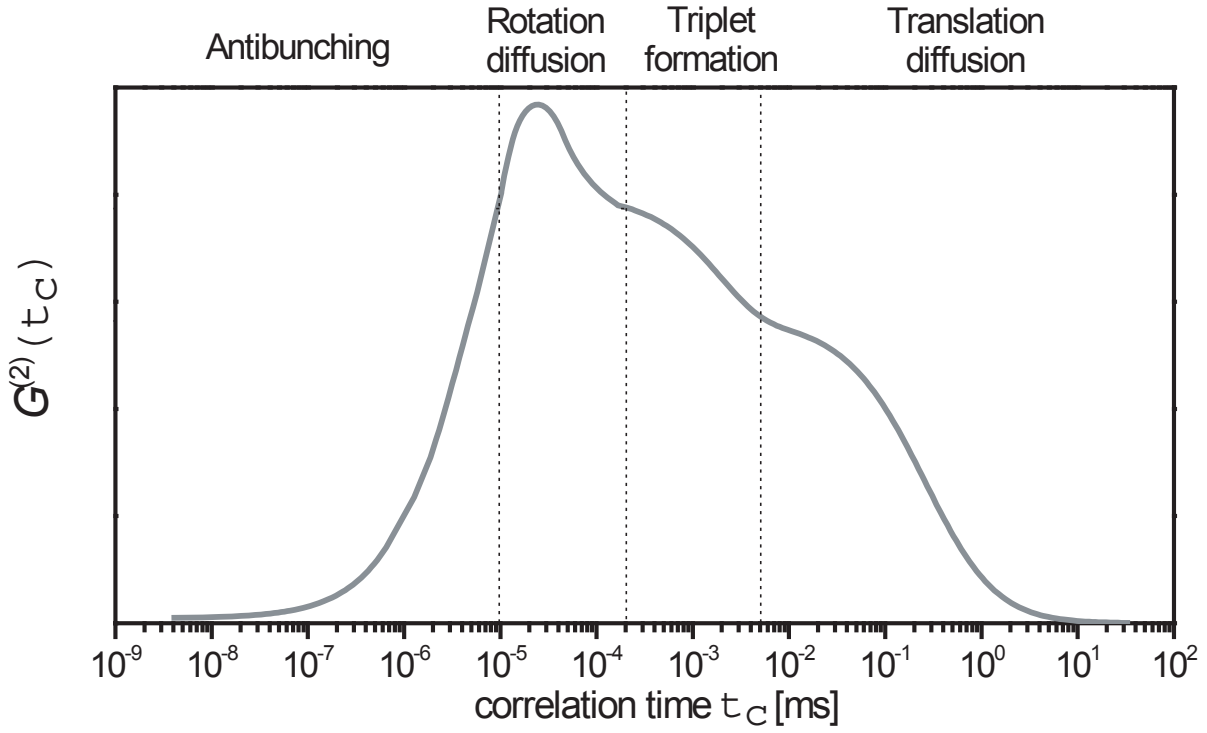

Figure 4-1. Simulation of a FCS curve of fluorescently labelled DNA.

If the timescale of each process differs from the other by at least one order of magnitude it is possible to express the correlation function as the product of the different correlation terms

normalised by the average number of molecules in the detection volume, N (Mets and Rigler 1994)

$$G^2(t_C) = 1 + \frac{1}{N}\left[G_D(t_c)\cdot G_T(t_c)\cdot G_R(t_c)\cdot G_A(t_c)\right] \qquad \text{(Eq. 4-2)}$$

where D, T, R and A refer to diffusion, triplet, rotation and antibunching, respectively.
If the focal volume has the shape of a three-dimensional Gaussian with spatial distribution of the detection probabilities

$$w(x,y,z) = \exp\left(-2\left(x^2+y^2\right)/\omega_0^2\right)\exp\left(-2z^2/z_0^2\right) \qquad \text{(Eq. 4-3)}$$

where ω_0 and z_0 are the $1/e^2$ radii in the lateral or in the axial direction, respectively, it is possible to rewrite equation 4-2 as (Mets and Rigler 1994)

$$G^2(t_C) = 1 + \frac{1}{N}\cdot\left[\frac{1}{1+\frac{t_C}{t_D}}\cdot\frac{1}{\sqrt{1+\frac{t_C}{\left(\frac{z_0}{\omega_0}\right)^2\cdot t_D}}}\cdot\left(1-T+T\cdot\exp\left[-\frac{t_C}{t_T}\right]\right)\cdot\left(1+R\cdot\exp\left[-\frac{t_C}{t_R}\right]\right)\cdot\left(1-A\cdot\exp\left[-\frac{t_C}{t_A}\right]\right)\right] \qquad \text{(Eq. 4-4)}$$

where t_D is the diffusion time, T and t_T are the triplet's amplitude and characteristic time, R and t_R are the amplitude and characteristic time of rotational diffusion and A and t_A are the amplitude and characteristic time of the antibunching process.
Knowing t_D and the radius ω_0 it is possible to calculate the diffusion coefficient of the fluorescently labelled molecule as

$$D = \frac{\omega_0^2}{4\cdot t_D} \qquad \text{(Eq. 4-5)}$$

Although N can be obtained by fitting a correlation curve, in single-molecule experiments the presence of dark counts and scattered light distorts the correlation amplitude, $1/N$, and makes

it impossible to obtain the correct number of molecules in the focus unless proper correction is applied (Koppel 1974).

Reactions between different species present in solution can produce a variation in the brightness of the fluorophores and thus influence the correlation curve. Here the term reaction has to be considered in a general sense and includes not only chemical reactions but a broader array of processes, i.e. conformational dynamics, binding equilibria.

If the diffusion times of all the *reactants* and *products* are the same, or very similar, the correlation function can be factored as (Palmer III and Thompson 1987)

$$G^2(t_c) = 1 + \frac{1}{N} \cdot G(t_c) \cdot X(t_c) \qquad \text{(Eq. 4-6)}$$

where $G(t_c)$ is the correlation function as described in equation 4-2 ($G(t_c) = G_D(t_c) \cdot G_T(t_c) \cdot G_R(t_c) \cdot G_A(t_c)$), and $X(t_c)$ the term containing the kinetic dependence. Usually $X(t_c)$ has the form

$$X(t_c) = 1 - \sum_i A_i \exp[-\lambda_i t_c] \qquad \text{(Eq. 4-7)}$$

where λ_i are the solutions of the characteristic polynomial of the matrix describing the kinetics of the reaction and A_i the relative amplitudes (Palmer III and Thompson 1987).

In the case that the diffusion properties of the molecules are too different a more general approach (Elson and Magde 1974) has to be used to compute the correlation function.

4.1 Filtered Fluorescence Correlation Spectroscopy (fFCS)

When more than one species is simultaneously present in solution, equation 4-4 does not hold anymore. For a mixture of species, the correlation function becomes

$$G(t_C) = 1 + \frac{1}{N} \cdot \frac{\sum_i^n x_i \cdot Q_i^2 \cdot G_i^2(t_C)}{\left(\sum_i^n x_i \cdot Q_i\right)^2} \qquad \text{(Eq. 4.1-1)}$$

where x_i , Q_i and $G_i^2(t_C)$ are the fraction, brightness and normalised correlation function of the *i*-th species, respectively. In this case, even though the brightness of each species would be exactly known, it would be very difficult to sort the species correctly unless the diffusion times differ significantly.

Enderlein and co-workers (Böhmer and Enderlein 2003; Enderlein and Gregor 2005; Gregor and Enderlein 2007) suggested the use of the fluorescence lifetime decay as a pattern to distinguish the different species present in solution.

In the past, the lifetime information was used in gated FCS where only those photons that arrive at the detector in a certain TAC time interval are correlated (Shera, Seitzinger et al. 1990; Herman, Londo et al. 1992; Li and Davis 1995; Creasey, Halford-Maw et al. 1998; Xiao and Selvin 1999). By contrast, the new approach, uses fluorescence lifetime to build filters that attribute a certain likelihood (also negative) to each photon of belonging to a determined species. In this way, all photons are correlated with weight corresponding to the filter value for the chosen species. Filtered FCS has therefore two main advantages over gated FCS: (i) all photons are correlated while in gated FCS those that fall out of the designated TAC-gate, whose setting is arbitrary; are disregarded; (ii) the FCS curves for all the species are obtained simultaneously. Moreover, by using the instrumental response function as an additional pattern it is possible to eliminate the scatter photon contribution and compute the correct correlation amplitude even in single-molecule experiments.

4.1.1 Fluorescence Lifetime Filters (FLF)

For simplicity, a mixture of two molecular species is considered, each one with fluorescence decay patterns $\left\{{}^{\parallel}p_j^{(i)}\right\}$ and $\left\{{}^{\perp}p_j^{(i)}\right\}$, where *i* refers to the species, *j* denotes the number of the TCSPC channel and $\parallel$ and $\perp$ the polarisation of the emitted light in respect to a linearly polarised excitation. In this way ${}^{\parallel}p_j^{(i)}$ and ${}^{\perp}p_j^{(i)}$ represent normalised probabilities. Any measured TCSPC decay histograms ${}^{\parallel}H_j$ and ${}^{\perp}H_j$ of the mixture can be expressed as a linear combination of the decay patterns of the two species

$$\begin{cases} {}^{\parallel}H_j = \sum_{i=1}^{n(=2)} w^{(i)}.{}^{\parallel}p_j^{(i)} = w^{(1)}.{}^{\parallel}p_j^{(1)} + w^{(2)}.{}^{\parallel}p_j^{(2)} \\ {}^{\perp}H_j = \sum_{i=1}^{n(=2)} w^{(i)}.{}^{\perp}p_j^{(i)} = w^{(1)}.{}^{\perp}p_j^{(1)} + w^{(2)}.{}^{\perp}p_j^{(2)} \end{cases} \qquad \text{(Eq. 4.1.1-1)}$$

where $w^{(i)}$ is the amplitude of the photon count contribution (in photons number) of the *i*-th species. As described in (Böhmer, Wahl et al. 2002) it is possible to build two filters ${}^{\parallel}f_j^{(i)}$ and ${}^{\perp}f_j^{(i)}$, so that

$$\left\langle \sum_{j=1}^{L} {}^{\parallel}f_j^{(i)} \cdot {}^{\parallel}H_j \right\rangle = {}^{\parallel}w^{(i)}, \left\langle \sum_{j=1}^{L} {}^{\perp}f_j^{(i)} \cdot {}^{\perp}H_j \right\rangle = {}^{\perp}w^{(i)} \qquad \text{(Eq. 4.1.1-2)}$$

where ${}^{\parallel}w^{(i)}$ and ${}^{\perp}w^{(i)}$ are the photon count contributions of the *i*-th species in the parallel and perpendicular detection channel, respectively (${}^{\parallel}w^{(i)} + {}^{\perp}w^{(i)} = w^{(i)}$), L is the total number of TCSPC channels, and the brackets denote averaging over an infinite number of measurements.

The correlation function between different polarisations of the same spectral range of the *i*-th species, auto/cross $G_{\perp,\parallel}^{(i)}(t_c)$, can be then calculated as

$$G_{\perp,\parallel}^{(i)}(t_c) = \frac{\left\langle \left(\sum_{j=1}^{L} {}^{\perp}f_j^{(i)} \cdot {}^{\perp}S_j(t) \right) \cdot \left(\sum_{j=1}^{L} {}^{\parallel}f_j^{(i)} \cdot {}^{\parallel}S_j(t+t_c) \right) \right\rangle}{\left\langle \sum_{j=1}^{L} {}^{\perp}f_j^{(i)} \cdot {}^{\perp}S_j(t) \right\rangle \cdot \left\langle \sum_{j=1}^{L} {}^{\parallel}f_j^{(i)} \cdot {}^{\parallel}S_j(t+t_c) \right\rangle} \qquad \text{(Eq. 4.1.1-3)}$$

where ${}^{\perp}S_j(t)$ is the fluorescence signal in the *j*-th TCSPC channel of the perpendicular signal at measurement time *t* and ${}^{\parallel}S_j(t+t_c)$ is the fluorescence signal in the *j*-th TCSPC channel of the parallel signal at measurement time.

As described in Paper I fluorescence lifetime filters can be calculated not only for the different polarisations of the same spectral range, but also for any combination of polarisation and *colour*, i.e. $G_{G_\perp,R_\perp}^{(i)}(t_c)$, $G_{G_\parallel+R_\parallel,G_\parallel+R_\parallel}^{(i)}(t_c)$ (see Paper IV). Moreover, with the possibility to discriminate photons pertaining to different population it is possible to cross-correlate different species (sccFCS) and study processes like the interconversion between different FRET states (see Paper I and section 8).

5 Multi-parameter Fluorescence Detection (MFD)

As explained in section 3.4, with the setup used for single-molecule experiments several fluorescence parameters are recorded at once; the combination of more parameters is the basis of Multi-Parameter Fluorescence Detection (MFD). The advantages of this method over standard one-dimensional techniques lie in the fact that with MFD it is possible to distinguish measurement artefacts from real events and to efficiently sort multiple FRET species present in solution simultaneously (Widengren, Kudryavtsev et al. 2006).

5.1 Two-dimensional plots

To illustrate the efficiency of MFD a double stranded DNA molecule, labelled with Alexa 488 and Atto 680 at a distance of 12 base pairs, is investigated. In figure 5.1-1A, the histogrammed values of green to red signal ratio, S_G/S_R, green lifetime, $\tau_{D(A)}$, and green scatter corrected anisotropy, r_S, represent the results that could be obtained by independent intensity, TCSPC and polarisation experiments, respectively.

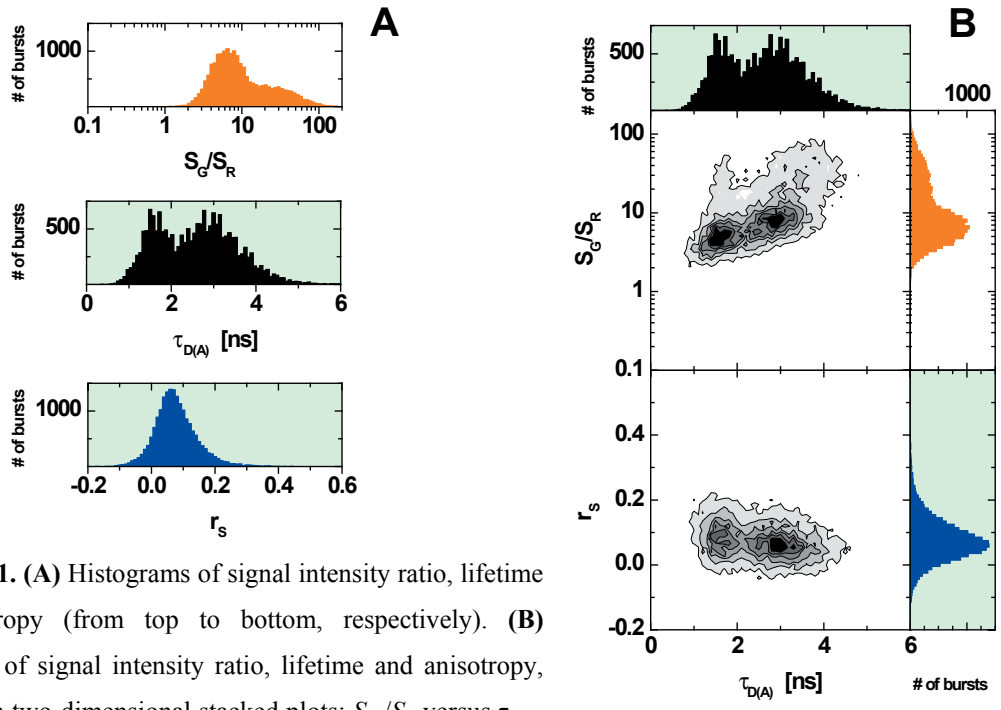

Figure 5.1-1. (A) Histograms of signal intensity ratio, lifetime and anisotropy (from top to bottom, respectively). **(B)** Histograms of signal intensity ratio, lifetime and anisotropy, combined in two-dimensional stacked plots: S_G/S_R versus $\tau_{D(A)}$ (top); r_S versus $\tau_{D(A)}$ (bottom).

Examining the histograms, it is clear that at least two species are present in solution and with the help of equations 2-1, 2-2 and 2.1-2 it would, in principle, be possible to link together the

S_G/S_R, $\tau_{D(A)}$ and r_S values of each population. However, due to the broad distribution of the signals, the matching of the different parameters is subject to a certain degree of uncertainty and the number of species can be underestimated. If the one-dimensional histograms are combined in two-dimensional plots the species are better resolved and turn out to be four instead of two (see figure 5.1-1B). Furthermore, due to the good separation of the different populations, only one portion of data can be selected and further analysed.

5.2 MFD equations

In addition to qualitative analysis it is possible to devise relations between the fluorescence parameters and thus obtain quantitative results. In case of FRET, the fluorescence intensities of donor and acceptor can be expressed modifying equation 3.2-1 to take into account the energy transferred from the donor to the acceptor

$$F_D = \Phi_{FD(0)}\left(1 - E_{FRET}\right) I_{Abs} \qquad \text{(Eq. 5.2-1)}$$

$$F_A = \Phi_{FA} E_{FRET}\, I_{Abs} \qquad \text{(Eq. 5.2-2)}$$

The resulting intensity ratio, F_D/F_A, is independent from the absorbed energy and is a function of quantum yields and FRET efficiency only. Furthermore, if equation 2.2-7a is used to express E_{FRET}, F_D/F_A can be obtained as a function of $\tau_{D(A)}$

$$\frac{F_D}{F_A} = \frac{\Phi_{FD(0)}}{\Phi_{FA}} \cdot \frac{1 - E_{FRET}}{E_{FRET}} = \frac{\Phi_{FD(0)}}{\Phi_{FA}} \cdot \frac{\tau_{D(A)}}{\tau_{D(0)} - \tau_{D(A)}} \qquad \text{(Eq. 5.2-3a)}$$

If plotted on an MFD two-dimensional plot, equation 5.2-3a has the shape of a sigmoidal and, being independent of FRET efficiency, has the property to link, for any given donor-acceptor system, all the possible FRET states. Equation 5.2-3a is a very important tool of MFD because deviations from the curve it describes are indicators of the presence of processes other than FRET, i.e. donor quenching, acceptor quenching or interconversion between different FRET states (see following sections). Considering the relation between lifetime and quantum yield obtained by combining equations 2-2 and 2-3, $\Phi_{FD} = k_f \tau_D$, equation 5.2-3a can be rewritten as

$$\frac{F_D}{F_A} = \frac{k_f}{\Phi_{FA}} \cdot \frac{\tau_{D(0)}\tau_{D(A)}}{\tau_{D(0)} - \tau_{D(A)}} = \frac{k_f}{\Phi_{FA}} \cdot \frac{\tau_{D(A)}}{E_{FRET}} \qquad \text{(Eq. 5.2-3b)}$$

By overlaying equation 5.2-3b on a two-dimensional plot it is possible to estimate the FRET efficiency of each species present in solution.

Having access to lifetime and anisotropy simultaneously the Perrin equation (eq. 2.1-2) can be plotted as well.

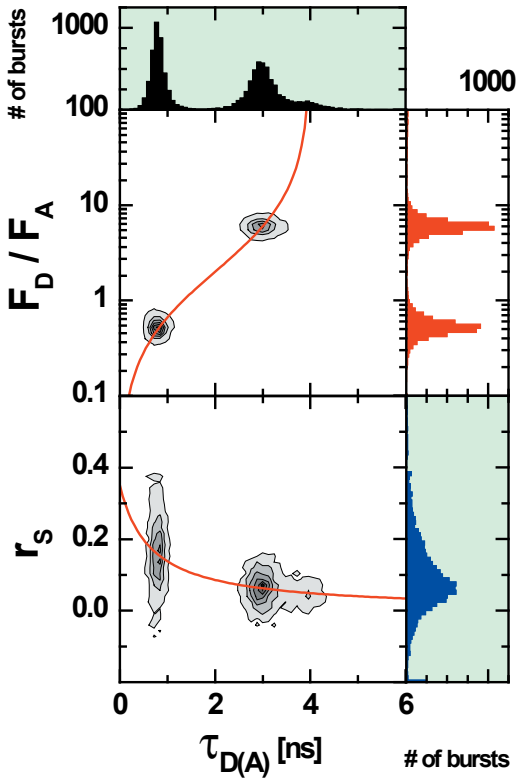

Figure 5.2-1. Combined two-dimensional plots of F_D/F_A and r_S versus $\tau_{D(A)}$. The data are simulations of a three populations system. The species consist of donor and two FRET states with an average number of molecules in the detection volume of 0.001, 0.003 and 0.003, respectively. The parameters used to generate the data are $\tau_{D(0)}$ = 4 ns, τ_A = 2ns, $\Phi_{FD(0)}$ = 0.8, $\Phi_{FA(0)}$ = 0.4, α = 0.01, R_0 = 50 Å, E_{FRET1} = 0.25, E_{FRET2} = 0.80, g_G = 0.5, g_R = 1.0, rotation correlation time ρ = 0.65 ns for all species, diffusion time t_D = 1.5 ms for all species, B_G = 2.8 kHz, B_R = 1.2 kHz and donor F_G = 100 kHz (comparable with measurements performed in our group). Equation 5.2-3a (upper bi-dimesional plot) and the Perrin equation (lower bi-dimesional plot) are plotted in red.

5.2.1 Dye quenching

In this section the deviations from equation 5.2-3a caused by donor or acceptor quenching will be described. In the case of donor quenching, equation 2.2-5a has to be modified to account for the extra quenching process

$$E'_{FRET} = \frac{k_{FRET}}{k_0 + k_Q + k_{FRET}} \qquad \text{(Eq. 5.2.1-1)}$$

where k_Q is the quenching rate constant. For simplicity, in this derivation it is considered a quenching process that can be described by a zero-order kinetics. The results, however, are of general character and can be applied to any quenching process. Analogously to FRET efficiency, the expressions for $\Phi'_{FD(0)}$ and $\tau'_{D(A)}$ have to be modified

$$\tau'_{D(A)} = \frac{1}{k_0 + k_Q + k_{FRET}} \qquad \text{(Eq. 5.2.1-2)}$$

$$\Phi'_{FD(0)} = \frac{k_f}{k_0 + k_Q} \qquad \text{(Eq. 5.2.1-3)}$$

On the other hand, quantum yield of the acceptor is not affected and $\Phi'_{FA} = \Phi_{FA}$. Fluorescence intensity ratio in presence of donor quenching, $\left(\frac{F_D}{F_A}\right)'$, is then equal to

$$\left(\frac{F_D}{F_A}\right)' = \frac{\Phi'_{FD(0)}}{\Phi_{FA}}\left(\frac{1-E'_{FRET}}{E'_{FRET}}\right) = \frac{k_f}{k_0+k_Q}\cdot\frac{k_0+k_Q}{k_{FRET}} = \frac{k_f}{k_{FRET}} = \frac{\Phi_{FD(0)}}{\Phi_{FA}}\left(\frac{1-E_{FRET}}{E_{FRET}}\right) = \frac{F_D}{F_A} \qquad \text{(Eq. 5.2.1-4)}$$

The result of equation 5.2.1-4 combined with the shortening of lifetime leads to a horizontal shift from the curve described by equation 5.2-3a.

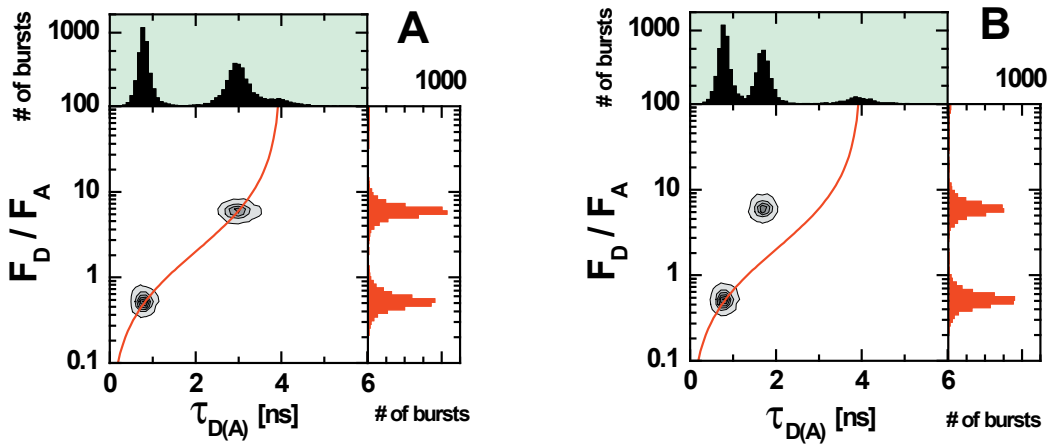

Figure 5.2.1-1. Effect of donor quenching. **(A)** Simulated data as those in figure 5.2-1. **(B)** For the lower FRET state, a donor quenching process with $k_{Q,donor} = k_{0,donor}$ was added to the simulations. Comparing panel A and B, a horizontal shift from the expected behaviour is clearly observed.

In case of acceptor quenching, only the quantum yield of the acceptor will change, $\Phi'_{FA} < \Phi_{FA}$, and as a consequence

$$\left(\frac{F_D}{F_A}\right)' > \frac{F_D}{F_A} \qquad \text{(Eq. 5.2.1-5)}$$

As a result a vertical shift from the theoretical curve is observed.

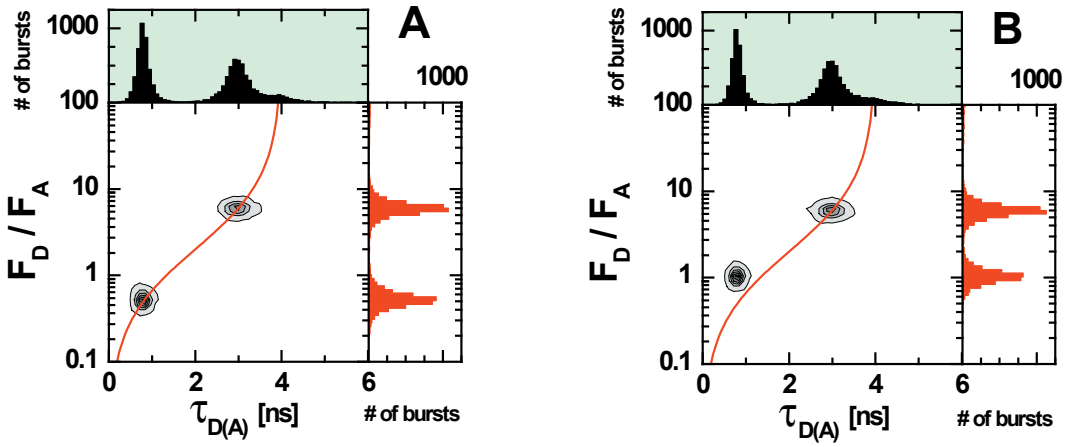

Figure 5.2.1-2. Effect of acceptor quenching. **(A)** Simulated data as those in figure 5.2-1. **(B)** For the higher FRET state, an acceptor quenching process with $k_{Q;acceptor} = k_{0;acceptor}$ was added to the simulations. Comparing panel A and B, a vertical shift from the expected behaviour is clearly observed.

5.2.2 Interconversion of FRET states

In the case of a dynamic system, in which a molecule switches between different states, each characterised by a different transfer efficiency, a deviation from the behaviour described by equation 5.2-3a is observed. For simplicity the case of a two-state system is considered. If the interconversion between the two states is slower than the dwell time in the focus, the molecule shows only one state at the time and resembles the case of a static system with two different species. In the two-dimensional plot, fluorescence bursts are grouped in separate islands, both of which lying on the sigmoidal line of equation 5.2-3a (depending on the time scale of the dynamic process some mixed bursts can still be visible). If the interconversion is of the same order of the dwell time, or faster, each recorded bursts will be a mixture of the two states. In this case the bursts deviate from the sigmoidal line. This effect is due to fluorescence intensity and lifetime of each state being weighted differently in the averaged signals.

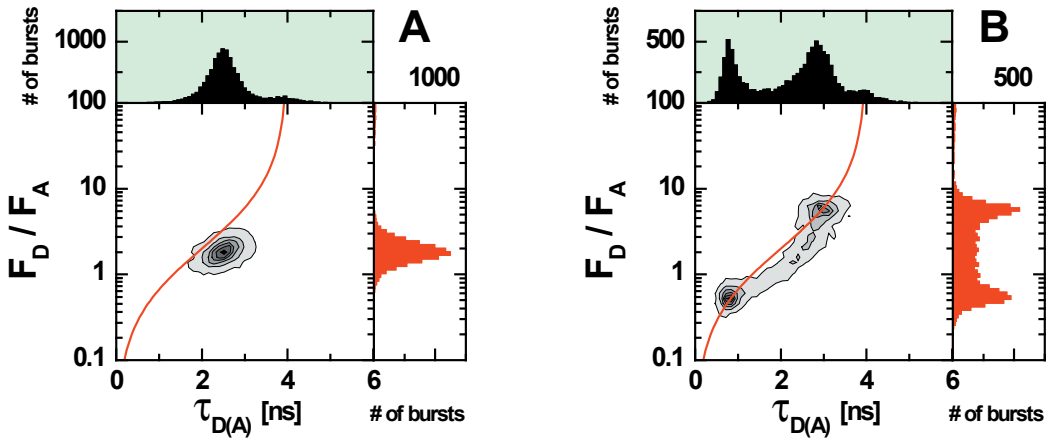

Figure 5.2.2-1. Effect of FRET state interconversion. Two time regimes for the interconversion between the FRET states described in figure 5.2-1, are reported. **(A)** Fast interconversion with rate constants out of the states $k_{12} = k_{21} = 5$ ms^{-1}. Only one island is observed. **(B)** Slow interconversion with rate constants out of the states $k_{12} = k_{21} = 0.1$ ms^{-1}. The two original FRET populations are observed with only few bursts showing averaging.

Fluorescence intensities are obtained by single photon counting and are, therefore, weighted by the fraction of each species, x_i

$$F_{ave,x} = \sum_i x_i F_i \qquad \text{with} \qquad \sum_i x_i = 1 \qquad \text{(Eq. 5.2.2-1)}$$

where *ave,x* stands for species weighted average. In the case of FRET experiments, donor and acceptor intensities result to be dependent on the average FRET efficiency $\sum_i x_i E_i$

$$F_{D,ave,x} \propto \Phi_{FD(0)} \sum_i x_i (1 - E_i) = \Phi_{FD(0)} \left(1 - \sum_i x_i E_i\right) \qquad \text{(Eq. 5.2.2-2)}$$

$$F_{A,ave,x} \propto \Phi_{FA} \sum_i x_i E_i \qquad \text{(Eq. 5.2.2-3)}$$

Fluorescence lifetimes, on the other hand, are obtained by Maximum Likelihood Estimator (MLE) fitting (Maus, Cotlet et al. 2001) and are therefore fluorescence intensity weighted average quantities

$$\tau_{ave,a} = \sum_i a_i \tau_i \qquad \text{with} \qquad a_i = \frac{x_i \tau_i}{\sum_i x_i \tau_i} \qquad \text{(Eq. 5.2.2-4)}$$

where *ave,a* stands for fluorescence weighted average. Analogously to equation 5.2.2-1, $\sum_i x_i\tau_i$ in equation 5.2.2-4 represents the species weighted average lifetime, $\tau_{ave,x}$.

To express the relation between fluorescence intensity ratio and lifetime averages, a new equation has to be devised. In the case of only two interconverting species $\tau_{ave,x}$ is

$$\tau_{ave,x} = x_1\tau_1 + (1-x_1)\tau_2 \qquad \text{(Eq. 5.2.2-5)}$$

while $\tau_{ave,a}$ is

$$\tau_{ave,a} = a_1\tau_1 + (1-a_1)\tau_2 = \frac{x_1\tau_1^2 + (1-x_1)\tau_2^2}{\tau_{ave,x}} \qquad \text{(Eq. 5.2.2-6a)}$$

Calculating x_1 from equation 5.2.2-5 and substituting it in 5.2.2-6a, $\tau_{ave,a}$ can be expressed as a function of $\tau_{ave,x}$

$$\tau_{ave,a} = \frac{\left(\frac{\tau_{ave,x}-\tau_2}{\tau_1-\tau_{ave,x}}\right)\tau_1^2 + \left(1-\frac{\tau_{ave,x}-\tau_2}{\tau_1-\tau_{ave,x}}\right)\tau_2^2}{\tau_{ave,x}} \qquad \text{(Eq. 5.2.2-6b)}$$

that rearranged results in

$$\tau_{ave,x} = \frac{\tau_1\tau_2^2 - \tau_2\tau_1^2}{\tau_{ave,a}(\tau_1-\tau_2) - \tau_1^2 + \tau_2^2} \qquad \text{(Eq. 5.2.2-7)}$$

If equation 5.2-3a is written for species weighted averages

$$\left(\frac{F_D}{F_A}\right)_{ave,x} = \frac{k_f}{\Phi_{FA}}\tau_0\frac{\tau_{ave,x}}{\tau_0-\tau_{ave,x}} \qquad \text{(Eq. 5.2.2-8)}$$

and $\tau_{ave,x}$ is expressed as in equation 5.2.2-7, the desired relation is obtained

$$\left(\frac{F_D}{F_A}\right)_{ave,x} = \frac{k_f}{\Phi_{FA}}\tau_0 \frac{\tau_1\tau_2^2 - \tau_2\tau_1^2}{\tau_0\left[\tau_{ave,a}(\tau_1 - \tau_2) - \tau_1^2 + \tau_2^2\right] - \tau_1\tau_2^2 + \tau_2\tau_1^2} \qquad \text{(Eq. 5.2.2-8)}$$

Equation 5.2.2-8 presupposes the knowledge of the lifetimes of the interconverting states and as such can only be used in combination with other independent measurements of the single states or as an *a posteriori* test.

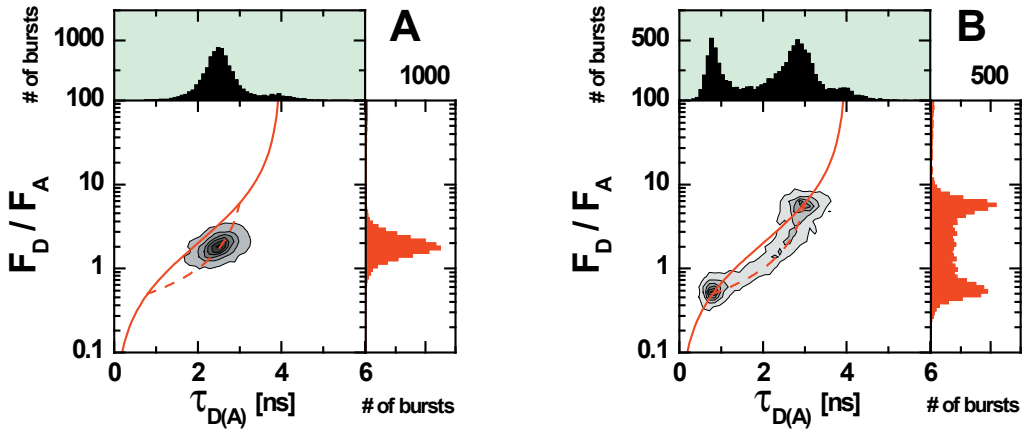

Figure 5.2.2-2. $\tau_{D(A)}$ averaging correction. The dashed line represents equation 5.2.2-8. The correction is independent from the time regime and, therefore, it is the same for panel A and B.

An effect similar to dynamic averaging of the FRET states can be observed in thick solutions of heterogeneous samples. In this case, in fact, more than one molecule is simultaneously present in the focus and mixing of the signals from the different species ensues. The two sources of averaging can be easily discriminate by checking: (i) the presence of any dynamic term in FCS (section 4) or in dynamic PDA (section 6.4), (ii) the number of bursts per second that in single-molecule experiments is around 10.

5.2.3 Dye linker movement

As a special case of interconversion of FRET states the effect produced by the chain diffusion of the dye linkers will be discussed in this section. As shown in figure 2-1B, dyes are usually coupled to biomolecules through long aliphatic chains. Due to the flexibility of these chains the fluorophores are allowed to explore multiple positions in space during the diffusion of the labelled molecule in the focus. Independently of the chain diffusion timescale, the detected signals are averaged over different FRET states, and therefore deviation from equation 5.2-3a are expected. As in section 5.2.2, a correction function will be calculated.

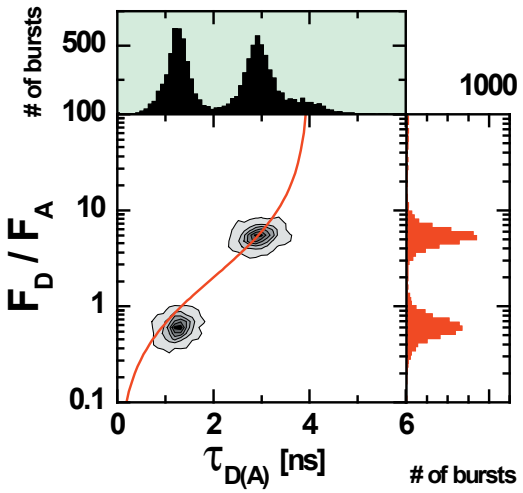

Figure 5.2.3-1. Effect of linker movement. The system in figure 5.2-1 is modified by simulating a σ = 6 Å and inerconversion rate constansts between the $R_{DA} \pm \sigma$ states of 5 ms^{-1}.

Due to chain diffusion each possible donor-acceptor distance R_{DA} will produce two distances $R_{DA} \pm \sigma$, where σ is the maximum displacement introduced by the linker movement. Knowing σ, the $\tau_{ave,a}$ and $\tau_{ave,x}$ associated to $R_{DA} \pm \sigma$ can be calculated. If $\tau_{ave,x}$ is plotted as a function of $\tau_{ave,a}$, figure 5.2.3-2, it is possible to obtain, by polynomial fitting, a correction function which expresses an average as a function of the other

$$\tau_{ave,x} = f\left(\tau_{ave,a}\right) \qquad \text{(Eq. 5.2.3-1)}$$

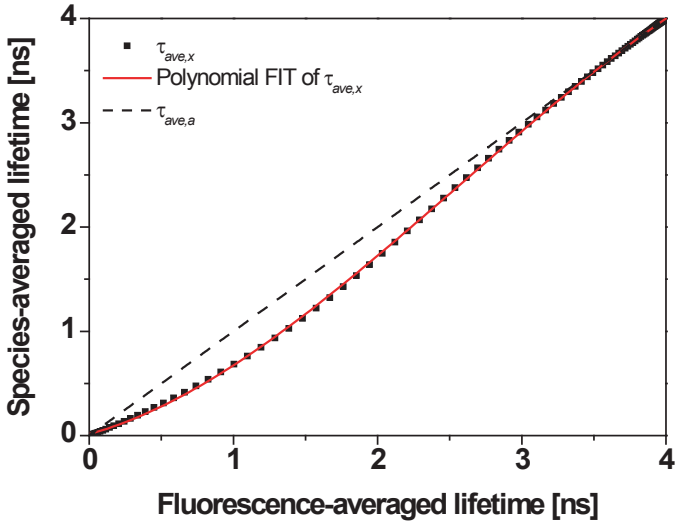

Figure 5.2.3-2. Correction function for linker movement. $\tau_{ave,\,x}$ is plotted as a function of $\tau_{ave,\,a}$ (black squares) and fitted by a polynomial of third order (red line, $\tau_{ave,x} = 0.0142 + 0.38\tau_{ave,a} + 0.32\tau_{ave,a}^2 - 0.042\tau_{ave,a}^3$). At $\tau_{ave,x}$ = 3 ns the difference between averages is negligible while at $\tau_{ave,x}$ = 1 ns it becomes substantial (comparison

between the red line and the dashed black line). This explains why in figure 5.2.3-1 only the higher FRET population is off the sigmoidal line.

Substitution of equation 5.2.3-1 in equation 5.2.2-8 yields the corrected relation between $\left(\frac{F_D}{F_A}\right)_{ave,x}$ and $\tau_{ave,a}$

$$\left(\frac{F_D}{F_A}\right)_{ave,x} = \frac{k_f}{\Phi_{FA}}\tau_0\frac{\tau_{ave,x}}{\tau_0-\tau_{ave,x}} = \frac{k_f}{\Phi_{FA}}\tau_0\frac{f\left(\tau_{ave,a}\right)}{\tau_0-f\left(\tau_{ave,a}\right)} \qquad \text{(Eq. 5.2.3-2)}$$

Bulk TCSPC measurements on short DNA fragments (unpublished results), indicate that for the linkers described in figure 2-1C σ is 6Å. However, the value can vary from molecule to molecule and usually different values for σ should be tested.

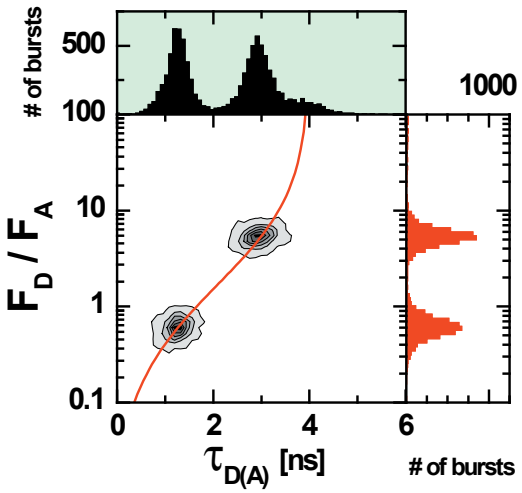

Figure 5.2.3-3. Corrected sigmoidal line. The red line is obtained by substituting $\tau_{ave,x} = 0.0142 + 0.38\tau_{ave,a} + 0.32\tau_{ave,a}^2 - 0.042\tau_{ave,a}^3$ in equation 5.2.3-2.

5.3 Conversion of fluorescence intensity ratio into E_{FRET} and R_{DA}

The MFD relations shown so far have been developed for F_D/F_A because it is the most direct signal that can be computed from signal ratio S_G/S_R. Sometimes, however, it is better to plot quantities as R_{DA} and E_{FRET} that are immediately recognisable. In these cases the equations can be easily rearranged taking into account the relations

$$E = \left[\frac{F_D \Phi_{FA}}{F_A \Phi_{FD(0)}} + 1 \right]^{-1} \qquad \text{(Eq. 5.3-1)}$$

$$R_{DA} = R_0 \sqrt[6]{\frac{F_D \Phi_{FA}}{F_A \Phi_{FD(0)}}} \qquad \text{(Eq. 5.3-2)}$$

6 Probability Distribution Analysis (PDA)

When analysing single-molecule FRET data, the goal is to obtain distances with the highest accuracy possible. This task is complicated by the fact that fluorescence bursts are not defined by a single value of lifetime or signal intensity but, due to shot-noise and background, are distributed around certain values. The most common practice is to interpret the data simply as a sum of Gaussian distributions centred on mean values that are intended to represent the average lifetime or fluorescence signal. The limit of this procedure lies in the scarce importance given to the shape of the distributions. In fact, if it is true that the detection of photons is a stochastic process and a distribution of values is indeed expected, shot-noise, it is very difficult to calculate the exact broadening beforehand. Moreover, the small deviations of the shape are usually disregarded even if they can be directly translated into the information about the conformation's distributions.

To distinguish between shot-noise limited distributions and distributions arising from conformational heterogeneities probability distribution analysis, PDA, was developed.

6.1 Theory

Considering the SMD setup described in section 3.4, the stream of detected photons can be schematically represented as in figure 6.1-1.

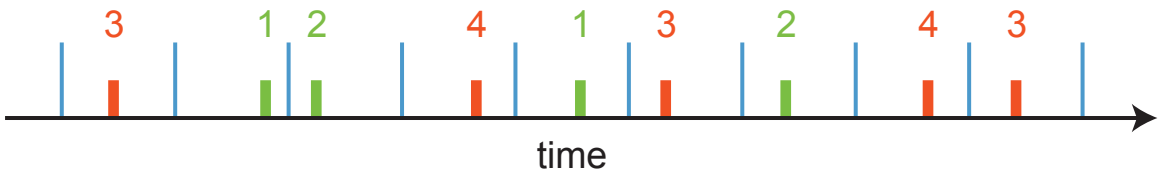

Figure 6.1-1. Stream of detected photons. Laser pulses are indicated in light blue and the detected photons are colour coded according to their spectral range. The numbers refer to the detector registering the photon: 1 and 3 for parallel channels; 2 and 4 for perpendicular channels.

To each photon is assigned a channel number from 1 to 4 depending on whether the photon is recorded in the green parallel, red parallel, green perpendicular or red perpendicular channel. If we consider the signal recorded in two different channels i and j, with the PDA method we calculate the theoretical probability of recording that particular combination of S_i and S_j, $P(S_i, S_j)$ (Antonik, Felekyan et al. 2006; Kalinin, Felekyan et al. 2007; Kalinin, Felekyan et al. 2008)

$$P(S_i, S_j) = \sum_{F_i + B_i = S_i, F_j + B_j = S_j} P(F) P(F_i, F_j | F) P(B_i) P(B_j) \qquad \text{(Eq. 6.1-1)}$$

where $P(F)$ describes the probability of observing F fluorescence photons ($F = F_i + F_j$), $P(F_i, F_j | F)$ is the conditional probability of observing a certain combination of fluorescence photons in the i-th and j-th channel provided the total number of fluorescence photons is F and $P(B_i)$ and $P(B_j)$ represent the background intensity distributions for the i-th and j-th channel, respectively. Of all the possible combinations of channels not all are of real interest; our attention will be focused on $P(S_1, S_3)$, $P(S_2, S_4)$ for polarisation experiments and $P(S_{1+3}, S_{2+4})$ (which corresponds to $P(S_G, S_R)$) for FRET experiments. In the following, to simplify the derivations, the photon stream is considered to be divided into bins of equal length, Δt.
The last three terms of equation 6.1-1 can be analytically described. Background intensity is described by a Poisson distribution (Fries, Brand et al. 1998)

$$P(B) = \frac{\langle B \rangle^B \exp[-\langle B \rangle]}{B!} \qquad \text{(Eq. 6.1-2)}$$

where $\langle B \rangle$ is the average number of background photons per time window. For FRET and polarisation experiments, the conditional probability $P(F_i, F_j | F)$ is described by a binomial distribution, see equation 6.1-3. In these experiments, in fact, the recorded photon is either green or red, parallel or perpendicular in respect to the linearly polarised excitation light, see sections 6.1.1 and 6.1.2

$$P(F_i, F_j | F) = \frac{F!}{F_i!(F - F_i)!} p_i^{F_i} (1 - p_i)^{F - F_i} \qquad \text{(Eq. 6.1-3)}$$

Here, p_i is the probability that the emitted photon is green or red, parallel or perpendicular. $P(F)$ is not directly measurable but can be modelled analytically (Fries, Brand et al. 1998). However, to avoid any *a priori* assumption it is preferable to substitute it with a measurable quantity. From equations 3.4.1-1a and 3.4.1-1b we know that $F = S - B$, therefore, under the assumption that S and B are uncorrelated ($S >> B$) we can substitute $P(F)P(F_i, F_j | F)$ with $P(S)P(F_i, F_j | S - B_i - B_j)$, where $P(S)$ is directly measurable

$$P(S_i, S_j) = \sum_{F_i + B_i = S_i, F_j + B_j = S_j} P(S) P(F_i, F_j | S - B_i - B_j) P(B_i) P(B_j) \qquad \text{(Eq. 6.1-4)}$$

It is evident from equation 6.1-4 that when fitting the distribution $P(S_i, S_j)$, the only floating parameter is the probability p_i.

In the case of low photon counts ($S \approx B$) the substitution made in equation 6.1-4 is not correct anymore and a model function of $P(F)$, $P_M(F)$, has to be calculated explicitly.

For a single species $P_M(F)$ can be expressed as a weighted sum of Poisson distributions, representing contributions from different spatial elements of the illumination volume (Rigler and Mets 1992; Fries, Brand et al. 1998; Kask, Palo et al. 1999)

$$P_M(F) = \sum_i P(q_i) \frac{q_i^F \exp(-q_i)}{F!} \qquad \text{(Eq. 6.1-5)}$$

where q_i is the expected number of photons emitted by a molecule situated in the ith volume element, and $P(q_i)$ the probability of finding a molecule in the corresponding volume element. Equation 6.1-5 does not require any *a priori* assumptions regarding the distribution of $P(q_i)$ and hence of shape of the detection volume, which is one of the most notable differences between the PDA and FIDA methods (Kask, Palo et al. 1999; Kask, Palo et al. 2000). The distribution of $P(q_i)$ is reconstructed by using the maximum entropy method (Livesey and Skilling 1985; Brochon 1994), that is by maximising the function

$$\Theta = vs - \chi^2 \rightarrow MAX \qquad \text{(Eq. 6.1-6)}$$

where v is a constant, s an entropy-like function for the coefficients q_i ($s = \sum_i - P(q_i) \log P(q_i) + const$) and χ^2 is estimated through

$$\chi^2 = \sum_{S=0}^{S_{Max}} W(S) [P(S) - P_M(F) \otimes P(B)]^2 \qquad \text{(Eq. 6.1-7)}$$

In equation 6.1-7 the weights $W(S)$ are equal to 1/ $P(S)$ because each point of the experimental intensity distribution $P(S)$ obeys Poisson statistics.

By fitting equation 6.1-1 or 6.1-4 we gain simultaneous access to S_i and S_j and therefore we can generate 1D histograms of any parameter that can be expressed as a function of S_i and S_j, such as:

- S_G/S_R, proximity ratio, E_{FRET} and R_{DA} for FRET experiments (section 6.1.1)
- polarisation, experimental anisotropy and scatter-corrected anisotropy for polarisation experiments (section 6.1.2)

6.1.1 FRET experiments

In FRET experiments, equation 6.1-3 can be rewritten as (Antonik, Felekyan et al. 2006)

$$P\left(F_G, F_{RT} \middle| F\right) = \frac{F!}{F_G!\left(F - F_G\right)!} p_G^{F_G} \left(1 - p_G\right)^{F - F_G} \qquad \text{(Eq. 6.1.1-1a)}$$

or

$$P\left(F_G, F_{RT} \middle| F\right) = \frac{F!}{F_{RT}!\left(F - F_{RT}\right)!} \varepsilon^{F_{RT}} \left(1 - \varepsilon\right)^{F - F_{RT}} \qquad \text{(Eq. 6.1.1-1b)}$$

where p_G is the probability that a detected photon is green , ε the probability that a detected photon is red ($F_G + F_{RT} = F$ and $p_G + \varepsilon = 1$). Because of its definition, ε represents an apparent transfer efficiency (Antonik, Felekyan et al. 2006) and is related to E_{FRET} through equation 6.1.1-2

$$\varepsilon = \frac{F_{RT}}{F_G + F_{RT}} = 1 - \frac{1}{1 + \frac{\Phi_{FA}}{\Phi_{FD} G} \frac{E}{\left(1 - E\right)} + \alpha} \qquad \text{(Eq. 6.1.1-2)}$$

For the definition and relationship between the different fluorescence signals refer to sections 3.4.1 and 5.2.

The theoretical 1D histograms of E_{FRET} are built calculating the sum of probabilities $P(S_G, S_R)$ for which the corresponding efficiency falls into the same i-th histogram bin

$$P\left(E_i \le E < E_{i+1}\right) = \sum_{E_i \le E(S_G, S_R) < E_{i+1}} P\left(S_G, S_R\right) \qquad \text{(Eq. 6.1.1-3)}$$

Other parameters frequently used in FRET experiments, that depended on S_G and S_R are the intensity ratio S_G/S_R, the proximity ratio $S_R/(S_G+S_R)$, and the donor-acceptor distance R_{DA}

$$R_{DA} = R_0 \sqrt[6]{\frac{S_G - B_G}{G\left(S_R - \alpha\left(S_G - B_G\right) - B_R\right)}} \qquad \text{(Eq. 6.1.1-4)}$$

6.1.2 Polarisation experiments

In polarisation experiments, equation 6.1-3 can be rewritten as (Kalinin, Felekyan et al. 2007)

$$P\left(F_{\parallel}, F_{\perp} \middle| F\right) = \frac{F!}{F_{\parallel}!\left(F - F_{\parallel}\right)!} p_{\parallel}^{F_{\parallel}} \left(1 - p_{\parallel}\right)^{F - F_{\parallel}} \qquad \text{(Eq. 6.1.2-1a)}$$

or

$$P\left(F_{\parallel}, F_{\perp} \middle| F\right) = \frac{F!}{F_{\perp}!\left(F - F_{\perp}\right)!} p_{\perp}^{F_{\perp}} \left(1 - p_{\perp}\right)^{F - F_{\perp}} \qquad \text{(Eq. 6.1.2-1b)}$$

where $p_{||}$ is the probability that a detected photon's polarisation is parallel to the linearly polarised excitation light (channel 1 for green and 2 for red), $p_{\perp}$ the probability that a detected photon's polarisation is perpendicular to the linearly polarised excitation light (channel 3 for green and 4 for red), $p_{||} + p_{\perp} = 1$ and $F_{\parallel} + F_{\perp} = F$ (in polarisation experiments performed on donor-acceptor samples the total number of photons F refers to the photons of a single colour). Assuming that in one time window the molecule can sample all the possible orientations with respect to the polarisation of the excitation light, the probabilities $p_{||}$ and $p_{\perp}$ are related to fluorescence anisotropy through (Lakowicz 1999; Valeur 2002)

$$p_{\parallel} = \left\langle \frac{F_{\parallel}}{F_{\parallel} + F_{\perp}} \right\rangle = \frac{1 + 2\langle r \rangle}{2 + \langle r \rangle} \qquad \text{(Eq. 6.1.2-2a)}$$

$$p_{\perp} = \left\langle \frac{F_{\perp}}{F_{\parallel} + F_{\perp}} \right\rangle = \frac{1 - \langle r \rangle}{2 + \langle r \rangle} \qquad \text{(Eq. 6.1.2-2b)}$$

As described in section 3.4.2 fluorescence signal is additionally depolarised by the microscope objective, therefore taking into account the l_1 and l_2 correction factors (Koshioka, Saski et al. 1995)

$$p_{\parallel} = \frac{1 + \langle r \rangle (2 - 3l_1)}{1 + \langle r \rangle (2 - 3l_1) + G - G\langle r \rangle (1 - 3l_2)}; \qquad p_{\perp} = 1 - p_{\parallel} \qquad \text{(Eq. 6.1.2-3)}$$

As in FRET experiments, once we have calculated $P(S_{\parallel}, S_{\perp})$, it is possible to build the theoretical 1D histograms of several parameters of interest e.g. scatter corrected anisotropy, r_S, (Eq. 3.4.2-1), experimental anisotropy, r_{exp}, (Eq. 3.4.2-2) and polarisation, p,

$$p = \frac{\left(S_{\parallel} - \langle B_{\parallel} \rangle\right) - \left(S_{\perp} - \langle B_{\perp} \rangle\right)}{\left(S_{\parallel} - \langle B_{\parallel} \rangle\right) + \left(S_{\perp} - \langle B_{\perp} \rangle\right)} \qquad \text{(Eq. 6.1.2-4)}$$

6.2 Multiple species and brightness correction

The factorisation of equation 6.1-1 is valid only in the case that all four distributions are independent. In particular it is assumed that the distributions $P(F)$ and $P(F_i, F_j | F)$ are uncorrelated. These assumptions hold only if one fluorescence state is considered or if all fluorescence states have the same total brightness. In real experiments the assumptions made are the exception rather than the rule, therefore equation 6.1-1 has to be extend to take into account the presence of multiple fluorescence states. Let us consider n different states, each one characterised by fluorescence intensity distribution $P_k(F)$. If we assume that the distributions $P_k(F)$ are relative to the same concentration and only single-molecule events are taken into account we can write

$$P(S_i, S_j) = \sum_{k=1}^{n} \left[c_k \sum_{F_i + B_i = S_i, F_j + B_j = S_j} P_k(F) P_k(F_i, F_j | F) P(B_i) P(B_j) \right] \qquad \text{(Eq. 6.2-1)}$$

where $P_k(F_i, F_j | F)$ is the probability to observe a particular combination of F_i and F_j photons for the species k, provided that the total number of fluorescence photons is F. Depending on how well the different species can be separated by a burst classification algorithm and/or additional data are available, different procedures of obtaining the individual $P_k(F)$ can be applied (as described in Paper I)

6.3 Multi-molecular events

The equations derived so far for $P(S_i, S_j)$ are true only for fluorescence intensity distributions of single molecules. When more than one molecule is detected at the same time the observed probability $P(S_i, S_j)$ is a combination of the probabilities $P'(S_i, S_j)$ of the different molecules. To account for multi-molecular events a convolution of m single-molecule terms $P'(S_i, S_j)$ is calculated, where $1/m$ is equal to the dilution factor of the original sample. The convolution can be obtained with the help of generating functions (Kask, Palo et al. 1999; Kask, Palo et al. 2000; Gopich and Szabo 2005) or via 2D discrete Fourier transform, *DFT*, (Saffarian, Li et al. 2007)

$$P(F_i, F_j) = P'(F_i, F_j) \underbrace{\otimes \ldots \otimes}_{m\,times} P'(F_i, F_j) = DFT^{-1}\left(\left[DFT\left(P'(F_i, F_j)\right)\right]^m\right) \qquad \text{(Eq. 6.3-1)}$$

where DFT^{-1} denotes the inverse transform

6.4 Dynamic systems

Usually in FRET experiments due to dye motions, molecular fluctuations, and conformational changes, the experimental system exhibits more than a single FRET efficiency value. Depending on the timescale, such fluctuations may have an effect on the shape of FRET related parameter histograms. In such cases it is necessary to develop a suitable model describing the distribution of FRET efficiencies, $P(E)$, and incorporate that model into the PDA analysis.

If we consider that the molecule has two states, A and B, with the rate constants out of the states being k_A and k_B, respectively, and E_A and E_B the FRET efficiencies of each state, the observed efficiency, E, for a particular time window is given by

$$E = \frac{Q_A T_A E_A + Q_B T_B E_B}{Q_A T_A + Q_B T_B} \qquad T_A + T_B = \Delta t \qquad \text{(Eq. 6.4-1)}$$

In equation 6.4-1 T_A is the total time the molecule spends in state A and T_B the total time it spends in state B. The brightness Q_A and Q_B have the meaning of the total count rate (green plus red) at a given excitation intensity, and at a concentration of one molecule per observation volume. Via equation 6.4-1, the problem of determining the distribution of FRET

efficiencies $P(E)$ is transformed into one of determining a probability density distribution of dwell times $P(T_A)$,

$$P(T_A) =$$

$$= \left[\frac{2k_B k_A}{k_A + k_B} I_0\left(2\sqrt{k_A k_B T_A T_B}\right) + \frac{k_B T_A + k_A T_B}{k_A + k_B} \cdot \frac{\sqrt{k_A k_B}}{\sqrt{T_A T_B}} I_1\left(2\sqrt{k_A k_B T_A T_B}\right) \right] \exp(-k_A T_A - k_B T_B) \qquad \text{(Eq. 6.4-2)}$$

where $I_0()$ and $I_1()$ denote Bessel functions of order 0 and 1, respectively.
For the special case where this integration interval includes either 0 or Δt, the probability that the molecule persists in a single state over the entire time window must be separately calculated and included

$$p(0) = p(T_A = 0) = \frac{k_A}{k_A + k_B} \exp(-k_B \Delta t) \qquad \text{(Eq. 6.4-3a)}$$

$$p(\Delta t) = p(T_B = 0) = \frac{k_B}{k_A + k_B} \exp(-k_A \Delta t) \qquad \text{(Eq. 6.4-3b)}$$

The extension of PDA theory to dynamic systems constitutes the main topic of Paper III and for further details it ca be seen there.

6.5 Dye heterogeneities

Photophysical processes, transitions of the dyes between preferential environments and dye linker movement can be the cause of dye brightness heterogeneities.
As a consequence, in presence of such processes the fluorescence bursts are mixtures of different FRET states and the recorded signal is an average of the different FRET signals (for the effects of different FRET averaging regimes see (Wozniak, Schröder et al. 2008)).
The averaging effect introduces an extra broadening in the photon distributions and R_{DA} histograms, for instance, are not described anymore by single distances but rather by Gaussian distribution of distances characterised by a mean distance $R_{DA,mean}$ and half width HW. If $R_{DA,mean}$ reflects the effective mean distance between the dyes, HW on the contrary is an

apparent parameter and there is no obvious relation between its value, 2Å to 4Å in our experiments, and the source of the broadening.

Dye heterogeneities will obviously affect dynamic PDA too. Unfortunately a formal description for the interconversion between Gaussian distributions of distances to include in PDA theory is not trivial to derive and an approximation has to be made. Keepng in mind that in PDA each Gaussian distribution of distances can be formally described by the sum of two single distances: $R_{DA,mean}$-HW and $R_{DA,mean}$+HW, the interconversion between two Gaussian distributions can be approximated with the sum of two dynamic terms with the same rate constants: one for the interconversion between R_{DA1}-HW_1 and R_{DA2}-HW_2, and one for the interconversion between R_{DA1}+HW_1 and R_{DA2}+HW_2. The model is schematically described in figure 6.5-1.

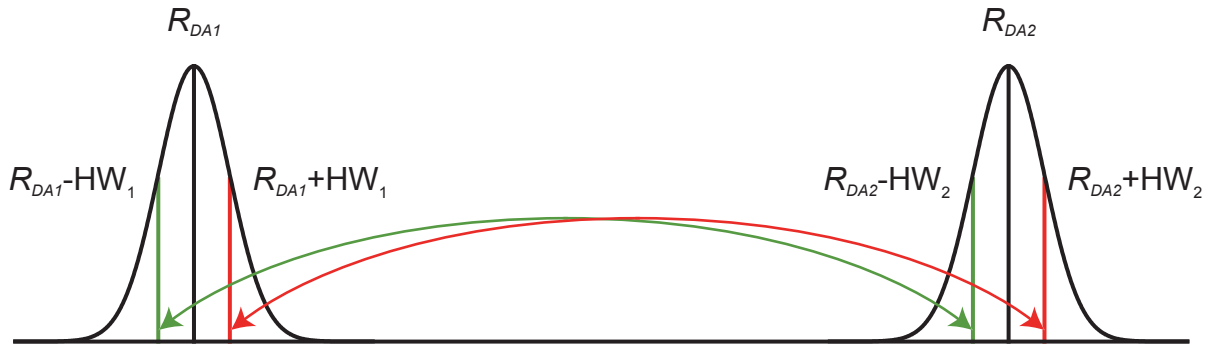

Figure 6.5-1. Schematic representation of the interconversion between two Gaussian distributions of distances as the sum of two dynamic processes. These processes have the same rate constants and correspond to: (i) the interconversion between R_{DA1}-HW_1 and R_{DA2}-HW_2 (green arrows); (ii) the interconversion between R_{DA1}+HW_1 and R_{DA2}+HW_2 (red arrows).

7 Two-step FRET

To test the capabilities of MFD, the principles described in chapter 5 were applied to the study of a complex system. The sample in exam consisted of a double strand of DNA labelled with three fluorophores: one donor, D, and two acceptors, A1 and A2. The dyes were chosen and positioned along the double helix so that it was possible to have FRET between D and A1 and between A1 and A2. In this way the energy absorbed by the donor could be transferred by two consecutive FRET steps to the second acceptor, A2. The dyes chosen for this particular sample were Alexa488 (D), Alexa594 (A1) and Atto680 (A2), with DA1 and DA2 distances of 6 and 12 basepairs, respectively.

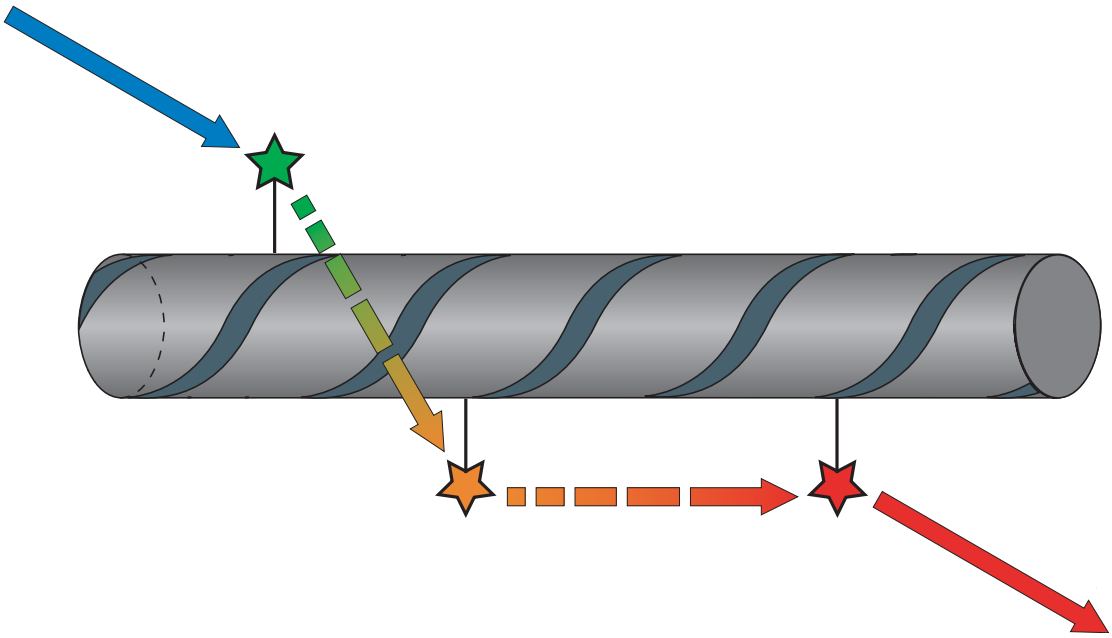

Figure 7-1. Schematic representation of a double stranded DNA labelled with three dyes. Alexa 488, Alexa 594 and Atto 60 are shown as green, orange and red star, respectively. Continuous arrows indicate excitation and emission light, blue and red, respectively. Dashed arrows represent the FRET steps D-A1 (green to orange arrow) and A1-A2 (orange to red arrow). Emission from D and A1 are not reported.

7.1 Material and methods

The experiments were carried out with a confocal epi-illuminated setup as described in section 3.4. The fluorescently labelled complexes were excited by a linearly polarised, active-mode-locked Argon-ion laser (476 nm, 73 MHz, 150 ps). The laser was focused into the dilute solution (< 20 pM) of labelled nucleosome complexes by a 60x water immersion objective (UPLAPO 60x, Olympus, Hamburg, Germany). Fluorescence from the sample was

collected by the same lens and separated from the excitation by a beamsplitter (Q485LP, AHF, Tübingen, Germany). Collected fluorescence photons were divided first into their parallel and perpendicular components by a polarising beamsplitter cube (VISHT11, Gsänger, Planegg, Germany) and then by dichroic beamsplitters (Q595LPXR, AHF and DC660) into three wavelength ranges; (i) below 595 nm; (ii) between 595 and 660 nm; (iii) above 660 nm. Additionally, green (HQ 520/66 nm), yellow (HQ 630/60) and red (HQ 760/150 nm) filters were put in front of the detectors to ensure that only fluorescence photons coming from the donor (Alexa 488) and the two acceptors (Alexa 594, Atto 680) are registered. An estimate of the focal geometry is acquired by determining the diffusion correlation time of 224.5 ± 2.1 µs for Rhodamine 110 in water and knowing its diffusion coefficient of 0.34 ± 0.03 $\mu m^2/ms$. Moreover, correction factors $l_1 = 0.0308$ and $l_2 = 0.0368$ are used to account for the mixing of polarisation by the microscope objective and *G*-factors ($G_{Green} = 1.05$ for the green channels, $G_{Yellow} = 1.09$ for the yellow channels and $G_{Red} = 1.80$ for the red channels) are applied to compensate for the slightly different detection efficiency of the two polarisation components. Detection is performed using six avalanche photodiodes. The signals from all detectors are passed through a passive delay unit and two routers to two synchronised time-correlated single photon counting boards (SPC 132, Becker and Hickl, Germany) which are connected to a PC. Fluorescence bursts are distinguished from the background of 5-6 kHz by applying certain threshold intensity criteria (0.1 ms interphoton time, 80 photons minimum per burst).
Two-step FRET samples were obtained by annealing three different DNA strands:

TF-D: 5′-d(GCA ATA CTT CTC GTC GTA ATA AA**T(Alexa488)** AAT GAA TGG TAA TAG CAA TAA ATA TCT AAT AGG CCG)

TF-A1: 5′-d(**T(Alexa594)**TC ATT ATT TAT TAC GAC GAG AAG TAT TGC)

TF-A2: 5′-d(CGG CCT ATT AGA TAT TTA TTG CTA **T(Atto680)**TA CCA)

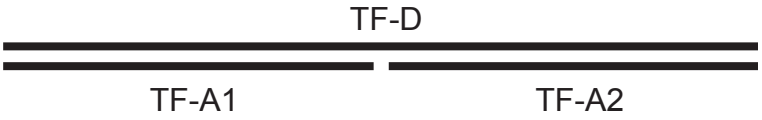

Figure 7.1-1. Annealing scheme of the two-step FRET sample.

DNA strands were purchased from IBA, Göttingen, Germany (TF-D and TF-A2) and from Purimex, Grebenstein, Germany (TF-A1). Three strands were needed to avoid the problems relative to the synthesis of double labelled DNA single strands at specific sites.
Atto 680 is a commercially available dye still patent pending and therefore its structure has not been disclosed yet (it is known that the dye belongs to the oxazine family, figure 7.1-2, personal communication from ATTO-TEC, Siegen, Germany).

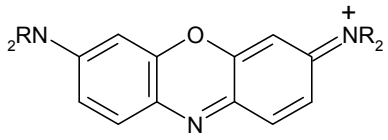

Figure 7.1-2. Generic structure of an oxazine dye

The samples were hybridised in two steps: (i) a solution of TF-D and TF-A1 (3.5 and 10.5 µM, respectively) in buffer (10 mM Na-Cacodylate, 100 mM NaCl, 10 mM $MgCl_2$ pH=7.5) was heated up to 70 °C and let cool overnight; (ii) 10µl of the previous solution were mixed with 2.1 µl of a solution 90 µM of TF-A1, heated up to 70 °C and let cool overnight.
All measurements were performed at 20 °C in buffer (20 mM Tris, 50 mM NaCl, 0.2 mM EDTA, pH=7.5).
As controls, DA1 and DA2 labelled samples were prepared as well. These molecules were obtained using unlabelled analogues of the TF-A2 and TF-A1 strands, respectively (the sample shown in section 5.1 corresponds therefore to a DA2 sample).

7.2 Single-molecule experiments

Due to the incomplete labelling of the single DNA strands, annealing of TF-D, TF-A1 and TF-A2 resulted in a mixture of DA1A2, DA2, DA1 and Donor-only (DOnly) labelled molecules. As a consequence more than one population was detected in SMD experiments (see figure 7.2-1).

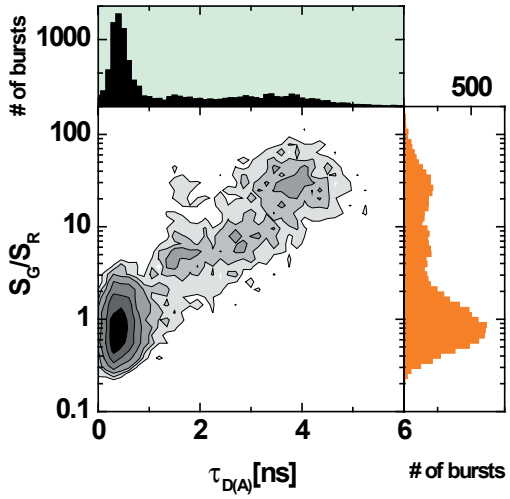

Figure 7.2-1. S_G/S_R versus $\tau_{D(A)}$ plot of a two-step FRET sample.

To successfully sort and analyse the different species sub-ensemble analysis was necessary, the populations were chosen as indicated in figure 7.2-2.

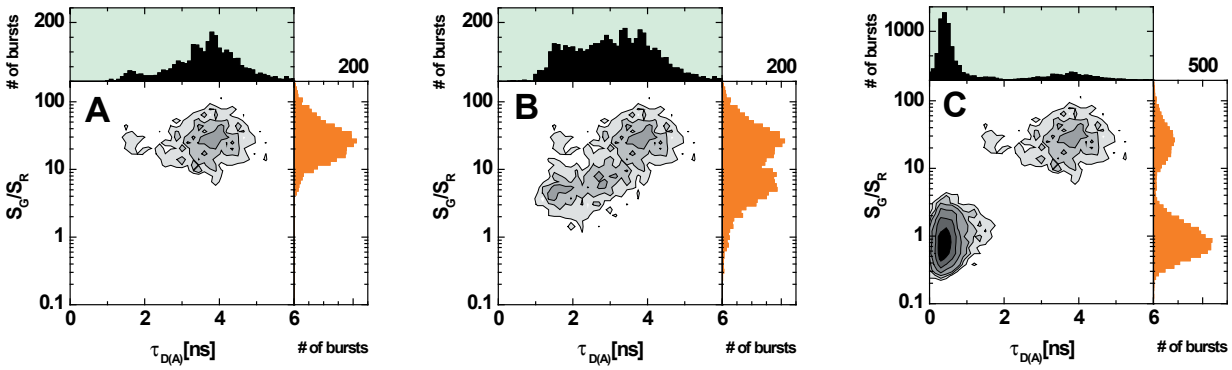

Figure 7.2-2. Sub-ensemble populations used in graphical MFD analysis. Lifetime, $\tau_{D(A)}$, is used as the selection criterion.

7.2.1 Donor only molecules

The most abundant species in figure 7.2-2A displayed the highest intensity ratio and a lifetime consistent with free Alexa488 ($\tau_{D(A)}$ = 3.85 ns). This species was therefore associated with DOnly labelled molecules. The smaller population, on the other hand, had almost the same intensity ratio but a shorter lifetime ($\tau_{D(A)}$ = 1.65 ns). As explained in section 5.2.1, the horizontal shift of the smaller population is not consistent with a FRET related process but rather with a donor quenching (the nature of which will not be addressed in this thesis).

Knowing the $\Phi_{FD(0)}$ of Alexa 488 ($\Phi_{FD(0)}$ = 0.82), with the help of equations 2-2 and 2-3, it was possible to calculate the quantum yield of Alexa 488 in presence of the quenching

process, $\Phi_{FD(Q)}$ = 0.35. The estimation of $\Phi_{FD(Q)}$ is valid only in the hypothesis that the quenching process constitutes just an additional deactivation pathway of the donor (additional rate constatnt k_Q in the denominators of Eq. 2-2 and 2-3) and that the fluorescence rate constant k_f is unaffected by it.

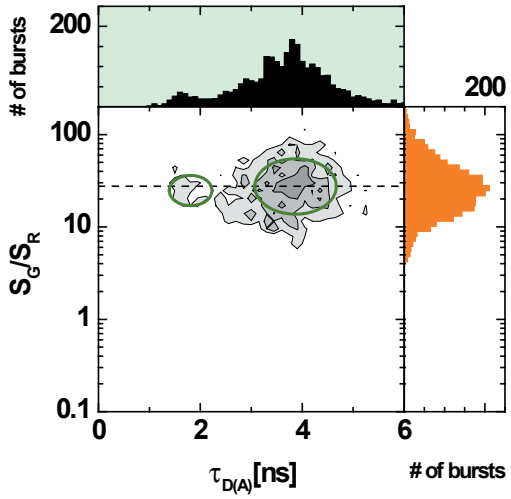

Figure 7.2.1-1. Donor only molecules. The green ellipses are introduced only to guide the eye and do not have any quantitative meaning.

It has to be noted that the horizontal shift described in section 5.2.1 refers to pure fluorescence signal ratio F_D/F_A and not to signal ratio S_G/S_R. For donor only molecules however, F_A is equal to zero making impossible to estimate the donor quenching shift directly from a two-dimensional plot. The derivation of an equation as 5.2.1-3 for S_G/S_R is not straightforward as for F_D/F_A, and in this text only an approximated, but sufficient, relation is proposed. Taking into account equations 3.4.1-4 and 3.4.1-5, for DOnly species S_G and S_R can be expressed as

$$S_G = g_G F_D + B_G \qquad \text{(Eq. 7.2.1-1)}$$

$$S_R = \alpha(g_G F_D) + B_R \qquad \text{(Eq. 7.2.1-2)}$$

In the case that $\alpha(g_G F_D)$ is negligible in comparison to B_R S_G/S_R can be expressed as

$$\frac{S_G}{S_R} \approx \frac{g_G F_D}{B_R} + \frac{B_G}{B_R} = \frac{g_G\left(\frac{\Phi_{FD(Q)}}{\Phi_{FD}}\right)F_{D(Q)}}{B_R} + \frac{B_G}{B_R} = \frac{g_G\left(\frac{\Phi_{FD(Q)}}{\Phi_{FD}} - 1\right)F_{D(Q)}}{B_R} + \frac{g_G F_{D(Q)}}{B_R} + \frac{B_G}{B_R} =$$

$$= \frac{g_G\left(\frac{\Phi_{FD(Q)}}{\Phi_{FD}} - 1\right)F_{D(Q)}}{B_R} + \left(\frac{S_G}{S_R}\right)' = K + \left(\frac{S_G}{S_R}\right)'$$

(Eq. 7.2.1-3)

where $\Phi_{FD(Q)}$ and $F_{D(Q)}$ are the quantum yield and the fluorescence signal of the donor in presence of the quenching process and $(S_G/S_R)'$ is the green to red signal ratio in presence of the quenching process. In the experimental conditions $S_G/S_R \approx 35$ kHz and $K \approx 6$ kHz yielding $(S_G/S_R)' \approx 29$ kHz. Therefore on the logarithmic scale $S_G/S_R \approx (S_G/S_R)'$

7.2.2 DA2 molecules

Once the two populations in figure 7.2-2A were assigned to DOnly species it was possible to study the populations that in figure 7.2-2B displayed $S_G/S_R < 10$. The lifetimes were too long to be compatible with DA1 energy transfer but were in agreement with DA2 transfer (this assumption is verified by comparing Fig. 7. 2-2B to Fig. 5.1-2). However it remained unclear why for DA2 energy transfer two populations were observed. It can be excluded that the two islands come from the two DOnly populations because: (i) the relative fractions of the FRET islands do not correspond to the fractions of the DOnly islands (ii) using in equation 5.2-3a the two quantum yields found for Alexa 488 and the same quantum yield for Atto 680 ($\Phi_{FA2} = 0.27$) it is impossible to obtain curves that overlaid can satisfactory describe the populations. Moreover, the red curve in figure 7.2.2-1 does not describe the second population either and therefore can also be excluded that the two islands arise from different donor-acceptor distances of the same donor acceptor couple.

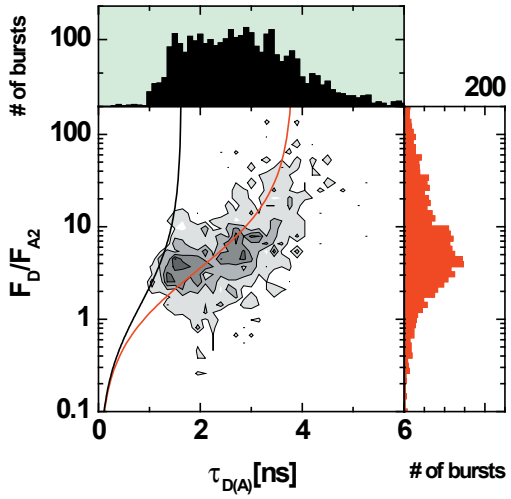

Figure 7.2.2-1. DA2 molecules. The red and black lines represent the equations $F_D/F_{A2} = (\Phi_{FD(0)} / \Phi_{FA2})\ (\tau_{D(A)} /(\tau_{D(0)}-\tau_{D(A)}))$ and $F_D/F_{A2} = (\Phi_{FD(Q)} / \Phi_{FA2})\ (\tau_{D(A)} /(\tau_{D(Q)}-\tau_{D(A)}))$, respectively. Neither of the two curves describes accurately the data.

It was then clear that the observation of two distinct islands was not due to donor heterogeneity and therefore acceptor heterogeneity was tested. Steady state fluorescence did not show any significant difference from the specifications provided by the manufacturer, quantum yield of Atto680 in TF-A2 was $\Phi_{FA2} = 0.27$ whereas the expected value is $\Phi_{FAtto680} = 0.30$. TCSPC however revealed that TF-A2 had bi-exponential decay (see table 7.2.2-1).

	Amplitude	τ_A [ns]	Φ_F
A2’	0.81	2.6	0.30
A2’’	0.19	1.3	0.15

Table 7.2.2-1. Lifetime decay fit for the single strand TF-A2. Quantum yields, Φ_{FA}, were calculated from $\Phi_{FA2} = 0.27$.

Under the assumption that the quantum yield measured with steady state signal gives the average of the two populations found by TCSPC (Lakowicz 1999) two separate quantum yields could be calculated $\Phi_{FA2'} = 0.30$ and $\Phi_{FA2''} = 0.15$. Substituting these quantum yields in equation 5.2-3a, two sigmoidal curves were calculated (see fig. 7.2.2-2).

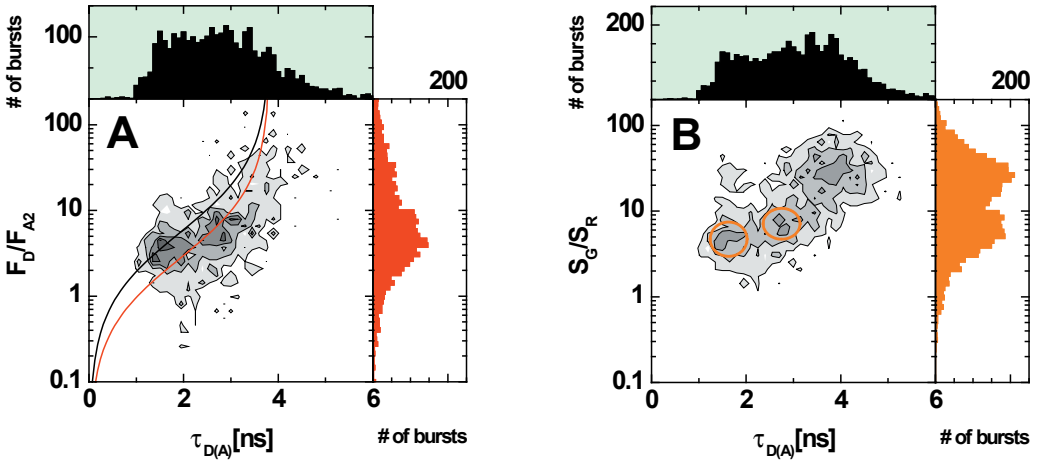

Figure 7.2.2-2. Identification of the two DA2 populations. **(A)** The red and black lines are a representation of the equations $F_D/F_{A2} = (\Phi_{FD(0)} / \Phi_{FA2'}) (\tau_{D(A)} /(\tau_{D(0)}-\tau_{D(A)}))$ and $F_D/F_{A2} = (\Phi_{FD(0)} / \Phi_{FA2''}) (\tau_{D(A)} /(\tau_{D(0)}-\tau_{D(A)}))$, respectively. Both curves satisfactory describe the data. **(B)** The orange circles represent, qualitatively, the regions of the two DA2 populations.

Both DA2 populations, DA2' and DA2'', are well described by the two sigmoidals, confirming that the two species are due to the different states of Atto 680. In this analysis, the discrepancies between the amplitudes in the single strand and the populations in double labelled strand were neglected.

7.2.3 A1 containing molecules

As a last step the populations in figure 7.2.3-1C were analysed. By exclusion all these species contain the first acceptor Alexa 594. In addition, knowing that A2 has two states three species (DA1, DA1A2' and DA1A2'') were expected. From figure 7.2.3-1C, however, it was not possible to distinguish the three different islands, and therefore it had to be checked if all of them were present. If F_D/F_{A1} is plotted versus $\tau_{D(A)}$, part of the bursts are on the sigmoidal but others show a vertical shift, consistent with acceptor quenching.

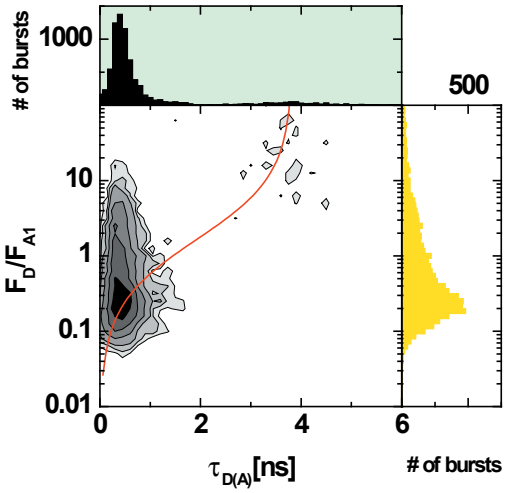

Figure 7.2.3-1. DA1 containing molecules. The red line represents equation $F_D/F_{A1} = (\Phi_{FD(0)} / \Phi_{FA1}) (\tau_{D(A)} /(\tau_{D(0)}-\tau_{D(A)}))$ with $\Phi_{FA1} = 0.50$.

This result is not surprising because energy transfer between A1 and A2 act as quenching of A1. Once the presence of the three species was assured, different pairs of fluorescence parameters were tested in search for a suitable set to separate the species (or at least DA1 from DA1A2). The right set of axis resulted to be S_Y/S_R versus $\tau_{D(A)}$ (Fig. 7.2.3-2B). In this plot it was possible to isolate DA1 (Fig. 7.2.3-2C) that is the population with the highest intensity ratio because it lacks of A2 and hence of red photons other then the ones from B_R. The selected sub-population was plotted again as S_G/S_R versus $\tau_{D(A)}$ (Fig. 7.2.3-2D) and therefore it was possible to individuate it also in figure 7.2.3-2E. The remaining bursts were obviously the completely labelled molecules. The different species are indicated in figure 7.2.3-2F.

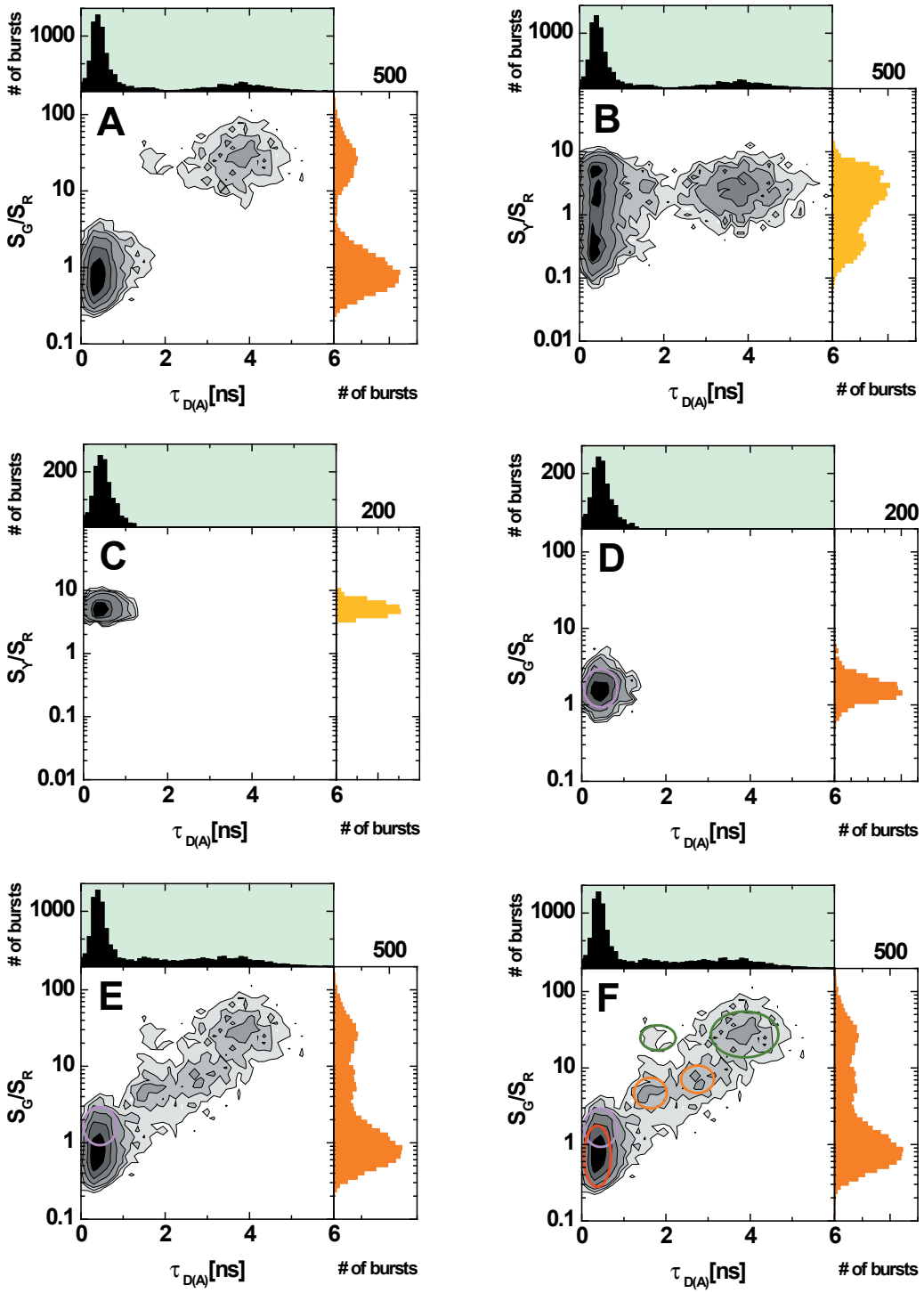

Figure 7.2.3-2. Graphical sub-ensemble analysis. **(A-B)** A1-containing molecules are plotted in two different set of axes. S_Y/S_R versus $\tau_{D(A)}$ yields a good separation of the species. **(C-D)** DA1 molecules are identified and plotted again as S_G/S_R versus $\tau_{D(A)}$ where they are indicated by the light magenta circle. **(E-F)** The DA1 molecules are individuated in the complete sample and DA1A2 molecules are identified by exclusion (red circle).

7.3 Distances

Unfortunately, more than a qualitative analysis of the DA1A2 samples was not possible because the complex photophysics of A2 prevented a reliable calculation of the R_{DA} distances. In fact, when E_{FRET} for DA1A2' and DA1A2'' were estimated with equation 5.2-3b (see fig. 7.3-1), two different values were obtained $E_{FRET,\ DA2'} = 0.34$ and $E_{FRET,\ DA2''} = 0.60$.

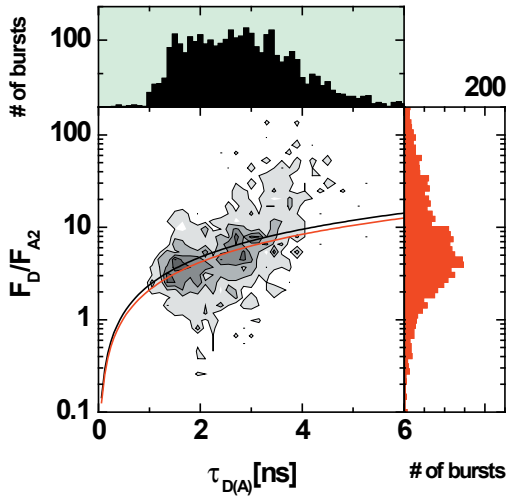

Figure 7.3-1. Estimation of the FRET efficiency for the DA2 populations. The red and black lines are a representation of the equations $F_D/F_{A2} = (k_{fD} / \Phi_{FA2'})\ (\tau_{D(A)} / E_{FRET,\ DA2'})$ and $F_D/F_{A2} = (k_{fD} / \Phi_{FA2''})\ (\tau_{D(A)} / E_{FRET,\ DA2''})$, respectively, with $k_{fD} = 0.214$. The estimated FRET efficiencies are $E_{FRET,\ DA2'} = 0.34$ and $E_{FRET,\ DA2''} = 0.60$.

Under the assumption that the R_{DA} distances for the two states were the same (which implies that the differences between A2' and A2'' are purely photophysical), the discrepancy between the FRET efficiencies could be explained only by a difference in κ^2 and/or J (see eq. 2.2-1). Being impossible to correct for these parameters, the distance information was lost.

7.4 Conclusions

In this section it has been demonstrated graphically how, through the use of MFD, it is possible to divide a complex system in its building blocks, and assign to each population lifetimes and fluorescence intensities.

Moreover, through the use of MFD equations, quenching processes of Alexa 488 and photophysical heterogeneities of Atto 680 were easily detected. Two main A2 populations were individuated and characterised, even though their origin was not investigated. The effect of the quenched population of Alexa 488 was negligible in the determination of quantitative

parameters (E_{FRET} and R_{DA}). On the other hand lack of proper corrections for Atto 680's photophysical properties made impossible to calculate donor-acceptor distances. The data presented here, however, show that due to a good signal separation two-step FRET is a viable method to study multi-molecular assemblies or multi-domain biomolecules.

8 Four-way DNA junctions

Four-way DNA junctions, or Holliday junctions (Holliday 1964), are the branchpoints formed during DNA strand exchange of homologous duplexes and therefore are central intermediates in genetic recombination (Broker and Lehman 1971; Sigal and Alberts 1972; Orrweaver, Szostak et al. 1981; Schwacha and Kleckner 1995), a process important in DNA repair and in providing the genetic diversity necessary for evolution.

When the region of homology extends further from the branching point, it is possible to observe sequential exchange of basepairing and the Holliday junction effectively migrates along the DNA sequence, this process is illustrated in figure 8-1.

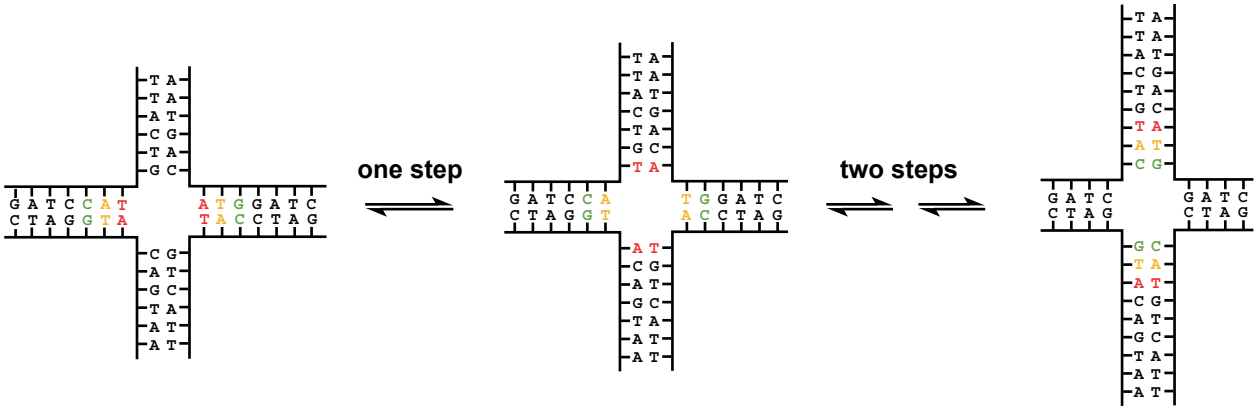

Figure 8-1. Schematic representation of the branch migration of a Holliday junction.

It has been shown that upon addition of divalent metal ions the overall structure folds with the helices coaxially paired in a right-handed anti-parallel fashion, with an angle of approximately 60° between the helices axes (Duckett, Murchie et al. 1988; Murchie, Clegg et al. 1989; Eichman, Vargason et al. 2000). Two conformers are possible depending on the way the four arms are stacking, see figure 8-2.

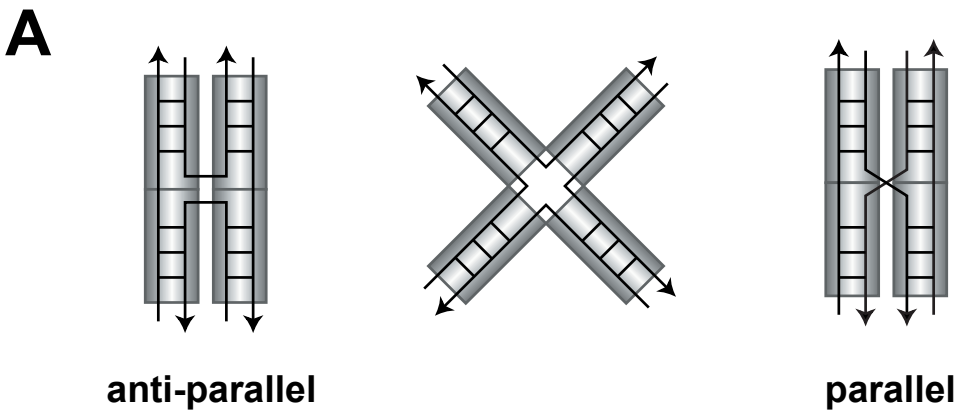

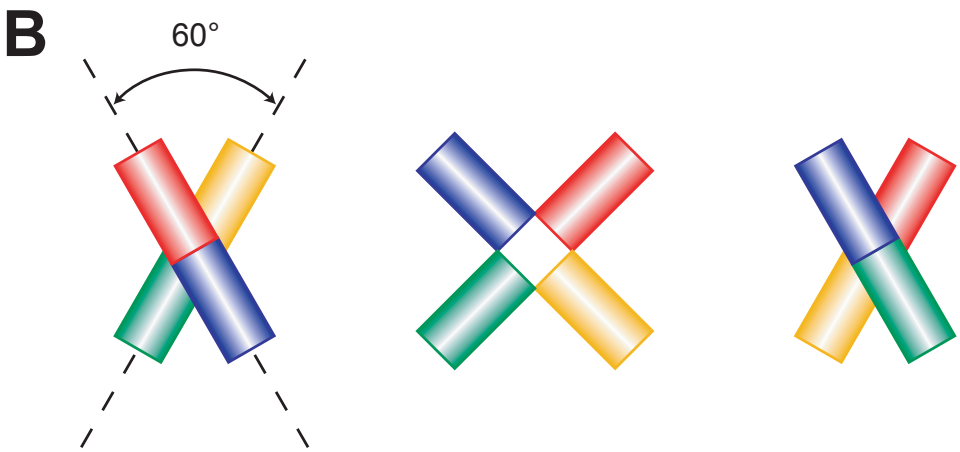

Figure 8-2. Three-dimensional sketches of the Holliday Junction conformers. **(A)** From the cruciform structure, the branches can stack onto each other in two different conformations: (i) anti-parallel, on the left; (ii) parallel, on the right. **(B)** Open and possible anti-parallel stacking conformers.

Depending on the DNA sequence, especially near the branching point, one of the conformer can be predominantly populated. The most probable explanation for the stacking of the branches is that the metal ions shield the electrostatic repulsion between the backbone phosphate moieties allowing the structure to fold. Computational simulations (Olmsted and Hagerman 1994; Fenley, Manning et al. 1998) and experimental results (Mollegaard, Murchie et al. 1994; Nowakowski, Shim et al. 1999; Lilley 2000) suggest that divalent ions (or more complex ions i.e. hexammine cobalt(III)) are likely to be site-bound to the pocket formed by the four phosphate groups near the branching point. Monovalent metal ions, on the other hand, are diffusely associated to the junction through electrostatic interaction with the DNA backbone phosphates. The interconversion rate between conformers depends on the metal ions concentration, with high salt slowing the exchange. The presence of metal ions is also known to decrease branch migration rates up to three orders of magnitude (Panyutin and Hsieh 1994) indicating a strong correlation between the rates and the state of folding of the structure. It has been proposed that conformer exchange and branch migration go through the same, highly flexible state where the metal ions are not bound (Lilley 2000; McKinney, Déclais et al. 2003), a state that corresponds to the Open, unstacked, conformer.

8.1 Magnesium dependence

Under the assumptions of Lilley and Ha (Lilley 2000; McKinney, Déclais et al. 2003) the kinetic model for conformer interconversion is

$$\mathbf{A/B} \underset{k_{\text{Fold 1}}}{\overset{k_{\text{Open 1}}}{\rightleftharpoons}} \mathbf{Open} \underset{k_{\text{Open 2}}}{\overset{k_{\text{Fold 2}}}{\rightleftharpoons}} \mathbf{A/D} \qquad \text{(Eq. 8.1-1)}$$

where A/B and A/D are the stacked conformers, Open is the unstacked conformer, k_{Open1} and k_{Open2} are the opening rate constants of the folded structures and k_{Fold1} and k_{Fold2} are the folding rate constants of the open structure. It is important to note that the folding rate constants are apparent rate constants while the formally correct expressions are

$$k_{\text{Fold1}} = k_{\text{Open}\rightarrow\text{A/B}} \cdot \text{Mg} \text{ and } \quad k_{\text{Fold2}} = k_{\text{Open}\rightarrow\text{A/D}} \cdot \text{Mg} \qquad \text{(Eq. 8.1-2)}$$

where Mg is the Mg^{2+} concentration and $k_{\text{Open}\rightarrow\text{A/B}}$ and $k_{\text{Open}\rightarrow\text{A/D}}$ are the second order rate constants for the folding processes. Recent NMR studies (Scwalbe, Frankfurt Main, unpublished results) have shown that the Mg-dependence, in equation 8.1-2, is also a simplification because several metal ion binding sites are present and distributed rates are expected.

The open conformer in equation 8.1-1 has never been directly detected in presence of divalent ions, implying that either the folding rate constants are several orders of magnitude bigger than the opening ones or that the open conformer is just a transition state and therefore not observable. In both cases equation 8-1 is equivalent to

$$\mathbf{A/B} \underset{k_{21}}{\overset{k_{12}}{\rightleftharpoons}} \mathbf{A/D} \qquad \text{(Eq. 8.1-3)}$$

where k_{12} and k_{21} are apparent rate constants because, as described before, the interconversion is Mg-dependent and in k_{12} and k_{21} the ion concentration is not explicitly expressed.

8.2 Material and methods

Single-molecule experiments were carried out with a confocal epi-illuminated setup based on an Olympus IX70 inverted microscope as described in section 3.4. The fluorescently labelled molecules were excited by a linearly polarised, active-mode-locked Argon-ion laser (Innova Sabre, Coherent) at 496 nm, active-mode-locked (73.5 MHz, 150 ps) mode. The laser beam

passed through a confocal pinhole of 100 µm diameter and was focused into the dilute solution (< 50 pM) of labelled molecules by a 60x water immersion objective (UPLAPO 60x, Olympus, Hamburg, Germany). Fluorescence from the sample was collected by the same lens and separated from the excitation by a beamsplitter (Q505LPXR, AHF, Tübingen, Germany). Collected fluorescence photons were divided first into their parallel and perpendicular components by a polarising beamsplitter cube (VISHT11, Gsänger, Planegg, Germany) and then by dichroic beamsplitters (Q595LPXR, AHF) into wavelength ranges below and above 595 nm. Additionally, green (HQ 533/46 nm) and red (HQ 720/150 nm) filters were put in front of the detectors to ensure that only fluorescence photons coming from donor (Alexa 488) and acceptor (Atto 647N) dyes were registered. Detection was performed using four avalanche photodiodes (PDM050CTC, MPD, Italy, for the green channels, and SPCM-AQR-14, Laser Components, Germany, for the red channels). The signals from all detectors passed through a passive delay unit and two routers to two synchronised time-correlated single photon counting boards (SPC 132, Becker and Hickl, Germany) which were connected to a PC. An estimate of the focal geometry was acquired by determining the diffusion correlation time of 218 ± 18 µs for Rhodamine 110 in water and knowing its diffusion coefficient of 0.34 ± 0.03 μm^2/ms. Moreover, correction factors $l_1 = 0.0308$ and $l_2 = 0.0368$ were used to account for the mixing of polarisation by the microscope objective and *G*-factors ($G_{Green} = 1.058$ for the green channels and $G_{Red} = 1.020$ for the red channels) were applied to compensate for the slightly different detection efficiency of the two polarisation components. Fluorescence bursts were distinguished from the background of 4-4.3 kHz by applying threshold intensity criteria (0.1 ms interphoton time, 100 photons minimum per burst).

For sccFCS purposes, to extend the observation time, the beam diameter was broadened and a confocal pinhole of 150µm was used. The increased focal volume yielded for Rhodamine 110 a diffusion time of 625 ± 41 µs.

Functional Holliday four-way junctions were obtained by annealing four different single strands of DNA:

HJ_1N_D: 5′-d(CCT AAT **T(Alexa488)** AC CAG TCC AGA TTA ATC AGT ACG)
HJ_2N_A: 5′-d(CGT ACT GAT **T(Atto647N)** AA TCT CCG CAA ATG TGA ACG)
HJ_3N: 5′-d(CGT TCA CAT TTG CGG TCT TCT ATC TCC ACG)
HJ_4N: 5′-d(CGT GGA GAT AGA AGA GGA CTG GTA ATT AGG)

The labelled DNA strands were purchased from Purimex, Grebenstein, Germany. To couple the dyes to the DNA the commercially available C6-aminolinker was chosen.

The configuration of the bases in proximity of the branching point was chosen so that the sliding of the junction along any of the arms is forbidden. In this way the only observable configurational fluctuation is the switching between the two stacking conformers A/B and A/D, see figure 8.2-1. To allow for a good identification of the conformers through FRET the dyes were positioned so that the different conformers would display significantly different donor-acceptor distances, with conformer A/B having the shorter R_{DA}.

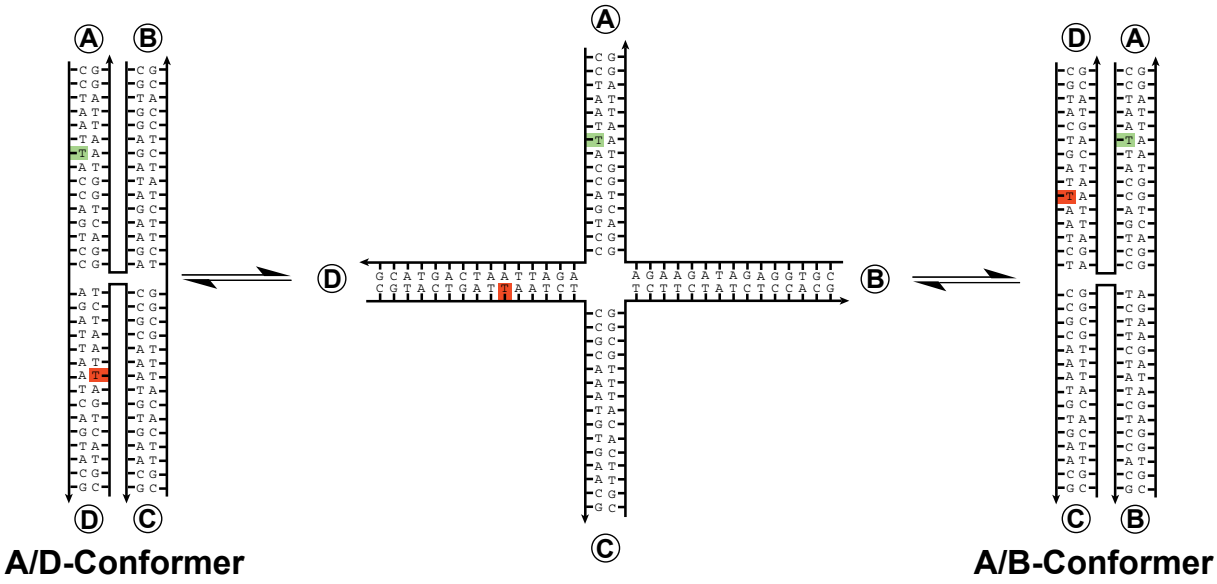

Figure 8.2-1. Possible conformers of the Holliday Junction. The green and red squares indicate the position where donor and acceptor dye are attached, respectively. The letters A, B, C and D indicate the different branches, while the numbers 1, 2, 3 and 4 refer to the HJ_1N_D, HJ_2N_A, HJ_3N and HJ_4N strand, respectively. A/B- and A/D- conformer refer to the conformations where the branch A stacks onto branch B and D, respectively.

The samples were hybridised by heating up to 90 °C a solution of HJ_1N_D, HJ_2N_A, HJ_3N and HJ_4N (5, 5, 15 and 15 µM, respectively) in buffer (20 mM Tris, 50 mM NaCl, 10 mM $MgCl_2$ pH=7.5) and letting it cool overnight.

All measurements were performed at 20 °C in buffer (10 mM Tris, 50 mM NaCl, pH=7.5) and the desired Mg^{2+} concentrations were obtained by adding aliquots of a 1 M stock solution of $MgCl_2$.

When the Holliday Junctions were diluted from bulk to single-molecule concentration the FRET signal decreased. Furthermore, after the dilution the number of molecules in the focus

dropped continuously. These effects depended probably on the dissociation of the hybridised samples and on the interaction between the molecules and the surface. Passivation of the cover-slides surface with PEG 400 led to more stable conditions, but seemed to influence the dynamic properties of the system. Measurements used for dynamic-PDA were performed at 150 – 300 pM concentrations to counter balance the dilution destabilisation of the sample and have a better statistics (these conditions are at the limit for multi-molecular correction, see section 6.3)

Bulk experiments were performed at 20 °C with the same buffers used for single-molecule experiments.

8.3 Single-molecule experiments

The functionality of the Holliday Junctions, HJ, was tested measuring the sample under different $MgCl_2$ concentrations, results shown in figure 8.3-1.

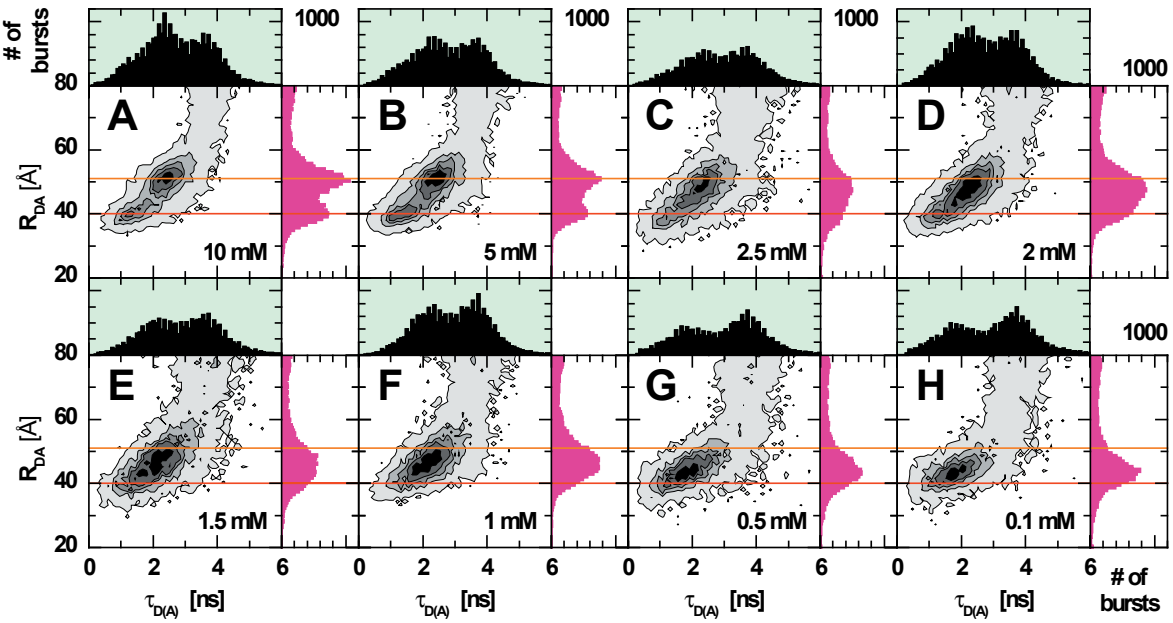

Figure 8.3-1. Series of single-molecule measurements under different Mg^{2+} concentrations. The orange and red lines help track the centers of the distance distributions in conditions where it is not possible to separate the species. The measurements were performed with PEG 400 passivated cover slides.

As expected, Holliday junction dynamics was strongly dependent on $MgCl_2$. At high salt concentrations two distinct populations could be observed, characterised by a R_{DA} of

approximately 40 Å (A/B conformer) and 50 Å (A/D conformer). As the salt concentration was lowered the populations started to merge, indicating that the species interconverted faster and faster. A shift of the average FRET signal to higher values was observed as the Mg^{2+} concentration decreased.

Close inspection of figure 8.3-1A, where the mixing of the states due to kinetic was not expected, revealed substantial deviation from the expected behaviour described by equation 5.2-3a (to be plotted in the R_{DA} versus $\tau_{D(A)}$ plot, Eq. 5.2-3a was modified as described in section 5.3).

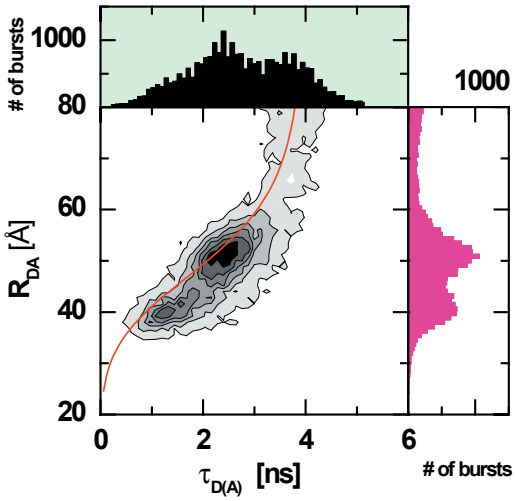

Figure 8.3-2. R_{DA} versus $\tau_{D(A)}$ plot at 10 mM Mg^{2+}. The parameters used to plot the red line, $R_{DA} = R_0 (\tau_{D(A)} /(\tau_{D(0)}-\tau_{D(A)}))^{1/6}$, are $R_0 = 49.33$ and $\tau_{D(0)} = 4.00$ ns.

The strong deviation of the A/B population, combined with the relatively small deviation of the A/D one, suggested that these deviations could be due to linker movement (see section 5.2.3). For the dyes in study, in fact, the difference between species averaged and fluorescence averaged lifetimes is greater for $\tau_{ave,a} = 1.25$ ns than for $\tau_{ave,a} = 2.50$ ns (see fig. 8.3-3). Furthermore, the shift of both populations is in the direction opposite to the one expected for quenching processes (section 5.2.1), excluding in this way the presence of any specific quenching of the dyes.

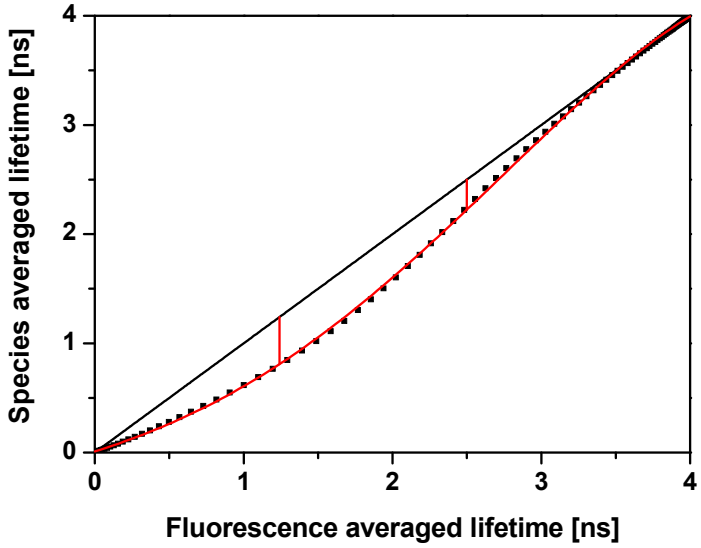

Figure 8.3-3. Species averaged life time (black squares) and fluorescence averaged lifetime (black line) as a function of fluorescence averaged lifetime. Red line is a polynomial fit of the species averaged lifetime $\tau_{ave,x} = 0.0089 + 0.44\tau_{ave,a} + 0.11\tau_{ave,a}^2 + 0.059\tau_{ave,a}^3 - 0.013\tau_{ave,a}^4$. The red vertical lines at $\tau_{ave,a}$ 1.25 ns and 2.5 ns illustrate the difference between the two averages for the conformer A/B and A/D, respectively.

The assumption of deviations due to dye linker dynamics was proved by computing and applying a correction function for a linker displacement of 7 Å (procedure described in section 5.2.3)

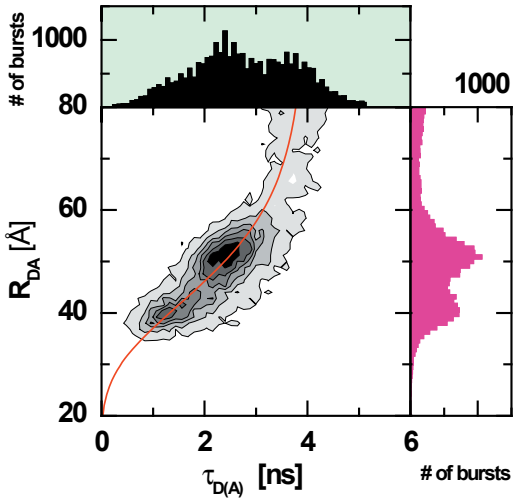

Figure 8.3-4. R_{DA} versus $\tau_{D(A)}$ plot at 10 mM Mg^{2+}. The red line, $R_{DA} = R_0\ (f(\tau_{ave,a})/(\tau_{D(0)} - f(\tau_{ave,a})))$, includes the correction function $f(\tau_{ave,a}) = 0.0089 + 0.44\tau_{ave,a} + 0.11\tau_{ave,a}^2 + 0.059\tau_{ave,a}^3 - 0.013\tau_{ave,a}^4$.

A displacement of 7 Å is in good agreement with recent studies made in our group, data not published.

8.4 Dynamic PDA

To obtain the rate constants of conformer interconversion, dynamic-PDA fit of R_{DA} histograms was performed. The model used to fit the data consisted of two static populations (molecules labelled with donor only, *DOnly*, and impurities) and a dynamic population (internconversion between A/B and A/D, see equation 8.1-3). Due to the presence of dyes' heterogeneities (see section 6.5), each conformer is described by an apparent Gaussian distribution of distances, with mean distance R and half-width HW. Thus, the dynamic population was treated as the sum of two processes with the same rate constants k_{12} and k_{21}

$$R_{A/B}+HW_{A/B} \underset{k_{21}}{\overset{k_{12}}{\rightleftharpoons}} R_{A/D}+HW_{A/D}$$

$$R_{A/B}-HW_{A/B} \underset{k_{21}}{\overset{k_{12}}{\rightleftharpoons}} R_{A/D}-HW_{A/D} \qquad \text{(Eq. 8.4-1)}$$

To distinguish real static populations from fast-interconverting populations, dynamic-PDA fits were performed globally with a set of three different time binning: 0.5 ms, 1.0 ms and 3.0 ms. Gaussian distribution of distances, in fact, are characterised by the same mean distances and half widths irrespective of the time binning while the shapes of the apparent distributions obtained by fast interconversion depend strongly on the binning size. This procedure resulted to be particularly important for low salt concentrations.

To test for the presence of the open conformer, 0 mM $MgCl_2$ was instead fitted with three static distributions: *DOnly*, impurities and the open conformer, *Open*.

Surprisingly, the data could not be fitted. This result is of extreme importance because contradicts the commonly accepted idea (Lilley 2000) that in the absence of Mg^{2+} ions, the only populated conformer is the Open one (that would show up as a single distribution). To test if a dynamic process is compatible with the measured data, Holliday Junctions at 0 mM $MgCl_2$ were fitted with the same model used for the other concentrations.

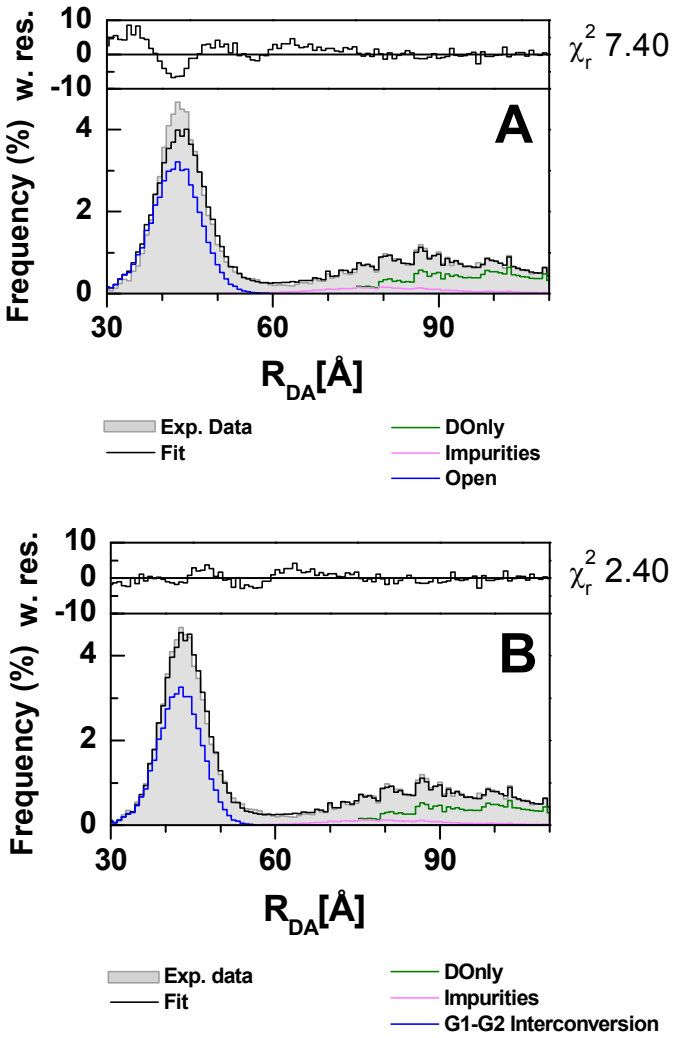

Figure 8.4-1. Holliday Junctions at 0 mM Mg^{2+}. **(A)** R_{DA} histograms (grey) are obtained using a time binning of 3 ms. The black bold line is the fit to a three state model accounting for Open, DOnly and impurities (blue, green and magenta line, respectively). The fit includes also corrections for the simultaneous transit of more than one molecule in the detection volume (contribution not shown). Weighted residuals of the fit are displayed on top of the R_{DA} histogram. Open and Impurities are fitted with Gaussian distributions of distances while DOnly is described by a single distance $R_{DA,\ DOnly} \rightarrow \infty$. The fit parameters for each species are $R_{DA,\ Open}$ = 42.2 Å, HW_{Open} = 4.0 Å, X_{Open} = 0.42, $R_{DA,\ Impurities}$ = 86 Å, $HW_{Impurities}$ = 13.5 Å, $X_{Impurities}$ = 0.06 and X_{DOnly} = 0.52. **(B)** R_{DA} histograms (grey) are obtained using a time binning of 3 ms. The black bold line is the fit to a three state model accounting for Open, DOnly and impurities (blue, green and magenta line, respectively). The fit includes also corrections for the simultaneous transit of more than one molecule in the detection volume (contribution not shown). Weighted residuals of the fit are displayed on top of the R_{DA} histogram. Open is fitted as the interconversion between two Gaussian distributions of distances, G1 and G2, impurities are fitted with a Gaussian distribution of distances while DOnly is described by a single distance $R_{DA,\ DOnly} \rightarrow \infty$. The fit parameters for each species are $R_{DA,\ G1}$ = 38.9 Å, HW_{G1} = 4.0 Å, $R_{DA,\ G2}$ = 49.7 Å, HW_{G2} = 6.0 Å, $X_{(G1+G2)}$ = 0.43, k_{12} = 0.99 ms^{-1}, k_{12} = 2.37 ms^{-1}, $R_{DA,\ Impurities}$ = 86 Å, $HW_{Impurities}$ = 13.5 Å, $X_{Impurities}$ = 0.05 and X_{DOnly} = 0.52

As shown in figure 8.4-1, the substitution of a static population with a dynamic population yielded better fit results, suggesting that at 0 mM Mg^{2+} Holliday Junctions is indeed a dynamic structure.

It is important to note that, however, a purely dynamic model was not sufficient to describe properly the conformer interconversion. This was true not only at high salt concentrations where the sample is almost static and the recovery of the rate constants was expected to be sub-optimal, but also at low salt concentrations. As an example, in figure 8.4-2 is shown the PDA fit of Holliday Junctions at 0.75mM $MgCl_2$.

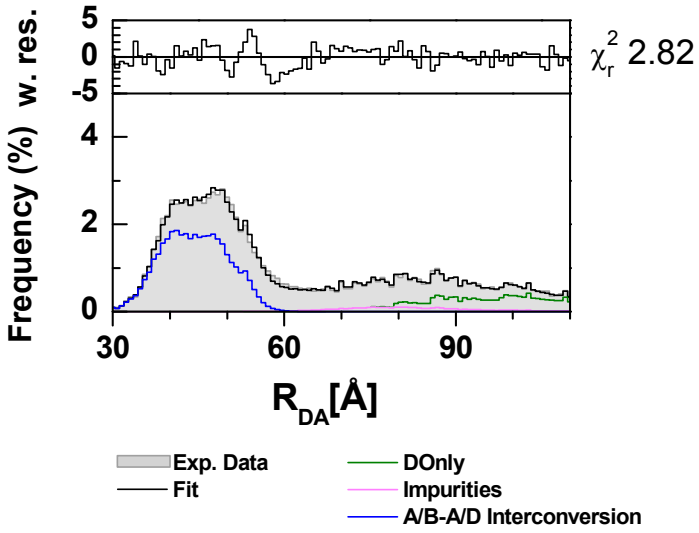

Figure 8.4-2. Holliday Junctions at 0.75 mM Mg^{2+}. R_{DA} histograms (grey) are obtained using a time binning of 3 ms. The black bold line is the fit to a three state model accounting for A/B-A/D interconversion, DOnly and impurities (blue, green and magenta line, respectively). The fit includes also corrections for the simultaneous transit of more than one molecule in the detection volume (contribution not shown). Weighted residuals of the fit are displayed on top of the R_{DA} histogram. Here A/B-A/D interconversion is fitted as the interconversion between to Gaussian distributions of distances $G_{A/B}$ and $G_{A/D}$, impurities are fitted with a Gaussian distribution of distances while DOnly is described by a single distance $R_{DA,\ Donly} \rightarrow \infty$. The fit parameters for each species are $R_{DA,\ A/B}$ = 38.2 Å, $HW_{A/B}$ = 3.2 Å, $R_{DA,\ A/D}$ = 51.2 Å, $HW_{A/D}$ = 4.9 Å, $X_{Interconversion\ A/B\ A/D}$ = 0.48, k_{12} = 0.20 ms^{-1}, k_{12} = 0.26 ms^{-1}, $R_{DA,\ Impurities}$ = 86 Å, $HW_{Impurities}$ = 13.5 Å, $X_{Impurities}$ = 0.05 and X_{Donly} = 0.47

To obtain satisfactory fit results for all salt concentrations, two additional static Gaussian distributions of distances, G1 and G2, were needed.

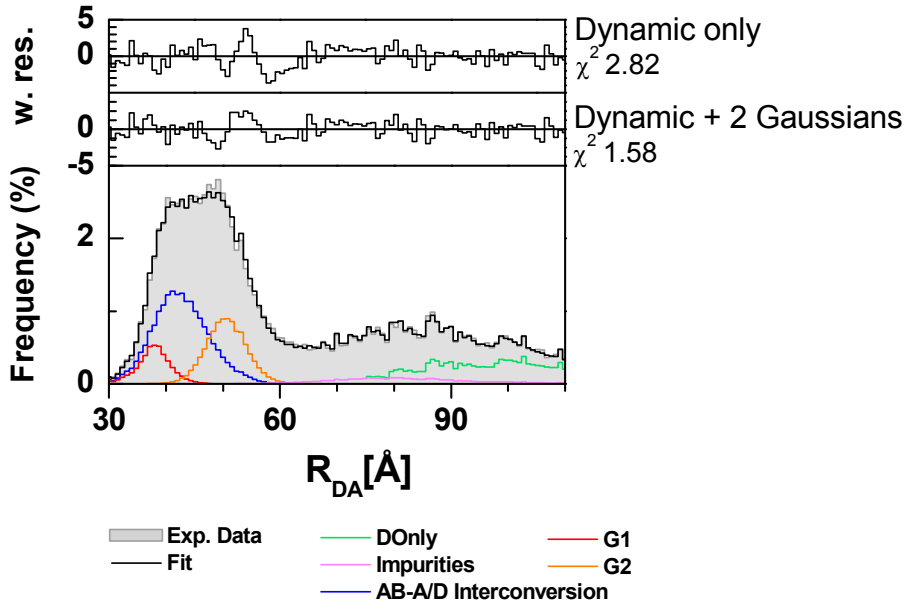

Figure 8.4-3. Holliday Junctions at 0.75 mM Mg^{2+}. R_{DA} histograms (grey) are obtained using a time binning of 3 ms. The black bold line is the fit to a three state model accounting for A/B-A/D interconversion, DOnly, impurities and two additional Gaussian distribution of distances G_1 and G_2 (blue, green, magenta, red and orange line, respectively). The fit includes also corrections for the simultaneous transit of more than one molecule in the detection volume (contribution not shown). Weighted residuals of the fit are displayed on top of the R_{DA} histogram. Here A/B-A/D interconversion is fitted as the interconversion between to Gaussian

distributions of distances $G_{A/B}$ and $G_{A/D}$, impurities, G_1 and G_2 are fitted with a Gaussian distribution of distances while DOnly is described by a single distance $R_{DA,\ DOnly} \rightarrow \infty$. The parameter for each species are $R_{DA,\ A/B}$ = 38.1 Å, $HW_{A/B}$ = 1.8 Å, $R_{DA,\ A/D}$ = 51.7 Å, $HW_{A/D}$ = 3.5 Å, $X_{Interconversion\ A/B\ A/D}$ = 0.28, k_{12} = 0.36 ms^{-1}, k_{12} = 0.87 ms^{-1}, $R_{DA,\ Impurities}$ = 86 Å, $HW_{Impurities}$ = 13.5 Å, $X_{Impurities}$ = 0.05 $R_{DA,G1}$ = 37.8 Å, HW_{G1} = 0.04 Å, X_{G1} = 0.07, $R_{DA,G2}$ = 50.6 Å, HW_{G1s} = 3.0 Å, X_{G2} = 0.14 and X_{DOnly} = 0.46

To minimise the number of floating parameters and have more stable fits, mean distances and half widths of the dynamic population were fixed. Because at 10 mM $MgCl_2$ Holliday Junctions can be assumed to be static, the values of $R_{A/B,}$ $HW_{A/B}$, $R_{A/D,}$ and $HW_{A/D}$ obtained by fitting this data set as the sum of two static populations represent the best estimates of the distance distributions of A/B and A/D and therefore the best choice as parameters for the dynamic population. In table 8.4-1 are reported the fit results for all concentrations.

	$R_{A/B}$ [Å]	$HW_{A/B}$ [Å]	$R_{A/D}$ [Å]	$HW_{A/D}$ [Å]
Dynamic Population	38.1	1.79	51.7	3.52
	R_{DA1} [Å]	HW_1 [Å]	R_{DA2} [Å]	HW_1 [Å]
10 mM Mg^{2+}	38.4	1.97	51.8	3.36
7.5 mM Mg^{2+}	38.0	1.68	51.6	3.58
5.0 mM Mg^{2+}	38.2	1.82	51.7	3.38
2.5 mM Mg^{2+}	37.9	1.34	51.0	3.31
1.25 mM Mg^{2+}	37.6	1.10	51.0	3.25
1.0 mM Mg^{2+}	37.2	1.03	50.8	3.19
0.75 mM Mg^{2+}	37.8	0.04	50.6	3.00
0.5 mM Mg^{2+}	36.9	0.03	50.0	2.70
0.2 mM Mg^{2+}	36.3	1.64	49.1	4.35
0.1 mM Mg^{2+}	---[a]	---[a]	---[a]	---[a]
0.0 mM Mg^{2+}	37.1	6.18	50.2	3.15

[a] fit not stable.

Table 8.4-1. Comparison between the parameters of the Gaussian distribution of distances G1 and G2 and the dynamic population accounting for the interconversion of A/B and A/D.

The parameters characterising G1 and G2 (R_{G1}, HW_{G1} and R_{G2}, HW_{G2}, respectively) matched those used to model the A/B and A/D conformers (eq. 8.4-2) suggesting that the additional static distributions originate from the same, or at least very similar, molecular structures in the dynamic population.

$R_{A/B} \approx R_{G1}$ and $HW_{A/B} \approx HW_{G1}$

(Eq. 8.4-2)

$R_{A/B} \approx R_{G1}$ and $HW_{A/B} \approx HW_{G1}$

To take into account these findings, a new fit model in which the parameters of G1 and G2 were forced to be equal to the ones in equation 8.4-1 was introduced. Fit results for all concentrations are plotted in figure 8.4-4.

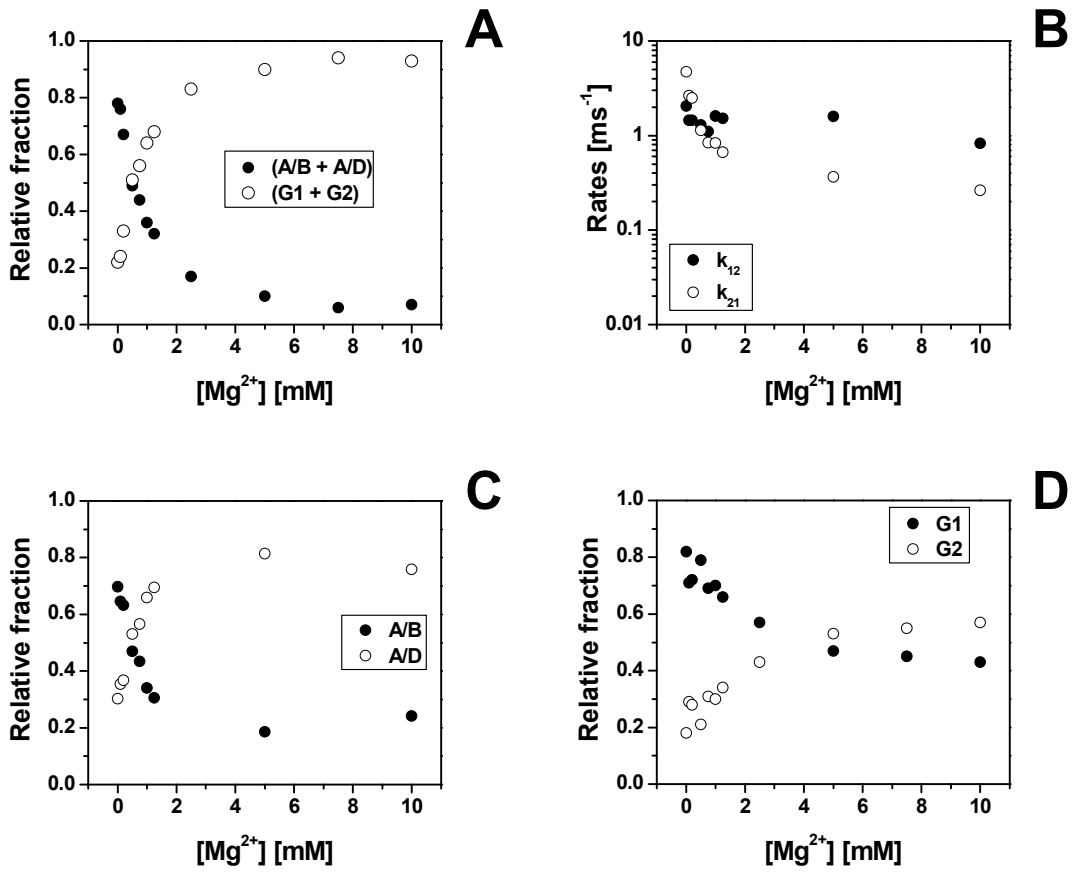

Figure 8.4-4. PDA results. Rate constants and absolute fractions of (A/B + A/D), G1 and G2 are obtained directly from the fit as floating parameters while fractions A/B and A/D are calculated from the interconversion rate constants, A/B = k_{21} / (k_{12}+k_{21}) and A/D = k_{12} / (k_{12}+k_{21}). **(A)** Species (A/B + A/D) and (G1 + G2) as fractions of the total FRET active population. **(B)** Interconversion rates **(C)** Species A/B and A/D as fractions of the dynamic population only. **(D)** Species G1 and G2 as fractions of the static FRET population only.

It is important to note that at zero $MgCl_2$, a purely dynamic term was not sufficient to fit the data. This result is consistent with the notion that also Na^+ ions can induce the folding of the structure, as demonstrated by Ha and co-workers (McKinney, Déclais et al. 2003), and therefore support the idea that folding can be induced not only by the coordination of divalent

ions in the pocket at the branchpoint but also by diffuse electrostatic interactions between the DNA backbone and the metal ions.

8.5 Alternative kinetic models

The presence of the additional static distributions and the fact that in the absence of Mg^{2+} a single distribution of distances was insufficient led to a revision of the kinetic models introduced so far (Eq. 8.1-1 and 8.1-3). The simplest models required to explain the PDA results are

$$\left[\mathrm{A/B_{(Mg)}} \underset{k^{+}_{\mathrm{A/B(Mg)}}}{\overset{k^{-}_{\mathrm{A/B(Mg)}}}{\rightleftharpoons}} \mathrm{A/B} \right] \underset{k_{21}}{\overset{k_{12}}{\rightleftharpoons}} \left[\mathrm{A/D} \underset{k^{-}_{\mathrm{A/D(Mg)}}}{\overset{k^{+}_{\mathrm{A/D(Mg)}}}{\rightleftharpoons}} \mathrm{A/D_{(Mg)}} \right] \qquad \text{(Eq. 8.5-1a)}$$

$$\left[\mathrm{A/B_{(Mg)}} \underset{k^{+}_{\mathrm{A/B(Mg)}}}{\overset{k^{-}_{\mathrm{A/B(Mg)}}}{\rightleftharpoons}} \mathrm{A/B} \right] \underset{k_{\mathrm{Fold\,1}}}{\overset{k_{\mathrm{Open\,1}}}{\rightleftharpoons}} \mathrm{Open} \underset{k_{\mathrm{Open\,2}}}{\overset{k_{\mathrm{Fold\,2}}}{\rightleftharpoons}} \left[\mathrm{A/D} \underset{k^{-}_{\mathrm{A/D(Mg)}}}{\overset{k^{+}_{\mathrm{A/D(Mg)}}}{\rightleftharpoons}} \mathrm{A/D_{(Mg)}} \right] \qquad \text{(Eq. 8.5-1b)}$$

where $A/B_{(Mg)}$ and $A/D_{(Mg)}$ are the folded Mg-bound structures, A/B and A/D are the folded structures in absence of the divalent ions, $k^{+}_{A/B(Mg)}$ and $k^{+}_{A/D(Mg)}$ the rate constants of Mg^{2+} binding, $k^{-}_{A/B(Mg)}$ and $k^{-}_{A/D(Mg)}$ the rate constants of Mg^{2+} unbinding, k_{12} and k_{21} the rate constants of interconversion between conformers, k_{Open1} and k_{Open2} the opening rate constants of the folded structures and k_{Fold1} and k_{Fold2} the folding rate constants of the open structure. The considerations about the open state and the folding rate constants made in section 8.1 hold also for equations 8.5-1a and 8.5-1b making them equivalent for PDA fitting purposes. Thus, only equation 8.5-1a will be taken into account.

In the new kinetic model, the Mg-binding/unbinding equilibria are supposed to take place on a much slower time scale than the interconversion equilibrium and diffusion. For this reason the processes will result decoupled and the Mg-bound states will contribute to the PDA fit with apparent static distributions of distances.

In practice these models presuppose that in absence of metal ions the Holliday Junction is not static and does not populate the Open conformer only. On the contrary the junction is constantly oscillating between the two folded conformers and when Mg^{2+} is coordinated it fixes the junction in the conformation it is at the moment.

Under these assumptions, the static fractions G1 and G2 correspond to the steady state fractions of $A/B_{(Mg)}$ and $A/D_{(Mg)}$, and the rate constants of the dynamic population to k_{12} and k_{21}.

8.6 FCS

To access simultaneously slow and fast rates sccFCS was performed. The fluorescence lifetime filters (section 4.1.1) were built from the lifetime decays of four species (A/B, A/D, DOnly and the Instrumental Response Function, IRF) and using the combined green perpendicular and red parallel decays as patterns. The lifetimes of A/B and A/D were obtained by the TAC histograms of the species selected as described in figure 8.6-1A Species cross-correlations, $G_{(G_\perp + R_\parallel)A/B,(G_\perp + R_\parallel)A/D}(t_c)$, were performed as described in Paper I.

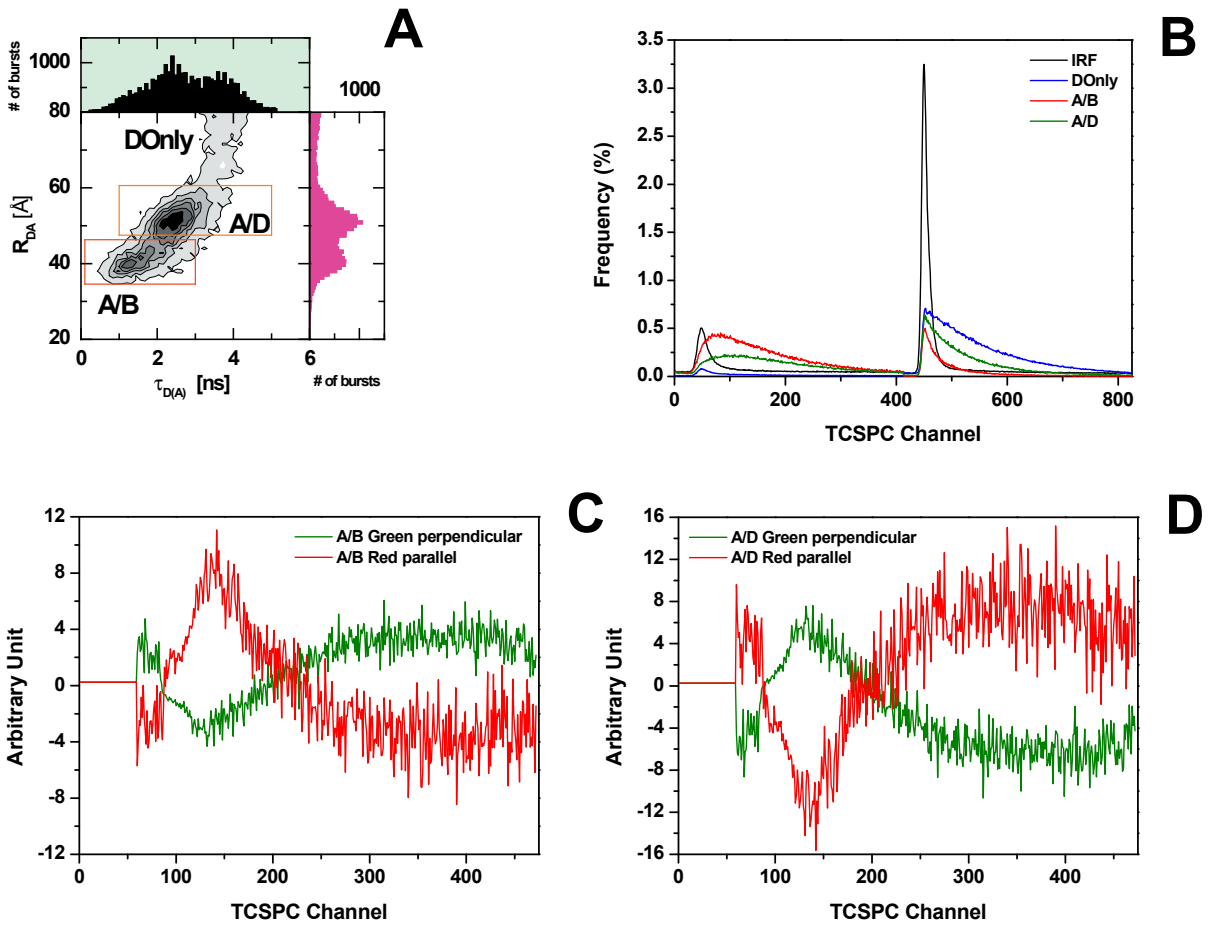

Figure 8.6-1. Fluorescence lifetime filters. **(A)** Orange and red boxes indicate how the species (A/D + $A/D_{(Mg)}$) and (A/B + $A/B_{(Mg)}$), respectively, are selected. **(B)** Red parallel and green parallel lifetime decays of the four species. **(C-D)** Fluorescence lifetime filters for A/B and A/D.

Due to the fact that A/B and A/B_{Mg} and A/D and A/D_{Mg} have very similar structure, and therefore the same fluorescence lifetime and brightness, the selected populations corresponded to $(A/B+A/B_{(Mg)})$ and $(A/D+A/D_{(Mg)})$. Under these conditions the cross correlation between the selected populations can be schematically represented as the sum of the following processes

$$\mathbf{A/B_{(Mg)} \rightleftharpoons A/D}$$

$$\mathbf{A/B_{(Mg)} \rightleftharpoons A/D_{(Mg)}}$$

$$\mathbf{A/B \rightleftharpoons A/D}$$

$$\mathbf{A/B \rightleftharpoons A/D_{(Mg)}}$$

(Eq. 8.6-1)

Species cross-correlation fit function was computed in a similar way as described by Gopich and co-workers (Nettels, Gopich et al. 2007) and resulted of the form

$$G(t_c) = 1 + \frac{1}{N} \cdot G_{diff}(t_c) \cdot X(t_c) \qquad \text{(Eq. 8.6-2)}$$

where $G_{diff}(t_c)$ is the diffusion term and $X(t_c)$ is the term accounting for the kinetic processes in equation 8.5-1a. In $X(t_c)$ three correlation times were expected which represent the solutions of equation 8.6-3

$$\lambda^3 + \lambda^2\left(k_{12} + k_{21} + k^+_{A/B(Mg)}\mathrm{Mg} + k^+_{A/D(Mg)}\mathrm{Mg} + k^-_{A/B(Mg)} + k^-_{A/D(Mg)}\right) +$$

$$\lambda\Big((k_{12} + k_{21})(k^-_{A/B(Mg)} + k^-_{A/D(Mg)}) + k_{12}k^+_{A/D(Mg)}\mathrm{Mg} + k_{21}k^+_{A/B(Mg)}\mathrm{Mg} +$$

$$(k^+_{A/B(Mg)}\mathrm{Mg} + k^-_{A/B(Mg)})(k^+_{A/D(Mg)}\mathrm{Mg} + k^-_{A/D(Mg)})\Big) +$$

$$\Big(k_{12}k^-_{A/B(Mg)}(k^+_{A/D(Mg)}\mathrm{Mg} + k^-_{A/D(Mg)}) + k_{21}k^-_{A/D(Mg)}(k^+_{A/B(Mg)}\mathrm{Mg} + k^-_{A/B(Mg)})\Big) = 0$$

(Eq. 8.6-3)

To solve analytically equation 8.6-3 some approximations had to be made. Under the assumption that $k^+_{A/B(Mg)} = k^+_{A/D(Mg)} = k^+_{Mg}$ and $k^-_{A/B(Mg)} = k^-_{A/D(Mg)} = k^-_{Mg}$ and with k_{12}, k_{21} >>

$k^{+}_{A/B(Mg)}Mg$, $k^{+}_{A/D(Mg)}Mg$, $k^{-}_{A/B(Mg)}$, $k^{-}_{A/D(Mg)}$ (as proved with PDA), the solutions of equation 8.6-3 were

$$\begin{aligned}\lambda_1 &= -(k_{12}+k_{21}) = -1/\tau_{1relax}\\ \lambda_2 &= -k^{-}_{Mg} = -1/\tau_{2relax}\\ \lambda_3 &= -(k^{-}_{Mg}+k^{+}_{Mg}Mg) = -1/\tau_{3relax}\end{aligned} \qquad \text{(Eq. 8.6-4a)}$$

with amplitudes

$$A_1 = -\frac{K_{Mg}}{1+K_{Mg}}$$

$$A_2 = -\frac{1}{1+K_{Mg}} \qquad \text{where} \qquad K_{Mg} = \frac{k^{+}_{Mg}Mg}{k^{-}_{Mg}} \qquad \text{(Eq. 8.6-4b)}$$

$$A_3 = 0$$

Under the conditions stated above (A_3 = 0) a double-exponential relaxation model for the kinetic part of the FCS function was used

$$G(t_c) = 1+\frac{1}{N}\cdot G_{diff}(t_c)\cdot\left(1+X\cdot\left(A_1\cdot e^{-\frac{t_c}{\tau_{1relax}}}+A_2\cdot e^{-\frac{t_c}{\tau_{2relax}}}\right)\right) \qquad \text{(Eq. 8.6-5)}$$

where $G_{diff}(t_c)$ is the diffusion term, X the fraction of dynamic molecules, A_1 and A_2 are the fractions of the first relaxation component, respectively, and τ_{1relax} and τ_{2relax} are the characteristic relaxation times. In figure 8.6-2 are reported, as an example, the correlation curves and relative fits of 0, 0.2 and 0.75 mM $MgCl_2$

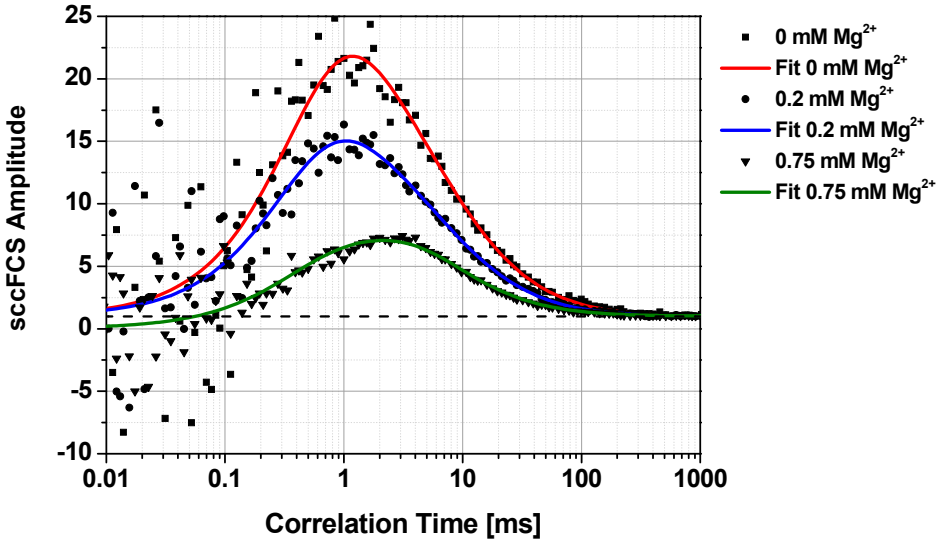

Figure 8.6-2. sccFCS curves for Holliday junction at 0, 0.2, 0.75 mM Mg^{2+} (squares, circles and triangles, respectively) and relative fits (red, blue and green line respectively).

	τ_{1relax}	τ_{2relax}	A_1	A_2	t_{Diff}
0.00 mM Mg^{2+}	0.43	-	1.00	0.00	5.24
0.20 mM Mg^{2+}	0.35	3.1	0.93	0.07	4.99
0.75 mM Mg^{2+}	0.35	2.5	0.42	0.58	4.79

Table 8.6-1. Fit results for the sccFCS curves in figure 8.6-2

The fit results, for all Mg^{2+} concentrations are plotted in figure 8.6-3.

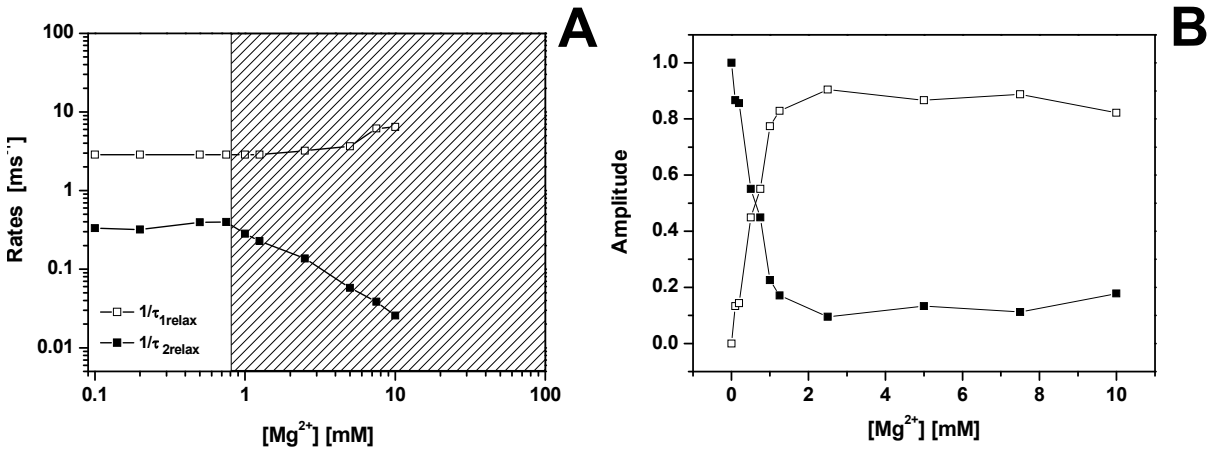

Figure 8.6-3. sccFCS results for HJ. **(A)** Relaxation rate constants. **(B)** Amplitudes of the relaxation process, A_1 (black squares) and A_2 (open black squares).

As expected from equation 8.6-4a, at low salt concentrations where the assumption that k_{12}, k_{21} >> $k^{+}_{A/B(Mg)}$Mg, $k^{+}_{A/D(Mg)}$Mg, $k^{-}_{A/B(Mg)}$, $k^{-}_{A/D(Mg)}$ is strictly true, the relaxation rates found by

FCS are with good approximation Mg-independent. At high salt concentrations, shaded area in figure 8.6-3, k_{12}, k_{21}, $k^{+}_{A/B(Mg)}Mg$ and $k^{+}_{A/D(Mg)}Mg$ become comparable, the apparent rates recovered by sccFCS are a mix of them, and therefore strongly Mg-dependent. To test if the behaviours observed for $1/\tau_{1relax}$ and $1/\tau_{2relax}$ were to be expected, equation 8.6-3 was numerically solved for a set of arbitrary (but reasonable) rate constants.

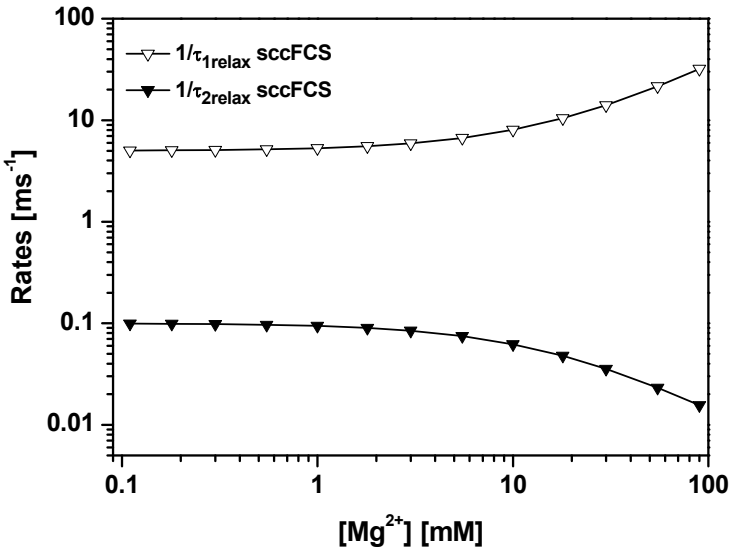

Figure 8.6-4. Theoretical Mg-dependence for sccFCS. $1/\tau_{1relax}$ and $1/\tau_{2relax}$ are numerical solutions of eq. 8.6-3 in the case that k_{12} = 1 ms^{-1}, k_{21} = 1 ms^{-1}, $k^{+}_{A/B(Mg)} = k^{+}_{A/D(Mg)}$ = 0.3 ms^{-1} and $k^{-}_{A/B(Mg)} = k^{-}_{A/D(Mg)}$ = 0.1 ms^{-1}.

Figure 8.6-4 shows how the relaxation rates obtained with sccFCS are perfectly in line with the theoretical model.

8.7 Comparison between PDA, FCS and other techniques

At low salt concentrations, where the equilibria in equation 8.5-1a are effectively decoupled, the rate constants obtained with PDA describe the same relaxation process that in sccFCS is associated to τ_{1relax}. To test this assumption dynamic-PDA and sccFCS results were compared (see Fig. 8.7-1).

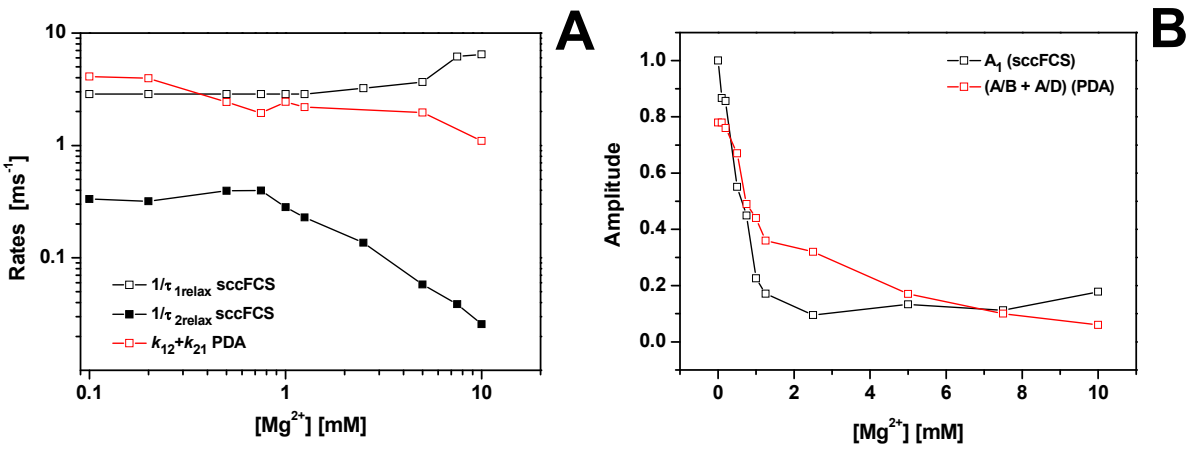

Figure 8.7-1. Comparison between dynamic-PDA and sccFCS results for HJ. **(A)** Relaxation rate constants $1/\tau_{1relax}$ and $1/\tau_{2relax}$ (open black and black squares respectively) found in sccFCS and sum of the interconversion rate constants k_{12}, k_{21} found in dynamic-PDA (open red squares). **(B)** Amplitude A_1 (open black squares) and (A/B + A/D) as fraction of the FRET population only (open red squares).

The rate constants recovered with the two techniques are essentially the same over the range of Mg^{2+} concentrations investigated. The different trend for the rate constants at Mg^{2+} concentrations higher than 1 mM could be explained by the fact that at these conditions the equilibria in equation 8.5-1a are not completely decoupled and averaging is expected (PDA rates become a combination of k_{12}, k_{21}, $k^{+}_{A/B(Mg)}Mg$ and $k^{+}_{A/D(Mg)}Mg$).

The relative fractions of the slow and fast relaxation processes in sccFCS are also in good agreement with the relative fractions of (A/B+A/D) and ($A/B_{(Mg)}$ + $A/B_{(Mg)}$) found in dynamic-PDA, with 0 mM $MgCl_2$ being a point of major difference. Most probably at this condition a small amount of static population is still expected due to the presence of Na^+ ions (see section 7) but due to the low amount of static population it is difficult to judge whether this is the case or not. It is, however, important to highlight how both dynamic-PDA and sccFCS detect the presence of dynamic processes at conditions where only the open conformation is supposed to be populated.

From the dynamic-PDA fits, average FRET efficiencies could be calculated for each salt concentration, data shown in figure 8.7-2.

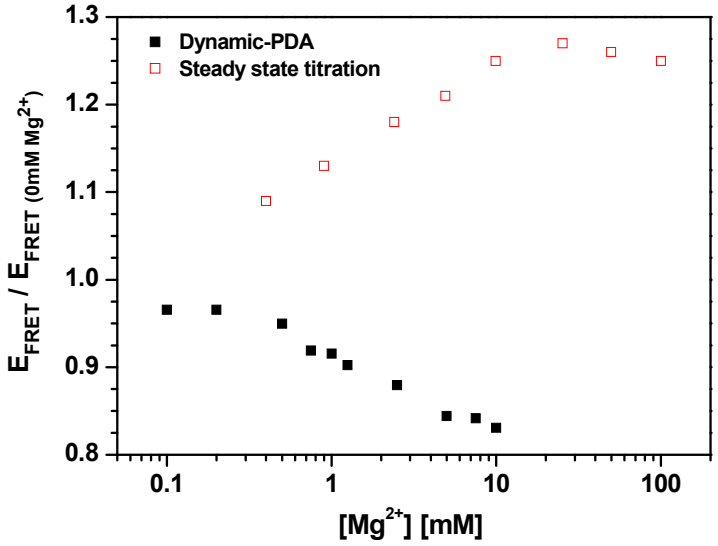

Figure 8.7-2. Comparison between the average FRET Efficiency in single-molecule (black squares) and steady state experiments (red open squares). FRET efficiencies are normalised by of E_{FRET} at 0 mM Mg^{2+}

As qualitatively seen in the two-dimensional plots in figure 8.3-1, the average FRET efficiency drops with Mg^{2+} concentration. This behaviour is opposite to the one reported in literature (Lilley 2000) for steady state fluorescence titrations of similar junctions with the same labelling scheme. To compare single-molecule measurements with published results, a steady state fluorescence titration was performed (see fig. 8.7-2). The bulk measurements are in agreement with the published results and opposite to the single-molecule results.

A possible explanation of the contradictory trends would be that Mg^{2+} induces a reversible association/dissociation equilibrium of the four strands and therefore the change in FRET signal of ensemble measurement is the net result between two processes: (i) the shift of the FRET population from A/D to A/B at low salt concentrations; (ii) the change in the number of double labelled molecule in solution. To test this hypothesis a TCSPC titration of Holliday Junctions similar to those used by Ha, HJ7 (McKinney, Déclais et al. 2003; Hohng, Zhou et al. 2007), was performed going from low to high salt concentrations. To distinguish the different junctions studied, the molecules investigated so far will be referred to as HJ. Fluorescence lifetime were fitted as a sum of three exponential decays, accounting for Donly, A/B and A/D

$$F(t) = A_{DOnly} \exp\left[-\frac{t}{\tau_{DOnly}}\right] + A_{A/B} \exp\left[-\frac{t}{\tau_{A/B}}\right] + A_{A/D} \exp\left[-\frac{t}{\tau_{A/D}}\right] \qquad \text{(Eq. 8.7-1)}$$

where A_{DOnly}, $A_{A/B}$, $A_{A/D}$, are the fractions of DOnly, A/B and A/D, respectively, and τ_{DOnly}, $\tau_{A/B}$, and $\tau_{A/D}$ the lifetimes of DOnly, A/B and A/D, respectively. It is important to note that here A/B and A/D refer to the total populations of the conformers and therefore, if equation 8.5-1a is considered $A/B_{TCSPC} = A/B + A/B_{(Mg)}$ and $A/D_{TCSPC} = A/D + A/D_{(Mg)}$

The average lifetimes for the three species resulted to be

τ_{DOnly} = 3.90 ns
$\tau_{A/B}$ = 0.75 ns (Eq. 8.7-2)
$\tau_{A/D}$ = 2.73 ns

with fractions

	$A_{A/B}$	$A_{A/D}$	A_{DOnly}	$A_{A/B,\ Relative}$	$A_{A/D,\ Relative}$
0 mM Mg^{2+}	0.11	0.34	0.55	0.24	0.76
0.1 mM Mg^{2+}	0.11	0.34	0.55	0.25	0.75
0.2 mM Mg^{2+}	0.12	0.34	0.54	0.26	0.74
0.5 mM Mg^{2+}	0.13	0.34	0.53	0.28	0.72
1 mM Mg^{2+}	0.09	0.39	0.52	0.20	0.80
2 mM Mg^{2+}	0.12	0.38	0.50	0.23	0.77
5 mM Mg^{2+}	0.17	0.36	0.47	0.32	0.68
10 mM Mg^{2+}	0.19	0.36	0.45	0.34	0.66
50 mM Mg^{2+}	0.20	0.37	0.43	0.35	0.65
200 mM Mg^{2+}	0.20	0.40	0.40	0.34	0.66

Table 8.7-1. TCSPC titration results for HJ7. Only the populations are reported. $A_{A/B,\ Relative}$ and $A_{A/B,\ Relative}$ are fractions relative to the FRET population only and are calculated from the absolute fractions as $A_{A/B,\ Relative} = A_{A/B} /(A_{A/B} + A_{A/D})$ and $A_{A/D,\ Relative} = A_{A/D} /(A_{A/B} + A_{A/D})$.

In table 8.7-1, two effects can be seen: (i) the fraction of DOnly decreases with increasing Mg^{2+}, supporting the idea that a dissociation/association equilibrium is present (ii) there is a slight shift in the FRET populations, with A/D being favoured at low salt concentrations (trend opposite to HJ).

To have an idea of the impact of each effect on the total FRET signals, average FRET efficiencies were calculated from both absolute and relative FRET fractions (see fig 8.7-3). E_{FRET} obtained from the absolute FRET fractions, in fact, takes into account both the association/dissociation equilibrium and the shift in populations while E_{FRET} obtained from the relative FRET fractions is affected only by the latter process.

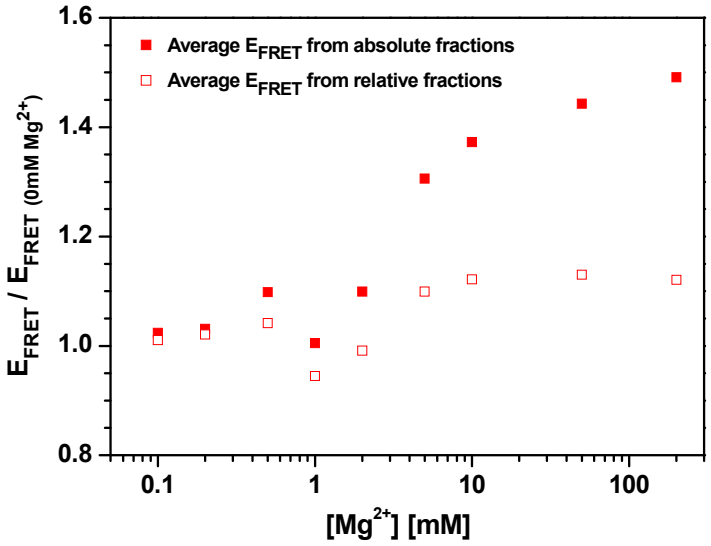

Figure 8.7-3. TCSPC titration of HJ7 junctions. FRET efficiencies are normalised by of E_{FRET} at 0 mM Mg^{2+} Red squares represent the FRET efficiencies calculated from the absolute fractions of the FRET species, while the open squares represent the FRET efficiencies calculated from the relative fractions in table 8.7-1.

At all salt concentrations, the population shift contributes only marginally to the overall change in FRET, meaning that is the association/dissociation equilibrium that plays a major role.

These results confirm the fact that the different behaviours observed for HJ in bulk and single-molecule experiments are not contradictory, but rather in line with the different capability of the techniques to cope with sample heterogeneities. In bulk the heterogeneities are averaged while in single-molecule are discriminated.

At this point it is only possible to speculate that the different shift in the FRET populations in HJ and HJ7 is due to the different sequences.

It is also important to note, that at 0 mM Mg^{2+} the lifetimes relative to A/B and A/D were still needed to fit the lifetime decay, implying that stacked conformers are still present at this condition, even though no assumption can be made about their interconversion.

Moreover no time dependence of the FRET signals were observed (stopped flow experiments, not reported), indicating that the association/dissociation of the HJ is *instantaneous* at our observation timescales.

To further investigate how the results obtained so far compare with literature, especially in view of the revision of the kinetic model, dynamic-PDA and sccFCS results were compared with the work of Ha and co-workers (McKinney, Déclais et al. 2003; Joo, McKinney et al. 2004). In these studies Holliday Junction dynamics is investigated by fitting the lifetime of each FRET state in single immobilised molecules.

For the kinetic scheme in equation 8.5-1a, a double-exponential state lifetime is expected. To obtain the decay rates equation 8.5-1a has first to be divided into two half processes

$$\mathbf{A/B_{(Mg)}} \rightleftharpoons \mathbf{A/B} \longrightarrow \mathbf{A/D} \qquad \text{(Eq. 8.7-3a)}$$

$$\mathbf{A/D_{(Mg)}} \rightleftharpoons \mathbf{A/D} \longrightarrow \mathbf{A/B} \qquad \text{(Eq. 8.7-3b)}$$

Assuming, for equation 8.7-3a, that at t = 0 the system is state A/B and solving for the probability of being in states A/D or $A/B_{(Mg)}$ at time t, two rates, $\lambda_{A/B}^{(\pm)}$, are obtained

$$\lambda_{A/B}^{(\pm)} = \frac{1}{2}\left(-k_{12} - k_{\mathrm{A/B(Mg)}}^{+}\mathrm{Mg} - k_{\mathrm{A/B(Mg)}}^{-} \pm \sqrt{(k_{12} + k_{\mathrm{A/B(Mg)}}^{+}\mathrm{Mg} + k_{\mathrm{A/B(Mg)}}^{-})^2 - 4k_{12}k_{\mathrm{A/B(Mg)}}^{-}}\right) \qquad \text{(Eq.8.7-4a)}$$

with amplitudes

$$x_{A/B}^{(\pm)} = \frac{\pm\lambda_{A/B}^{(\mp)} \pm k_{12}}{\lambda_{A/B}^{(-)} - \lambda_{A/B}^{(+)}} \qquad \text{(Eq. 8.7-4b)}$$

The same can be done for equation 8.7-3b, yielding

$$\lambda_{A/D}^{(\pm)} = \frac{1}{2}\left(-k_{21} - k_{\mathrm{A/D(Mg)}}^{+}\mathrm{Mg} - k_{\mathrm{A/D(Mg)}}^{-} \pm \sqrt{(k_{21} + k_{\mathrm{A/D(Mg)}}^{+}\mathrm{Mg} + k_{\mathrm{A/D(Mg)}}^{-})^2 - 4k_{21}k_{\mathrm{A/D(Mg)}}^{-}}\right) \qquad \text{(Eq.8.7-5a)}$$

with amplitudes

$$x_{A/D}^{(\pm)} = \frac{\pm\lambda_{A/D}^{(\mp)} \pm k_{21}}{\lambda_{A/D}^{(-)} - \lambda_{A/D}^{(+)}} \qquad \text{(Eq. 8.7-5b)}$$

Simulation of these rates for the same rate constants used for sccFCS simulations are reported in figure 8.7-4.

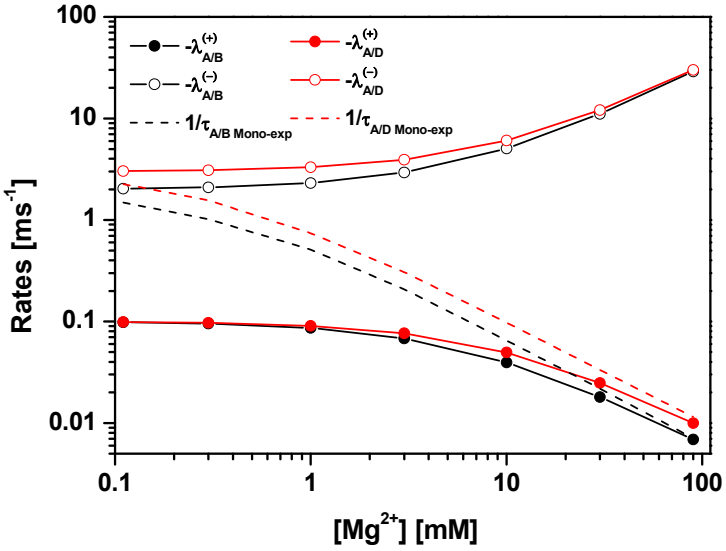

Figure 8.7-4. Theoretical Mg-dependence for state lifetime fit. $\lambda^{(\pm)}_{A/B}$ and $\lambda^{(\pm)}_{A/B}$ are numerical solutions of eq. 8.7-4a and eq. 8.7-4b while $\tau_{A/B\ Mono\text{-}exp}$ and $\tau_{A/D\ Mono\text{-}exp}$ are the characteristic times of the states A/B and A/D, respectively, found by mono-exponential fit of the state durations. The rate constants used to simulate the Mg-dependence are the same used in fig. 8.6-4.

Due to decoupling of fast and slow processes, at lower Mg^{2+} concentrations, rates show only a minor dependence on the ion concentration. However, at higher Mg^{2+} concentration the rate of Mg binding becomes comparable with k_{12} and k_{21}. The apparent fast process becomes faster, and the slow slower. For equation 8.7-3a, this can be understood as a competition of A/B → A/D and A/B → $A/B_{(Mg)}$ processes, which shortens the lifetime of A/B (and the same is true for equation 8.7-3b). It is important to note how these rates have trends equal to the relaxation rates found for sccFCS (see fig. 8.6-4).

Of particular interest are the mean rates which rapidly fall with Mg^{2+} concentration. These rates are obtained by fitting the state lifetimes with a single-exponential decay and correspond to the rates found by Ha and co-workers (McKinney, Déclais et al. 2003; Joo, McKinney et al. 2004).

In figure 8.7-5, are reported the rates found by Ha for junctions similar to HJ, HJ1 and HJ7 (green and blue open squares, respectively), the relaxation rate $1/\tau_{relax}$ corresponds to $1/\tau_{A/B\ Mono\text{-}exp} + 1/\tau_{A/D\ Mono\text{-}exp}$.

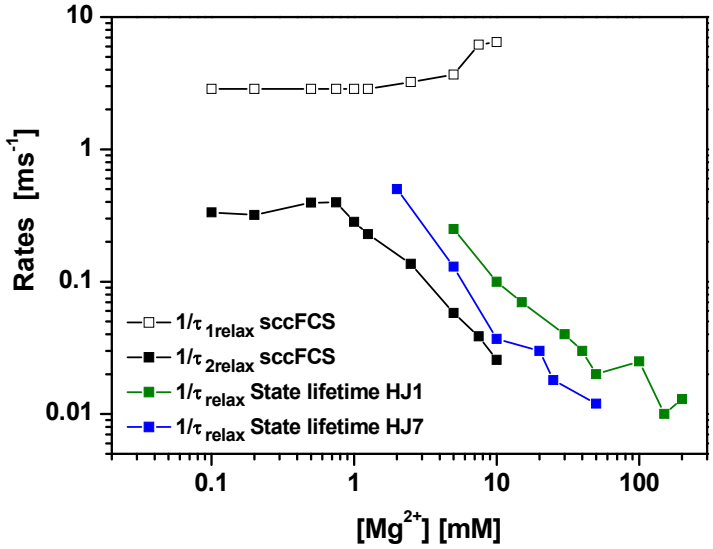

Figure 8.7-5. Comparison between the sccFCS results for HJ (open and black squares) and the state lifetime fit results for HJ1 (green squares) and HJ7 (blue squares).

To test if the differences between the two methods are expected, the theoretical magnesium dependences were plotted together (see fig. 8.7-6).

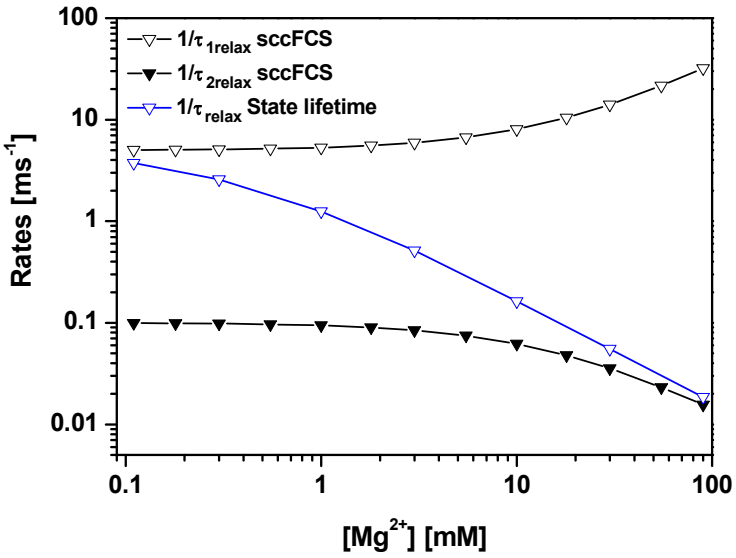

Figure 8.7-6. Comparison between the theoretical Mg-dependences for sccFCS (open and black triangles) and state lifetime fit (open blue triangles).

The simulation results describe quite well the differences between sccFCS and state lifetime fit, indicating that the rates recovered by state lifetime fit are averages of all the processes and that the Mg-binding/unbinding rate constants (that dominate the rates at high salt concentrations) are very similar for the Holliday Junctions. This in turn indicates that these

rate constants are sequence independent and that Mg-binding/unbinding is probably governed by electrostatic interactions only.

8.8 Comparison with other Holliday Junction sequences

Different Holliday Junctions, HJ_ES (Schweinberger 2002), were tested to investigate eventual sequence-dependent effects. Each branch of the HJ_ES has the three bases nearest to the branchpoint equal to HJ but different length (HJ_ES arms are six basepairs shorter) and overall sequence. Dynamic-PDA fits for the two junctions are compared in figure 8.8-1.

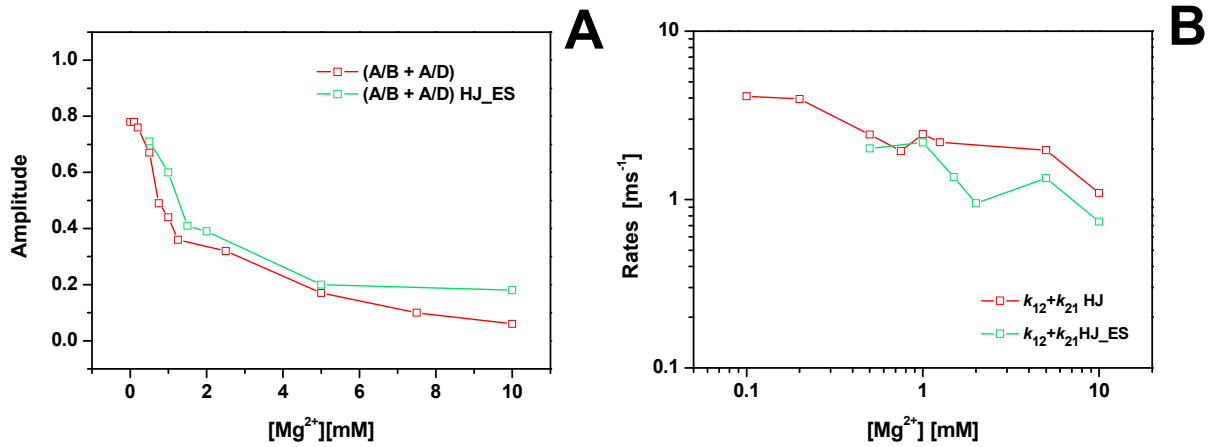

Figure 8.8-1. Comparison of dynamic-PDA results for HJ and HJ_ES. **(A)** Species (A/B + A/D) as fraction of the total FRET population for HJ (open red squares) and HJ_ES (open green squares). **(B)** Sum of the rate constants k_{12} and k_{21} for HJ (open red squares) and HJ_ES (open green squares).

The timescales of interconversion and the fractions of the dynamic species relative to the total FRET population are the same for both junctions over all the range of Mg^{2+} concentrations. Taking into account that the equilibrium concentrations of the dynamic and static species depend on the relative timescales of the Mg-binding/unbinding and interconversion equilibria ensues that the timescales of all rate constants, $k^{+}_{A/B(Mg)}$, $k^{+}_{A/D(Mg)}$, $k^{-}_{A/B(Mg)}$, $k^{-}_{A/D(Mg)}$, k_{12} and k_{21} are comparable in the different junctions. Therefore any major sequence dependency can be excluded.

8.9 Conclusions

With the use of dynamic-PDA and sccFCS has been demonstrated that the commonly accepted model for Holliday Junction conformers' interconversion (Eq. 8.1-1 and 8.1-3) is not

adequate. At least two relaxation mechanisms are present, acting on timescales differing for one or more orders of magnitude. In both relaxation mechanism are involved the same molecular species displaying FRET distances consistent with the folded structures A/B and A/D. Two new, simple but sufficient models, equation 8.5-1a and 8.5-1b, have been introduced to explain the experimental data. The results however cannot clarify whether the open state is present (Eq. 8.5-1b) or is simply a transition state in the interconversion between the A/B and A/D conformers (Eq. 8.5-1a).

The observation of dynamic processes at 0 mM Mg^{2+} is in contrast with the common view of a static situation where the only populated conformer is the Open one (Lilley 2000) but is absolutely consistent with the models proposed.

Comparison with different Holliday Junctions (Schweinberger 2002; McKinney, Déclais et al. 2003; Joo, McKinney et al. 2004) showed how the timescales of the processes seem to be sequence independent, with Mg-binding/unbinding governed by purely electrostatic interactions. On the other hand, the Mg-dependent shift in conformer population between A/B and A/D is characteristic of the Holliday Junctions investigated in this thesis, suggesting that the ratio of the interconversion rates is the only parameter that is effectively influenced by the DNA sequence.

It is important to note that almost all the apparent differences between the results presented in this work and those reported in literature (Lilley 2000; McKinney, Déclais et al. 2003; Joo, McKinney et al. 2004) can be explained by taking into account the different experimental conditions and different spectroscopy technique adopted, suggesting that these results are not contradictory but rather complementary.

9 Nucleosomes

The nucleosome is the basic unit of genome compaction (Kornberg 1974; Olins and Olins 1974). It consists of an octamer of histone proteins around which about two turns of double-stranded DNA are wound. Its detailed structure has been elucidated in crystallographic studies (Richmond, Finch et al. 1984; Luger, Mäder et al. 1997; Schalch, Duda et al. 2005) down to a resolution of 1.9 Å (Davey, Sargent et al. 2002). Central to nucleosomal function is its restructuring during processes that act on DNA, e.g. transcription or replication. Various mechanisms for nucleosome unfolding, unwrapping or repositioning have been proposed (Schiessel, Widom et al. 2001; Kulic and Schiessel 2003), but so far no direct physical evidence (e.g. detection of intermediate states) exists for any particular one. Here single-molecule FRET experiments were performed to collect quantitative structural information that will elucidate such mechanisms.

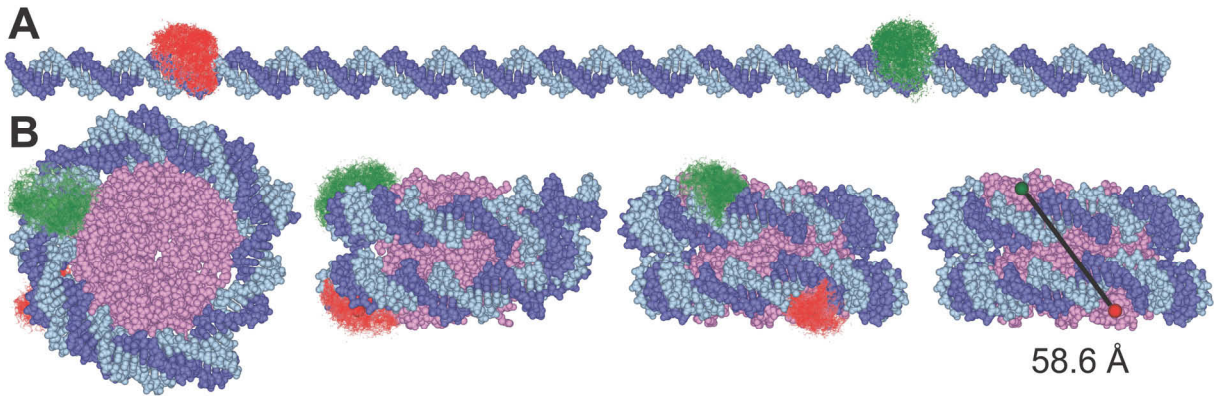

Figure 9-1. (A) Nucleosomal DNA in extended conformation. The conformational space of the D and A dyes obtained by MD simulations is shown in green and red, respectively. **(B)** Structure of a nucleosome. The first three structures from the left show different views of the nucleosome (crystal structure 1KX5 from the RCSB protein Data Bank, only the histone core is considered while lateral chains extending over the DNA were cut)(Davey, Sargent et al. 2002). The histone octamere is depicted in pink while the nucleosomal DNA duplex is represented in blue colours. The fourth structure of 9-1B is an alternative representation of the third view where the dye distributions are replaced by their centers of mass with the corresponding interdye distance. The planes of the nucleotide bases linked to the dyes are depicted in white.

9.1 Single-molecule experiments

Three populations with distinct fluorescence properties are immediately distinguishable in figure 9.1-1. One small population is characterised by FRET efficiency, E_{FRET}, and donor

lifetime, $\tau_{D(A)}$ similar to those of free donor dye ($E_{FRET} \approx 0$ and $\tau_{D(A)} \approx 4$ ns). It displays little or no FRET and will be referred to as Low-FRET and D-Only (*LF+DOnly*). The other two major populations overlap and display higher E_{FRET} and shortening of the donor lifetime. These species are FRET-active and will be referred to as Mid-FRET (*MF*) ($E_{FRET} \approx 0.3$ and $\tau_{D(A)} \approx 2.9$ ns) and High-FRET (*HF*) ($E_{FRET} \approx 0.5$ and $\tau_{D(A)} \approx 2.2$ ns). On the basis of the structure in figure 9-1B *MF* and *HF* were assigned to conformations in which the DNA is wrapped around the histones and *LF* to species where the DNA fragment is more extended.

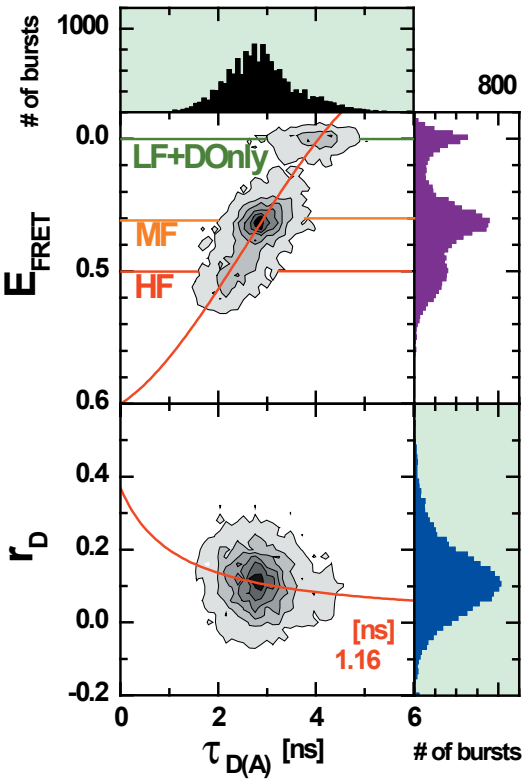

Figure 9.1-1. MFD plots of single nucleosomes at 5 mM NaCl. In the upper panel, FRET efficiency is plotted versus lifetime of the donor in presence of the acceptor, $\tau_{D(A)}$. FRET efficiencies are obtained from raw signals S by correcting for green and red background (B_G = 2.3 kHz, B_R = 1.2 kHz), spectral crosstalk (α = 0.07), detection efficiencies (g_G / g_R = 0.58), direct excitation of the acceptor (DE = 1.35 kHz), quantum yield of the donor in the absence of the acceptor ($\Phi_{FD(0)}$ = 0.70) and quantum yield of the acceptor (Φ_{FA} = 0.70). The red overlaid line is calculated from the empirical equation $E = 1\text{-}(0.00479+0.4813\tau_{D(A)}+0.26694\tau^2_{D(A)}-0.03435\tau^3_{D(A)}) / \tau_{D(0)}$, where $\tau_{D(0)}$ = 4.1 ns is the donor lifetime in absence of acceptor. The equation is a modification of the theoretical equation $E = 1\text{-} \tau_{D(A)} / \tau_{D(0)}$ and is needed to take into account the dye movement due to the flexible alkylchains in the linkers. In the lower panel, donor anisotropy, r_D, is plotted versus donor lifetime, $\tau_{D(A)}$, together with an overlaid curve computed from the Perrin equation $r_D = r_0 /(1+\tau_{D(A)} / \rho_D)$, using a value for fundamental anisotropy of r_0 = 0.37 and a mean rotational correlation time, ρ_D, of 1.16 ns.

9.2 Geometrical model

A geometric model based on the crystal structure and the dye positions in Fig 9-1 was introduced to describe the FRET species during nucleosome disassembly. In order to compare theory and experiment, FRET efficiency histograms were computed.

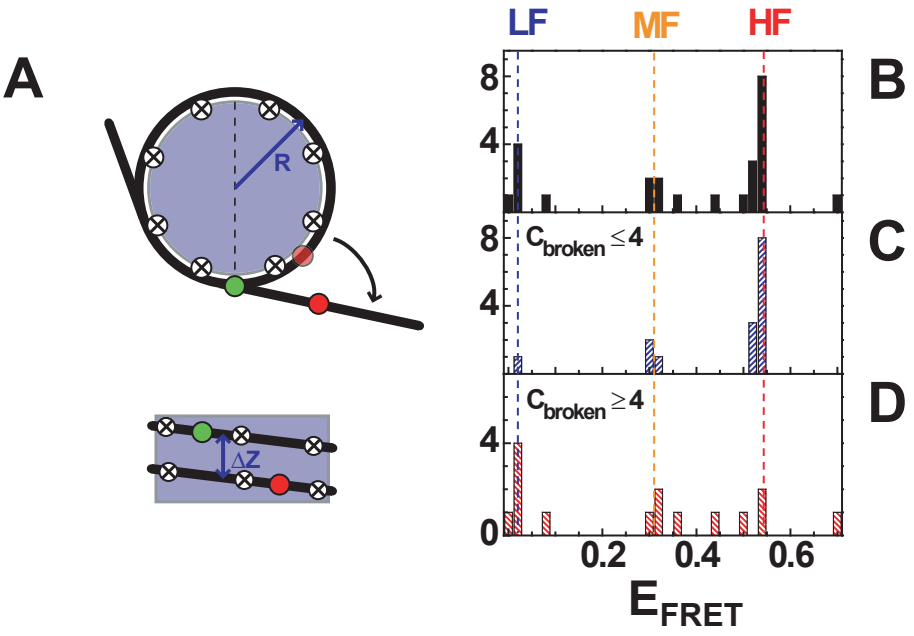

Figure 9.2-1. Unfolding of nucleosomes. **(A)** Geometric model for the unfolding of a nucleosome, top and side view. DNA is represented in black, histones in pink, contact points with circled crosses, donor and acceptor dye in green and red, respectively. In the top view, the semi-transparent red circle represents the position in which the acceptor dye would be in the case that DNA is completely wound around the histone core. Model parameters: Effective nucleosome radius R = 40 Å, rise per turn Δz = 45 Å, 80 base pairs per nucleosome turn, DNA length of 170 base pairs, donor dye position at 46.5 base pairs, acceptor dye position 136.5 base pairs, scaled Förster radius βR_0 = 61.2 Å with ß = 1.1 (for further details see supplementary information, section 2.7). Unfolding of nucleosomes. **(B-D)** Possible FRET efficiency values as calculated from the geometrical model of the nucleosome unfolding: **(B)** all possible values, **(C)** values obtained for the loss of up to 4 contact points, **(D)** values obtained for the loss of at least 4 contact points.

The model accounts for the fact that DNA dissociates stepwise at defined "contact points" from either end. From the X-ray structure 12 contact points *C* were identified within 4 Å shell from the core, DNA is therefore assumed to dissociate in steps of 10 to 11 basepairs. Detached part(s) of DNA are assumed to be straight and tangential to the nucleosome core at the detachment point(s). For simplicity, all combinations of dissociated contacts of the donor and acceptor arm are considered to be equally probable. There is no doubt that in reality this assumption may be violated. However, this will change only amplitudes but not the positions of the FRET peaks in the histograms. Fig. 9.2-1B shows the computed FRET histogram for nucleosome intermediates with partly dissociated DNA, where one to eight contact points are broken. Three peaks are clearly visible, for which the predicted FRET efficiencies nicely agree with those values measured for the *LF*, *MF* and *HF* species. If one distinguishes between different numbers of broken contact points, it is evident that for small numbers mainly two narrow distributions of FRET species are expected (Fig. 9.2-1C). For a larger number of broken contact points ($C_{broken} > 4$) a broad E_{FRET} distribution is expected ranging

from *LF* to *HF* (Fig. 9.2-1D). Figure 9.2-2 shows a cartoon of all possible disassembly intermediates based on the geometric model.

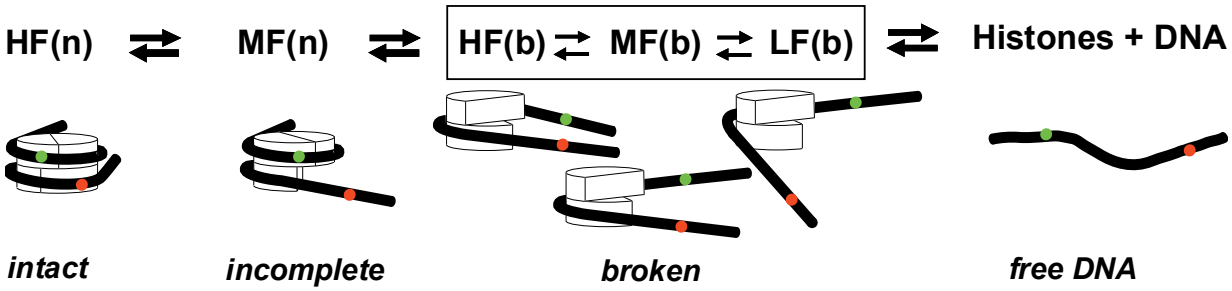

Figure 9.2-2. Sketches of the possible nucleosomal species. Nucleosomes lacking one H2A/H2B unit are indicated as *Incomplete*, while nucleosomes lacking more than one H2A/H2B units are indicated as *Broken*. Depending on the progress of disassembly the width of the corresponding FRET efficiency distributions of the species *LF*, *MF* and *HF* can be either narrow (n) or broad (b).

It turns out that not only the level of FRET efficiency is characteristic but also the width of the individual FRET distributions. Depending on the progress of disassembly the width of the corresponding FRET efficiency distributions of the species *LF*, *MF* and *HF* can be either narrow (n) or broad (b), i.e. a *HF* signal is not per-se indicative for an intact nucleosome.
The study of nucleosome disassembly is detailed in Paper IV

Summary

This thesis presents developments in fluorescence techniques that allow the study of Fluorescence Resonance Energy Transfer between multiple chromophores in single molecules in solution. Single-molecule techniques have been proved far superior to ensemble techniques in the study of heterogeneous samples because averaging of different FRET signal is avoided. In this thesis are presented advances in the fields of FCS and PDA and their application to the study of DNA model systems.

Filtered FCS and Species Cross Correlation Function

In heterogeneous samples it is usually difficult to separate the correlation contributions of each species. To solve this problem, an extended analysis method of time-, polarisation- and colour- resolved fluorescence correlation spectroscopy (filtered FCS or fFCS) is introduced. This method takes advantage of the MFD information to distinguish the fluorescence signal of the multiple species and of the scatter contributions. In this way it is possible to obtain the separate correlation functions of the different species and perform quantitative analysis of molecular fractions. In comparison to recently introduced fluorescence lifetime correlation spectroscopy (FLCS) this method, using differences in time resolved fluorescence anisotropy, is able to distinguish species even with the same fluorescence lifetime. The possibility to distinguish the different molecular species present in solution is here exploited to compute the cross-correlation function between only two species of a multi-component sample (sccFCS).

Probability distribution analysis

Probability distribution analysis (PDA) allows one to quantitatively analyse single-molecule data obtained in FRET or fluorescence polarization experiments. Here, PDA theory is further developed to encompass heterogeneous static systems and dynamic two-state interconverting systems.

1. In order to describe systems consisting of multiple non-interconverting fluorescent states, several extensions to the PDA theory are presented. Effects of brightness variations and multiple molecule events are considered independently of the detection volume parameters, using only the overall experimental signal intensity distribution. Correction of the PDA model function for the presence of multiple molecule events is introduced extending the useful range of measurement concentrations. Tools such as

maximum entropy method and combined mean donor fluorescence lifetime analysis have been developed to distinguish whether extra broadening of PDA histograms could be attributed to structural heterogeneities or dye artifacts. Resolution in FRET experiments in the range of a few Ångström is achieved making possible the distinction between a set of fixed distances and a distribution of distances.

2. An analytical solution describing the interconversion between two FRET states is introduced. It is demonstrated that relaxation times on the timescale of the diffusion time (typically milliseconds) can be accurately recovered. The dynamic range accessible to the method is of about three orders of magnitude. Major factors limiting the absolute precision of dynamic-PDA are identified as brightness variations, shortening of the observation time due to diffusion, and contributions of multi-molecular events. These effects are shown to considerably bias dynamic-PDA often leading to under- or overestimation of the rate constants by factor of two or more. Correction procedures are proposed.

The extended PDA theories were verified by analysing simulations and experimental data.
The combination of MFD, PDA and FCS techniques was used to study three different systems.

Two-step FRET

The possibility to observe and characterise multiple-step FRET in single molecules was tested by investigating double stranded DNA labelled with three fluorophores, one donor (D) and two acceptors (A1 and A2). The sequence was designed so that the single FRET steps take place between D and A1 and between A1 and A2, even though D-A2 transfer was also observed. Fluorescence signal from each dye was detected, and good separation was achieved. These results suggested that, already as qualitative essay, it is possible to label multi-domain or multi-molecular systems and have information about proximity or simultaneous presence of the labelled positions. Exploiting the MFD capabilities, donor quenching and A2 heterogeneity were detected. Quantitative analysis of the system was precluded due to the complex photophysics of A2.

Holliday Junctions

The interconversion between the stacking conformers, A/B and A/D, of a Holiday junction was studied as a function of Mg^{2+} concentration. The dynamic processes were monitored by the fluctuations of the FRET between donor and acceptor dyes coupled to two consecutive branches. Dynamic-PDA revealed that the Holliday junction is a complex dynamic system, where at least 3 equilibria, taking place at different timescales, are present. The equilibria were associated to the transitions between the conformer A/B and its Mg-bound form, A/B and A/D and A/D and its Mg-bound form. Accurate rate constants were obtained by sccFCS. Magnesium dependence of the rate constants resulted consistent with the behavior shown by simulated data. Comparison between different Holliday junctions suggested that the timescales of the different equilibria are sequence independent and only the interconversion between A/B and A/D is characteristic of each junction. The open cruciform structure was not observed (TCSPC, Dynamic-PDA and sccFCS analysis), even in the absence of Mg^{2+} where it is supposed to be the only populated conformer. These results led to a revision of the commonly accepted interconversion model (Lilley 2000). In the model proposed in this work it is hypothesised that in absence of metal ions the Holliday junction is not static but it is oscillating between the two folded conformers and only when Mg^{2+} is coordinated the junction is fixed in the conformation it is at the moment.

Nucleosomes

The disassembly of mononucleosomes was studied by quantitative single-molecule FRET with high spatial resolution, using the SELEX-generated "Widom 601" positioning sequence labelled with donor and acceptor fluorophores. Reversible dissociation was induced by increasing NaCl concentration. At least three species with different FRET efficiencies were identified: the most stable high-FRET species corresponding to the intact nucleosome, a less stable mid-FRET species that was attributed to a first intermediate with a partially unwrapped DNA, and a low-FRET species characterised by a very broad FRET distribution, representing a highly unwrapped structure formed at the expense of the other two species. fFCS analysis indicated that even in the low-FRET state, some histones are still bound to the DNA. The interdye distance of 54.0 Å measured for the high-FRET species is consistent with the known crystallographic structure. A geometric model of the nucleosome disassembly predicts exactly the presence of the observed FRET species and confirms their assignment to two populations in the unwrapping pathway.

Literature

Antonik, M., S. Felekyan, et al. (2006). "Separating structural heterogeneities from stochastic variations in fluorescence resonance energy transfer distributions via photon distribution analysis." Journal of Physical Chemistry B **110**(13): 6970-6978.

Böhmer, M. and J. Enderlein (2003). "Fluorescence spectroscopy of single molecules under ambient conditions: Methodology and technology." ChemPhysChem **4**(8): 793-808.

Böhmer, M., M. Wahl, et al. (2002). "Time-resolved fluorescence correlation spectroscopy." Chemical Physics Letters **353**(5-6): 439-445.

Brochon, J. C. (1994). Maximum Entropy Method of Data Analysis in Time-Resolved Spectroscopy. Methods of Enzymology, Vol. 240. New York, Academic Press**:** 262-311.

Broker, T. R. and I. R. Lehman (1971). "Branched DNA Molecules - Intermediates in T4 Recombination." Journal of Molecular Biology **60**(1): 131-&.

Creasey, D. J., P. A. Halford-Maw, et al. (1998). "Fast photomultiplier tube gating system for photon counting applications." Review of Scientific Instruments **69**(12): 4068-4073.

Davey, C. A., D. F. Sargent, et al. (2002). "Solvent mediated interactions in the structure of the nucleosome core particle at 1.9 a resolution." J Mol Biol **319**(5): 1097-113.

Duckett, D. R., A. I. H. Murchie, et al. (1988). "The structure of the Holliday junction and its resolution." Cell **55**: 79-89.

Dyson, H. J. and P. E. Wright (2005). "Intrinsically unstructured proteins and their functions." Nature Reviews Molecular Cell Biology **6**(3): 197-208.

Eggeling, C., S. Berger, et al. (2001). "Data registration and selective single-molecule analysis using multi-parameter fluorescence detection." Journal of Biotechnology **86**(3): 163-180.

Eichman, B. F., J. M. Vargason, et al. (2000). "The Holliday junction in an inverted repeat DNA sequence: Sequence effects on the structure of four-way junctions." Proc.Natl.Acad.Sci.USA. **97**(8): 3971-3976.

Eisenmesser, E. Z., O. Millet, et al. (2005). "Intrinsic dynamics of an enzyme underlies catalysis." Nature **438**(7064): 117-121.

Elson, E. L. and D. Magde (1974). "Fluorescence Correlation Spectroscopy. I. Conceptual Basis and Theory." Biopolymers **13**: 1-27.

Enderlein, J. and I. Gregor (2005). "Using fluorescence lifetime for discriminating detector afterpulsing in fluorescence-correlation spectroscopy." Review of Scientific Instruments **76**(3).

Fenley, M. O., G. S. Manning, et al. (1998). "Excess counterion binding and ionic stability of kinked and branched DNA." Biophysical Chemistry **74**(2): 135-152.

Förster, T. (1948). "Zwischenmolekulare Energiewanderung und Fluoreszenz." Annalen der Physik **2**: 55-75.

Fries, J. R., L. Brand, et al. (1998). "Quantitative identification of different single-molecules by selective time-resolved confocal fluorescence spectroscopy." Journal of Physical Chemistry A **102**: 6601-6613.

Gopich, I. and A. Szabo (2005). "Theory of photon statistics in single-molecule Förster resonance energy transfer." Journal of Chemical Physics(122): 014707.

Gregor, I. and J. Enderlein (2007). "Time-resolved methods in biophysics. 3. Fluorescence lifetime correlation spectroscopy." Photochem. Photobiol. Sci. **6**(1): 13-18.

Henzler-Wildman, K. and D. Kern (2007). "Dynamic personalities of proteins." Nature **450**(7172): 964-972.

Herman, J. R., T. R. Londo, et al. (1992). "Normally on Photomultiplier Gating Circuit with Reduced Post-gate Artifacts for Use in Transient Luminescence Measurements." Review of Scientific Instruments **63**(11): 5454-5458.

Hirschfeld, T. (1976). "Quantum efficiency independence of the time integrated emission from a fluorescent molecule." Applied Optics **15**(12): 3135-3139.

Hohng, S., R. B. Zhou, et al. (2007). "Fluorescence-force spectroscopy maps two-dimensional reaction landscape of the Holliday junction." Science **318**(5848): 279-283.

Holliday, R. (1964). "A new mechanism of gene conversion in fungi." Genetical Research **5**: 282-304.

Joo, C., S. A. McKinney, et al. (2004). "Exploring Rare Conformational Species and Ionic Effects in DNA Holliday Junctions Using Single-molecule Spectroscopy." Journal of Molecular Biology **341**: 739-751.

Kalinin, S., S. Felekyan, et al. (2007). "Probability distribution analysis of single-molecule fluorescence anisotropy and resonance energy transfer." Journal of Physical Chemistry B **111**(34): 10253-10262.

Kalinin, S., S. Felekyan, et al. (2008). "Characterizing Multiple Molecular States in Single-Molecule Multiparameter Fluorescence Detection by Probability Distribution Analysis." Journal of Physical Chemistry B **112**(28): 8361-8374.

Kapanidis, A. N., N. K. Lee, et al. (2004). "Fluorescence-aided molecule sorting: Analysis of structure and interactions by alternating-laser excitation of single molecules." Proceedings of the National Academy of Sciences of the United States of America **101**(24): 8936-8941.

Kasha, M. (1950). "Characterization of electronic transitions in complex molecules." Discussion of the Faraday Society **9**: 14.

Kask, P., K. Palo, et al. (2000). "Two-Dimensional Fluorescence Intensity Distribution Analysis: Theory and Application." Biophysical Journal **78**(4): 1703-1713.

Kask, P., K. Palo, et al. (1999). "Fluorescence-intensity distribution analysis and its application in biomolecular detection technology." Proc.Natl.Acad.Sci.USA. **96**(24): 13756-13761.

Koppel, D. E. (1974). "Statistical accuracy in fluorescence correlation spectroscopy." Physical Review A **10**(6): 1938-1945.

Kornberg, R. D. (1974). "Chromatin structure: a repeating unit of histones and DNA." Science **184**(139): 868-71.

Koshioka, M., K. Saski, et al. (1995). "Time-Dependent Fluorescene Depolarization Analysis in Three Dimensional Microscopy." Applied Spectroscopy **49**(2): 224-228.

Kühnemuth, R. and C. A. M. Seidel (2001). "Principles of Single Molecule Multiparameter Fluorescence Spectroscopy." Single Molecules **2**(4): 251-254.

Kulic, I. M. and H. Schiessel (2003). "Nucleosome repositioning via loop formation." Biophys J **84**(5): 3197-211.

Lakowicz, J. R. (1999). Principles of Fluorescence Spectroscopy. New York, Kluwer Academic/ Plenum Publishers.

Lee, N. K., A. N. Kapanidis, et al. (2007). "Three-color alternating-laser excitation of single molecules: Monitoring multiple interactions and distances." Biophysical Journal **92**(1): 303-312.

Li, L. Q. and L. M. Davis (1995). "Rapid and efficient detection of single chromophore molecules in aqueous solution." Applied Optics **34**(18): 3208-3217.

Lilley, D. M. J. (2000). "Structures of helical junctions in nucleic acids." Quarterly Reviews of Biophysics **33**(2): 109-159.

Livesey, A. K. and J. Skilling (1985). "Maximum-Entropy Theory." Acta Crystallographica Section A **41**(MAR): 113-122.

Luger, K., A. W. Mäder, et al. (1997). "Crystal structure of the nucleosome core particle at 2.8 Å resolution." Nature **389**: 251-260.
Magde, D., E. L. Elson, et al. (1972). "Thermodynamic fluctuations in a reacting system - measurement by fluorescence correlation spectroscopy." Physical Review Letters **29**: 705-708.
Magde, D., E. L. Elson, et al. (1974). "Fluorescence Correlation Spectroscopy. II. An Experimental Realization." Biopolymers **13**: 29-61.
Maus, M., M. Cotlet, et al. (2001). "An Experimental Comparison of the Maximum Likelihood Estimation and Nonlinear Least-Squares Fluorescence Lifetime Analysis of Single Molecules." Analytical Chemistry **73**: 2078-2086.
McKinney, S. A., A. C. Déclais, et al. (2003). "Structural dynamics of individual Holliday junctions." Nature Structural & Molecular Biology **10**: 93-97.
Mets, Ü. and R. Rigler (1994). "Submillisecond Detection of Single Rhodamine Molecules in Water." Journal of Fluorescence **4**(3): 259-264.
Moerner, W. E. and D. P. Fromm (2003). "Methods of single-molecule fluorescence spectroscopy and microscopy." Review of Scientific Instruments **74**(8): 3597-3619.
Moerner, W. E. and L. Kador (1989). "Optical Detection and Spectroscopy of Single Molecules in a Solid." Physical Review Letters **62**(21): 2535-2538.
Mollegaard, N. E., A. I. H. Murchie, et al. (1994). "Uranyl Photoprobing of a 4-way DNA Junction - Evidence for Specific Metal-ion binding." EMBO Journal **13**(7): 1508-1513.
Murchie, A. I. H., R. M. Clegg, et al. (1989). "Fluorescence energy transfer shows that the four-way DNA junction is a right-handed cross of antiparallel molecules." Nature **341**: 763-766.
Nettels, D., I. V. Gopich, et al. (2007). "Ultrafast dynamics of protein collapse from single-molecule photon statistics." Proceedings of the National Academy of Sciences of the United States of America **104**(8): 2655-2660.
Nowakowski, J., P. J. Shim, et al. (1999). "Crystal structure of an 82-nucleotide RNA-DNA complex formed by the 10-23 DNA enzyme." Nature Structural Biology **6**(2): 151-156.
Olins, A. L. and D. E. Olins (1974). "Spheroid chromatin units (v bodies)." Science **183**(122): 330-2.
Olmsted, M. C. and P. J. Hagerman (1994). "Excess Counterion Accumulation around Branched Nucleic-Acids." Journal of Molecular Biology **243**(5): 919-929.
Orrweaver, T. L., J. W. Szostak, et al. (1981). "Yeast Transformation - A Model System for the Study of Recombination." Proceedings of the National Academy of Sciences of the United States of America-Biological Sciences **78**(10): 6354-6358.
Palmer III, A. G. and N. L. Thompson (1987). "Theory of sample translation in fluorescence correlation spectroscopy." Biophysical Journal **51**: 339-343.
Panyutin, I. G. and P. Hsieh (1994). "The kinetics of spontaneous DNA branch migration." Proceedings of the National Academy of Sciences of the United States of America **91**(6): 2021-2025.
Richmond, T. J., J. T. Finch, et al. (1984). "Structure of the nucleosome core particle at 7 A resolution." Nature **311**(5986): 532-537.
Rigler, R. and Ü. Mets (1992). "Diffusion of single molecules through a Gaussian laser beam." SPIE **1921**: 239-248.
Saffarian, S., Y. Li, et al. (2007). "Oligomerization of the EGF receptor investigated by live cell fluorescence intensity distribution analysis." Biophysical Journal **93**(3): 1021-1031.
Schalch, T., S. Duda, et al. (2005). "X-ray structure of a tetranucleosome and its implications for the chromatin fibre." Nature **436**(7047): 138-41.

Schiessel, H., J. Widom, et al. (2001). "Polymer Reptation and Nucleosome Repositioning." Phys Rev Lett **86**(19): 4414-4417.

Schwacha, A. and N. Kleckner (1995). "Identification of double Holliday Junctions as Intermediates in Meiotic Recombination." Cell **83**(5): 783-791.

Schweinberger, E. (2002). Multidimensionale Einzelmolekül-Fluoreszenz-Spektroskopie von fluoreszenzmarkierten Biomolekülen, Georg-August-Universität Göttingen.

Shera, E. B., N. K. Seitzinger, et al. (1990). "Detection of single fluorescent molecules." Chemical Physics Letters **174**(6): 553-557.

Sigal, N. and B. Alberts (1972). "Genetic Recombination - Nature of a Crossed Strand-exchange between two Homologous DNA Molecules." Journal of Molecular Biology **71**(3): 789-&.

Stryer, L. and R. P. Haugland (1967). "Energy Transfer: A Spectroscopic Ruler." Proc.Natl.Acad.Sci.USA. **58**: 719-726.

Valeur, B. (2002). Molecular Fluorescence: Principles and Applications, Wiley-VCH Verlag Weinheim.

van der Meer, B. W., G. Cooker, et al. (1994). Resonance Energy Transfer: Theory and Data. New York, VCH Publishers.

Widengren, J., V. Kudryavtsev, et al. (2006). "Single-molecule detection and identification of multiple species by multiparameter fluorescence detection." Analytical Chemistry **78**(6): 2039-2050.

Widengren, J. and Ü. Mets (2002). Conceptual Basis of Fluorescence Correlation Spectroscopy and Related Techniques as Tools in Bioscience Single Molecule Detection in Solution: Methods and Applications. C. Zander, J. Enderlein and R. A. Keller**:** 69-120.

Wozniak, A. K., G. Schröder, et al. (2008). "Single molecule FRET measures bends and kinks in DNA " Proceedings of the National Academy of Sciences of the United States of America **105**: 18337-18342.

Xiao, M. and P. R. Selvin (1999). "An improved instrument for measuring time-resolved lanthanide emission and resonance energy transfer." Review of Scientific Instruments **70**(10): 3877-3881.

Acknowledgments

First and foremost I would like to thank my supervisor, **Prof. Dr. Claus A. M. Seidel**, for giving the opportunity to work in his group. In the years much I have learned from him the determination and the enthusiasm in the work we do. He thought me how to be a better scientist and for this I am truly grateful.

I gratefully acknowledge

Dr. Suren Felekyan for helping me through all the steps of my thesis. His support in the lab and his knowledge were invaluable to me. He has been an excellent discussion and working partner and I was happy to learn from him. Thanks to Suren I know more about science and Armenian cognac.

Dr. Stanislav Kalinin for being always right in theoretical and experimental matters. For being nice and patient when trying to make complicated ideas stick into my head.

Dr. Matthew Antonik for fruitful discussions and for sharing his knowledge. For trying to teach me American English. For the hours spent playing board games and for introducing me to the American way of life.

Prof. Dr. Filipp Oesterhelt for his interest in my work, the useful discussions and constructive criticism.

Dr. Volodymyr Kudryavtsev for being the best second-officer that I could ever have. For the discussions about science and life we had in our kitchen.

Dr. Alexandr Gaiduk for having always a nice word and being positive. For the oscilloscope in his lab during the WM 2006.

Heike Hornen and Andreas Renner. My first students in the fluorescence Praktikum, for the shared interest in the local cuisine of the world. For being nice travel companions.

Stefan Marawske, for being such a challenging opponent in our after-lunch activities and for *forcing* me to be social.

Sebastian Overmann for being the best office-mate ever. I really enjoyed our chats about movies and videogames.

Dr. Ralf Kühnemuth for sharing with me his knowledge and experience. For the late night pizzas and chats.

Dr Paul Rothwell and Evangelos Sisamakis for the nicotine based discussions about science and European geopolitics.

Dr. Steven Magennis for his support and encouragement. For introducing me to the Highlander culture and the Craig Ferguson Show. For the karaoke nights.

Simon Sindbert for reading this thesis notwithstanding the *horrors* in English.

Denis Dörr for sharing his extensive knowledge in dangerous chemical reactions. For his Siberian anecdotes.

Daniela Pfiffi for taking care of the most important aspect of the scientific research…coffee.

Richard Janissen for practicing Portuguese/Brazilian language. For being always helpful.

Marcel Merkwitz for helping me find an exit in the maze of computers and for indulging me with my extravagant ideas. You will be forever my *adminin*.

Bärbel Hoffman and Veronika Mendorf for making the life of us foreigners easier. For the countless paperwork they took care of. Your work is really appreciated.

Martin Schramm for always being nice and positive, for helping me with electronic devices and other *technicalities* during my work.

Dr. Marcelle König and Dr. Anna Wozniak for helping me adapt to Germany. For the nice parties in Göttingen and Düsseldorf.

Dr. Enno Schweinberger for teaching me when I was a rookie in the lab. For remembering my birthday even if I do not remember his.

Dr. Alexander Gansen, Dr. Katalin Tóth and Prof. Dr. Jörg Langowski for fruitful collaboration in the investigation of Nucleosomes.

I would like to thank all my colleagues in Göttingen and Düsseldorf for these years in which they have always been friendly and helpful: **Dr. Pierre-Alain Müller, Ralf Müller, Carl Sandhagen, Dr. Manuel M. Lohrengel, Dr. Olga Franco, Dr. Aike Stortelder, Dr. Peter Karageorgiev, Ming Chang Tsai, Opas Tojira, Harekrushna Sahoo, Leoni Oberbarnscheidt, Dmytro Rodnin, Daniel Rohrbeck, Markus Richert, Stephanie Rehwald, Stefanie Weidtkamp-Peters.**

I extend my gratitude to my family for being supportive and for being always there even at 1400 Km of distance. For the patience they had.

And last but not least, I would like to thank Carla Sofia, for her help and constant encouragement especially during the last stages of my thesis.

Alessandro Valeri, February 2009

I

Filtered FCS and Species Cross Correlation Function

Suren Felekyan, Stanislav Kalinin, Alessandro Valeri, Claus A. M. Seidel
Institut für Physikalische Chemie, Lehrstuhl für Molekulare Physikalische Chemie,
Heinrich-Heine-Universität, Universitätsstraße 1, Geb 26.32, 40225 Düsseldorf, Germany

ABSTRACT

An extended analysis method of time, polarization and color resolved fluorescence correlation spectroscopy (filtered FCS) is introduced. It uses multiparameter fluorescence detection (MFD) [1-3] to separate pure fluorescence signal of multiple species and scatter contributions. This method allows monitoring of simultaneous and independent diffusion of several molecular species in one sample and makes possible accurate and quantitative analyses of fractions. The proposed method is simple to implement experimentally, because it requires only single wavelength excitation and MFD widely used in single molecule experiments. In comparison to recently introduced fluorescence lifetime correlation spectroscopy (FLCS) [4-7] this method is able to distinguish species when they have very close or even the same fluorescence lifetime using just differences in time resolved fluorescence anisotropy.

Keywords: FCS, TCSPC, FLCS, MFD, Fluorescence Lifetime, Time Resolved Fluorescence Anisotropy, Correlation.

1. INTRODUCTION

Fluorescence correlation spectroscopy (FCS) has been developed in early 1970 [8, 9] and has become a very powerful spectroscopic technique in the 1990s due to significantly improved optics and excitation sources [10, 11]. FCS is an ultrasensitive method for detection and monitoring of molecular binding/unbinding processes, chemical reaction kinetics [12-19] and diffusion constant. However the method can not distinguish between molecules which have similar diffusion constants. The FCS curve for a mixture of more than one fluorescent molecular species with different brightness and diffusion constants has a complex structure.

The combination of time-resolved fluorescence detection with FCS has already been described in the literature. In [20], time-gating of the fluorescence signal in the nanosecond range was used for suppressing light scattering or the fluorescence of a dye with a fast fluorescence decay time (with respect to a dye with a long fluorescence decay time). All photons arriving outside the time-gate were ignored and not included in the analysis. This is analogous to using a spectral filter for blocking unwanted signals outside of the spectral window of interest. The idea of setting a time-gate for suppressing unwanted signals in ultrasensitive fluorescence and luminescence detection is a well known and widely used technique [21-25]. However this technique has a disadvantage: it is too subjective in definition of time-gate and can not fully remove unwanted signal because of "crosstalk" into time gate.

Recently a completely different strategy which uses the differing fluorescence decay characteristics of dyes for separating their FCS curves was proposed [4-6]. The lifetime information of the measured fluorescence signal was used for extracting two independent FCS curves for two different dyes without discarding any of the detected photons. As authors note it is "similar to recording a complete spectrum and deconvoluting it into the different contributions from the various emitting species. The main advantages are that: (i) no part of the measured signal is discarded, (ii) FCS curves of different dyes are obtained independently and simultaneously, (iii) the method can be generalized for more than two dyes, provided that they have sufficiently distinct fluorescence decay characteristics (i.e. sufficiently different decay times for fluorophores)" [4].

The third statement is one of the limitations of this new method since "sufficiently different decay times" in practice (from our experience) means at least 1.0-1.5 ns difference (20-30 %) in lifetimes for fast separation and very often used fluorescent dye molecules have lifetime in a range from 1 to 5 ns which restricts dyes selection significantly.

This method is designed for use in mono color detection and auto correlation which makes experimental setup quite simple and not expensive. As has been shown in [5] it is also applicable for discrimination detector afterpulsing from fluorescence signal.

Of course suggested method has real advantages and we will extend it for MFD case when signals detected within several detection channels at different wavelengths are also split into parallel and perpendicular polarizations relative to linearly polarized excitation laser beam. In this way we can include time resolved anisotropy as second parameter and spectral differences of species as third one in addition to fluorescence lifetime to distinguish different molecular species from mixture. Two dimensional filtering (lifetime and anisotropy or lifetime and color) makes this method more precise in general and particularly makes possible to separate the FCS curves for different molecular species when they have very similar lifetimes (even equal) but they are sufficiently distinct in fluorescence anisotropy (i.e. sufficiently different (at least 0.2-0.3 ns difference) rotational correlation times).

Especially important case is FRET experiments: usually it is impossible to avoid Donor-only (D-only) labeled species in mixture with Donor and Acceptor (DA) labeled species in solution. This makes the situation more complex when one should expect also FRET efficiency change due to conformational change and as a consequence brightness's change during diffusion time of DA labeled molecule.

The fluorescence registration within several detection channels at different wavelengths makes possible not only a separate determination of the FCS curves for different molecular species but also offers the possibility to perform a species cross-correlation analysis.

We have designed these new filters especially for accurate separation of pure fluorescence from scattered signal, further global two colors FCS and species cross-correlation analysis.

2. THEORY

2.1 Fluorescence Lifetime Filters (FLF) and normalization

The autocorrelation function allows direct assessment of the diffusion constant *D*. The amplitude at zero time of the autocorrelation function *G* (τ), allows one to determine the mean number of molecules *N* in the detection volume V_{det} or the concentration *c*, if the parameters of detection volume are known

$$\frac{1}{\mathrm{G}(0)-1}=N, \qquad or \qquad c=\frac{N}{V_{\text{det}}} \tag{1}$$

Unfortunately, the situation becomes significantly more complicated if more than one molecular species are simultaneously present in solution. For a mixture of *n* species, with corresponding brightnesses $Q^{(i)}$, diffusion constants $D^{(i)}$ and fractions $x^{(i)}$, *i=1,..., n*, the autocorrelation function reads

$$G(t_c)=1+\frac{1}{N}\cdot\frac{\sum_i^n x^{(i)}\cdot(Q^{(i)})^2\cdot G_{diff}^{(i)}(t_c)}{\left(\sum_i^n x^{(i)}\cdot Q^{(i)}\right)^2}, \tag{2}$$

where $c^{(i)}$ concentration, $Q^{(i)}$ brightness and $x^{(i)}=\frac{c^{(i)}}{\sum_i c^{(i)}}$ fraction of species *i*, and

$$G_{diff}^{(i)}(t_c)=\left(1+\frac{t_c}{t_D^{(i)}}\right)^{-1}\cdot\left(1+\left(\frac{\omega_0}{z_0}\right)^2\cdot\frac{t_c}{t_D^{(i)}}\right)^{-\frac{1}{2}} \tag{3}$$

is the normalized $G_{diff}^{(i)}(0)=1$ correlation function. This model assumes a 3-dimensional (3D) Gaussian shaped volume element with spatial distribution of the detection probabilities: $w(x,y,z)=\exp\left(-2\left(x^2+y^2\right)/\omega_0^2\right)\exp\left(-2z^2/z_0^2\right)$. The $1/e^2$ radii in *x* and *y* or in *z* direction are denoted by ω_0 or z_0, respectively. The characteristic diffusion times $t_D^{(i)}$ can be used to estimate the diffusion coefficients $D^{(i)}$: $t_D^{(i)}=\omega_0^2/4D^{(i)}$ (for 1-photon excitation).

A simple relation like Eq. (1) can not be found for multiple species. Even if one knows the brightness $Q^{(i)}$ for each species, the diffusion coefficients $D^{(i)}$ still have to be significantly distinct for successful extraction of $c^{(i)}$ values.

As it is shown in [4] the situation changes when different molecular species show differences in fluorescence lifetime which can be measured by time-correlated single-photon counting (TCSPC) [26, 27]. For simplicity, we will consider only two molecular species with fluorescence decay patterns $\{{}^{\parallel}p_j^{(i)}\}$ and $\{{}^{\perp}p_j^{(i)}\}$, where i =1; 2 and j denotes the number of the TCSPC channel, ${}^{\parallel}p_j^{(i)}$ and ${}^{\perp}p_j^{(i)}$ are the normalized probabilities (see later) of measuring a photon within the jth channel for species i in parallel and perpendicular polarizations relative to linearly polarized excitation laser beam respectively.

Any measured TCSPC decay histograms $\{{}^{\parallel}H_j\}$ and $\{{}^{\perp}H_j\}$ of a mixture of the two species will be superposition of the form

$$\begin{cases} {}^{\parallel}H_j = \sum_{i=1}^{n(=2)} w^{(i)}\cdot{}^{\parallel}p_j^{(i)} = w^{(1)}\cdot{}^{\parallel}p_j^{(1)} + w^{(2)}\cdot{}^{\parallel}p_j^{(2)} \\ {}^{\perp}H_j = \sum_{i=1}^{n(=2)} w^{(i)}\cdot{}^{\perp}p_j^{(i)} = w^{(1)}\cdot{}^{\perp}p_j^{(1)} + w^{(2)}\cdot{}^{\perp}p_j^{(2)} \end{cases} \quad (4)$$

where $w^{(i)}$ is the amplitude of the photon count contribution (in photons number) of the ith species. Now, following [4] two filter sets ${}^{\parallel}f_j^{(i)}$ and ${}^{\perp}f_j^{(i)}$, i =1; 2, can be devised with the properties

$$\left\langle \sum_{j=1}^{L} {}^{\parallel}f_j^{(i)}\cdot{}^{\parallel}H_j \right\rangle = {}^{\parallel}w^{(i)}, \quad \left\langle \sum_{j=1}^{L} {}^{\perp}f_j^{(i)}\cdot{}^{\perp}H_j \right\rangle = {}^{\perp}w^{(i)} \quad (5)$$

where ${}^{\parallel}w^{(i)}$ and ${}^{\perp}w^{(i)}$ are the photon count contributions of the ith species in parallel and perpendicular detection channels respectively (${}^{\parallel}w^{(i)}+{}^{\perp}w^{(i)} = w^{(i)}$), L is the total number of TCSPC channels, and the brackets denote averaging over an infinite number of measurements. ${}^{\parallel}f_j^{(i)}$ and ${}^{\perp}f_j^{(i)}$ has to be chosen in such a way as to minimize the relative errors in both channels simultaneously

$$\left\langle \left(\sum_{j=1}^{L} {}^{\parallel}f_j^{(i)}\cdot{}^{\parallel}H_j - {}^{\parallel}w^{(i)} \right)^2 \right\rangle \to \min \quad \text{and} \quad \left\langle \left(\sum_{j=1}^{L} {}^{\perp}f_j^{(i)}\cdot{}^{\perp}H_j - {}^{\perp}w^{(i)} \right)^2 \right\rangle \to \min \quad (6)$$

Since single photon detection in each channel follows Poissonian statistics [28], then ${}^{\parallel}f_j^{(i)}$ and ${}^{\perp}f_j^{(i)}$ are expressed, with the help of the weighted pseudoinverse of the matrices ${}^{\parallel}\hat{M}$ and ${}^{\perp}\hat{M}$, (${}^{\parallel}\hat{M}_{ij}={}^{\parallel}p_j^{(i)}$ and ${}^{\perp}\hat{M}_{ij}={}^{\perp}p_j^{(i)}$), as

$$\begin{cases} {}^{\parallel}f_j^{(i)} = \left(\left[{}^{\parallel}\hat{M}\cdot diag\left\langle {}^{\parallel}H_j \right\rangle^{-1}\cdot {}^{\parallel}\hat{M}^T \right]^{-1}\cdot {}^{\parallel}\hat{M}\cdot diag\left\langle {}^{\parallel}H_j \right\rangle^{-1} \right) \\ {}^{\perp}f_j^{(i)} = \left(\left[{}^{\perp}\hat{M}\cdot diag\left\langle {}^{\perp}H_j \right\rangle^{-1}\cdot {}^{\perp}\hat{M}^T \right]^{-1}\cdot {}^{\perp}\hat{M}\cdot diag\left\langle {}^{\perp}H_j \right\rangle^{-1} \right) \end{cases} \quad (7)$$

where $diag\left\langle {}^{\parallel}H_j \right\rangle^{-1}$ and $diag\left\langle {}^{\perp}H_j \right\rangle^{-1}$ are $L\times L$-dimensional diagonal matrices with diagonal elements $\left\langle {}^{\parallel}H_j \right\rangle^{-1}$ and $\left\langle {}^{\perp}H_j \right\rangle^{-1}$, j =1; . . . ; L, and the superscript T denotes matrix transposition. The direct calculation proves that the filters ${}^{\parallel}f_j^{(i)}$, ${}^{\perp}f_j^{(i)}$ and the patterns ${}^{\parallel}p_j^{(i)}$, ${}^{\perp}p_j^{(i)}$ are orthonormal systems,

$$\sum_{j=1}^{L} {}^{\parallel}f_j^{(i)}\cdot{}^{\parallel}p_j^{(k)} = \begin{cases} 1, & i = k, \\ 0, & i \neq k. \end{cases}, \qquad \sum_{j=1}^{L} {}^{\perp}f_j^{(i)}\cdot{}^{\perp}p_j^{(k)} = \begin{cases} 1, & i = k, \\ 0, & i \neq k. \end{cases} \quad (8)$$

With the filters ${}^{\parallel}f_j^{(i)}$ and ${}^{\perp}f_j^{(i)}$ it is now possible to obtain the FCS curves of the two molecular species separately. Consider the TCSPC-filtered fluorescence auto/cross correlation functions between perpendicular and parallel fluorescence signals $G_{\perp,\parallel}^{(i)}(t_c)$ as defined by

$$G_{\perp,\parallel}^{(i)}(t_c)=\frac{\left\langle\left(\sum_{j=1}^{L}{}^{\perp}f_j^{(i)}\cdot{}^{\perp}S_j(t)\right)\cdot\left(\sum_{j=1}^{L}{}^{\parallel}f_j^{(i)}\cdot{}^{\parallel}S_j(t+t_c)\right)\right\rangle}{\left\langle\sum_{j=1}^{L}{}^{\perp}f_j^{(i)}\cdot{}^{\perp}S_j(t)\right\rangle\cdot\left\langle\sum_{j=1}^{L}{}^{\parallel}f_j^{(i)}\cdot{}^{\parallel}S_j(t+t_c)\right\rangle} \tag{9}$$

where ${}^{\perp}S_j(t)$ is the fluorescence signal in the *j*th TCSPC channel of total perpendicular signal at measurement time *t* and ${}^{\parallel}S_j(t+t_c)$ is the fluorescence signal in the *j*th TCSPC channel of total parallel signal at measurement time $t+t_c$. If these signals have the form of Eq. (4), then the orthonormality relation Eq. (8) ensures that the auto/cross correlation functions $G_{\perp,\parallel}^{(i)}(t_c)$ and $G_{\parallel,\perp}^{(i)}(t_c)$ have the average values (averaged over an infinite number of measurements or over sufficiently long measurement time ($>>t_c$))

$$G_{\perp,\parallel}^{(i)}(t_c)=\frac{\left\langle{}^{\perp}F^{(i)}(t)\cdot{}^{\parallel}F^{(i)}(t+t_c)\right\rangle}{\left\langle{}^{\perp}F^{(i)}(t)\right\rangle\cdot\left\langle{}^{\parallel}F^{(i)}(t+t_c)\right\rangle}\quad\text{and}\quad G_{\parallel,\perp}^{(i)}(t_c)=\frac{\left\langle{}^{\parallel}F^{(i)}(t)\cdot{}^{\perp}F^{(i)}(t+t_c)\right\rangle}{\left\langle{}^{\parallel}F^{(i)}(t)\right\rangle\cdot\left\langle{}^{\perp}F^{(i)}(t+t_c)\right\rangle} \tag{10}$$

where ${}^{\perp}F^{(i)}(t)$ and ${}^{\parallel}F^{(i)}(t+t_c)$ are pure fluorescence signals from the molecular species *i*th type (summed over all TCSPC channels). Thus, $G_{\perp,\parallel}^{(i)}(t_c)$ and $G_{\parallel,\perp}^{(i)}(t_c)$, where *i* = 1; 2, reproduce the standard FCS curves for both species separately. The global fit of two auto/cross correlation curves significantly reduces the statistical errors and makes separation of species correlation curves from mixture data more sensitive and accurate. Moreover, since the anisotropy differences are counted in addition to lifetimes the total statistical noise is further reduced.

2.2 How to get ${}^{\parallel}p_j^{(i)}$ and ${}^{\perp}p_j^{(i)}$ normalized probabilities

The case when the single signal from mixture of two (or more) species should be split is described in [4]. For that, to obtain the TCSPC-decay patterns of species, TCSPC measurement of pure 2.5x10^{-8} M (in average about 30 molecules in a 2 fl detection volume) solutions of both species were performed. Then TCSPC histograms $\{H_j^{(i)}\}$ were normalized by total number of photons in the following way:

$$p_j^{(i)}=\frac{H_j^{(i)}}{\sum_{j=1}^{L}H_j^{(i)}}\qquad\Rightarrow\qquad\sum_{j=1}^{L}p_j^{(i)}=1 \tag{11}$$

where *i*=1, 2; *j* =1; ... ; L; and *L* is the number of histogram bins (or TCSPC channels).

The situation turns not so trivial in the case of MFD detection where fluorescence signal from mixture is divided into its parallel and perpendicular components and into color ranges.

The probability distributions are not available with such a simple separate normalization way since certain relations between ${}^{\parallel}p_j^{(i)}$ and ${}^{\perp}p_j^{(i)}$ due to specific anisotropy decay should be kept for each *i*th species. Each registered photon emitted by *i*th species is detected with probabilities ${}^{\parallel}p^{(i)}$, ${}^{\perp}p^{(i)}$ in either parallel or perpendicular detection channel respectively. Applying a normalization similar to Eq. (11) to the combined TCSPC histogram of *i*th species (see Fig. 1, rows 1-2) one gets corresponding probabilities as follows:

$${}^{\parallel}p^{(i)}+{}^{\perp}p^{(i)}=1, \tag{12}$$

where $$ {}^{\parallel}p^{(i)} = \frac{{}^{\parallel}w^{(i)}}{{}^{\parallel}w^{(i)}+{}^{\perp}w^{(i)}} = \frac{\sum_{j=1}^{L}{}^{\parallel}H_j^{(i)}}{\sum_{j=1}^{L}{}^{\parallel}H_j^{(i)}+\sum_{j=1}^{L}{}^{\perp}H_j^{(i)}} = \sum_{j=1}^{L}\frac{{}^{\parallel}H_j^{(i)}}{\sum_{j=1}^{L}{}^{\parallel}H_j^{(i)}+\sum_{j=1}^{L}{}^{\perp}H_j^{(i)}} = \sum_{j=1}^{L}{}^{\parallel}p_j^{(i)} \text{ and } {}^{\perp}p^{(i)} = \sum_{j=1}^{L}{}^{\perp}p_j^{(i)} \quad (13) $$

${}^{\parallel}p_j^{(i)}$ and ${}^{\parallel}p_j^{(i)}$ represent the conditional probabilities to register a photon in the *j*th bin of parallel or perpendicular TCSPC channels, provided that photon is emitted by *i*th species . These probabilities are defined as

$$ {}^{\parallel}p_j^{(i)} = \frac{{}^{\parallel}H_j^{(i)}}{\sum_{j=1}^{L}{}^{\parallel}H_j^{(i)}+\sum_{j=1}^{L}{}^{\perp}H_j^{(i)}} \quad , \qquad {}^{\perp}p_j^{(i)} = \frac{{}^{\perp}H_j^{(i)}}{\sum_{j=1}^{L}{}^{\parallel}H_j^{(i)}+\sum_{j=1}^{L}{}^{\perp}H_j^{(i)}} \quad (14) $$

To get these distributions of conditional probabilities TCSPC measurement of pure thick solutions (≥25 nM) of each species are performed and TCSPC histograms are normalized as described by Eq. (14).

2.3 Simultaneous (or global) minimization

The total number of registered photons in either parallel ${}^{\parallel}W$ or perpendicular ${}^{\perp}W$ detection channel is the sum of photon numbers emitted by all species in mixture solution (integral from Eq. (4)):

$$ {}^{\parallel}W = \sum_{i=1}^{n(=2)}{}^{\parallel}w^{(i)} = \sum_{i=1}^{n(=2)} w^{(i)}\cdot{}^{\parallel}p^{(i)}, \quad {}^{\perp}W = \sum_{i=1}^{n(=2)}{}^{\perp}w^{(i)} = \sum_{i=1}^{n(=2)} w^{(i)}\cdot{}^{\perp}p^{(i)} \text{ and } W={}^{\parallel}W+{}^{\perp}W \quad (15) $$

where W is the total number of registered photons. Taking into account Eqs. (4) and (13) we get

$$ {}^{\parallel}W+{}^{\perp}W = \sum_{i=1}^{n(=2)} w^{(i)}\cdot{}^{\parallel}p^{(i)} + \sum_{i=1}^{n(=2)} w^{(i)}\cdot{}^{\perp}p^{(i)} = \sum_{i=1}^{n(=2)}\left(w^{(i)}\cdot({}^{\parallel}p^{(i)}+{}^{\perp}p^{(i)})\right) = \sum_{i=1}^{n(=2)}\left(w^{(i)}\cdot\left[\sum_{j=1}^{L}{}^{\parallel}p_j^{(i)}+\sum_{j=1}^{L}{}^{\perp}p_j^{(i)}\right]\right) $$

or

$$ \sum_{j=1}^{L}{}^{\parallel}H_j + \sum_{j=1}^{L}{}^{\perp}H_j = \sum_{i=1}^{n(=2)}\left(w^{(i)}\cdot\left[\sum_{j=1}^{L}{}^{\parallel}p_j^{(i)}+\sum_{j=1}^{L}{}^{\perp}p_j^{(i)}\right]\right) \quad (16) $$

where left part of Eq. (16) represents the sum of integrals of TCSPC histograms from parallel and perpendicular detection channels, $w^{(i)}$ is the photon count contribution of the *i*th species and the content of [] brackets is the sum of integrals from conditional probabilities to register emitted by *i*th species photon in *j*th bin of parallel or perpendicular TCSPC channels. Graphically the left part of Eq. (16) is the area under measured decay histograms and the content of [] is equal to unit area defined by Eqs. (12) and (13). Instead of two measured decay histograms (${}^{\parallel}H_j$ and ${}^{\perp}H_j$) and four (double of species number n (n=2)) conditional probability distributions (${}^{\parallel}p_j^{(i)}$ and ${}^{\parallel}p_j^{(i)}$) we introduce bimodal one decay histogram H_j and two conditional probability distributions $p_j^{(i)}$ with total number of TCSPC channels *2L*.

$$ \sum_{j=1}^{2L}H_j = \sum_{i=1}^{n(=2)} w^{(i)}\cdot\sum_{j=1}^{2L}p_j^{(i)} = \sum_{j=1}^{2L}\sum_{i=1}^{n(=2)} w^{(i)}p_j^{(i)} \quad (17) $$

where

$$ H_j = \begin{cases} {}^{\parallel}H_j \ , & when\ 1\le j\le L \\ {}^{\perp}H_{j-L}, & when\ L+1\le j\le 2L \end{cases}, \qquad p_j^{(i)} = \begin{cases} {}^{\parallel}p_j^{(i)} \ , & when\ 1\le j\le L \\ {}^{\perp}p_{j-L}^{(i)}, & when\ L+1\le j\le 2L \end{cases}, $$

$$ H_j = \sum_{i=1}^{n(=2)} w^{(i)}p_j^{(i)}, \qquad \sum_{j=1}^{2L}p_j^{(i)} = 1 \quad (18) $$

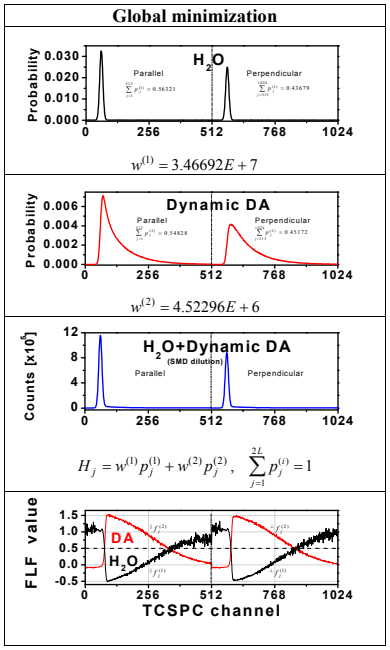

Fig. 1. Demonstration of global minimization: bimodal probability distributions of components, decay histogram of mixture and generated by global minimization bimodal filters.

In this shape, following to [4] two bimodal filters $f_j^{(i)}$, i =1, 2, will be devised with the properties

$$\left\langle \sum_{j=1}^{2L} f_j^{(i)} \cdot H_j \right\rangle = w^{(i)}, \tag{19}$$

where the brackets denote averaging over long time of measurements. Filters $f_j^{(i)}$ has to be chosen in such a way as to minimize the relative errors

$$\left\langle \left(\sum_{j=1}^{2L} f_j^{(i)} \cdot H_j - w^{(i)} \right)^2 \right\rangle \to \min \tag{20}$$

When $f_j^{(i)}$ filters are created we can get ${}^{\parallel}f_j^{(i)}$ and ${}^{\perp}f_j^{(i)}$ as first and second halves of $f_j^{(i)}$ arrays (Fig. 1):

$$\begin{aligned} {}^{\parallel}f_j^{(i)} &= f_j^{(i)}, \quad 1 \le j \le L \\ {}^{\perp}f_{j-L}^{(i)} &= f_j^{(i)}, \quad L+1 \le j \le 2L \end{aligned} \tag{21}$$

Auto/cross correlation functions $G_{\perp,\parallel}^{(i)}(t_c)$ and $G_{\parallel,\perp}^{(i)}(t_c)$ can be calculated as defined by Eq. (9).

2.4 Species cross correlation function

Filters $f_j^{(i)}$ in Eq. (20) were chosen in such a way as to minimize the relative errors for parallel and perpendicular channels simultaneously (Fig. 1). The idea of one bimodal decay histogram H_j and two conditional probability distributions $p_j^{(i)}$ with total number of TCSPC channels *2L* makes possible calculation of Species Cross Correlation (SCC) function even for the species with absolutely same fluorescence lifetime but different rotational correlation time. Now we will keep the filters as they are generated for the case of global minimization and we transform our raw data streams into modified format where TCSPC channels for photons from second detector are increased by *L*. So, we describe each of species by single bimodal decay pattern and SCC function $G^{(i,j)}(t_c)$ between *i* and *j* species is defined as

$$G^{(i,j)}(t_c) = \frac{\left\langle \left(\sum_{k=1}^{2L} f_k^{(i)} \cdot S_k(t) \right) \cdot \left(\sum_{k=1}^{2L} f_k^{(j)} \cdot S_k(t+t_c) \right) \right\rangle}{\left\langle \sum_{k=1}^{2L} f_k^{(i)} \cdot S_k(t) \right\rangle \cdot \left\langle \sum_{k=1}^{2L} f_k^{(j)} \cdot S_k(t+t_c) \right\rangle} \tag{22}$$

where $S_k(t)$ is the fluorescence signal in the *k*th TCSPC channel of total signal at measurement time *t* and $S_k(t+t_c)$ is the fluorescence signal in the *k*th TCSPC channel at measurement time $t+t_c$. The orthonormality relation as

$$\sum_{k=1}^{2L} f_k^{(i)} \cdot p_k^{(j)} = \begin{cases} 1, & i = j, \\ 0, & i \ne j. \end{cases}, \tag{23}$$

ensures that the species cross correlation functions $G^{(i,j)}(t_c)$ and $G^{(j,i)}(t_c)$ have the average values (averaged over an infinite number of measurements or over sufficiently long measurement time (>>t_c))

$$G^{(i,j)}(t_c)=\frac{\left\langle F^{(i)}(t)\cdot F^{(j)}(t+t_c)\right\rangle}{\left\langle F^{(i)}(t)\right\rangle\cdot\left\langle F^{(j)}(t+t_c)\right\rangle} \quad \text{and} \quad G^{(j,i)}(t_c)=\frac{\left\langle F^{(j)}(t)\cdot F^{(i)}(t+t_c)\right\rangle}{\left\langle F^{(j)}(t)\right\rangle\cdot\left\langle F^{(i)}(t+t_c)\right\rangle} \tag{24}$$

where $F^{(i)}(t)$ and $F^{(j)}(t+t_c)$ are pure fluorescence signals from the molecular species *i*th and *j*th type (summed over all TCSPC channels). Thus, since the anisotropy differences are counted in addition to lifetimes, it becomes possible to highlight any dynamic process between two species in mixture solution if they differ in rotational correlation time or lifetime. In contrast to standard auto/cross correlation curves the amplitude of dynamic term per molecule in species cross correlation function is equal to -1 like in an antibunching term. If dynamics between species is missing then SCC function is showing no additional correlation amplitude above baseline equal to 1.

3. SIMULATIONS

3.1 Data generator

Simulations of single-molecule measurements were performed by using Brownian dynamics approach [29-32]. The spatial intensity distribution of the observation volume was assumed to be a 3D Gaussian [33]

$$I(x,y,z)=\sqrt{8}\exp\left(-\frac{2x^2+2y^2}{\omega_0^2}-\frac{2z^2}{z_0^2}\right) \tag{25}$$

The $1/e^2$ radii in x and y or in z direction are denoted by ω_0 or z_0, respectively.

In most of the literature, Brownian diffusion is modelled in a box with periodic boundary conditions (see e.g. [30]). In our approach instead, "molecules" diffuse freely in an "open" volume. This means that the molecules are allowed to leave the simulation volume, after which they are not further tracked. To keep the desired average number of molecules constant, new molecules are added at each time step as described below.

The simulation volume is defined by a surface $I(x,y,z)=const$, which for the case of observation volume given by Eq. (25) is an ellipsoid

$$\frac{x^2+y^2}{\omega_0^2}+\frac{z^2}{z_0^2}=m^2 \tag{26}$$

In this work m = 10 was used unless stated otherwise. One can show that the average number of molecules entering the simulation volume per time step Δt is given by

$$\left\langle N_{\text{in}}\right\rangle = cS\sqrt{D\Delta t/\pi} \tag{27}$$

while the distribution of distances Δl of new molecules from the surface (Eq. (26)) is

$$P(\Delta l)\propto\int_{\Delta l}^{\infty}\exp\left(\frac{-l^2}{4D\Delta t}\right)dl \tag{28}$$

In Eqs. (27) and (28) c stand for the concentration of the molecules, S is the surface area of the ellipsoid (Eq. (26)), and D stands for the diffusion coefficient. Eqs. (27) and (28) can be obtained by solving the diffusion equation with initial conditions $c(l<0,\ t=0)=c$ and $c(l\geq 0,\ t=0)=0$. The curvature of the surface (Eq. (26)) is thereby neglected, which requires that the time step Δt is small (i.e. $D\Delta t << m\omega_0$). The number of new molecules per time step (Δt=0.005 ms) was generated according to a Poisson distribution with a mean value given by Eq. (27). Test simulations have shown that the number of molecules calculated by FCS analysis (Eq. (1)) of simulated data agree with the assumed values within 0.2-0.5%. The FCS curve obtained by open volume simulation may exhibit some unexpected features, but they are less pronounced and shifted towards longer correlation times in comparison to the simulation in box with periodic boundary conditions. Simulation artefacts disappear when the simulation volume becomes reasonably large ($m \geq 10$).

TCSPC data were generated as proposed by Chowdhury et al [34], assuming Gaussian excitation pulse profile with FWHM of 0.3 ns or 0.5 ns. Background signal consists of dark counts (uniformly distributed over TCSPC channels) and

scatter contribution (repeating instrument response function (IRF) of the setup). Simulated data were saved in data format of SPC-132 TCSPC cards (Becker & Hickel GmbH, Berlin, Germany) and suitable for direct software testing. The algorithm was thoroughly tested by analyzing simulated data by FCS, FIDA, and BIFL [1, 19, 29, 35] methods.

3.2 Stability of filtered FCS

We have simulated mixture of two species with the same 4 ns lifetime but different characteristic rotational correlation times (0.1 ns and 0.3 ns, 0.1 ns and 1.0 ns) in water. The fraction of the second species in the mixture was 2 times higher than fraction of the first.

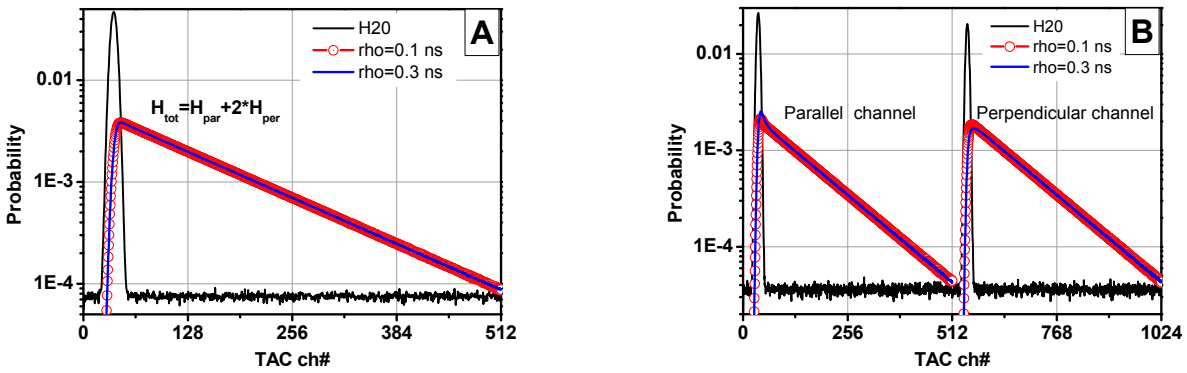

Fig. 2. Probability distributions: A) for a case of time resolved FCS. Since distributions are absolutely identical then separation of species correlation curves is not possible. B) for the case of time and polarization resolved FCS probability patterns are slightly different and it makes separation of species correlation curves possible.

The geometric shape of the excitation focus was defined as 3D Gaussian with $\omega_0 = 0.5\,\mu m$ and $z_0 = 1.5\,\mu m$. Dark counts = 0.2 kHz, scatter = 2.5 kHz. Both species had the same $t_D^{(1)} \equiv t_D^{(2)} = 0.25\,ms$ diffusion time and the same $Q_1 = Q_2 = 200\,kcpm$ brightness. The average number of molecules in a focus was $N = 0.3988$ ($N_1 = 0.1329$ and $N_2 = 0.2659$). Simulated data were analyzed as described in [4-7] and as reported in this paper (corresponding probability distributions are presented in Fig. 2).

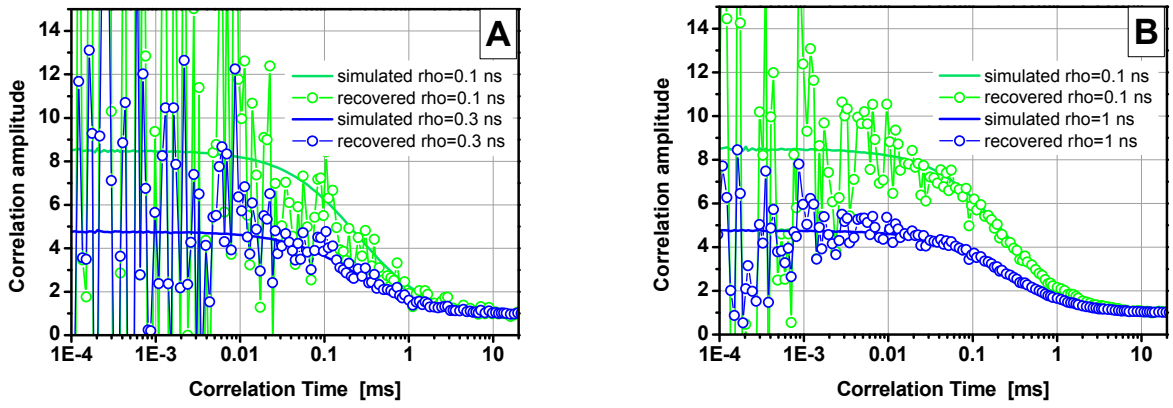

Fig. 3. Overlay of recovered by filtered FCS and simulated correlation curves: A) a case of 0.2 ns difference in rotational correlation times of species, B) a case of 0.9 ns difference in rotational correlation times of species.

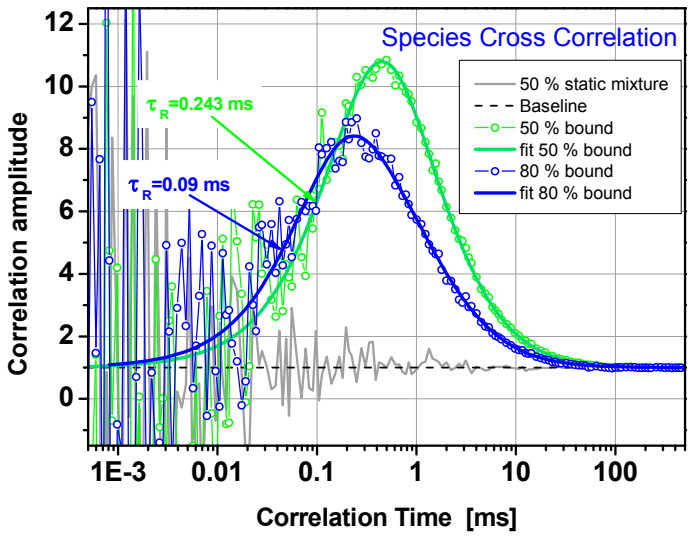

Fig. 4. Overlay of calculated by filtered FCS species cross correlation function and fitted curves for mixture of two species (free labeled DNA (ρ^{DNA}=2.71 ns) and labeled DNA-unlabelled protein complex ($\rho^{complex}$=5.18 ns)) in water: A) a case of 50 by 50 percent static mixture of species, B) a case of 50 by 50 percent dynamic mixture of species ($k_{1,2}=k_{2,1}$=2000 s^{-1} or τ_R=0.25 ms), C) a case of 17 by 83 percent dynamic mixture of species ($k_{1,2}$=10000 s^{-1}, $k_{2,1}$=2000 s^{-1} or τ_R=0.083 ms)

From Fig. 3 it follows that even 0.2 ns difference in rotational correlation times allows one to separate species from the mixture and estimate the absolute concentrations with 11 % error and diffusion times with up to 19 % error. Simulated data correspond to 2429 s real experiment and it is clear that by increasing measurement time it is also possible to reduce relative error. In the case when difference in rotational correlation times was 0.9 ns the parameters were recovered with less than 5 % error.

Then we have simulated mixtures of two dynamically interconverting each into other species with off-rate constants $k_{1,2}$ and $k_{2,1}$, the same 4 ns lifetime but different characteristic rotational correlation times ($\rho^{(1)}$=2.71 ns and $\rho^{(2)}$=5.18 ns) in water in order to imitate the dynamic binding process of labeled DNA with unlabelled protein. The fractions of species in the mixture were defined by the off-rate constants:

$$X_1 = \frac{k_{2,1}}{k_{1,2}+k_{2,1}} \quad \text{and} \quad X_2 = \frac{k_{1,2}}{k_{1,2}+k_{2,1}} \tag{29}$$

The geometric shape of the excitation focus was defined as 3D Gaussian with $\omega_0 = 0.2\,\mu m$ and $z_0 = 0.6\,\mu m$. Dark counts = 0.2 kHz, scatter = 1.8 kHz. Both species had the same $t_D^{(1)} \equiv t_D^{(2)} = 1\,ms$ diffusion time and the same $Q_1 = Q_2 = 100\,kcpm$ brightness. The average number of molecules in the focus was $N = 0.1$. Simulated data were analyzed as described in section 2.4. Generation of filters was done by global minimization and SCC functions were calculated according to Eq. (22). The dynamics was nicely highlighted and relaxation times were accurately recovered by time and polarization resolved FCS as one can see in Fig. 4, which was impossible with FLCS.

As a control the static mixture of this species was also simulated to show the absence of SCC amplitude (Fig. 4).

Summarizing we can conclude that filtered FCS becoming a powerful tool for analyzing dynamics resulting in change of lifetime or anisotropy of labeled biomolecule interacting with some other unlabelled molecule.

4. MATERIALS AND METHODS

4.1 Setup

The experiments were carried out with a confocal epi-illuminated setup based on an Olympus IX70 inverted microscope as described in [2, 3, 19, 35].

The fluorescent molecules are excited by a linearly polarized argon-ion-laser (Innova Sabre, Coherent) at 496 nm, active-mode-locked (73.5 MHz, 150 ps) mode. The HF-source for the mode-locker serves as the common time base for sync (TCSPC stop signal) and the macro time counter for both SPC-132 counting boards. The laser is focused into the sample by a NA=1.2 water-immersion objective lens (UPLAPO 60x, Olympus, Hamburg, Germany).

The fluorescence is collected by the same lens and separated from the excitation by a beamsplitter (Q505LPXR, AHF, Tübingen, Germany). A confocal pinhole of 100 µm diameter and the slightly underfilled objective yield a detection

volume element of approximately 1 μm diameter and 3 fl size, as determined by fluorescence correlation spectroscopy [36]. The collected fluorescence photons are divided first into its parallel and perpendicular components by a polarizing beamsplitter cube (VISHT11, Gsänger, Planegg, Germany), then by dichroic beamsplitters (Q595LPXR, AHF) into wavelength ranges below and above 595 nm. Fluorescence bandpass filters (HQ533/46 and HQ720/150, AHF) block residual laser light and reduce Raman scattering from the solvent.

The detectors used were Micro Photon Devices (MPD PDM-50, Bolzano, Italy) as green and single photon avalanche diodes (SPCM-AQR-14, Perkin Elmer, Germany) as red.

4.2 Four-way DNA junctions

Four-way DNA junctions, or Holliday junctions [37], are the branchpoints formed during DNA strand exchange of homologuous duplexes. Holliday junctions are central intermediates in homologous genetic recombination [38], a process important in DNA repair and in providing the genetic diversity necessary for evolution.

When the region of homology extends further from the branching point, it is possible to observe sequantial exchange of basepairing and the Holliday junction effectively migrates along the DNA sequence [38].

It has been shown that upon addition of divalent metal ions the overall structure is preferentially folded with the helices coaxially paired in a right-handed anti-parallel fashion, with an angle of approximately 60° between the helices axes [39-42]. Two conformers are possible depending on the way the four arms are stacking, Fig. 5.

Depending on the DNA sequence, especially near the branching point, one of the conformers can be predominantly populated. The most probable explanation for the stacking of the branches is that the metal ions partially shield the electrostatic repulsion between the backbone phosphates allowing the complete structure to fold.

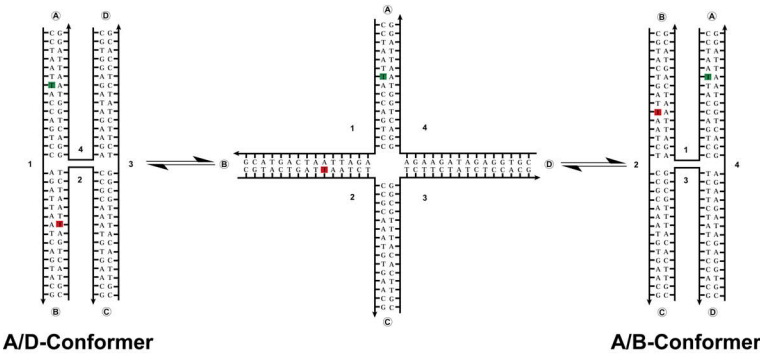

Fig. 5. Three possible conformers of Holliday junctions: 1) A/D conformer (R_{DA}~50 Å, MF), 2) Cross (or completely unstacked conformer), 3) A/B conformer (R_{DA}~40 Å, HF).

The interconversion rate between conformers depends on the metal ions concentration, with high salt slowing the exchange. Metal ions are also known to decrease branch migration rates up to three orders of magnitude [43] suggesting a strong correlation between the rates and the folding of the structure. These findings suggest also that most likely conformer exchange and branch migration go through a highly flexible state where the metal ions are not bound. So far [38, 44], it has been proposed that this state corresponds to the completely unstacked conformer (Fig. 5, cross conformer).

4.3 Molecules

Functional Holliday four-way junctions (HJ) were obtained by annealing four different single strands of DNA:

HJ_1N_**D**:	5′-d(CCT AAT **T(Alexa488)** AC CAG TCC AGA TTA ATC AGT ACG)
HJ_2N_**A**:	5′-d(CGT ACT GAT **T(Atto647N)** AA TCT CCG CAA ATG TGA ACG)
HJ_3N:	5′-d(CGT TCA CAT TTG CGG TCT TCT ATC TCC ACG)
HJ_4N:	5′-d(CGT GGA GAT AGA AGA GGA CTG GTA ATT AGG)

The DNA strands (Purimex, Grebenstein, Germany) were labelled by covalently bonding the dyes to dTs modified with C6-aminolinkers.

The configuration of the nucleobases in proximity of the branching point is such that the sliding of the junction along any of the arms is forbidden. In this way the only observable configurational fluctuation is relative to the switching between the two stacking conformers A/B and A/D. To allow for a good identification of the conformers through FRET the dyes are positioned so that the different conformers are characterized by significantly different donor-acceptor distances R_{DA}.

4.4 Salt dependence

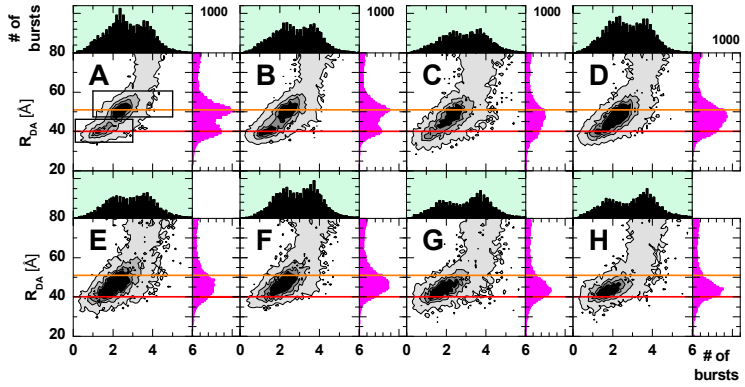

Fig. 6. Comparison R_{DA} vs $\tau_{D(A)}$ 2D plots for different $MgCl_2$ concentrations. A) 10 mM, B) 5 mM, C) 2.5mM, D) 2mM, E) 1.25mM, F) 1 mM, G) 0.5mM, H) 0.1 mM.

The functionality of the Holliday junction was tested measuring the sample under different $MgCl_2$ concentrations, results shown in the Fig. 6.

As expected, Holliday junctions show a strong dependence on $MgCl_2$ concentration. At high salt two distinct populations can be observed, characterized by a R_{DA} of approximately 40Å and 50 Å respectively. As the salt concentration is lowered the populations start to merge indicating that the species interconvert faster and faster.

4.5 Models, results and discussion

To obtain the rate constants of the process, we studied the sample with probability distribution analysis (PDA) [45-47]. In the hypothesis of fast unbinding of Mg^{2+} the following dynamic models can be considered:

$$1)\ A/B \underset{k_{21}}{\overset{k_{12}}{\rightleftharpoons}} A/D \qquad 2)\ A/B \underset{k_{Fold\,1}}{\overset{k_{Open\,1}}{\rightleftharpoons}} Open \underset{k_{Open\,2}}{\overset{k_{Fold\,2}}{\rightleftharpoons}} A/D$$

In latter case, by dynamic PDA [in preparation] we will get apparent rates but the formal description is still correct. The PDA fit of 0.75 mM $MgCl_2$ shows surprising results. Both the completely static and completely dynamic models fail. The fit gets better only in the case of a mixed model. As a compromise the following two models were discussed:

$$3)\ \left[A/B_{(Mg} \underset{k^{+}_{A/B(Mg)}}{\overset{k^{-}_{A/B(Mg)}}{\rightleftharpoons}} A/B \right] \underset{k_{21}}{\overset{k_{12}}{\rightleftharpoons}} \left[A/D \underset{k^{-}_{A/D(Mg)}}{\overset{k^{+}_{A/D(Mg)}}{\rightleftharpoons}} A/D_{(Mg)} \right] \qquad 4)\ \left[A/B_{(Mg)} \underset{k^{+}_{A/B(Mg)}}{\overset{k_{A/B(Mg)}}{\rightleftharpoons}} A/B \right] \underset{k_{Fold\,1}}{\overset{k_{Open\,1}}{\rightleftharpoons}} Open \underset{k_{Open\,2}}{\overset{k_{Fold\,2}}{\rightleftharpoons}} \left[A/D \underset{k^{-}_{A/D(Mg)}}{\overset{k^{+}_{A/D(Mg)}}{\rightleftharpoons}} A/D_{(Mg)} \right]$$

Detailed analyses of data with the model 3 have shown that it is more than enough to explain our experimental findings. The simulations and direct theoretical calculations (or estimations) have shown that in case if Mg^{2+} ion binding does not change or slightly changes the brightness Q of conformers (i.e. $Q_{A/B(Mg)} \cong Q_{A/B}$ and $Q_{A/D} \cong Q_{A/D(Mg)}$) then two characteristic relaxation times should be expected for these type dynamic processes. Since our sample should contain Donly, $DA_{A/B(Mg)}$, $DA_{A/B}$, $DA_{A/D}$ and $DA_{A/D(Mg)}$ species in mixture then it was good chance to test the filtered FCS technique.

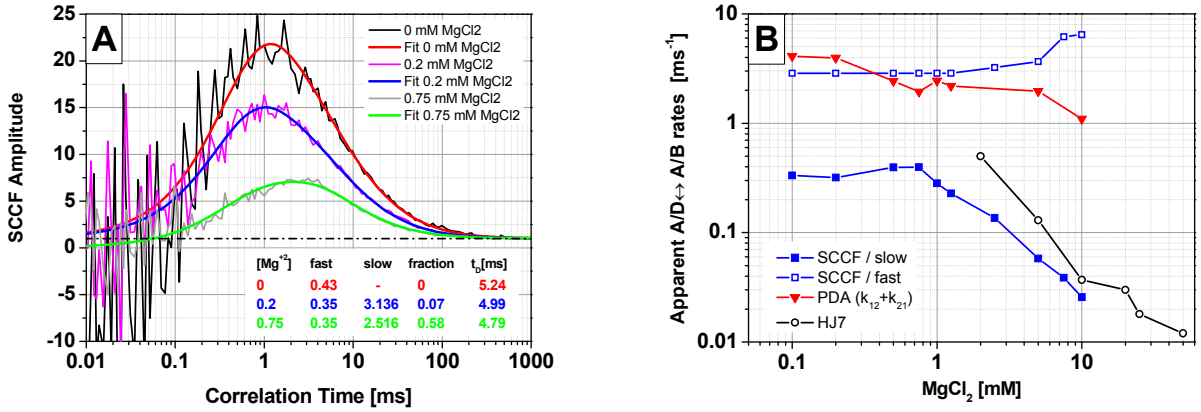

Fig. 7. A) Overlay of SCCF curves for different $MgCl_2$ concentrations. a) 0 mM (black), b) 0.2 mM (magenta) and c) 0.75 mM (gray). Inset presents fit results for fast and slow relaxation times [ms] and fraction of slow term. Diffusion times t_D [ms] are also presented. B) Overlay of appatent rates ($1/\tau_{1relax}$ and $1/\tau_{2relax}$) obtained by SCCF for different $MgCl_2$ concentrations (blue) and apparent rate ($k_{12}+k_{21}$) by dynamic PDA (red). Corresponding values from literature [44, 48] are also presented (black).

The decay patterns of two conformers ($DA_{A/B(Mg)}$+$DA_{A/B}$ and $DA_{A/D}$+$DA_{A/D(Mg)}$) were obtained from 10 mM $MgCl_2$ measurement by selecting middle FRET (MF) or high FRET (HF) bursts from 2D plots like presented on Fig. 6A. For Donly decay pattern we took measurement of Donly sample directly. Filter sets are generated by using decay patterns of green and red parallel detection channels.

In Fig. 7A SCCF curves for 0, 0.2 and 0.75 mM $MgCl_2$ measurements are presented. To fit curves a function with two antibunching and diffusion term is used:

$$G(t_c) = 1 + \frac{1}{N} \cdot G_{diff}(t_c) \cdot \left(1 - A \cdot \left(X \cdot e^{-\frac{t_c}{\tau_{1relax}}} + (1 - X) \cdot e^{-\frac{t_c}{\tau_{2relax}}} \right) \right) \tag{30}$$

where $G_{diff}(t_c)$ is a diffusion term, A-fraction of dynamic molecules, X-fraction of the first relaxation component and τ_{1relax} and τ_{2relax} are the characteristic relaxation times of the two components. Fit results for these $MgCl_2$ concentrations are given in the inset. Characteristic relaxation times for fast and slow processes are given in [ms].

The results as apparent rates obtained by dynamic PDA method and SCCF are summarized in Fig. 7B. In this figure the results for junction 7 from Ha and coworkers [44, 48] are also reported. In fact this literature values follow the line of slow apparent rate, in general defined by unbinding of Mg^{2+}, suggesting that:

i) the process is purely electrostatic an therefore does not depend on the actual sequence of the HJ, and

ii) the surface measurements do not see the fast interconversion of A/B and A/D conformers.

5. CONCLUSIONS

From our experimental data it is not so obvious the existence of intermediate cross state but also we have not enough evidence to state that it does not exist at all. We simply claim that the model with three states (model 2) is not explaining experimental results and a new model with at least four states (model 3) is valid.

It is also obvious that SCCF exhibits its powerful ability to become very convenient tool for dynamic processes study in biomolecules.

ACKNOWLEDGMENT: The authors thank Ralf Kühnemuth, Volodymyr Kudryavtsev and Evangelos Sisamakis for many helpful discussions and suggestions and the Deutsche Forschungsgemeinschaft SFB 590 and EU (FP7-Health-2007-A-201837) for funding during this work.

REFERENCES

[1] Eggeling, C., et al., "Data registration and selective single-molecule analysis using multi-parameter fluorescence detection," Journal of Biotechnology, **86**(3), 163-180 (2001).

[2] Kühnemuth, R., Seidel, C.A.M., "Principles of Single Molecule Multiparameter Fluorescence Spectroscopy," Single Molecules, **2**(4), 251-254 (2001).

[3] Widengren, J., et al., "Single-molecule detection and identification of multiple species by multiparameter fluorescence detection," Analytical Chemistry, **78**(6), 2039-2050 (2006).

[4] Böhmer, M., et al., "Time-resolved fluorescence correlation spectroscopy," Chemical Physics Letters, **353**(5-6), 439-445 (2002).

[5] Enderlein, J., Gregor, I.,"Using fluorescence lifetime for discriminating detector afterpulsing in fluorescence-correlation spectroscopy," Review of Scientific Instruments, **76**(3), 033102 (2005).

[6] Gregor, I., Enderlein, J., "Time-resolved methods in biophysics. 3. Fluorescence lifetime correlation spectroscopy," Photochem. Photobiol. Sci., **6**(1), 13-18 (2007).

[7] Kapusta, P., et al., "Fluorescence lifetime correlation spectroscopy," Journal of Fluorescence, **17**(1), 43-48 (2007).

[8] Magde, D., Elson, E.L., Webb, W.W., "Thermodynamic fluctuations in a reacting system - measurement by fluorescence correlation spectroscopy," Physical Review Letters, **29**, 705-708 (1972).

[9] Webb, W.W., "Applications of fluorescence correlation spectroscopy," Q. Rev. Biophys., **9**(1), 49-68 (1976).

[10] Thompson, N.L., in Lakowicz, J.R., (Ed.) "Fluorescence Correlation Spectroscopy," Topics in Fluorescence Spectroscopy, Plenum Press, New York, 337-378 (1991).

[11] Widengren, J., Mets, Ü., "Conceptual Basis of Fluorescence Correlation Spectroscopy and Related Techniques as Tools in Bioscience in Single Molecule Detection in Solution," in [Methods and Applications], C. Zander, J. Enderlein, and R.A. Keller, (Eds.), 69-120 (2002).

[12] Schwille, P., Meyer-Almes, F.J., Rigler, R., "Dual-color fluorescence cross-correlation spectroscopy for multicomponent diffusional analysis in solution," Biophysical Journal, **72**(4), 1878-1886 (1997).
[13] Rigler, R., et al., "Fluorescence cross-correlation: A new concept for polymerase chain reaction," Journal of Biotechnology, **63**(2), 97-109 (1998).
[14] Kettling, U., et al., "Real-time enzyme kinetics monitored by dual-color fluorescence cross-correlation spectroscopy," Proc. Natl. Acad. Sci. USA., **95**, 1416-1420 (1998).
[15] Koltermann, A., et al., "Rapid assay processing by integration of dual-color fluorescence cross-correlation spectroscopy: High throughput screening for enzyme activity," Proc. Natl. Acad. Sci. USA, **95**, 1421-1426 (1998).
[16] Winkler, T., et al., "Confocal fluorescence coincidence analysis: An approach to ultra high-throughput screening," Proc. Natl. Acad. Sci. USA, **96**(4), 1375-1378 (1999).
[17] Heinze, K.G., Koltermann, A., Schwille, P., "Simultaneous two-photon excitation of distinct labels for dual-color fluorescence crosscorrelation analysis," Proc. Natl. Acad. Sci. USA, **97**(19), 10377-10382 (2000).
[18] Bieschke, J., et al., "Ultrasensitive detection of pathological prion protein aggregates by dual-color scanning for intensely fluorescent targets," Proc. Natl. Acad. Sci. USA, **97**(10), 5468-5473 (2000).
[19] Al-Soufi, W., et al., "Fluorescence correlation spectroscopy, a tool to investigate supramolecular dynamics: Inclusion complexes of pyronines with cyclodextrin," Journal of the American Chemical Society, **127**(24), 8775-8784 (2005).
[20] Lamb, D.C., et al., "Sensitivity enhancement in fluorescence correlation spectroscopy of multiple species using time-gated detection," Biophysical Journal, **79**(2), 1129-1138 (2000).
[21] Herman, J.R., et al., "Normally on photomultiplier gating circuit with reduced post-gate artifacts for use in transient luminescence measurements," Review of Scientific Instruments, **63**(11), 5454-5458 (1992).
[22] Shera, E.B., et al., "Detection of single fluorescent molecules," Chemical Physics Letters, **174**(6), 553-557 (1990).
[23] Li, L.Q., Davis, L.M., "Rapid and efficient detection of single chromophore molecules in aqueous solution," Applied Optics, **34**(18), 3208-3217 (1995).
[24] Creasey, D.J., et al., "Fast photomultiplier tube gating system for photon counting applications," Review of Scientific Instruments, **69**(12), 4068-4073 (1998).
[25] Xiao, M., Selvin, P.R., "An improved instrument for measuring time-resolved lanthanide emission and resonance energy transfer," Review of Scientific Instruments, **70**(10), 3877-3881 (1999).
[26] O'Connor, D.V., Phillips, D., "Time-correlated Single Photon Counting," New York, Academic Press (1984).
[27] Becker, W., et al., "Time-resolved detection and identification of single analyte molecules in microcapillaries by time-correlated single-photon counting (TCSPC)," Review of Scientific Instruments, **70**(3), 1835-1841 (1999).
[28] Enderlein, J., Erdmann, R., "Fast fitting of multi-exponential decay curves," Optics Communications, **134**(1-6), 371-378, (1997).
[29] Kask, P., et al., "Fluorescence-intensity distribution analysis and its application in biomolecular detection technology," Proc. Natl. Acad. Sci. USA, **96**(24), 13756-13761 (1999).
[30] Dix, J.A., Hom, E.F.Y., Verkman, A.S., "Fluorescence correlation spectroscopy simulations of photophysical phenomena and molecular interactions: A molecular dynamics/Monte Carlo approach," Journal of Physical Chemistry B, **110**(4), 1896-1906 (2006).
[31] Laurence, T.A., et al., "Photon arrival-time interval distribution (PAID): A novel tool for analyzing molecular interactions," Journal of Physical Chemistry B, **108**(9), 3051-3067 (2004).
[32] Enderlein, J., et al., "The statistics of single molecule detection: an overview," Bioimaging, **5**, 88-98 (1997).
[33] Rigler, R., et al., "Fluorescence correlation spectroscopy with high count rate and low background: analysis of translational diffusion," European Biophysics Journal, **22**, 169-175, (1993).
[34] Chowdhury, F.N., Kolber, Z.S., Barkley, M.D., "Monte-Carlo Convolution Method for Simulation and Analysis of Fluorescence Decay Data," Review of Scientific Instruments, **62**(1), 47-52 (1991).
[35] Felekyan, S., et al., "Full correlation from picoseconds to seconds by time-resolved and time-correlated single photon detection," Review of Scientific Instruments, **76**(8), 083104 (2005).
[36] Schaffer, J., et al., "Identification of single molecules in aqueous solution by time-resolved fluorescence anisotropy," Journal of Physical Chemistry A, **103**(3), 331-336 (1999).
[37] Holliday, R., "A new mechanism of gene conversion in fungi," Genetical Research, **5,** 282-304 (1964).
[38] Lilley, D.M.J., "Structures of helical junctions in nucleic acids," Quarterly Reviews of Biophysics, **33**(2), 109-159 (2000).
[39] Duckett, D.R., et al., "The structure of the Holliday junction and its resolution," Cell, **55**, 79-89 (1988).
[40] Murchie, A.I.H., et al., "Fluorescence energy transfer shows that the four-way DNA junction is a right-handed cross of antiparallel molecules," Nature, **341**, 763-766 (1989).
[41] Clegg, R.M., et al., "Fluorescence resonance energy transfer analysis of the structure of the four-way DNA junction," Biochemistry, **31**, 4846-4856 (1992).
[42] Eichman, B.F., et al., "The Holliday junction in an inverted repeat DNA sequence: Sequence effects on the structure of four-way junctions," Proc. Natl. Acad. Sci. USA, **97**(8), 3971-3976 (2000).
[43] Panyutin, I.G., Hsieh, P., "The kinetics of spontaneous DNA branch migration," Proc. Natl. Acad. Sci. USA, **91**(6), 2021-2025 (1994).
[44] McKinney, S.A., et al., "Structural dynamics of individual Holliday junctions," Nature Structural & Molecular Biology, **10,** 93-97 (2003).

[45] Antonik, M., et al., "Separating structural heterogeneities from stochastic variations in fluorescence resonance energy transfer distributions via photon distribution analysis," Journal of Physical Chemistry B, **110**(13), 6970-6978 (2006).
[46] Kalinin, S., et al., "Probability distribution analysis of single-molecule fluorescence anisotropy and resonance energy transfer," Journal of Physical Chemistry B, **111**(34), 10253-10262 (2007).
[47] Kalinin, S., et al., "Characterizing Multiple Molecular States in Single-Molecule Multiparameter Fluorescence Detection by Probability Distribution Analysis," Journal of Physical Chemistry B, **112**(28), 8361-8374 (2008).
[48] Joo, C., et al., "Exploring Rare Conformational Species and Ionic Effects in DNA Holliday Junctions Using Single-molecule Spectroscopy," Journal of Molecular Biology, **341**, 739-751 (2004).

II

Characterizing Multiple Molecular States in Single-Molecule Multiparameter Fluorescence Detection by Probability Distribution Analysis

Stanislav Kalinin,* Suren Felekyan, Alessandro Valeri, and Claus A. M. Seidel*

Institut für Physikalische Chemie, Lehrstuhl für Molekulare Physikalische Chemie, Heinrich-Heine-Universität, Universitätsstraβe 1, Geb 26.32, 40225 Düsseldorf, Germany

Received: December 20, 2007

Probability distribution analysis (PDA) [M. Antonik et al., *J. Phys. Chem. B* **2006**, *110*, 6970] allows one to quantitatively analyze single-molecule (SM) data obtained in Förster resonance energy transfer (FRET) or fluorescence polarization experiments. By taking explicitly background and shot noise contributions into account, PDA accurately predicts the shape of one-dimensional histograms of various parameters, such as FRET efficiency or fluorescence anisotropy. In order to describe complex experimental SM-FRET or polarization data obtained for systems consisting of multiple non-interconverting fluorescent states, several extensions to the PDA theory are presented. Effects of brightness variations and multiple-molecule events are considered independently of the detection volume parameters by using only the overall experimental signal intensity distribution. The extended PDA theory can now be applied to analyze any mixture, by using any a priori model or a model-free deconvolution approach based on the maximum entropy method (MEM). The accuracy of the analysis and the number of free parameters are limited only by data quality. Correction of the PDA model function for the presence of multiple-molecule events allows one to measure at high SM concentrations to avoid artifacts due to a very long measurement time. Tools such as MEM and combined mean donor fluorescence lifetime analysis have been developed to distinguish whether extra broadening of PDA histograms could be attributed to structural heterogeneities or dye artifacts. In this way, an ultimate resolution in FRET experiments in the range of a few Ångström is achieved which allows for molecular Ångström optics distinguishing between a set of fixed distances and a distribution of distances. The extended theory is verified by analyzing simulations and experimental data.

1. Introduction

Data obtained in single-molecule Förster resonance energy transfer (SM-FRET) measurements are usually visualized as 1D histograms of the FRET efficiency or other related parameters.[1–13] These histograms are often fitted with a weighted sum of Gaussian distributions, for which the mean values are calculated. Under certain conditions, this approach to the analysis of SM-FRET data may provide correct mean FRET efficiencies,[14] which can be further used to calculate donor−acceptor (DA) distances.[15] However, experimental histograms contain a lot more information than just these mean values and allow one to reveal heterogeneities often found in biological systems. This information can be extracted by analyzing the width and the shape of FRET efficiency distributions, which is usually ignored in standard analysis.

The major challenge for quantitative analysis of SM data histograms is to separate shot-noise broadening from actual distributions of physical parameters. Even early attempts to predict the effect of shot-noise broadening[8,16] reveal, for instance, structural dynamics of syntaxin 1.[8] Recently, several quantitative methods have been developed, which extract useful information by analyzing photon statistics in SM experiments.[6,14,17–19] The probability distribution analysis (PDA) method[6] is intended mainly for the analysis of experimental distributions obtained from diffusing molecules. In PDA, both mean and width of a shot-noise broadened distribution are the functions of one parameter, for example, the mean FRET efficiency. PDA automatically accounts for shot-noise contribution and can unambiguously indicate whether any observed distribution is due to shot noise only or whether there must be a real distribution of the parameter of interest. However, in its present form, PDA has only a very limited potential to extract meaningful parameters of the individual states. This work shows how to handle various possible complications, which are typical for systems consisting of multiple fluorescent states. We also demonstrate how one can model underlying distributions of the parameters of interest in a rather general case. The ability to resolve multiple states is the main advantage of SM experiments, and thus, such an extension to PDA is clearly needed in order to be able to characterize individual states in a quantitative manner.

Intuitively, it might seem that in terms of the theory of PDA, such a modification is trivial. One may ask why the overall histogram obtained for a mixture of several species should not be just a sum of histograms calculated by using the reported PDA theory[6] and weighted by the fractions of the species. The main problem is that the theory of PDA makes use of the fact that photon distribution between color or polarization detection channels and the total signal intensity distribution, $P(S)$, are independent. The key idea of PDA is that the latter distribution is measurable and can be used as is, without much loss of relevant information (e.g., on FRET efficiency distributions). One of the important advantages of using the experimental $P(S)$ is the possibility to work with arbitrary long time windows (comparable with the diffusion time), which obviously contain large numbers of photons. This feature of PDA has proved to

* Corresponding authors. E-mail: stanislav.kalinin@uni-duesseldorf.de and cseidel@gwdg.de.

10.1021/jp711942q CCC: $40.75
Published on Web 06/21/2008

be especially helpful in resolving heterogeneous populations.[20] However, if the fluorescence intensity distribution is not the same for all species, the brightness and the photon distribution between color or polarization detection channels become correlated. In this work, we present an example when the use of the same (overall) fluorescence intensity distribution for all species produces completely erroneous results.

In contrast to PDA, fluorescence intensity distribution analysis (FIDA)[19,21] predicts the signal intensity distribution by modeling the shape of the detection volume. Therefore, the fluorescence intensity distribution for each species, at SM concentration, is obtained as an intermediate result, and the above-mentioned problem does not arise. The situation is similar for the rigorous treatment of photon statistics in SM fluorescence experiments, developed by Gopich and Szabo.[14] However, this theory requires the knowledge of the spatial intensity distribution, which in reality can strongly deviate from 3D Gaussian and depends on many experimental parameters that are difficult to control.[22–24] If we decide to stay only with the experimental signal intensity distribution, individual contributions of all species have to be extracted from that distribution.

This procedure is trivial only if the total brightness (i.e., signal sum of all detectors) of all species is the same or the individual fluorescence intensity distributions can be somehow measured independently. Equal brightness of all states was implicitly assumed when a Gaussian distribution of DA distances was fitted to experimental data obtained from a labeled DNA sample.[6] However, in reality, this is usually not the case because of different quantum yields of the dyes and unequal detection efficiencies of the donor and the acceptor detection channels. This problem has been pointed out by Nir et al. in their work on proximity ratio histogram (PRH) analysis,[18] which applies to bursts of varying duration. PRH analysis is based on principles similar as those of PDA and makes use of the experimental burst size distribution. Nir et al. suggested that the desired detection efficiencies can be "artificially achieved by misaligning one of the detectors or by discarding a constant fraction of the detected photons by one of the channels".[18] Although this idea may work well for pure FRET, it certainly does not cover all possible scenarios such as local dye quenching or the presence of several states, differing not only by the DA distance. Moreover, discarding photons leads to a loss of useful data and therefore increases the contribution of shot noise. In this work, we propose a general extension to PDA which takes into account brightness variations and recovers correct underlying values of FRET efficiencies or fluorescence anisotropies, as well as fractions of the species.

Another common problem of SM measurements on complex systems is a simultaneous observation of several molecules in the laser focus.[25,26] These multiple-molecule events appear in 1D histograms as a small mixed population between major peaks and can be easily misinterpreted as an individual population or as an indication of conformational dynamics. In this work, we propose an approach to correct the PDA model function for the presence of multiple-molecule events, which under certain conditions requires no additional model parameters. Exactly for the same reason as that for brightness correction, treatment of multimolecule events in PDA is not straightforward. In addition to what is done in FIDA, for example, one has to extract several individual fluorescence intensity distributions, which correspond to SM concentration, starting only from the experimental signal intensity distribution obtained for a concentrated mixture of several species. Correction for multiple-molecule events may help reduce the measurement time as well as the influence of laser instabilities and adsorption on the glass surface. It can also be applied when high concentrations cannot be avoided, for instance, when molecular complexes with moderate affinity are investigated.

The theory of PDA extended as discussed above allows one to test any underlying distribution against experimental data, which include shot-noise and background contributions. Complex underlying distributions are usually modeled as a number of discrete states or continuous distributions. An alternative approach to the modeling of these distributions is model-free deconvolution based on the maximum entropy method (MEM).[27–29] We demonstrate how MEM can be combined with PDA in order to extract unbiased underlying distributions from measurements on diffusing molecules. As applied to SM-FRET data, the combination of PDA and MEM naturally recovers distributions of DA distances. The proposed procedure is to a large extent similar to the approach introduced by Watkins et al.[17] for the analysis of photon traces of immobilized molecules. Applications of MEM to simulated and experimental data demonstrate its advantages and limitations and also reveal some general restrictions of the PDA method.

Recently, in many papers,[6,9,12,18] possible reasons for broadening of FRET efficiency distributions have been discussed, such as (1) optical misalignment of the green and red detection volumes, (2) photobleaching or blinking of the acceptor dye, (3) saturation of the acceptor dye, and (4) local quenching of the donor and/or acceptor dye, which is a very frequent cause. Here, we present a simple analysis tool in combination with 2D FRET analysis, which describes the correlation between mean donor lifetime distributions and FRET efficiencies. The use of these tools allows one to judge with high confidence whether the experimental broadening is caused by dye quenching.

2. Theory

2.1. Basic Theory of PDA. ***2.1.1. Single Species.*** The measured signal S consists of fluorescence (F) and background (B) photons. In this work, the values of S, F, and B are expressed in photon counts per time window of a fixed length (Δt). The signal is measured by two or more single-photon counting detectors and divided into two components (for example, green (G) and red (R) or parallel (||) and perpendicular ($\perp$)). The PDA method[6,20] starts from the calculation of the probability of observing a certain combination of photon counts in two detection channels 1 and 2, $P(S_1, S_2)$. For a single fluorescent state $P(S_1, S_2)$ is given by a product of independent probabilities.[6]

$$P(S_1, S_2) = \sum_{F_1+B_1=S_1;F_2+B_2=S_2} P(F)\, P(F_1, F_2|F) P(B_1)\, P(B_2) \tag{1}$$

In eq 1, $P(F)$ describes the fluorescence intensity distribution (i.e., the likelihood to observe F fluorescence photons in a time interval Δt). $P(B_1)$ and $P(B_2)$ represent the background intensity distributions, which are usually assumed to obey a Poisson distribution[25,30] with known mean intensities $\langle B_1 \rangle$ and $\langle B_2 \rangle$. $P(F_1,F_2|F)$ stands for the conditional probability of observing a particular combination of F_1 and F_2, provided that the total number of registered fluorescence photons is F. $P(F_1,F_2|F)$ can be expressed as a binomial distribution.[6,18]

$$P(F_1, F_2|F) = \frac{F!}{F_1!\,(F-F_1)!} {p_1}^{F_1} (1-p_1)^{F-F_1} \tag{2}$$

In eq 2, p_1 stands for the probability of a detected photon to be registered by the first detector (e.g., green in a FRET experiment

or parallel in an anisotropy experiment). The knowledge of $P(S_1, S_2)$ is sufficient to generate 1D histograms of any parameter, which can be expressed as a function of S_1 and S_2 (e.g., signal ratio S_1/S_2, FRET efficiency or fluorescence anisotropy).[20] Fitting of such histograms obtained for a single species requires only one floating parameter, p_1. In FRET experiments, the value of p_1 is unambiguously related to the FRET efficiency E according to eq 3.

$$p_1 = \left(1 + \alpha + \frac{E\Phi_{FA}}{(1-E)G\Phi_{FD}}\right)^{-1} \quad (3)$$

In eq 3, G stands for the ratio of the detection efficiencies, g_G and g_R, of the two detection channels ($G = g_G/g_R$), Φ_{FD} and Φ_{FA} are the fluorescence quantum yields of the donor and the acceptor, respectively, and α is the crosstalk from green donor signal into the red detection channel of acceptor.

The distribution $P(F)$ in eq 1 is not directly measurable. One can overcome this problem by using a sufficiently high threshold $S_{min} \gg B$ (where $B = B_1 + B_2$) and approximate $P(F)$ by $P(S)$, which is directly obtained from the measurement (eq 4).[6]

$$P(S_1, S_2) = \sum_{F_1+B_1=S_1;F_2+B_2=S_2} P(S)\, P(F_1, F_2|S - B_1 - B_2) P(B_1)\, P(B_2) \quad (4)$$

The underlying distribution $P(F)$ can also be easily calculated by deconvolution from the total signal intensity distribution $P(S)$, which is given by

$$P(S) = P(F) \otimes P(B) \quad (5)$$

Details of the deconvolution procedure are described in ref 20. Most of the theoretical considerations presented in this work depend on the knowledge of the distribution $P(F)$; therefore, the deconvolution approach is preferred even when $S_{min} \gg B$ is fulfilled.

2.1.2. Multiple Species and Brightness Correction. Factorization in eq 1 is valid only when all four distributions are independent. In particular, it is assumed that the distributions $P(F)$ and $P(F_1,F_2|F)$ are uncorrelated. This is true only if a single fluorescent state is considered, or if the total brightness of all states is the same. In general, each state can be characterized by an individual FRET efficiency E_j or polarization anisotropy r_j, as well as by the brightness Q_j. Therefore, a general extension of eq 1 to the case of k different states requires the knowledge of individual fluorescence intensity distributions $P_j(F)$ ($j = 1,..., k$). Let us first assume that these distributions refer to the same concentration of the species and consider only SM events. The observed distribution $P(S_1, S_2)$ for $F > 0$ is then given by a sum of $P_j(S_1, S_2)$ terms, weighted by the concentrations c_j ($j = 1,..., k$):

$$P(S_1, S_2) = \sum_{j=1}^{k} \left[c_j \sum_{F_1+B_1=S_1;F_2+B_2=S_2} P_j(F)\, P_j(F_1, F_2|F)\, P(B_1)\, P(B_2) \right] = \sum_{F_1+B_1=S_1;F_2+B_2=S_2} \left(\sum_{j=1}^{k} [c_j P_j(F)\, P_j(F_1, F_2|F)]\, P(B_1)\, P(B_2) \right) \quad (6)$$

It is convenient to consider the point $F = 0$ and the convolution with background separately and to rewrite eq 6 as

$$P(F_1 = 0, F_2 = 0) = P(F = 0) \quad (7a)$$

$$P(F_1, F_2) = \sum_j [c_j P_j(F)\, P_j(F_1, F_2|F)] \qquad (F > 0) \quad (7b)$$

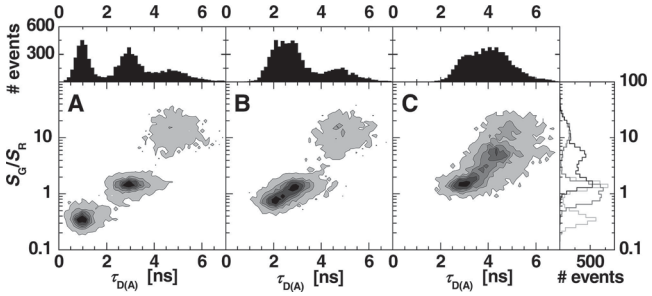

Figure 1. Three typical cases observed in FRET experiments on mixtures of two FRET-active species and one donor-only labeled species. Results of burstwise analysis of simulated data are presented in 2D histograms of G-to-R signal ratio, S_G/S_R, versus the donor fluorescence lifetime in the presence of the acceptor, $\tau_{D(A)}$. (A) All three species can be completely separated on the burst level or can be studied independently in a series of experiments. (B) The donor-only population can be separated, or an additional measurement on pure donor-only sample can be performed, but the two FRET species cannot be separated. (C) All three populations can be neither separated nor independently studied.

$$P(S_1, S_2) = \sum_{F_1+B_1=S_1;F_2+B_2=S_2} P(F_1, F_2)\, P(B_1)\, P(B_2) \quad (7c)$$

In eqs 6 and 7, $P_j(F_1,F_2|F)$ describes the probability of observing a particular combination of F_1 and F_2, for the jth species, provided that the total number of fluorescence photons is F, and $P(F)$ denotes the overall fluorescence intensity distribution.

Unfortunately, it is a rule rather than an exception that the brightness of different species is not the same. For instance, in FRET experiments the total brightness is determined by the fluorescence quantum yields of the donor and the acceptor and the corresponding detection efficiencies. Therefore, all fluorescence intensity distributions $\{P_j(F)\}$ have to be calculated or measured independently (cf. eqs 6 and 7). In the next sections, we show how one can calculate distributions $\{P_j(F)\}$ by starting only from the experimental $P(S)$, that is, by making no assumptions about the shape of the laser focus and the detection volume. In the following, applying eq 6 or eq 7 instead of eq 1 is referred to as brightness correction. The correction methods are described in Sections 2.2–2.6.

Depending on how well the species can be separated by a burst classification algorithm and/or what additional data are available, different procedures of obtaining individual fluorescence intensity distributions $\{P_j(F)\}$ can be applied. Three typical scenarios of SM multiparameter fluorescence detection (MFD) in FRET experiments are illustrated in Figure 1. With increasing complexity, Figure 1 shows typical 2D parameter histograms of S_G/S_R versus $\tau_{D(A)}$, where $\tau_{D(A)}$ stands for the donor lifetime in the presence of acceptor. In the next sections, we show how the distributions $\{P_j(F)\}$ can be obtained in each of these three cases, that is, (A) all species can be separated, (B) only donor-labeled species can be separated, and (C) all three populations overlap.

Please note that for cases B and C, it is of course not necessary that different species exhibit nonoverlapping peaks on the $\tau_{D(A)}$ versus S_G/S_R 2D histogram (Figure 1), because one can use also other dimensions of the fluorescence parameter data set.[7] Advanced SM analysis methods such as MFD [7,31] and ALEX [32–34] are of great help for separating individual species, simplifying further analysis by PDA.

2.2. Independent Measurements of $P_j(F)$ (Scaling of $P(F)$ with Concentration). In the simplest case of nonoverlapping populations (Figure 1A), 1D histograms of interest (e.g., FRET

efficiency distributions) can be generated separately for each species, and usually, there should be no need to apply PDA to the overall histogram. We briefly discuss this case to show how the individual fluorescence intensity distributions $P_j(F)$ depend on concentrations of the corresponding species, which is relevant if these distributions have been obtained from different measurements. At low (SM) concentrations, multiple-molecule events can be neglected. It then becomes convenient to consider the point $F = 0$ separately, because for $F > 0$, $P_j(F)$ is proportional to the concentration of the corresponding species, c_j. One can then express $P_j(F)$ as

$$P_j(F) = (1 - p_j^{\text{in}}) + p_j^{\text{in}} P_j(0|\text{in}) \qquad F = 0$$
$$P_j(F) = P_j(F) = p_j^{\text{in}} P_j(F|\text{in}) \qquad F > 0 \tag{8}$$

where p_j^{in} stands for the probability of finding a molecule of the jth kind in the observation volume and $P_j(F|\text{in})$ denotes the fluorescence intensity distribution, provided that a molecule of species j is situated in the laser focus. The exact value of p_j^{in} depends on how the observation volume is defined; however, for the analysis, it is sufficient that under SM conditions, p_j^{in} is directly proportional to the concentration of the jth species, c_j. Note that the values of $P_j(F = 0)$ enter only in $P(F_1 = 0, F_2 = 0)$, which is actually equal to $P(F = 0)$ (see eq 7a). Therefore, the values of individual $P_j(F = 0)$ are irrelevant (i.e., we are not interested in which exact species has emitted zero photons; only the overall $P(F = 0)$ is needed). For simplicity, we assume in the following that the point $F = 0$ is taken care of by setting $P(F_1 = 0, F_2 = 0) = P(F = 0)$ and do not consider this point explicitly. It is then clear from eq 8 that for $F > 0$, $P_j(F)$ can be simply rescaled by multiplying each point of this distribution by the value of the corresponding relative concentration c_j. In other words, the shape of the interesting part of $P_j(F)$ does not change with the concentration, as long as the concentrations are low and multiple-molecule events are rare.

The knowledge of the overall deconvoluted distribution $P(F)$ (cf. eq 5) allows us to avoid absolute concentrations $\{c_j\}$ (which are often irrelevant) and work with relative concentrations (i.e., fractions) of the species $\{x_j\}$ $\left(\sum_{j=1}^{k} x_j = 1\right)$. The individual distributions $P_j(F)$ must be then rescaled so that they obey eq 9.

$$\sum_{j=1}^{k} x_j P_j(F) = P(F) \tag{9}$$

The normalization constant for $\{P_j(F)\}$ can be easily obtained by requiring that the mean fluorescence signal, calculated from a set of $\{P_j(F)\}$, is equal to the experimental fluorescence signal $\langle F \rangle$ for the fluorescence counts F, (eq 10).

$$\langle F \rangle = \sum_{j=1}^{k} \sum_{F=0}^{\infty} F x_j P_j(F) = \sum_{F=0}^{\infty} F P(F) \tag{10}$$

Each $P_j(F)$ (for $F > 0$) is multiplied by the same factor so that eq 10 is satisfied. Thus, for a general k-state model, $2k - 1$ floating parameters are needed: k parameters describing mean FRET efficiencies E_j or fluorescence anisotropies r_j and $k - 1$ relative concentrations or fractions (x_1,..., x_{k-1}; $x_k = 1 - \sum_{j=1}^{k-1} x_j = 1$).

2.3. Calculating $P(F)$ from a Measurement on Another Species (Scaling with Brightness). In practice, it is not always possible to separate bursts from similar states (Figure 1B). However, very often, an independent measurement on the same molecule is available, in which a single fluorescent state can be observed. For instance, in FRET experiments, a donor-only (D-only) labeled sample is usually studied separately. For convenience, let us assign $j = 0$ to this reference state and set the relative brightness of this species, Q_0, to be equal to 1. The fluorescence intensity distribution for this species $P_0(F)$ allows one to calculate the corresponding brightness distribution, $P(q_i)$, as follows from the representation of $P_0(F)$ as a weighted sum of Poisson distributions.[21,25,35,36]

$$P_0(F) = \sum_i P(q_i) \frac{q_i^F \exp(-q_i)}{F!} \tag{11}$$

To describe the irradiance shells of the focal volume, we use a predefined set of brightness values $\{q_i\}$, consisting of 100−200 elements. Because we do not attempt to relate the brightness distribution $P(q_i)$ to any physical parameters of the detection volume, we adapt the coefficients $P(q_i)$ to fit the experimental distribution $P(S)$ (cf. eq 5). Therefore, we also do not need the assumption that fluorescence intensity emitted by a molecule is constant during a counting time interval. As we proposed before,[20] starting from the distribution $P_0(F)$ any other $P_j(F)$ can be derived, provided that (i) the relative brightness of the jth state, Q_j, is known, (ii) diffusion properties of species 0 and j are the same, and (iii) saturation effects are negligible or affect all species equally. Under these conditions,

$$P_j(F) = \sum_i P(q_i) \frac{(Q_j q_i)^F \exp(-Q_j q_i)}{F!} \tag{12}$$

The above requirements are, in general, reasonable. The brightness ratio Q_j/Q_0 can often be obtained from independent data (e.g., from lifetime distributions for anisotropy PDA) or by FIDA.[21] We refer to this case as manual brightness correction. In other cases, Q_j might be not known, but it is often directly related to the corresponding E_j or r_j. Thus, the calculation of the relative brightness Q_j can be built into a fitting procedure (automatic brightness correction) without introducing new free parameters in the analysis, as will be shown below. Please note that in this work, only relative brightness values are relevant. When these values are given in kiloHertz, they define the count rate which corresponds to a mean concentration of one molecule in the observation volume.[19,21]

The other two assumptions regarding diffusion and saturation effects are needed to justify the use of the same brightness distribution $P(q_i)$ for all species (eqs 11 and 12). The distribution $P(q_i)$ describes the probabilities that a molecule with a brightness of 1 takes a certain path through the observation volume, for which the mean number of emitted photons is q_i. It is clear that another (jth) species having the same diffusion coefficient would take the same path with the same probability $P(q_i)$, emitting however $Q_j q_i$ photons on average. Thus, the shape of $P(q_i)$ as it enters in eqs 11 and 12 is independent of the brightness of the molecule, being determined only by the shape of the observation volume and the molecular diffusion coefficient.

In practice, it is not unusual that the diffusion properties of all species in a series of experiments are similar. In particular, in FRET experiments, D-only and DA species differ only by the acceptor dye, which is usually much smaller than the macromolecule of interest and therefore has a negligible effect on the diffusion coefficient. A similar situation occurs when, for example, binding of a small ligand to a macromolecule is investigated.

Saturation effects (e.g., triplet formation) are more difficult to account for. These effects may change the effective shape of the observation volume,[24] possibly to a different extent depending on the fluorescence properties of the species. For example, in FRET experiments, the population of the triplet state of the

donor dye depends on its fluorescence lifetime, which in turn depends on the distance to the acceptor.[12] Moreover, at high excitation powers, the assumption of equal G and R observation volumes can be violated because of different triplet behavior of the donor and the acceptor dyes. Therefore, in real measurements, saturation effects must be controlled by selecting appropriate excitation intensities.

The proposed dependence of fluorescence intensity distribution on brightness (eq 12) is strictly valid only if the whole photon trace is analyzed. Burstwise analysis involves the use of a burst search algorithm, which is usually empirical and may change the shape of all $\{P_j(F)\}$ differently, depending on the mean brightness. One can overcome this problem to some extent by including adjacent background photons into fluorescence bursts (cf. ref 37). Instead of selecting bursts from the molecules of interest, one can also exclude bursts due to unwanted species and analyze the remaining data as a whole photon trace. Because less-bright bursts are usually not selected, this procedure cannot completely suppress the fluorescence of unwanted species; however, the final contribution of these species to the total signal is not expected to be significant.

2.4. Calculation of $P_j(F)$ in a General Case (Simultaneous Deconvolution). It is also possible to obtain the individual fluorescence intensity distributions $\{P_j(F)\}$ even if none of the species of interest can be studied separately (Figure 1C). In this case, one needs a guess for relative brightness and concentrations of all species, which can be, for instance, intermediate results of a fitting procedure. By assuming that all concentrations are low and eq 8 is valid and by combining eqs 9 and 12, one obtains

$$P(F) = \sum_{j=1}^{k} x_j P_j(F) = \sum_i P(q_i) \sum_{j=1}^{k} x_j \frac{(q_i Q_j)^F \exp(-q_i Q_j)}{F!} \tag{13}$$

Eq 13 is valid under the same conditions as those for eq 12, that is, when the diffusion coefficient is the same for all species, saturation effects are negligible, and a whole photon trace is considered. At this point, we assume that the values of $\{Q_j\}$ and $\{x_j\}$ are either known or represent the result of a fitting iteration. Therefore, eq 13 contains exactly the same set of free parameters as the original eq 11; that is, only the distribution $P(q_i)$ has to be calculated, which can be done in the same way as that for a single species.[20] From $P(q_i)$, any $P_j(F)$ is easily obtained according to eqs 11 and 12. This method is relatively time-consuming, because deconvolution has to be performed before each fit iteration.

In the next two sections, we demonstrate that in many typical cases, deconvolution of $\{P_j(F)\}$ can be combined with fitting procedure, without introducing extra unknown parameters.

2.5. Brightness Correction in FRET Experiments. So far, we have assumed that the relative brightness of each species Q_j is known, which is needed to calculate the distributions $\{P_j(F)\}$ according to eq 12 or by deconvolution (eq 13). Alternatively, the relative brightness of each species can be expressed as a function of the corresponding mean FRET efficiency E_j, that is, automatically calculated before each fit iteration. In this case, the fitting procedure has to be modified so that before each iteration, the set of $\{P_j(F)\}$ is also updated by using current values of $\{Q_j\}$ and $\{x_j\}$ where applicable. By assuming that all brightness variations are only due to FRET, one can show that Q_j is related to E_j according to (see Appendix)

$$Q_j \propto 1 - E_j\left(1 - \frac{\Phi_{FA}}{G\Phi_{FD}(1+\alpha)}\right) \tag{14}$$

For convenience, eq 14 is normalized so that the brightness of D-only species is equal to 1.

2.6. Brightness Correction in Anisotropy Experiments. Anisotropy values often vary because of local mobility of the dyes or local quenching. If only one of these processes is responsible for all anisotropy variations, it is possible to find a relationship between the mean anisotropy values r_j and the mean brightness Q_j, that is, to implement automatic brightness correction. Here, it is important to distinguish between experimental brightness, which is proportional to the fluorescence signal measured by two detectors and should be used in eq 12, and the theoretical one, which is related to the fluorescence emitted in all spatial directions. In the first case (i.e., different dye mobility), the theoretical total intensity does not change (for details, see Appendix); however, the observed brightness $(F_{\parallel} + F_{\perp})$ might be polarization-dependent. The mean measured brightness is then given by

$$Q_j \propto 1 + \frac{r_j(3Gl_2 - 3l_1 + 2 - G)}{1+G} \tag{15}$$

In eq 15, l_1 and l_2 denote the correction factors that describe depolarization by the microscope objective,[38] and $G = g_{\perp}/g_{\parallel}$. For realistic values of G, l_1, and l_2, the above-mentioned effect is relatively weak. For instance, if $G = 1$, $l_1 = 0.03$, and $l_2 = 0.04$, the anisotropy change from 0 to 0.4 leads only to ~20% increase in the measured brightness.

For the case of local quenching, we assume that all species exhibit the same single rotational correlation time. The anisotropy then obeys the Perrin equation.[15,39] Moreover, it is often reasonable to assume that the fluorescence quantum yield is proportional to the fluorescence lifetime. One then obtains (for details, see Appendix)

$$Q_j \propto \left(1 + \frac{r_j(3Gl_2 - 3l_1 + 2 - G)}{1+G}\right)\left(\frac{r_0}{r_j} - 1\right) \tag{16}$$

In eq 16, r_0 denotes the fundamental fluorescence anisotropy,[15,39] which is a property of the dye and can be precisely measured in ensemble experiments. Let us note that according to eq 16, for low anisotropies, Q_j becomes very large, which may cause numerical instabilities when using eq 16 in practice.

Such automatic brightness correction in PDA is not limited to these few common cases that we have discussed. Whenever one can find a relationship between the mean brightness and other parameters characterizing a fluorescent state, expressions similar to eqs 14–16 can be derived and included into the PDA model function to account for brightness effects, without introducing any unnecessary free parameters.

2.7. Model-Free Deconvolution. It has been shown that the PDA approach can unambiguously separate shot-noise broadening from the distribution of relevant physical parameters.[6] The underlying distribution can be modeled either with a fixed mean FRET efficiency (single distance) or alternatively by distributed FRET efficiencies (distribution of distances, e.g., Gaussian [6,18]). In practice, continuous distributions are usually modeled as a large number of discrete states, with the corresponding fractions being described by a function with a small number of parameters (e.g., a Gaussian distribution with known mean and width). In this way, PDA is a perfect tool to compare between experimental shot-noise broadened distributions and models which might include a certain number of static fluorescent states and continuous distributions. However, the opposite is not true: it

is clear that, in general, the underlying distribution cannot be unambiguously recovered by PDA because of limited data quality.

In addition to data fitting with a predefined model, a model-free deconvolution of the underlying distributions is possible, which is usually associated with the MEM.[27–29,40] Here, we present an extension to the PDA method inspired by the work of Watkins et al.,[17] who proposed to use MEM to extract distributions of distances from photon traces obtained from immobilized molecules. We adapt these ideas to diffusing molecules while using the PDA framework to account for shot-noise and background contributions.

The MEM is believed to extract the most unbiased distributions that satisfactory describe the experimental data.[27–29,40] Instead of minimization of reduced chi-squared values (χ_r^2), the following function is maximized (eq 17).

$$\Theta = \nu s - \chi_r^2 \tag{17}$$

In eq 17, ν is a constant, and s is an entropy-like function. [28]

$$s = \sum_j \left(X_j - M_j - X_j \log \frac{X_j}{M_j} \right) \tag{18}$$

where $X = \{X_j\}$ is the distribution of the parameter of interest (e.g., DA distance) and $M = \{M_j\}$ is the initial model for this distribution. The role of the factor ν in eq 17 is addressed differently by several authors. A theoretical approach is presented by Gull and Skilling.[40] However, in many other works, the value of ν is adjusted to maximize the entropy or the value of Θ, while the value of χ_r^2 is still statistically reasonable (see, for example, refs 17 and 27). In particular, Watkins et al.[17] proposed that χ_r^2 must be within $1 \pm 1/(n)^{1/2}$, where in our case, n would be the number of PDA histogram bins.

In our experience, somewhat more reproducible results (at least when applied in combination with PDA) can be obtained by requiring that, for a given data set, χ_r^2 shall not exceed its minimal possible value by more than $1/(n)^{1/2}$ (or any value proportional to $1/(n)^{1/2}$ which is believed to be statistically significant). This condition seems to be reasonable, because even for a perfect fit, χ_r^2 is not necessarily equal to 1 but is described by a distribution with a mean of 1 and a variance of $2/n$,[41] and therefore, in many cases, $\chi_r^2 < 1 + 1/(n)^{1/2}$ cannot be fulfilled. In reality, the minimal possible value of χ_r^2 can be even higher because of experimental artifacts, a few of which are discussed in refs 6 and 18. Thus, in this work, the value of ν was manually adjusted so that χ_r^2 exceeded its minimal value (usually corresponding to $\nu = 0$) by $1/(n)^{1/2}$, which effectively determines the width of the MEM distribution of X.

Another possible source of uncertainties in MEM is the initial model function M. The final result (X) can also vary (although usually not dramatically) depending on which parameter is assumed to be uniformly distributed a priori. The DA distance R (as used in this work) seems to be a good choice, but there is no obvious reason to prefer this parameter to the FRET efficiency, for example.

Maximization of Θ (eq 17) was performed as proposed by Vinogradov and Wilson.[42] The resulting distribution of DA distances was converted into a distribution of FRET efficiencies and further used to generate a shot-noise broadened PDA model histogram according to eq 1 or eq 7.

2.8. Multiple-Molecule Events. In this section, we show how the PDA model function can be corrected for the presence of multiple-molecule events in a SM measurement. As we will see, for burstwise data, an empirical probability of multimolecule events has to be introduced, whereas no extra free parameters are required if whole photon traces are analyzed.

The main idea of the correction procedure is the same as that in FIDA methods,[19,21] that is, to calculate a convolution of a number (m) of $P'(F_1, F_2)$ terms, where $P'(F_1, F_2)$ describes the probability of observing a particular combination (F_1, F_2) for single molecules and $1/m$ is equivalent to dilution factor of the original sample. The convolution can be calculated with the help of generating functions[14,19,21] or via 2D discrete Fourier transform (DFT, cf. ref 43).

$$P(F_1, F_2) = \underbrace{P'(F_1, F_2) \otimes \ldots \otimes P'(F_1, F_2)}_{m \text{ times}} = \mathrm{DFT}^{-1}([\mathrm{DFT}(P'(F_1, F_2))]^m) \tag{19}$$

In eq 19, DFT^{-1} denotes the inverse DFT. Let us first consider the case when the brightness of all species is similar and eq 1 can be used. Unlike in FIDA, in PDA, $P'(F_1, F_2)$ cannot be easily calculated because the corresponding SM fluorescence intensity distribution $P'(F)$ is not known and the distribution $P(F)$ is available only for a concentrated sample. Therefore, one has to find a distribution $P'(F)$ which would yield the experimental total $P(F)$ after m convolution steps. We can again make use of the DFT.

$$P'(F) = \mathrm{DFT}^{-1}([\mathrm{DFT}(P(F))]^{1/m}) \tag{20}$$

In eq 20, $P'(F)$ is a fluorescence intensity distribution for a sample, diluted m times as compared to the original mixture, for which the corresponding distribution is $P(F)$. Substitution of $P'(F)$ into eq 1 yields $P'(F_1, F_2)$. It is clear that by choosing sufficiently high values of m, contribution of multiple-molecule events to $P'(F_1, F_2)$ can be reduced to any desired level. In this work, the value of m is selected so that $P'(F = 0) > 0.99$, which roughly corresponds to the SM detection concentration, for example, the mean number of molecules in the observation volume of $N_{FCS} = 0.0015$ (for $Q = 100$ kHz).

This procedure can be extended to the case of different $P_j(F)$, provided that a reference (single-state, e.g., D-only) sample is available. First, each $P_j(F)$ has to be calculated according to eq 12 and then rescaled according to eqs 8 and 10 to include the fraction of the jth species. Before applying eq 20, a proper value of $P_j(F = 0)$ must be assigned (obviously, $P_j(F = 0) = 1 - \sum_{F>0} p_j(F)$). When all distributions $\{P_j'(F)\}$ are calculated (eq 20), $P'(F_1, F_2)$ can be obtained according to eq 7b. $P(F_1, F_2)$ is then calculated (see eq 19) and convoluted with background (eq 7c) to yield $P(S_1, S_2)$.

To our knowledge, all commonly used burst search algorithms tend to find bursts with high photon numbers; that is, multi-molecule events are preferentially selected. Therefore, the proposed correction for multiple-molecule events is strictly valid only if complete photon traces are analyzed. In a case of burstwise analysis, the contribution of multimolecule events becomes difficult to predict. At relatively low concentrations, it should be sufficient to consider only single- and double-molecule events with certain weights. Unfortunately, we have found no obvious relationship between these weights which would lead to the best fit and any parameters of our burst search algorithm. Thus, if a precise correction for multimolecule events is required, the whole photon trace should be analyzed.

3. Methods

3.1. Chemicals. Rhodamine 110 (Rh110) was purchased from Radiant Dyes (Germany) and used as received. Rhodamine

6G bound to a double-stranded DNA (Rh6G-dsDNA) was prepared as described elsewhere.[44]

3.2. SM Fluorescence Measurements. The experiments were performed by using a MFD technique, as described elsewhere.[8,9,45] Briefly, SM fluorescence detection was performed by using a confocal epi-illuminated microscope with excitation by an active mode-locked Ar^+ laser (73.5 MHz, 150 ps, Inova Sabre, Coherent, Palo Alto, CA) at 476.5 nm. The linearly polarized beam was focused into solution with a 60 × 1.2 water immersion objective (UPlan Apo, Olympus, Hamburg, Germany). The excitation power in the focus of the microscope objective was measured by a power meter (Fieldmaster FM-2, Coherent). The diameter of the focus in the *xy*-plane was about 1.2 μm, as estimated by fluorescence correlation spectroscopy (FCS) from diffusion time of Rh110 molecules ($t_D = 0.26$ ms) by using diffusion constant from the literature. Fluorescence detection was performed with the same objective by using a confocal pinhole ($\varnothing = 100$ μm) which results in a detection volume of ~3 fl. The fluorescence signal was separated from the laser light by a dichroic beamsplitter (Q485DCLP, AHF, Analysentechnik, Tübingen, Germany) and further divided into its parallel (||) and perpendicular ($\perp$) components by a polarizing beamsplitter cube (VISHT11, Gsänger, Planegg, Germany). The color range of detection channels was selected by interference filters (green HQ520/66 and red HQ630/60, AHF Analysentechnik, Tübingen, Germany). The photons were detected by four single photon avalanche diodes (Micro Photon Devices, Bolzano, Italy) coupled to PC-based time-correlated single-photon counting (TCSPC) modules (modified SPC 132, Becker and Hickel GmbH, Berlin, Germany). Experiments on Rh6G-dsDNA were performed as described in ref 44.

3.3. Simulations of SM Fluorescence Experiments. Simulations of SM measurements were performed by using the Brownian dynamics approach[21,46–48] with a few modifications as described elsewhere.[20] The maximal brightness was taken to be 100 kHz, which was similar to typical experimental values measured with our setup. The diffusion time of all species was 1 ms, and the simulation time step was 0.005 ms. Poisson-distributed background was added when necessary. The mean number of molecules in the focus (defined as in FCS[49]) was 0.01 unless stated otherwise. All simulations were performed on a 2.2 GHz PC; the speed was about 20 000 events/s. The data were stored in our regular data format[50] for standard analyses.

3.4. Data Analysis. The recorded sequence of photon events is used to compute the intensity trace of equal non-interleaving time windows (or time bins); the duration of the time window is $\Delta t = 1$ ms unless otherwise stated. The data are presented as 1D histograms of any ratiometric or normalized parameter of interest as described.[6,20] Calculation of $P(S_1, S_2)$ for the case of multiple states is conveniently performed via $P(F_1, F_2)$ (eq 7): convolution with the background distribution, which is usually the most time-consuming step, is performed only once irrespectively of the number of fluorescent states considered. The fitting procedure may however need a modification if the values of $\{Q_j\}$ are not known a priori. Then, it becomes necessary to recalculate the fluorescence intensity distributions $\{P_j(F)\}$ before each iteration. To summarize, for the case of SM-FRET data, the fitting procedure can be described as follows.

Step 1. Read data and calculate experimental $P(S_1, S_2)$. Generate a 1D histogram of choice from the experimental data. Deconvolute total $P(F)$. Suggest an initial guess for concentrations and FRET efficiencies or model parameters (e.g., the mean and the width of a Gaussian distribution of DA distances).

Step 2A. (All species are separated; cf. Figure 1A) Load previously calculated $\{P_j(F)\}$, or

Step 2B. (D-only species can be separated; cf. Figure 1B) load previously calculated $P(q_i)$, obtained from a D-only sample, for example (cf. Section 2.3). Calculate $\{Q_j\}$ for species 1 to j by using the latest $\{E_j\}$ (eq 14) and then $\{P_j(F)\}$ according to eq 12, or

Step 2C. (All populations overlap; cf. Figure 1C) calculate $\{Q_j\}$ and deconvolute $\{P_j(F)\}$ (eq 13) by using the latest values of $\{E_j\}$ and $\{x_j\}$.

Step 3. Calculate 2D model distribution $P(S_1, S_2)$ (eq 7). Generate a 1D model histogram and compare with the experimental data.

Step 4. Use an optimization algorithm (e.g., Levenberg–Marquardt) to find a new set of model parameters (e.g., $\{E_j\}$ and $\{x_j\}$). Repeat steps 2–4 until convergence is reached.

A general k-states model includes $2k - 1$ floating parameters: k mean FRET efficiencies or anisotropies and $k - 1$ relative concentrations (or fractions). Quality of the fits is judged by χ_r^2 values and weighted residuals plots.

4. Results and Discussion

4.1. Experimental Verification of Brightness Scaling Algorithm. The dependence of the fluorescence intensity distribution on the relative brightness (eq 12) is essential for all brightness correction procedures described in Sections 2.3–2.6. Although eq 12 itself is a direct consequence of the well-known Mandel's formula[35] (eq 11), deconvolution of the brightness distribution $P(q_i)$ from noisy data introduces numerical instabilities, which could make derived distributions (eq 12) unusable. We show that this is not the case by verification of eq 12 on experimental data, by considering also saturation effects that are not explicitly taken into account in eqs 11 and 12.

For this, we measured the fluorescence of Rh110 dye at SM concentration, at two different excitation intensities. The excitation power as measured in the focus of the microscope objective was 741 and 195 μW, which corresponds to the mean irradiance $I_0/2(H) = 65.5$ kW/cm^2 and $I_0/2(L) = 17.2$ kW/cm^2, respectively.[51] The brightness of Rh110 at these excitation intensities was $Q_H = 90.3$ kHz and $Q_L = 46.9$ kHz, as determined by FIDA,[19] and subscripts H and L refer to high and low excitation power, respectively. Note that the brightness ratio (0.52) is significantly different from the power ratio (~0.26), which indicates strong saturation.

Case 1: Different Detection Efficiencies. Because the signal is registered by four detectors, a lower apparent brightness can be simply achieved by disregarding photons with perpendicular polarization with respect to the polarization of excitation light, yielding the distribution $P_H(F_{||})$ and the corresponding brightness $Q_{||,H} = 46.2$ kHz. Figure 2A shows this distribution together with the distribution $P_H(F)$, scaled according to eq 12 ($Q_{||,H}/Q_H = 0.51$). It is clear that in this case, a good agreement between the experimental and calculated fluorescence intensity distributions is observed in the whole range of photon numbers, which proves that the proposed procedure of calculating unknown fluorescence intensity distributions according to eqs 11 and 12 is valid.

Case 2: Nonlinear Saturation. To study the influence of optical saturation, we compared the experimental fluorescence intensity distribution measured at lower power, $P_L(F)$, with that derived according to eq 12, starting from the distribution $P_H(F)$ measured at higher power. The relevant fluorescence intensity distributions calculated by deconvolution from the corresponding signal intensity distributions $P(S)$ are presented in Figure 2B.

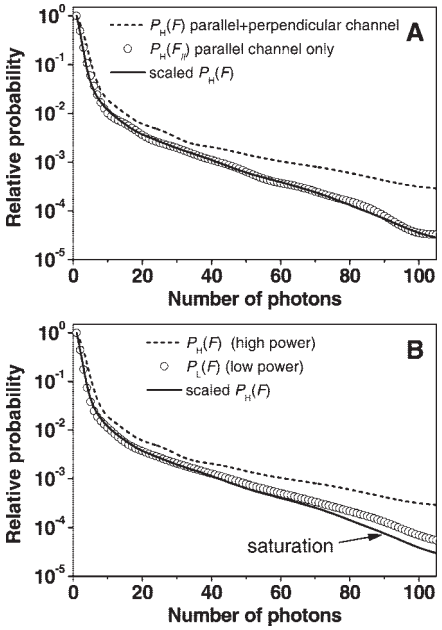

Figure 2. Dependence of fluorescence intensity distributions on the mean brightness. The dashed line on both plots shows the fluorescence intensity distribution of Rh110, $P_H(F)$, measured at 741 μW at the objective, detected by all four channels. (A) Experimental distribution $P_H(F_{||})$ of Rh110 measured at 741 μW (only photons with parallel polarization are counted, open circles) and distribution obtained from $P_H(F)$ by using eq 12 (solid line, $Q_{||H}/Q_H = 0.51$). (B) Comparison of the experimental distribution $P_L(F)$ measured at 195 μW (open circles) and the distribution obtained according to eq 12 (solid line, $Q_L/Q_H = 0.52$), starting from the experimental $P_H(F)$ measured at 741 μW.

Clearly, at low photon numbers, the scaled distribution $P_H(F)$ (eq 12) closely resembles the distribution $P_L(F)$. However, at higher photon numbers, small but systematic deviations can be observed, which can be expected because of triplet formation.[25] Nevertheless, the S_G/S_R signal ratio histogram obtained from Rh110 data can be satisfactorily fitted by using the scaled $P_H(F)$, providing $\chi_r^2 = 1.11$ and $\langle F_G/F_R \rangle = 10.97$. Common PDA fit (eq 1) of the same data yields $\chi_r^2 = 0.93$ and $\langle F_G/F_R \rangle = 10.91$ (data not shown). These results show that fluorescence intensity distributions can be scaled according to eq 12 for the whole range of excitation intensities relevant for SM fluorescence experiments.

It is important to emphasize that unlike in FIDA, the assumption of $\Delta t \ll t_D$ is not required: for Rh110, $t_D = 0.26$ ms and $\Delta t = 1$ ms. This fact allows us to work with large time windows and therefore high photon numbers, significantly improving the ability of PDA to resolve multiple species.[20]

4.2. Effect of Brightness Variations on PDA. ***4.2.1. Brightness Correction.*** At first, we verify the proposed brightness correction methods (sections 2.2–2.4) by applying them to simulated data which closely mimic experimental data. The analysis of simulations, for which the true parameters are exactly known, is performed in order to characterize stability of the analysis and search for systematic errors. Later, we apply PDA to real experimental data. We also show that in both cases, brightness variations could produce results that dramatically deviate from the expected (or simulated) values, if they are not taken into account by using appropriate brightness correction methods (eqs 6 and 7).

To test the proposed brightness correction methods, a system has been simulated which consists of two states, 1 and 2, where one state is partially quenched (Figure 3A) so that $Q_1 = 100$ kHz is reduced to $Q_2 = 33.7$ kHz. Because of local quenching,

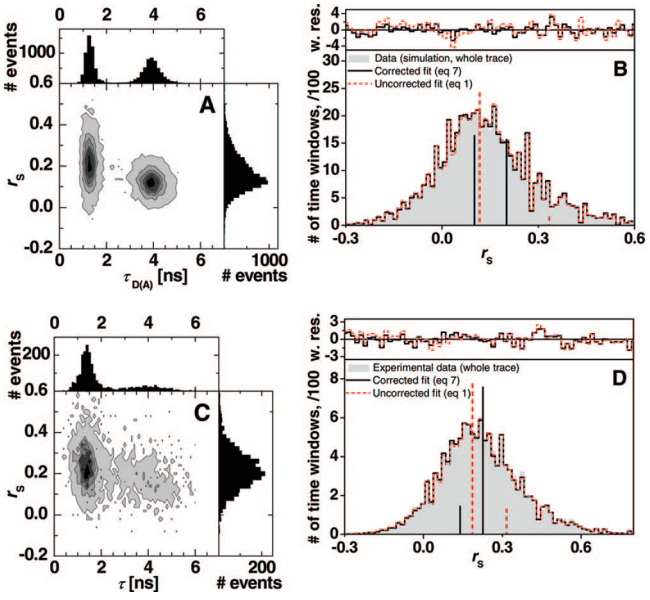

Figure 3. (A) 2D scatter-corrected fluorescence anisotropy (r_S) versus $\tau_{D(A)}$ histogram showing the results of burstwise analysis of simulated mixture of two static states, for which $r_1 = 0.1$ (50%), $r_2 = 0.2$ (50%), $Q_1 = 100$ kHz, and $Q_2 = 33.7$ kHz. The corresponding fluorescence lifetimes are 4 and 1.29 ns, respectively. $\langle B_{||} \rangle = 1.7$, $\langle B_{\perp} \rangle = 1.3$, and $t_D = 1$ ms. The population exhibiting lower anisotropy contains ~46% of all fluorescence bursts. To simplify burst search, we assumed that quenching of state 2 is due to FRET and added red photons, $Q_{red} = Q_1 - Q_2 = 66.3$ kHz. (B) 1D histogram of scatter-corrected fluorescence anisotropy obtained from the whole photon trace of the same data set (gray area). PDA fits with (solid black line) and without (dashed red line) brightness correction are shown. Fitting of the PDA model, corrected for brightness effects (eq 7), yields $r_1 = 0.102$ (53.3%) and $r_2 = 0.206$ (46.7%); $\chi_r^2 = 1.12$. Uncorrected fit (i.e., assuming the same $P(F)$ for both species) yields $r_1 = 0.117$ (94.7%) and $r_2 = 0.334$ (5.7%); $\chi_r^2 = 2.24$. Fixing true values and applying uncorrected model results in $\chi_r^2 = 22.79$. (C) Scatter-corrected fluorescence anisotropy (r_S) versus fluorescence lifetime histogram showing the results of burstwise analysis of Rh6G-labeled dsDNA fluorescence. The population exhibiting lower anisotropy contains ~24% of all fluorescence bursts. (D) 1D histogram of scatter-corrected fluorescence anisotropy obtained from the same data set (gray area). PDA fits with (solid black line) and without (dashed red line) brightness correction are shown. Fitting of the PDA model, corrected for brightness effects (eq 7), yields $r_1 = 0.140$ (16.0%) and $r_2 = 0.227$ (84.0%); $\chi_r^2 = 0.69$. Uncorrected fit yields $r_1 = 0.186$ (85.7%) and $r_2 = 0.317$ (14.4%); $\chi_r^2 = 0.83$.

the two states have different fluorescence anisotropies: $r_1 = 0.1$ and $r_2 = 0.2$. The corresponding fluorescence lifetimes of these two states are 4 and 1.29 ns, respectively, and the rotational correlation time (ρ) is the same for both states ($\rho_1 = \rho_2 = 1.43$ ns). In the simplest case, we can obtain $P_1(F)$ and $P_2(F)$ independently (Section 2.2; cf. Figure 1A). Then, we calculate the distribution $P_2(F)$ according to eq 12 (brightness correction with reference $P(F)$; cf. Figure 1B) by assuming that the first state can be studied independently and $P_1(F)$ is known. Finally, both individual fluorescence intensity distributions can be simultaneously deconvoluted by using eq 13.

Figure 3A shows the results of burstwise analysis of the simulated data in a scatter-corrected fluorescence anisotropy (r_S) versus $\tau_{D(A)}$ 2D frequency histogram. From Figure 3A, it is clear that two populations with $r_1 \approx 0.1$ and $r_1 \approx 0.2$ are present, which have approximately equal concentrations. A histogram of scatter-corrected fluorescence anisotropy (r_S)[20,52] generated from the same data set is presented in Figure 3B. If, however, this histogram is analyzed by the PDA model which takes no brightness effects into account (eq 1), $r_1 = 0.117$ (94.7%) and

TABLE 1: Comparison of Brightness Correction Methods as Applied to Simulated and Experimental Data Sets (Figure 3)

brightness correction/analysis method	Q_2/Q_1	r_1	r_2	χ_r^2
Simulated Data, $r_1 = 0.1$ (50%) and $r_2 = 0.2$ (50%) (Figure 3A,B)				
none, single state	not needed	0.125 (100%)		5.51
none, two states		0.117 (94.7%)	0.334 (5.7%)	2.24
		0.1 (50%) (fixed)	0.2 (50%) (fixed)	22.79
none, 1/10 data	not needed	0.117 (93.9%)	0.29 (6.1%)	1.12
individual $P_j(F)$	not needed	0.101 (53.7%)	0.206 (46.3%)	1.16
with reference $P(F)$ (eq 12)	0.337 (manual, fixed)	0.102 (53.3%)	0.206 (46.7%)	1.13
	automatic, eq 16	0.102 (52.3%)	0.204 (47.7%)	1.13
Simultaneous deconvolution (eq 13)	0.337 (manual, fixed)	0.101 (51.2%)	0.201 (48.8%)	1.11
	automatic, eq 16	0.103 (53%)	0.208 (47%)	1.10
Experimental Data (Figure 3C,D)				
none	not needed	0.186 (85.7%)	0.317 (14.4%)	0.83
simultaneous deconvolution (eq 13)	0.35 (manual, fixed)	0.132 (9.8%)	0.220 (90.2%)	0.84
	automatic, eq *16*	0.140 (16.0%)	0.227 (84.0%)	0.69
burst size distribution (from ref 44)		lower (18%)	higher (82%)	
selected data $\tau > 2.65$ ns	not needed	0.144		1.00
selected data $\tau < 2.65$ ns	not needed		0.214	1.01

$r_2 = 0.334$ (5.7%) are obtained, which is completely inconsistent with visual analysis of 2D histogram in Figure 3A. To prove that these results are not simply due to instabilities, we used the correct fixed values in the fit and obtained $\chi_r^2 = 22.79$, which indicates that eq 1 is inappropriate.

For an improved PDA analysis, let us first assume that the relative brightness of the second state is known (manual brightness correction). For instance, in the case shown in Figure 3A, one can estimate it from the fluorescence lifetime distributions ($Q_2/Q_1 \approx 1.29$ ns/4 ns $= 0.323$). Alternatively, the brightness values can be estimated by FIDA[21] if the difference in brightness is significant. In our case, the FIDA method yields $Q_1 = 98.4$ kHz and $Q_2 = 33.7$ kHz, which is in excellent agreement with the values used in the simulation.

The best fit of PDA model function, in which the brightness effects are taken into account by calculating $P_2(F)$ from reference $P_1(F)$ according to eqs 11 and 12, is also shown in Figure 3B. The recovered model parameters are in a good agreement with the values used in the simulations: $r_1 = 0.102$ (53.3%) and $r_2 = 0.206$ (46.7%) ($\chi_r^2 = 1.12$). All other brightness correction methods, that is, using precalculated individual $P_1(F)$ and $P_2(F)$ and simultaneous deconvolution of these distributions by using eq 13, produce very similar results (Table 1).

For the analysis of S_G/S_R distributions in FRET measurements, the influence of brightness effects is usually less dramatic. Strong correlation between the FRET efficiency and brightness may produce poor fits and wrong calculated fractions of the species. However, when the major peaks are well resolved, the mean positions of these peaks (i.e., mean FRET efficiencies) are usually not much affected by brightness variations and can be recovered with a reasonable accuracy (data not shown).

4.2.2. Automatic Brightness Correction. In the previous subsection, we have assumed that the values of Q_1 and Q_2 are known, which might not always be possible for a real system. Now, we show how automatic calculation of relative brightness of each state as described in Sections 2.5 and 2.6 can be applied. In other words, the values of Q_1 and Q_2 are updated depending on the intermediate values of r_1 and r_2 for each fit iteration. For the systems shown in Figure 3, eq 16 is relevant.

Table 1 summarizes the conclusions of the previous subsection, as well as the results obtained by automatic brightness correction, that is, when the value of Q_2/Q_1 is calculated according to eq 16.

Table 1 makes it clear that all brightness correction methods provide similar results. We have found no indications for severe instabilities introduced by any of these approaches, although the initial guess parameters are quite distant from the expected values $r_1 = 0$ (50%) and $r_2 = 0.27$ (50%). The accuracy of the methods based on the calculation of several unknown fluorescence intensity distributions is comparable with that of the approach which makes use of individual $\{P_j(F)\}$, directly obtained in a separate series of experiments. Simultaneous deconvolution of all $\{P_j(F)\}$ (eq 13) is clearly the most general approach, but it is also the slowest and is not compatible with our realization of MEM, which will be discussed in Section 4.4. Brightness correction with reference $P(F)$ (eq 12) does not require time-consuming computations and should be also often applicable. Automatic correction, that is, iterative calculation of $\{Q_j\}$ from other fit parameters, introduces no noticeable systematic errors or instabilities as compared to independent calculation of $\{Q_j\}$ but usually needs more iterations to converge. Another important outcome of the analyses of the simulated system is that sometimes, a PDA model function, not corrected for brightness variations (eq 1), might produce a reasonably good fit but completely wrong results. As shown in Table 1, χ_r^2 values do not always indicate that the model function is wrong, especially when data quality is limited by a low number of events (see example 1/10 data; $\chi_r^2 = 1.12$).

4.2.3. Application to Experimental Data. The dye Rhodamine 6G bound to the 5′ end of a double-stranded DNA exhibits multiple conformational states,[44] which are characterized by different fluorescence lifetimes and anisotropies (Figure 3C). In the present work, we use a two-state model, which is sufficient to fit the anisotropy data, although other methods indicate that the brighter subpopulation additionally consists of two states.[44] We are not able to resolve these two states solely by anisotropy PDA; however, we can show that brightness-corrected PDA provides at least qualitatively reasonable results, whereas the simple model (eq 1)[6,20] does not. Experimental histograms of scatter-corrected anisotropy r_S and PDA fits are presented in Figure 3D, and the results of anisotropy analyses are summarized in Table 1. It is clear that using the same fluorescence intensity distribution $P(F)$ for all states leads to severe errors in estimating both anisotropies and fractions of the two states. On the other hand, applying brightness correction yields reasonable fractions and mean anisotropies of individual conformations of Rh6G, in agreement with independent data.[44] The brightness values Q_1 and Q_2 can be estimated from the ratio of the mean fluorescence lifetimes of the two states ($Q_2/Q_1 \approx 0.35$; manual brightness correction) or automatically

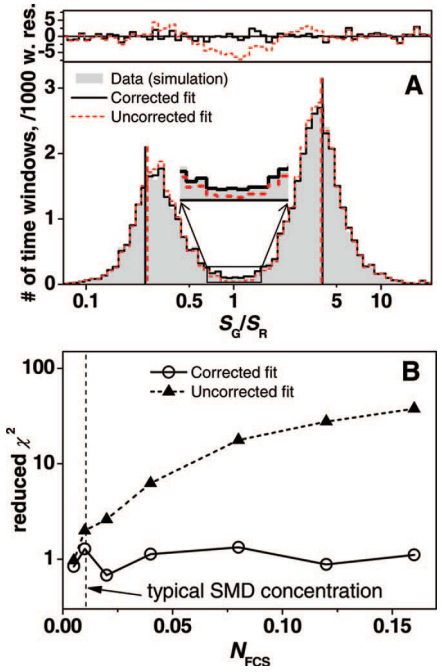

Figure 4. Effect of multiple molecule events on the quality of PDA fits. (A) S_G/S_R ratio histograms for the total FCS concentration of 0.04 (gray area) shown together with corrected PDA model (solid black line; $E_1 = 0.799$ (40.1%),$E_2 = 0.200$ (59.9%), $\chi_r^2 = 1.13$) and uncorrected PDA model (red dashed line; $E_1 = 0.794$ (40.0%), $E_2 = 0.203$ (60.0%), $\chi_r^2 = 6.22$). (B) χ_r^2 plotted versus the mean number of molecules in the focus (N_{FCS}), for the same values of E_1 and E_2 and relative concentrations. Simulation parameters: $E_1 = 0.8$ (40%); $E_2 = 0.2$ (60%); $Q_1 = Q_2 = 100$ kHz; $\langle B_G \rangle = 2$; $\langle B_R \rangle = 1.2$; $t_D = 1$ ms. The vertical dashed line indicates a typical SM concentration.

according to eq 16. These two brightness correction methods provide similar mean anisotropies of the individual conformations of Rh6G (Table 1), which also agree well with the values calculated by PDA of preselected data (Table 1).

To summarize, in its present form, the PDA method not only is able to detect heterogeneities but also accurately extracts relevant parameters of individual states. In the presented example with simulated data (Figure 3A,B), the parameters of two similar states have been extracted from one broad distribution with an accuracy of 3−4% or better. Application of PDA to experimental data reveals the presence of at least two conformations of Rh6G-DNA, which is not obvious from visual analysis of 1D anisotropy histograms (Figure 3C, right subplot). Recovered parameters of these states are in reasonable agreement with independent data.

4.3. Correction for Multiple-Molecule Events. In experiments with freely diffusing single molecules, it is usually not possible to completely avoid multimolecule events. The only way to reduce distortions of experimental SM histograms due to a small fraction of multiple-molecule events is to perform SMD experiments at very low concentrations (mean number of molecules in the focus $N_{FCS} \approx 0.001$), which necessarily implies much longer measurement times and huge data amounts (mostly scatter photons are recorded). Instead, one can use the correction procedure presented in Section 2.8 (eqs 19 and 20), as illustrated in this section.

An example showing the effect of multiple-molecule events on PDA histograms is presented in Figure 4. The simulated system models a mixture of two static FRET states, with $E_1 = 0.8$ (40%; $S_G/S_R = 0.25$) and $E_2 = 0.2$ (60%; $S_G/S_R = 4$). Already at a mean number of molecules in the focus of $N_{FCS} = 0.02$ (under our threshold conditions for burst selection, approximately 3−4 bursts per second at $Q = 100$ kHz), high reduced χ_r^2 values ($\chi_r^2 > 2$) can be easily misinterpreted as meaningful and motivate the use of unnecessarily complex models (e.g., broadened states or conformational dynamics). The deviations at $S_G/S_R \approx 1$ between the purely SM PDA model function and the simulated data can be clearly seen (Figure 4A). A good fit can be achieved by the multimolecule-correction procedure (eqs 19 and 20; $m = 10$), yielding $\chi_r^2 = 1.13$. The extracted values of $E_1 = 0.799$ and $E_2 = 0.20$ and the corresponding fractions are also in excellent agreement with the simulated values (see Figure 4 legend).

The extent to which multiple molecule events influence the fit quality depends on how well the major peaks are separated. Unlike brightness effects, which should be taken care of mainly when overlapping peaks are considered (cf. Figure 3), multiple-molecule events are especially pronounced for distant peaks (e.g., a high FRET and a D-only population) and result mainly in poor fit quality. However, the extracted values of FRET efficiencies are not strongly affected, although the results of the corrected fit are much closer to the simulated values (see legend of Figure 4). Correction procedure works at least up to $N_{FCS} = 0.16$ (~20 bursts/s), as shown in Figure 4B. At this concentration, the probability of multimolecule events is 0.084,[25] and the uncorrected two-state model yields $\chi_r^2 = 37.74$.

4.4. Model-Free Deconvolution Approach and its Limitations. In this section, we investigate the properties of MEM as applied to SM-FRET data on diffusing molecules. We do not consider explicitly simultaneous model-free deconvolution and brightness correction, because combining MEM with the reference $P(F)$ method described in Section 2.3 is trivial. However, our MEM algorithm[42] depends on the assumption that the analyzed distribution (i.e., 1D PDA histogram) is a linear combination of a set of precalculated distributions. The general deconvolution method (eq 13) introduces cross correlation between the fractions x_j and distributions $P_j(F)$ and therefore would require a major modification of the MEM algorithm. Therefore, we limit ourselves to the case when at least one distribution $P_0(F)$ can be measured separately (see Figure 1A,B), although combination of MEM with eq 13 is in principle possible. In the following, we analyze several FRET-distance scenarios by MEM (the analysis of corresponding FRET efficiency histograms is shown in the Supporting Information).

A simulation of a single FRET state with $R = R_0 = 50$ Å ($E = 0.5$) and the results of MEM deconvolution are presented in Figure 5A. Model-free deconvolution extracts a somewhat broader distribution with a standard deviation of ~0.25 Å (Figure 5B). In practice, this value sets the limit of broadening that can be detected by PDA. It is clear that the value of this intrinsic broadening depends on the data quality. The data sets shown in Figure 5 contain approximately 10^5 useful 1 ms time windows with a minimum photon number of 20, which roughly corresponds to a typical measurement time of 1−2 h at $N_{FCS} = 0.01$.

Figure 5B shows the case of two states, for which the DA-distances differ by 2 Å (4% of the Förster radius $R_0 = 50$ Å). A model with two distances (eq 7) can be fitted to these data, yielding $R_1 = 49$ Å (52.5%), $R_2 = 50.9$ Å (47.5%), and $\chi_r^2 = 1.04$. Interestingly, the shot-noise broadened distribution can be also satisfactorily fitted by assuming a Gaussian distribution of distances with a mean $\langle R \rangle = 50$ Å and a standard deviation $\sigma_R = 1.02$ Å ($\chi_r^2 = 1.37$). The dip in the MEM model function indicates that the two-state model is more appropriate than a Gaussian distribution, because any distribution smoother

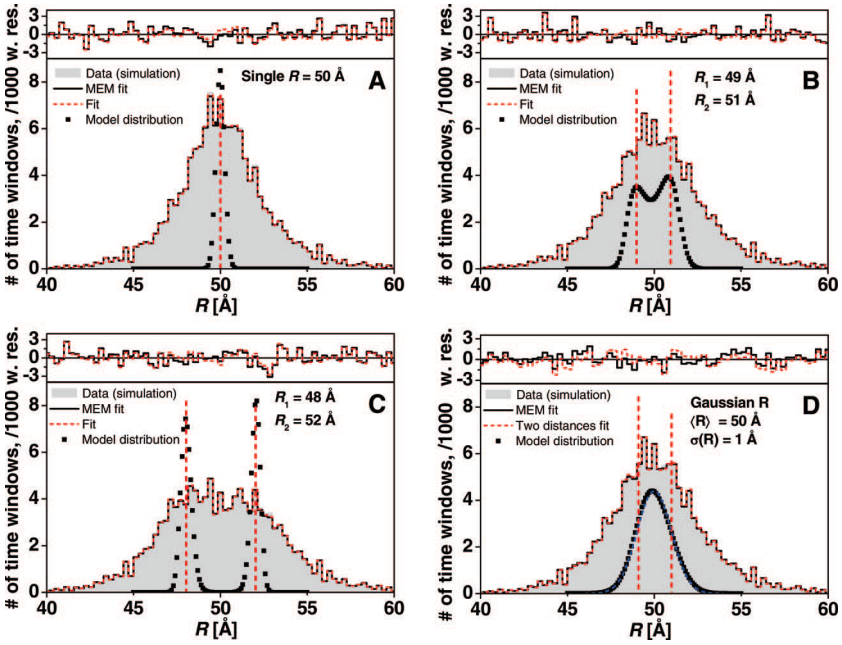

Figure 5. Model-free analyses of various FRET efficiency distributions by PDA. Histograms of simulated data are presented as gray areas, MEM distributions are shown as black squares, and the corresponding PDA model functions are represented by solid black line. One- or two-state models and the corresponding fit functions are shown as red dotted lines, and the solid blue line shows the simulated distribution. Weighted residuals are displayed above each plot. The following cases are considered. (A) One state with $R = 50$ Å. (B) Two states with $R_1 = 49$ Å and $R_2 = 51$ Å (50% each). (C) Two states with $R_1 = 48$ Å and $R_2 = 52$ Å (50% each). (D) Gaussian distribution of distances with $\langle R \rangle = 50$ Å and the standard deviation $\sigma_R = 1$ Å. Common parameters: $R_0 = 50$ Å, $\langle B_G \rangle = 2$, and $\langle B_R \rangle = 1.2$.

than that shown in Figure 5B must produce a statistically significant increase in the χ_r^2 value. It would be difficult to draw this conclusion just by comparing the variances of the underlying distributions of distances, which are essentially the same for the two-state and the Gaussian models. Note also that the peak positions of the distribution obtained by MEM closely match the expected values. If the two states are separated by 4 Å (8% of R_0), the peaks of the distance distribution recovered by MEM do not overlap anymore (Figure 5C). It can be unambiguously stated that at least two states are present. No unimodal distribution of distances can provide satisfactory fit quality.

Figure 5D illustrates the case of a Gaussian distribution of distances ($\langle R \rangle = 50$ Å; standard deviation $\sigma_R = 1$ Å; approximated by 12 discrete states), which is especially interesting to compare with the case of $R_1 = 49$ Å and $R_2 = 51$ Å (Figure 5B). A two-state model with $R_1 = 49.1$ Å (52.3%) and $R_2 = 51$ Å (47.7%) can be very well fitted to the observed distribution ($\chi_r^2 = 0.70$; Figure 5D). The underlying distributions have exactly the same variance, and there is no visible difference in shot-noise broadened distributions between these cases. Nevertheless, MEM is able to detect such a subtle difference and shows that in the latter case (Figure 5D), a smooth distribution is sufficient to fit the data. The extracted distribution of distances very closely resembles the simulated one (extracted $\sigma_R = 1.03$ Å), as shown in Figure 5D.

The analyses of simulated data reveal several limitations of PDA, which are common for many methods dealing with noisy data. In general, it is not always possible to unambiguously distinguish between several discrete states and a continuous underlying distribution. MEM can to some extent help choose the most appropriate model or at least determine the minimal number of states simply by visual analysis of deconvoluted distributions. However, the only way to resolve similar molecular states is to improve the data quality significantly. Exactly the same problem has been pointed out by Ware et al.[53,54] regarding the analysis of TCSPC data, which also obey Poisson statistics. However, there is an important difference between PDA and lifetime measurements in terms of recovered distributions of DA distances that these two methods can provide. In contrast to lifetime distributions, PDA histograms are not affected by fast (nanoseconds−microseconds) processes,[14] which in particular include local dye motions and even rotations.[55] Clearly, these processes are averaged out on the millosecond time scale. Thus, PDA perfectly complements bulk[56] and SM subensemble[3] lifetime measurements, making it possible to study slow processes and static heterogeneities selectively. If both fast dynamic and quasi-static heterogeneities affect the DA distance distribution, the width of these distributions recovered by lifetime analysis should be broader than that obtained by PDA.

4.5. Correlation between FRET Efficiencies and Fluorescence Lifetimes of the Donor. It has been shown that extra (i.e., beyond the shot noise) broadening of experimental FRET efficiency (E) histograms can be due to numerous artifacts and therefore must be interpreted with caution. For instance, poor overlap between green and red observation volumes[6,18] and significant population of the acceptor triplet state[12] may also contribute to the width of FRET efficiency distributions. Thus, it is often not obvious to what extent the observed extra broadening can be attributed to molecular structure, that is, real distance distributions, or to artifacts. Independent information on structural heterogeneities can be obtained by analyzing the shape of the distribution of donor lifetimes, calculated for individual bursts or time windows (tw), which is not sensitive to most of the optical and photophysical artifacts. To avoid confusion with distributions of fluorescence lifetimes, which one can extract from bulk or subensemble TCSPC data,[3,56] we will refer to this distribution as tw-lifetime distribution. In SM experiments with small photon numbers, tw-lifetimes are usually determined by a maximum likelihood estimator (MLE).[57,58] If the fluorescence decay is multi-exponential, MLE yields a mean lifetime, which is close to the fluorescence-weighted mean lifetime.[9] As mentioned before, the distribution of lifetimes as

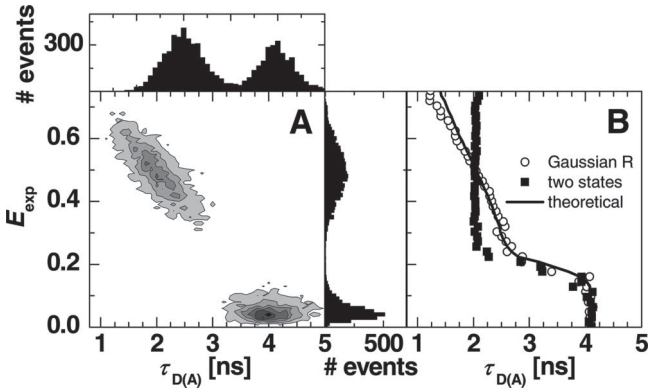

Figure 6. (A) 2D S_G/S_R signal ratio versus $\tau_{D(A)}$ histogram representing results of burstwise analysis of simulated data, mimicking a mixture of two types of molecules, FRET active and a D-only species. FRET species exhibits static Gaussian distribution of distances with $\langle R \rangle$ = 50 Å and a standard deviation σ_R = 3 Å. FRET population clearly shows a correlation between the S_G/S_R signal ratio and the donor lifetime. (B) Mean donor lifetimes calculated for tws falling into particular bins of proximity ratio histogram., plotted as a function of the proximity ratio. The distribution of tw-lifetimes obtained for static Gaussian distribution of distances (open circles; see also Figure 6A) agrees with the theoretical one (solid line) calculated according to eqs 21 and 22. If the PRH is broadened because of complex acceptor dye photophysics, for example, each state exhibits a single fluorescence lifetime (filled squares). Simulation parameters: $\langle B_G \rangle = 2$; $\langle B_R \rangle = 1.2$; R_0 = 50 Å; t_D = 1 ms.

obtained from ensemble (or subensemble) data contains information on fast dynamics (e.g., dye motions), whereas the width of tw-lifetime distributions is primarily determined by the shot noise and not by such fast processes. However, rigorous analysis of the shape of these distributions is a very challenging task because of the complex behavior of lifetime fitting algorithms. It might turn out to be easier to analyze the shape of mean TAC channel number distribution, as it is done in fluorescence intensity−lifetime distribution analysis.[59] Quantitative theory of tw-lifetime distributions is beyond the scope of this work.

Fortunately, for the qualitative tests performed here, the complete theory of the tw-lifetime distribution is not needed. The main idea is that real distance distributions (including those due to conformational dynamics) produce not only extra broad FRET efficiency histograms but also distributions of tw-lifetimes, which must be correlated with E distributions. In extreme cases, such a correlation is clearly visible on 2D burst frequency histograms of proximity ratio ($E_{exp} = S_R/(S_G+S_R)$) versus donor lifetime $\tau_{D(A)}$ (Figure 6A). Similar histograms have been introduced by Rothwell et al.[9] to distinguish FRET-related donor quenching from local dye quenching. Alternatively, one can compare the donor lifetimes calculated for bursts, which fall into left and right parts of E histogram, as proposed by Merchant et al.[60] However, such visual analyses can be often subjective. Here, we propose a simple approach to the analysis of the mean donor lifetimes calculated for each bin of a PDA histogram, which can be easily calculated theoretically and compared with the experimental data.

Let us assume that a PDA histogram of FRET efficiency $P(E_1)$,..., $P(E_n)$ is obtained, which can be fitted with a distance model $P(R_1)$,..., $P(R_m)$. For each distance R_j (j = 1,..., m), a shot-noise broadened PDA histogram $P(E_1|R_j)$,..., $P(E_n|R_j)$ can be calculated separately (with or without brightness correction). To obtain the theoretical mean value of the donor lifetime for each value of E, the lifetime must be averaged over the model distance distribution

$$\langle \tau_{D(A)}(E_i) \rangle = \sum_{j=1,...,m} \tau_{D(A)}(R_j)\, P(R_j)\, P(E_i|R_j) \qquad (21)$$

where $\tau_{D(A)}(R_j)$ corresponds to the donor lifetime of a FRET pair, for which the DA distance is equal to R_j. The value of $\tau_{D(A)}(R_j)$ can be calculated according to eq 22[15]

$$\tau_{D(A)}(R_j) = \tau_{D(0)} \frac{R_j^6}{R_0^6 + R_j^6} \qquad (22)$$

where $\tau_{D(0)}$ is the fluorescence lifetime of the donor dye in the absence of acceptor and R_0 is the Förster radius. The only requirement for using eq 21 is that the lifetime fitting algorithm provides unbiased mean values in the whole range of interest and for all photon numbers. For the MLE, this requirement is fulfilled.[58] We have demonstrated our approach on FRET efficiency distributions; however, it is clear that eqs 21 and 22 are valid also for other FRET-related parameters, such as the signal ratio S_G/S_R or the proximity ratio $S_R/(S_G + S_R)$.

Examples of $\langle \tau_{D(A)} \rangle$ versus proximity ratio plots are presented in Figure 6B, which shows that these plots indeed allow one to judge on the origin of extra broadening of FRET distributions. Distributions of DA distances result in a clear correlation between the mean FRET efficiency and the donor lifetime (open circles, Figure 6B), which can be predicted according to eqs 21 and 22. Small deviations in the range of short lifetimes can be attributed to difficulties in separating fluorescence decays from the scatter contribution.[61] If it is believed that extra broadening of FRET efficiency histograms is due to an artifact, $\tau_{D(A)}(R_j)$ is not expected to obey eq 22 (filled squares). Deviations of the mean $\langle \tau_{D(A)} \rangle$ values from the theory, which are clearly visible in Figure 6B, indicate that extra broadening is likely due to acceptor dye quenching or optical artifacts, for example. In other words, these effects do not produce a correlation between the proximity ratio and the donor lifetime, and for each subpopulation, $\tau_{D(A)}$ shows no dependence on the proximity ratio (Figure 6B).

5. Concluding Remarks

The theory of PDA has been extended to take into account various possible complications that may arise when several fluorescent states contribute to measured shot-noise broadened distributions. The improved PDA theory can be applied to analyze any mixture, by using any a priori model or model-free deconvolution approach. The accuracy of the analysis and the number of free parameters are limited only by data quality. The general case of brightness variations is considered without need to discard photons. In most of the typical cases, brightness correction does not require any additional knowledge of the system or new model parameters and can be built into a fitting procedure. Correction of the PDA model function for the presence of multiple-molecule events allows one to measure at above SM concentrations when necessary and to avoid artifacts due to long measurement time. PDA is now able to quantitatively analyze complex FRET efficiency and anisotropy distributions with multiple states and different brightness values. Tools such as MEM and combined mean donor fluorescence lifetime analysis have been developed to distinguish between states with fixed distances and a distribution of distances.

Acknowledgment. S.K. is grateful to the Alexander von Humboldt Foundation for financial support. This study was supported by the Deutsche Forschungsgemeinschaft (DFG) via the SFB 590 Inherent and adaptive differentiation and the Volkswagen foundation Grant I/78 837.

Appendix: On the Derivation of Eqs 14–16

Equation 14

The FRET efficiency is given by

$$E = \frac{F_A/\Phi_{FA}}{F_D/\Phi_{FD} + F_A/\Phi_{FA}} \quad \text{(A1)}$$

where F_D and F_A are the fluorescence intensities of the donor and the acceptor, respectively. These intensities are related to the observed green and red signals according to eq A2

$$F_G = g_G F_D \propto (1-E)\Phi_{FD} g_G \quad \text{(A2a)}$$

$$F_R = g_R F_A + \alpha g_G F_D \propto E\Phi_{FA} g_R + \alpha F_G \quad \text{(A2b)}$$

By assuming for convenience that the brightness of D-only species is equal to 1, the relative brightness of a FRET species ($F_G + F_R$) can be expressed as

$$Q = \frac{F_G + F_R}{Q(E=0)} = \frac{(1-E)\Phi_{FD} g_G (1+\alpha) + E\Phi_{FA} g_R}{\Phi_{FD} g_G (1+\alpha)} \quad \text{(A3)}$$

Eq A3 is equivalent to eq 14.

Equation 15

The fluorescence intensities measured by two polarization channels, $F_{||}$ and $F_{\perp}$, are given by

$$F_{||} = g_{||}(I_{||}(1-l_1) + l_1 I_{\perp}) \quad \text{(A4a)}$$

$$F_{\perp} = g_{\perp}(l_2 I_{||} + (1-l_2) I_{\perp}) \quad \text{(A4b)}$$

In eq A4, $I_{||}$ and $I_{\perp}$ denote the true intensities of the polarized components, which would be measured with a perfect setup. In reality, the fluorescence is partly depolarized by the microscope objective, as described by introducing the correction factors l_1 and l_2 in eq A4.[38] The difference in the detection efficiencies of the two channels is taken into account by introducing the instrumental G factor ($G = g_{\perp}/g_{||}$).

The total brightness $Q = F_{||} + F_{\perp}$ has to be expressed as a function of the fluorescence anisotropy (eq A6), that is,

$$Q = F_{||} + F_{\perp} \propto I_{||} - l_1 I_{||} + l_1 I_{\perp} + G(I_{\perp} + l_2 I_{||} - l_2 I_{\perp}) \quad \text{(A5)}$$

$$r = \frac{I_{||} - I_{\perp}}{I_{||} + 2I_{\perp}} \quad \text{(A6)}$$

Eq A6 is equivalent to the well-known expressions (eq A7)

$$I_{||} = I_0(1+2r)/3 \quad \text{(A7a)}$$

$$I_{\perp} = I_0(1-r)/3 \quad \text{(A7b)}$$

where I_0 denotes the total fluorescence intensity ($I_0 = I_{||} + 2I_{\perp}$). As assumed in the first part of Section 2.6, the total intensity does not change; that is, I_0 is the same for all species and can be omitted. Substitution of eq A7 into eq A5 and further normalization to $Q(r=0) = 1$ yields eq 15.

Equation 16

By rearranging Perrin equation,[15] we obtain

$$\frac{\tau}{\rho} = \frac{r_0}{r} - 1 \quad \text{(A8)}$$

In addition, the brightness is proportional to the fluorescence quantum yield, which is by our assumption proportional to the fluorescence lifetime. If the rotational correlation time ρ is the same for all species, the right-hand part of eq A8 becomes proportional to the total brightness and should thus appear as an additional factor in eq 16 as compared to eq 15.

References and Notes

(1) Ha, T.; Enderle, T.; Ogletree, D. F.; Chemla, D. S.; Selvin, P. R.; Weiss, S. *Proc. Natl. Acad. Sci. U.S.A.* **1996**, *93*, 6264–6268.

(2) Deniz, A. A.; Laurence, T. A.; Dahan, M.; Chemla, D. S.; Schultz, P. G.; Weiss, S. *Annu. Rev. Phys. Chem.* **2001**, *52*, 233–253.

(3) Laurence, T. A.; Kong, X. X.; Jager, M.; Weiss, S. *Proc. Natl. Acad. Sci. U.S.A.* **2005**, *102*, 17348–17353.

(4) Schuler, B.; Lipman, E. A.; Eaton, W. A. *Nature* **2002**, *419*, 743–747.

(5) Schuler, B.; Lipman, E. A.; Steinbach, P. J.; Kumke, M.; Eaton, W. A. *Proc. Natl. Acad. Sci. U.S.A.* **2005**, *102*, 2754–2759.

(6) Antonik, M.; Felekyan, S.; Gaiduk, A.; Seidel, C. A. M. *J. Phys. Chem. B* **2006**, *110*, 6970–6978.

(7) Widengren, J.; Kudryavtsev, V.; Antonik, M.; Berger, S.; Gerken, M.; Seidel, C. A. M. *Anal. Chem.* **2006**, *78*, 2039–2050.

(8) Margittai, M.; Widengren, J.; Schweinberger, E.; Schröder, G. F.; Felekyan, S.; Haustein, E.; König, M.; Fasshauer, D.; Grubmüller, H.; Jahn, R.; Seidel, C. A. M. *Proc. Natl. Acad. Sci. U.S.A.* **2003**, *100*, 15516–15521.

(9) Rothwell, P. J.; Berger, S.; Kensch, O.; Felekyan, S.; Antonik, M.; Wöhrl, B. M.; Restle, T.; Goody, R. S.; Seidel, C. A. M. *Proc. Natl. Acad. Sci. U.S.A.* **2003**, *100*, 1655–1660.

(10) Ha, T.; Hohng, S.; Joo, C.; Ha, T. *Biophys. J.* **2004**, *87*, 1328–1337.

(11) Ha, T. *Methods* **2001**, *25*, 78–86.

(12) Vogelsang, J.; Doose, S.; Sauer, M.; Tinnefeld, P. *Anal. Chem.* **2007**, *79*, 7367–7375.

(13) Tinnefeld, P.; Sauer, M. *Angew. Chem., Int. Ed.* **2005**, *44*, 2642–2671.

(14) Gopich, I.; Szabo, A. *J. Chem. Phys.* **2005**, 014707.

(15) Lakowicz, J. R. *Principles of Fluorescence Spectroscopy*, 2nd ed.; Kluwer Academic/ Plenum Publishers: New York, 1999.

(16) Deniz, A. A.; Dahan, M.; Grunwell, J. R.; Ha, T. J.; Faulhaber, A. E.; Chemla, D. S.; Weiss, S.; Schultz, P. G. *Proc. Natl. Acad. Sci. U.S.A.* **1999**, *96*, 3670–3675.

(17) Watkins, L. P.; Chang, H. Y.; Yang, H. *J. Phys. Chem. A* **2006**, *110*, 5191–5203.

(18) Nir, E.; Michalet, X.; Hamadani, K. M.; Laurence, T. A.; Neuhauser, D.; Kovchegov, Y.; Weiss, S. *J. Phys. Chem. B* **2006**, *110*, 22103–22124.

(19) Kask, P.; Palo, K.; Fay, N.; Brand, L.; Mets, Ü.; Ullmann, D.; Jungmann, J.; Pschorr, J.; Gall, K. *Biophys. J.* **2000**, *78*, 1703–1713.

(20) Kalinin, S.; Felekyan, S.; Antonik, M.; Seidel, C. A. M. *J. Phys. Chem. B* **2007**, *111*, 10253–10262.

(21) Kask, P.; Palo, K.; Ullmann, D.; Gall, K. *Proc. Natl. Acad. Sci. U.S.A.* **1999**, *96*, 13756–13761.

(22) Hess, S. T.; Webb, W. W. *Biophys. J.* **2002**, *83*, 2300–2317.

(23) Enderlein, J.; Gregor, I.; Patra, D.; Fitter, J. *Curr. Pharm. Biotechnol.* **2004**, *5*, 155–161.

(24) Gregor, I.; Patra, D.; Enderlein, J. *ChemPhysChem* **2005**, *6*, 164–170.

(25) Fries, J. R.; Brand, L.; Eggeling, C.; Köllner, M.; Seidel, C. A. M. *J. Phys. Chem.A* **1998**, *102*, 6601–6613.

(26) Orte, A.; Clarke, R.; Balasubramanian, S.; Klenerman, D. *Anal. Chem.* **2006**, *78*, 7707–7715.

(27) Skilling, J.; Bryan, R. K. *Mon. Not. R. Astr. Soc* **1984**, *211*, 111–124.

(28) Livesey, A. K.; Skilling, J. *Acta Crystallogr., Sect. A* **1985**, *41*, 113–122.

(29) Brochon J. C. *Methods of Enzymology*; Academic Press: New York, 1994; Vol. 240, pp 262−311.

(30) Qian, H.; Elson, E. L. *Biophys. J.* **1990**, *57*, 375–380.

(31) Kudryavtsev, V.; Felekyan, S.; Wozniak, A. K.; König, M.; Sandhagen, C.; Kühnemuth, R.; Seidel, C. A. M.; Oesterhelt, F. *Anal. Bioanal. Chem.* **2007**, *387*, 71–82.

(32) Kapanidis, A. N.; Lee, N. K.; Laurence, T. A.; Doose, S.; Margeat, E.; Weiss, S. *Proc. Natl. Acad. Sci. U.S.A.* **2004**, *101*, 8936–8941.

(33) Lee, N. K.; Kapanidis, A. N.; Wang, Y.; Michalet, X.; Mukhopadhyay, J.; Ebright, R. H.; Weiss, S. *Biophys. J.* **2005**, *88*, 2939–2953.

(34) Lee, N. K.; Kapanidis, A. N.; Koh, H. R.; Korlann, Y.; Ho, S. O.; Kim, Y.; Gassman, N.; Kim, S. K.; Weiss, S. *Biophys. J.* **2007**, *92*, 303–312.

(35) Mandel, L.; Sudarshan, E. C. G.; Wolf, E. *Proc. Phys. Soc.* **1964**, *84*, 435–444.

(36) Rigler, R.; Mets, Ü. *SPIE Proc.* **1992**, *1921*, 239–248.

(37) Laurence, T. A.; Kwon, Y.; Yin, E.; Hollars, C. W.; Camarero, J. A.; Barsky, D. *Biophys. J.* **2007**, *92*, 2184–2198.

(38) Koshioka, M.; Saski, K.; Masuhara, H. *Appl. Spectrosc.* **1995**, *49*, 224–228.

(39) Valeur, B. *Molecular Fluorescence: Principles and Applications*; Wiley-VCH Verlag: Weinheim, 2002.

(40) Gull, S. F.; Skilling, J. *Quantified Maximum Entropy MemSys5 User's Manual*; Maximum Entropy Data Consultants Ltd.: Suffolk, UK, 1999; Vol. 5[1.2].

(41) Soong, T. T. *Fundamentals of Probability and Statistics for Engineers*; John Wiley & Sons: West Sussex, England, 2004.

(42) Vinogradov, S. A.; Wilson, D. F. *Appl. Spectrosc.* **2000**, *54*, 849–855.

(43) Saffarian, S.; Li, Y.; Elson, E. L.; Pike, L. J. *Biophys. J.* **2007**, *93*, 1021–1031.

(44) Neubauer, H.; Gaiko, N.; Berger, S.; Schaffer, J.; Eggeling, C.; Tuma, J.; Verdier, L.; Seidel, C. A. M.; Griesinger, C.; Volkmer, A. *J. Am. Chem. Soc.* **2007**, *129*, 12746–12755.

(45) Kühnemuth, R.; Seidel, C. A. M. *Single Mol.* **2001**, *2*, 251–254.

(46) Enderlein, J.; Robbins, D. L.; Ambrose, W. P.; Goodwin, P. M.; Keller, R. A. *J. Phys. Chem. B* **1997**, *101*, 3626–3632.

(47) Laurence, T. A.; Kapanidis, A. N.; Kong, X. X.; Chemla, D. S.; Weiss, S. *J. Phys. Chem. B* **2004**, *108*, 3051–3067.

(48) Dix, J. A.; Hom, E. F. Y.; Verkman, A. S. *J. Phys. Chem. B* **2006**, *110*, 1896–1906.

(49) Magde, D.; Elson, E. L.; Webb, W. W. *Phys. Rev. Lett.* **1972**, *29*, 705–708.

(50) Felekyan, S.; Kühnemuth, R.; Kudryavtsev, V.; Sandhagen, C.; Becker, W.; Seidel, C. A. M. *Rev. Sci. Instrum.* **2005**, *76*, 083104−1083104−14.

(51) Eggeling, C.; Widengren, J.; Rigler, R.; Seidel, C. A. M. *Anal. Chem.* **1998**, *70*, 2651–2659.

(52) Schaffer, J.; Volkmer, A.; Eggeling, C.; Subramaniam, V.; Striker, G.; Seidel, C. A. M. *J. Phys. Chem. A* **1999**, *103*, 331–336.

(53) James, D. R.; Ware, W. R. *Chem. Phys. Lett.* **1985**, *120*, 455–459.

(54) James, D. R.; Ware, W. R. *Chem. Phys. Lett.* **1986**, *126*, 7–11.

(55) Isaksson, M.; Norlin, N.; Westlund, P. O.; Johansson, L. B. A. *Phys. Chem. Chem. Phys.* **2007**, *9*, 1941–1951.

(56) Haas, E.; Wilchek, M.; Katchalski-Katzir, E.; Steinberg, I. Z. *Proc. Natl. Acad. Sci. U.S.A.* **1975**, *72*, 1807–1811.

(57) Brand, L.; Eggeling, C.; Zander, C.; Drexhage, K. H.; Seidel, C. A. M. *J. Phys. Chem. A* **1997**, *101*, 4313–4321.

(58) Maus, M.; Cotlet, M.; Hofkens, J.; Gensch, T.; De Schryver, F. C.; Schaffer, J.; Seidel, C. A. M. *Anal. Chem.* **2001**, *73*, 2078–2086.

(59) Palo, K.; Brand, L.; Eggeling, C.; Jäger, S.; Kask, P.; Gall, K. *Biophys. J.* **2002**, *83*, 605–618.

(60) Merchant, K. A.; Best, R. B.; Louis, J. M.; Gopich, I. V.; Eaton, W. A. *Proc. Natl. Acad. Sci. U.S.A.* **2007**, *104*, 1528–1533.

(61) Eggeling, C.; Fries, J. R.; Brand, L.; Günther, R.; Seidel, C. A. M. *Proc. Natl. Acad. Sci. U.S.A.* **1998**, *95*, 1556–1561.

JP711942Q

III

Probability Distribution Analysis of a Two-State Interconverting FRET System

Stanislav Kalinin[1], Alessandro Valeri[1], Matthew Antonik,[1,†] Suren Felekyan and Claus A. M. Seidel*

Institut für Physikalische Chemie, Lehrstuhl für Molekulare Physikalische Chemie, Heinrich-Heine-Universität, Universitätsstraße 1, Geb 26.32, 40225 Düsseldorf, Germany

* To whom correspondence should be addressed.
E-mail: cseidel@gwdg.de

† Present address: Department of Physics & Astronomy, The University of Kansas, 1082 Malott Hall, 1251 Wescoe Hall Drive, Lawrence, KS 66045-7582; USA

[1] Contributed equally to this work

Abstract

Probability distribution analysis (PDA) (Antonik, Felekyan et al. 2006) is applied to characterize a two-state system undergoing simultaneous conformational dynamics and Förster resonance energy transfer (FRET). PDA accurately predicts the shape of FRET efficiency histograms in the presence of FRET fluctuations, explicitly taking into account shot noise and background contributions. Underlying theoretical model is presented and extensively tested by means of computer simulations. It is demonstrated that relaxation times on timescale of the diffusion time (typically milliseconds) can be accurately recovered, with the dynamic range of the method of about three orders of magnitude. Major factors limiting the absolute precision of dynamic-PDA are identified as brightness variations, shortening of the observation time due to diffusion, and a contribution of multi-molecular events. These effects considerably bias dynamic-PDA often leading to under- or overestimation of the rate constants by factor of two or more. Correction procedures are proposed.

1. Introduction

The conformational changes a biomolecule undergoes upon interaction with other molecules are a prerequisite to its ability to perform the task at hand. Host guest recognition in antibodies-antigens interactions, binding of an enzyme to its substrate, just to name some, rely on fluctuations of the spatial arrangement of specific domains. Furthermore, the knowledge of how molecules interact and the conformations they adopt when coming close together gives useful insights in the study of protein folding. It is then clear that if we want to understand these processes that are at the base of the biological activity, we have to develop tools able to detect and resolve, in space and time, the fluctuations of distance and relative orientation of the molecular domains of interest.

One of the techniques best suited to access this information is fluorescence resonance energy transfer, FRET. In this technique a molecule, or a complex of molecules, is labeled with two fluorescent dyes, a donor and an acceptor. Upon excitation, the donor transfers its energy to the acceptor with a certain probability depending on the donor-acceptor distance and mutual orientation of the dyes (Lakowicz 1999). The acceptor dye, in turn, becomes excited and emits. The parameter used to quantify the transfer is the energy transfer efficiency, E. In the last decade, single molecule techniques have gained increasing interest over other fluorescence techniques because, while not perturbing the system in study, they allow ultrasensitive detection and do not require any synchronization of the sample.

With passing time the measurement techniques have become more sophisticated and the quality of the recorded data have become more and more accurate, so that nowadays we are faced with the challenge of studying minimal fluorescence fluctuations and assess unambiguously when they depend on actual conformational changes and when determined by photon statistics (shot noise). So far, the most used technique to study the fluctuation of fluorescence signals in order to investigate dynamic processes was fluorescence correlation spectroscopy (FCS) (Widengren and Mets 2002). Unfortunately, the classical FCS has only a limited potential to reveal the static composition of a mixture and characterize the individual states. This information can be partly extracted by fluorescence intensity distribution analysis (FIDA) and related approaches [PCH, FFS], which allow one to resolve static heterogeneities based on brightness of different species. At the same time, most accurate structural information can be probably obtained by FRET, which potentially allows for quantitative distance measurements. However, quantitative methods of analysis of single-molecule FRET

intensity data have been developed only very recently ((Gopich and Szabo 2005; Antonik, Felekyan et al. 2006; Nir, Michalet et al. 2006). Being based on similar principles, these methods are applied to single-molecule fluorescence data divided into equal time bins (time windows), or to selected fluorescence bursts, as in proximity ratio histogram (PRH) analysis. All these approaches basically separate FRET distributions of interest from photon shot noise and background contributions.

At present, PDA and PRH analysis are applied mainly to investigate static heterogeneities [mix-PDA, more], although the potential to study FRET dynamics is also discussed (Nir, Michalet et al. 2006). Two major works demonstrating the possibility to characterize dynamic processes by analyzing intensity distributions (i.e. without explicit use of FCS) have been recently published by Kask et al and Gopich-Szabo. In the present work we combine a similar two-state interconversion model (A $\leftrightarrow$ B) with PDA, which we will refer to as dynamic-PDA. Our main goal is to develop a high resolution quantitative method directly applicable to experimental data. Although the theory underlying dynamic-PDA is largely similar to the one used in […], our work additionally includes several essential steps towards the analysis of real data. In particular, we test the validity of all approximations used to derive the model and show that most of them must be used with great caution. The corresponding systematic errors and stability of the analysis are discussed. A simple approach to distinguish between a dynamic and a static system based on varying time window length is proposed. Moreover, we address several common experimental issues such as brightness variations and multiple molecule events. Actually, we show that equal brightness of the states involved is generally not required. We demonstrate how dynamic-PDA is able to identify the different interconverting states and to retrieve the rate and equilibrium constants.

2. Theory

The usual case for FRET experiments is that, due to dye motions, molecular fluctuations, and conformational changes, the experimental system exhibits more than a single FRET efficiency value. Depending on timescale, such fluctuations may have an effect on the shape of FRET related parameter histograms. In such cases it is necessary to develop a suitable model describing the distribution of FRET efficiencies, $P(E)$, and incorporate that model into the PDA analysis. In Antonik, et. al. (Antonik, Felekyan et al. 2006), the case of a static Gaussian distribution of donor-acceptor distances R_{DA} was considered, and a suitable $P(E)$ was derived which corresponded to this distribution. Here, a model will be derived corresponding to a

two-state system, where a molecule switches between two states with distinct FRET efficiencies.

For a given donor-acceptor distance R_{DA} the transfer efficiency is given by $E = R_0^6 / (R_0^6 + R_{DA}^6)$ where R_0 is the Förster radius [Å] which accounts for the specific properties of the donor-acceptor pair. R_0 is calculated by $R_0 = \left(c_{FT} J \kappa^2 \Phi_{FD(0)} n^{-4}\right)^{(1/6)}$, where J is the overlap integral of the donor emission spectrum with the acceptor absorption spectrum with the units [M^{-1} cm^{-1} nm^4], κ^2 accounts for the relative orientation of donor and acceptor, $\Phi_{FD(0)}$ is the donor fluorescence quantum yield in absence of transfer, n is the refractive index of the medium (n = 1.33 for water) and c_{FT} is a proportionality constant (for the given units it equals 8.79 10^{-5} mol). Thus, possible reasons for distinct FRET efficiencies are changes in donor-acceptor distance or in system properties influencing the Förster radius R_0. The theory presented in the following can describe both cases. However, fluctuations of R_0 are usually considered as a source for artifacts in structural studies. As a typical application we describe therefore the case where a molecule switches with definite rate constants between two conformations, each with a distinct R_{DA}.

It is assumed for this derivation that the molecule has two states, A and B, with the rate constants out of the states being k_A and k_B, respectively. The FRET efficiencies of each state are given by E_A and E_B. The observation time of the molecule is divided into time windows with the lenght Δt. A molecule may switch between A and B multiple times during the time Δt . The total time the molecule spends in state A is given by T_A, and the total time in state B is T_B, where $T_A + T_B = \Delta t$. Provided that the total brightness (i.e. the sum of donor and acceptor signals) remains constant during the time interval Δt and does not change upon transition, the observed efficiency, E, for a particular time window is simply the time weighted average of E_A and E_B as given in eq 1

$$E = \frac{T_A E_A + T_B E_B}{T_A + T_B} \tag{1}$$

If the total brightness of state A, Q_A, is different from the brightness of state B, Q_B, the brightness values have to be taken in account as weights of E_A and E_B, leading to eq 2

$$E = \frac{Q_A T_A E_A + Q_B T_B E_B}{Q_A T_A + Q_B T_B} \tag{2}$$

The brightness in eq 2 has a meaning of the total count rate (green plus red) at a given excitation intensity, and at a concentration of one molecule per observation volume. Via eqs

1-2, the problem of determining a distribution of FRET efficencies $P(E)$ is transformed into one of determining a probability density distribution of dwell times $P(T_A)$, which has been computed in (eq 3)

$$P(T_A) = \left[\frac{2k_B k_A}{k_A + k_B} I_0\left(2\sqrt{k_A k_B T_A T_B}\right) + \frac{k_B T_A + k_A T_B}{k_A + k_B} \cdot \frac{\sqrt{k_A k_B}}{\sqrt{T_A T_B}} I_1\left(2\sqrt{k_A k_B T_A T_B}\right)\right] \exp(-k_A T_A - k_B T_B) \quad (3)$$

In eq 3, $I_0()$ and $I_1()$ denote Bessel functions of order 0 and 1, respectively, and $T_B = \Delta t - T_A$. For convenience, the derivation of eq 3 is given in the Appendix.

For the special case where this integration interval includes either 0 or Δt, the probability that the molecule persists in a single state over the entire time window must be separately calculated and included. Eq 4a calculates the probability that a molecule is never in state A, and switching the A's and B's provides the probability that the molecule is never in state B (eq 4b)

$$p(0) = p(T_A = 0) = \frac{k_A}{k_A + k_B} \exp(-k_B \Delta t) \quad (4a)$$

$$p(\Delta t) = p(T_B = 0) = \frac{k_B}{k_A + k_B} \exp(-k_A \Delta t) \quad (4b)$$

Eqs 1-2 provide the effective efficiency E corresponding to the parameters T_A, T_B, E_A and E_B. The corresponding probability $P(E)$ is determined indirectly by integrating eq 3 over a short time interval to determine the probability $P(T_A < t_A < T_A + \Delta T_A)$. Thus, substitution of eqs 3-4 into eqs 1-2 yields the distribution $P(E)$ which may be further used to generate a theoretical histogram of any FRET-related parameter as discussed elsewhere (Kalinin, Felekyan et al. 2007; Kalinin, Felekyan et al. 2008).

In practice the distribution $P(E)$ is usually calculated in its discrete form. Using a series of possible values of T_A, ($T_{A(i)} = i\Delta T$, $i = 0...n$, $n\Delta T = \Delta t$), by integrating eqs 3-4 over T_A one obtains eq 5,

$$P(T_{A(i)}) = \begin{cases} P(0)\Delta T/2 + p(0) & \text{for } i = 0 \\ P(i\Delta T)\Delta T & \text{for } i = 1...n-1 \\ P(\Delta t)\Delta T/2 + p(\Delta t) & \text{for } i = n \end{cases} \quad (5)$$

The values of E_i are then calculated for each $T_{A(i)}$ according to eq 1 or eq 2 which finally yields a discrete distribution $P(E_i)$. Next, for each E_i the probability of observing a certain combination of photon counts in "green" (G) and "red" (R) detection channels, $P(S_G, S_R)$, is calculated by using eq 6 (Antonik, Felekyan et al. 2006; Kalinin, Felekyan et al. 2007),

$$P(S_G, S_R) = \sum_{F_G+B_G=S_G;\, F_R+B_R=S_R} P(F)P(F_G, F_R \mid F)P(B_G)P(B_R) \quad (6)$$

The total fluorescence intensity distribution $P(F)$ is obtained by deconvolution from the signal intensity distribution $P(S)$ [a-PDA], and background intensity distributions in green and red channels $P(B_G)$ and $P(B_R)$ are typically assumed to obey a Poisson distribution with known mean intensities $\langle B_G \rangle$ and $\langle B_R \rangle$. $P(F_G, F_R \mid F)$ represents the conditional probability of observing a particular combination of F_G and F_R, provided the total number of registered fluorescence photons is F, and can be expressed as a binomial distribution [Matthew-PDA]

$$P(F_G, F_R \mid F) = \frac{F!}{F_G!F_R!} p_G{}^{F_G}(1-p_G)^{F_R} \quad (7)$$

In eq 7, the probability to register a "green" photon p_G is determined by FRET efficiency as given by eq 8,

$$p_G = \left(1 + \alpha + \frac{E\Phi_{FA}}{(1-E)G\Phi_{FD(0)}}\right)^{-1} \quad (8)$$

In eq 8 G stands for the ratio of the detection efficiencies, g_G and g_R, of the two detection channels ($G = g_G/g_R$), $\Phi_{FD(0)}$ and Φ_{FA} are the fluorescence quantum yields of the donor and the acceptor, respectively, and α is the crosstalk from green donor signal into the red detection channel of acceptor.

In case of $Q_A = Q_B$ the overall $P(S_G, S_R)$ is given by a fraction-weighted sum of contributions of all E_i- states, given by eqs 6-8. The procedure used to obtain $P(S_G, S_R)$ for the case of $Q_A \neq Q_B$ additionally involves deconvolution of individual fluorescence intensity distributions, as described in (Kalinin, Felekyan et al. 2008).

3. Material and Methods

3.1 Simulations of multi-parameter fluorescence detection (MFD)

Simulations of single-molecule MFD measurements were performed by using the Brownian dynamics approach {Enderlein, Robbins, et al. 1997 1953 /id}{Kask, Palo, et al. 1999 2619 /id}{Laurence, Kapanidis, et al. 2004 3237 /id}{Dix, Hom, et al. 2006 3601 /id}, as described elsewhere. The spatial intensity distribution of the observation volume was assumed to be a 3D Gaussian {Rigler, Mets, et al. 1993 68 /id} (please note that this is not required to obtain eqs 1-4, or the general theory of PDA). The brightness of the species (Q) was taken comparable to experimental values measured with our setup (ca. 100 kHz). Moreover, it was set to be equal for all states, except paragraph 4.5 where the brightness effects are investigated. The simulated fluorescence was collected by "green" and "red" detection channels, which covered the fluorescence peaks of the donor and the acceptor, respectively. The mean number of molecules in the "focus" (defined as in FCS, i.e., via the correlation amplitude, $G(t_c = 0) = 1/N_{FCS}$ (Magde, Elson et al. 1972)) was $N_{FCS} = 0.002$ unless stated otherwise. The diffusion times (t_D) of all species was 3 ms with the exception of the series where the effect of t_D was investigated (Section 4.4). Poisson-distributed background signal consisting of detector dark counts and scatter contribution was added. The following common parameters were used for all simulations: time step: 0.005 ms; green background $B_G = 2$ kHz; red background $B_R = 1.2$ kHz; crosstalk from donor signal into the "red" detection channel: $\alpha = 0.01$.

Simulations of conformational dynamics were performed via modeling A → B and B → A transitions. Initial fractions of molecules in states A and B were determined by the corresponding rate constants according to $A(t = 0) = k_B/(k_A + k_B)$ and $B(t = 0) = k_A/(k_A + k_B)$. The times the molecules spent in A and B states (t_A and t_B, respectively) were exponentially distributed with $P(t_A) = k_A^{-1}\exp(-k_A t_A)$ and $P(t_B) = k_B^{-1}\exp(-k_B t_B)$. To resemble as much as possible a real measurement a third state representing molecules labeled only with the donor dye was added. Simulated data were saved as a stream of detected fluorescence photons, in SPC-132 data format (Becker & Hickel GmbH, Berlin, Germany) for standard analyses using published procedures to calculate all fluorescence parameters.

3.2 Data fitting by PDA

The recorded sequence of photon events was used to compute the intensity trace of equal non-interleaving time windows (or time bins) of the length Δt. Typically, the whole photon trace was analyzed because this allows for rigorous correction for brightness variations and multiple molecule events (Kalinin, Felekyan et al. 2008). In some cases a burst search algorithm (Fries, Brand et al. 1998) was employed and time widows only within selected bursts were considered. The data were typically presented as one-dimensional (1D) histograms of green to red signal intensity ratio (S_G/S_R).

The model used to approximate PDA histograms of simulated data included two interconverting states (A and B; eqs 1-4) and a donor-only (D-only) species as often encountered in real experiments. Hence, five fitting parameters were needed: the individual FRET efficiencies E_A and E_B, the corresponding off-rates k_A and k_B, and the fraction of the D-only species. Convolution of the model distribution (eqs 1-4) with shot noise and background produced two-dimensional distributions $P(S_G, S_R)$, from which S_G/S_R histograms (i.e. the model functions) were generated and fitted to the simulated data (Antonik, Felekyan et al. 2006; Kalinin, Felekyan et al. 2007). The quality of fits was judged by reduced χ^2-values (χ_r^2) as well as by examining weighted residuals plots.

4. Results and Discussion

To test the applicability and the performance of dynamic-PDA we decide to use simulated data. This choice is mainly dictated by the need to have *standards* with exactly known rate constants against which we can benchmark our method, but give us also the possibility to study how the fit outcome depends on one parameter keeping the other constant. Re-analysis of simulated data allows us to characterize both random (Section 4.3) and systematic (Sections 4.4-4.6) errors inherent to dynamic-PDA. Systematic deviations are expected because the proposed theoretical model (eqs 1-4) is based on several approximations, in particular, on a critical assumption of constant brightness (which implies both constant brightness during the selected time window and $Q_A = Q_B$). The validity of these approximations is discussed in Sections 4.4-4.6.

4.1 Qualitative description of the method by using one- and two-dimensional fluorescence parameter histograms

At first we want to introduce some general concepts and a give purely qualitative description of the method. The section will result somehow descriptive, but nonetheless we think it is important to present these basic ideas here that will be used throughout the paper.

Let us consider the dynamic system described in section 3.1: a molecule, depending on its diffusion coefficient, dwells a certain amount of time in the laser focus, during this period, depending on the inter-conversion rate constants, it will switch a certain number of times between the two states. Depending on the number of these switches, the fluorescence bursts of the inter-converting molecules will show a different degree of mixing of the two states, A and B (Fig. 1).

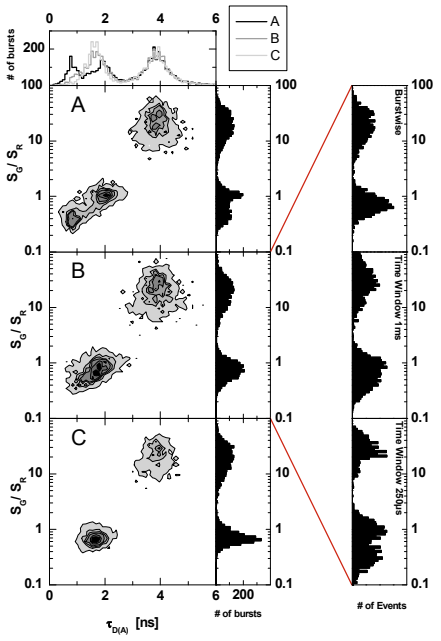

Figure 1. Burstwise analysis of three different dynamic regimes, **A)** $k_A = k_B = 0.1 ms^{-1}$, **B)** $k_A = k_B = 1\ ms^{-1}$, **C)** $k_A = k_B = 10\ ms^{-1}$. For each case green to red fluorescence intensity ratio, S_G/S_R, is plotted against the lifetime of the donor in presence of the acceptor, $\tau_{D(A)}$. On top of each 2D-plot is reported the histogram of $\tau_{D(A)}$, while on the right the S_G/S_R histograms of the three cases are overlaid. **Figure 2**. Effect of the application of TW of different length on the S_G/S_R histogram. In panel A the burst is considered as a whole, burstwise analysis, while in

panels B, C and D the burst has been divided in TW of 1ms, 500μs and 250μs respectively. The green dashed line represent the average S_G/S_R that can be devised from burstwise analysis while the red dashed lines indicate the S_G/S_R value of state A and B.

The three cases shown in Fig 1 represent the different kinds of time-averaging experimentalist encounter in the everyday life laboratory experience, but for the dynamic-PDA analysis they can be reduced to the same, or very similar, condition.
Let us focus our attention on the middle panel. If we take the full photon trace and we divide it in bins of equal length, time window (TW), depending on the duration of each TW we will have:

It is clear that the shorter the time window the more separated the peaks are. Choosing the appropriate TW length we will end up in a situation in which the histograms resemble the situation of panel A of Fig 1. With this we want to point out that in dynamic-PDA what really matters is the ratio between rate constants and the time windows. Of course the time windows have their limits, they cannot be indefinitely small because we will not have enough photons to have a good statistics, nor indefinitely long because when the time window approaches or exceed the diffusion time we will have problems in the estimation of the rate constants (see section 4.4). Fig 2 is also good to show qualitatively how the dynamic-PDA works. Here in fact we see again how the histograms give a signature of the states in which the molecules are. By comparing the different panels of Fig 2 it is possible to have a qualitative estimation of the rate constants and these have been done in the syntaxin paper.
The second dimension of fluorescence histograms in Fig 1, the apparent donor lifetime, could be also exploited. Figure 2 makes it clear that mixing of populations produce a deviation from expected correlation between fluorescence intensities of the donor and the acceptor (F_D and F_A, respectively), and the donor lifetime in the presence of FRET (τ)

$$E = \frac{F_A / \Phi_{FA}}{F_D / \Phi_{FD(0)} + F_A / \Phi_{FA}} = 1 - \frac{\tau}{\tau_0} \qquad (9)$$

In eq 9, τ_0 stands for the lifetime of the donor in absence of FRET. The origin of this deviation is in the different averaging of intensity parameters (E, F_D/F_A, or S_G/S_R) and apparent lifetime. The observed FRET efficiency E corresponds to the species-averaged one (eq 1). In case of multi-exponential fluorescence decay of the donor, τ in eq 9 has also a

meaning of species-average lifetime. On the other hand the maximum likelihood estimator (MLE) [ref] commonly used to estimate lifetimes within fluorescence bursts provides approximately the fluorescence-weighted average lifetime, $\langle \tau \rangle_f$ (eq 9)

$$\langle \tau \rangle_f = \frac{x_A \tau_A^2 + (1 - x_A)\tau_B^2}{x_A \tau_A + (1 - x_A)\tau_B} \tag{10}$$

In eq 10, τ_A and τ_B denote the lifetimes of the donor in the presence of FRET, in states A and B, respectively ($E_A = 1 - \tau_A/\tau_0$; $E_B = 1 - \tau_B/\tau_0$), and $x_A = T_A/\Delta t$. As shown in Fig. 2, lifetimes determined by MLE follow an "alternative" line described by eqs 1 and 10. It is also clear from Fig 2 that averaging regimes described by eqs 1 and 10 are significantly different, which results in deviations from well-known eq 9 if mixing of states occurs (Fig 2). Shifts towards longer lifetimes can thus be considered as another qualitative indication of the presence of FRET fluctuations.

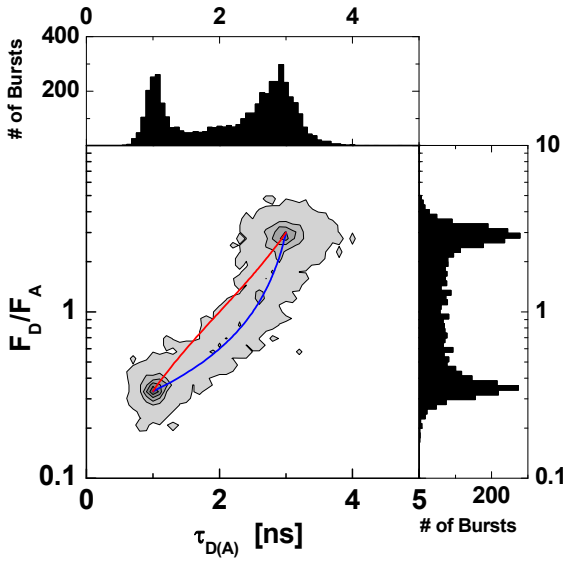

Figure 2. Correlation between the donor and acceptor signal intensity ratio and the apparent donor lifetime, in the presence of interconversion of states. Red solid line represents the correlation expected in the absence of state mixing, given by eq 9. Blue line shows the dependence given by eqs 1 and 10.

4.2 Distinguishing between a static and a dynamic system

Unfortunately, a possibility to fit the dynamic model (eqs 1-4) to the data does not prove the presence of dynamics. In other words, for any fixed time window it is possible to find also a static distribution $P(E)$ (or an equivalent distribution of distances) which would adequately describe the data, for example, by using model-free deconvolution [mix-PDA]. In particular, in the case of fast interconversion rates the distribution given by eq 3 can be very well approximated by a Gaussian distribution. One could argue that an evidence for the dynamical behavior of the system must be provided before fitting the model (eqs 1-4) to the data.

We will make use of the obvious fact that for a static system, the $P(E)$ distribution is independent of the time window length. On the other hand, fluctuations on the timescale of selected time windows (typically ms) produce such dependence (see eqs 1-4 and Fig 1). Thus, to distinguish between a static and a dynamic system, one could try to fit the experimental data using the same static model distribution $P(E)$ for a set of time windows of different length. As shown below, it is impossible to fit a dynamic data set using the same static $P(E)$ for all Δt-values (and vice versa), which allows one to judge whether any processes leading to FRET fluctuations on millisecond timescale take place.

Fitting of a single data set being cut into time windows of different length is illustrated in Fig 3. Using Δt = 1 ms (Fig 3A), fitting the dynamic model (eqs 1-4) yields E_A = 0.252, E_B = 0.747, k_A = 0.87 ms^{-1}; k_B = 0.89 ms^{-1}; 40.8% of D-only species; χ_r^2 = 1.19. However, the same histogram can be equally well fitted with a static model (for example, four static states, see Fig 3 legend; χ_r^2 = 1.20). Thus, dynamic-PDA using a single time window does not allow us to judge whether our system undergoes conformational dynamics, or a static model is more relevant (Fig 3A). To distinguish between these cases, we keep the recovered model parameters constant and try to approximate the same data but using Δt = 0.3 ms. As shown in Fig 3B, this results in a dramatic difference in the fit quality of the dynamic and the static models. Misfit of the static model yielding χ_r^2 = 58 clearly indicates the presence of FRET fluctuations on the timescale of milliseconds and allows one to rule out the static distance distribution model.

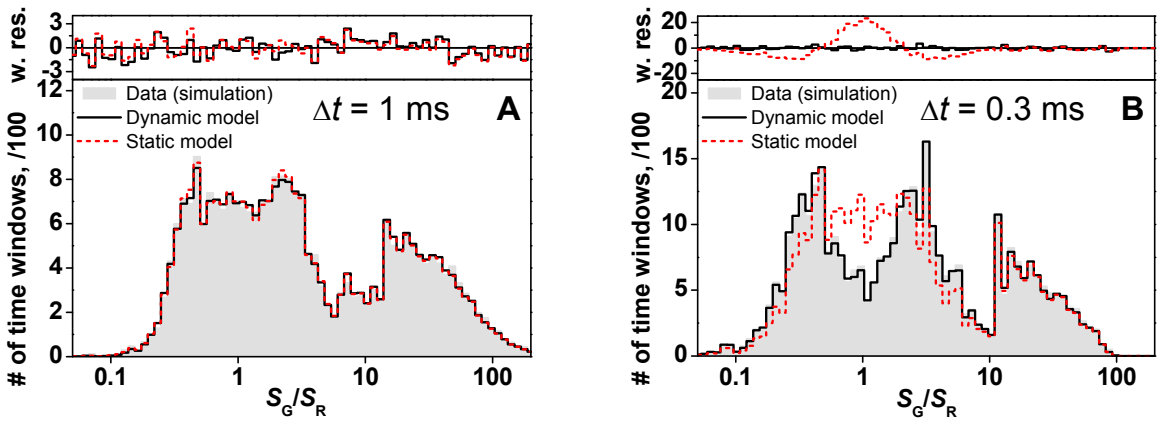

Figure 3. Global fit of S_G/S_R histograms obtained for a simulated dynamic system (grey area), using two-state dynamic (solid black lines) and static (dashed red lines) models. Time window duration Δt is (**A**) 1 ms and (**B**) 0.3 ms. Reduced χ^2-values are 1.19 (Δt = 1 ms, dynamic model; k_A = 0.89 ms^{-1}; k_B = 0.87 ms^{-1}), 1.20 (Δt = 1 ms, static model), 1.43 (Δt = 0.3 ms, dynamic) and 58 (Δt = 0.3 ms, static). Weighted residuals plots are displayed above main graphs. Simulation parameters are E_A = 0.25, E_B = 0.75, k_A = k_B = 1 ms^{-1}; 40% of D-only species; N_{FCS} = 0.002. Static model used to fit the data needs four states: D-only (40.2%), two Gaussian distributions of distances with $\langle R_1 \rangle = 1.18R_0$, $\sigma_1 = 0.03R_0$ (18.3%) $\langle R_2 \rangle = 0.98R_0$, $\sigma_2 = 0.09R_0$ (27.6%), and one state with fixed $R_3 = 0.84R_0$ (13.9%) (R_0 stands for the Förster radius). These parameters are given only to demonstrate the possibility to fit a static model to dynamic data and otherwise have no meaning.

4.3 Quantitative dynamic-PDA

Knowing that the system of interest exhibits conformational dynamics and the model (eqs 1-4) is applicable the interconversion rates can be extracted from the data by fitting the corresponding PDA histograms. In this section we investigate mainly the stability of dynamic-PDA as a quantitative method and the influence of the time window length on its accuracy.

The results of re-analysis of the simulated data are summarized in Fig. 4 (see also Table S1, SI). As expected, maximum accuracy is achieved when the time window duration Δt is comparable with the relaxation time $(k_A + k_B)^{-1}$, which essentially means that the molecules

undergo a few transitions during the observation time. Otherwise the histogram peaks are either completely separated or completely merged yielding the weighted average of E_A and E_B. The shape of S_G/S_R-histograms is thereby practically independent of the rates (Fig 1B), making it impossible to determine their exact values. Thus, the range of measurable k_A and k_B values depends on the time window length Δt, which is in turn limited by the diffusion time and low photon numbers for short time windows. In general, by choosing optimal Δt, rate constants on timescale of $0.1\Delta t$ to $10\Delta t$ can be recovered with a reasonable accuracy, as shown in Fig 4. Qualitatively, dynamic behavior can be detected outside this region. For the data shown in Fig. 4, meaningful qualitative results could be expected in the range of $0.03\Delta t$ to $30\Delta t$.

Another expected result is that *random* errors (shown as error bars in Fig 4) become smaller for longer time windows, which contain large number of photons. This observation is fully consistent with our previous results on detecting heterogeneities by PDA [anisotropy-PDA], clearly showing the advantages of using long time windows for resolving multiple states. The same holds for the qualitative analysis: for example, for $k_A = k_B = 0.03$ ms^{-1} and $\Delta t = 0.3$ ms zero rates are within statistical uncertainty (Table S*), whereas using $\Delta t = 3$ ms allows one at least to detect the presence of FRET fluctuations.

Instabilities in the range of high interconversion rates (cf. Fig 4) appear to be mainly due to a cross-correlation between the fitted rates and efficiencies E_A and E_B. Fixing the values of E_A and E_B significantly improves the precision of dynamic-PDA, especially in the range of fast dynamics (see Fig 4 inset). In practice an independent estimation of the individual FRET efficiencies could be possible if the system can be "locked" in one or both states.

In addition, systematic deviations of the recovered rates from the simulated values are observed. The most obvious effect (see Fig. 4) is a considerable systematic underestimation of the rates when using long time windows. We believe that this effect is mainly due to shortening of the effective observation time due to diffusion on Δt-timescale, as discussed in the following section.

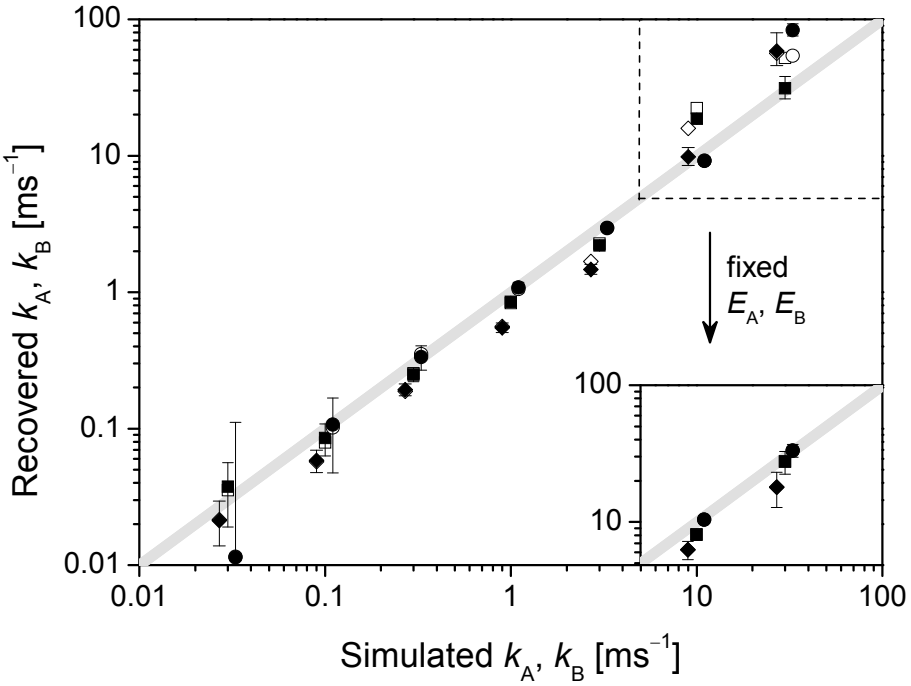

Figure 4. Interconversion rates k_A and k_B recovered by dynamic-PDA, plotted against their simulated values. Time window lengths are 0.3 ms (circles), 1 ms (squares) and 3 ms (diamonds). Full and empty symbols represent k_A and k_B values, respectively. Inset: the values of E_A and E_B have been fixed in the analysis. The diffusion time is t_D = 3 ms. Grey area indicates the region of calculated rate constants being within ± 10% of the simulated values. Error bars represent expected confidence intervals calculated from k_A vs. k_B χ^2-surfaces, which does not necessarily reflect cross-correlation between all model parameters. Other simulation parameters: E_A = 0.25, E_B = 0.75, 40% of D-only species; total N_{FCS} = 0.002. The total number of photons is 3×10^7, which corresponds to ca. 3×10^4 useful 1 ms time windows. Data for this figure are presented as a table in the supplement (Table **). A series of simulations with $k_A \neq k_B$ revealed no effects specific for this case (data not shown).

4.4 Fast diffusion effects

The theoretical model presented in Section 2 requires that the fluorescence intensity does not change during a time interval Δt. In practice this is not always the case, for two reasons. First, if $Q_A \neq Q_B$, the brightness would obviously change upon an A ↔ B transition. What is more

important, the time window lengths (Δt) used in SM analysis are often comparable with the diffusion time (t_D). As a result, the observation time, or the "effective" time window length becomes shorter than the specified one. This effect may result in a significant underestimation of the interconversion rates if our theory is applied without modifications. The problem is especially pronounced when long time windows are used to study slow dynamics and/or to take advantage of good photon statistics (cf. Δt = 3 ms series shown in Fig. 4).

To illustrate the influence of diffusion on dynamic-PDA we have simulated and re-analyzed a series of data sets using various diffusion times, whereas all other parameters have been kept constant. The results summarized in Fig. 5 clearly support the explanation presented above: dynamic-PDA underestimates the rates unless $\Delta t << t_D$. Strictly speaking, diffusion also leads to a distribution of observation times, which is inconsistent with eqs 1-4 and thereby results in generally higher χ^2-values for long time window series (Table supplement). It is clear that the discussed effects must be taken into account if possible.

Unfortunately, rigorous treatment of diffusion effects for an arbitrary $\Delta t / t_D$ ratio is far from straightforward [Gopich-Szabo] and also implies the exact knowledge of the spatial intensity distribution profile. Moreover, the use of an empirical burst search algorithm may change the distribution of observation times in a completely unpredictable way. To overcome this problem, Gopich and Szabo proposed that one could "impose a sufficiently high threshold to eliminate events where the molecule transiently leaves and immediately re-enters the laser spot". Clearly, applying a strict burst selection algorithm together with a high photon threshold should have a similar effect. Fig 5 makes it clear that, as predicted, restricting the analysis to time windows within intensive bursts reduces diffusion-related systematic deviations significantly. However, random erorrs (shown as error bars in Fig 5) increase, mainly because too many photons are disregarded during burst selection. Moreover, setting high photon threshold may suppress the signal from dimmer states, and at the same time increase the apparent contribution of multimolecular events (see Section 4.6)

In a general case, or if a better accuracy is required, corrections can be obtained by simulations, as follows. The rates recovered from experimental data by using eqs 1-4 are taken as the first approximation, and t_D can be measured by means of FCS. These parameters are used to perform a simulation, which is then re-analyzed in order to estimate to what extent dynamic-PDA is biased by diffusion, at given conditions. Calculated rates are expected to deviate from their simulated values. As discussed before in this section, relative errors of the rate constants show only a weak dependence on the absolute values of k_A and k_B (cf. Fig 5A and 5B). Thus, the ratio between simulated and recovered rates can be used as a correction

factor. In case simulations are impractical we propose also a simple semi-empirical equation (see supplement) which to some extent corrects for the presence of diffusion on Δt-timescale

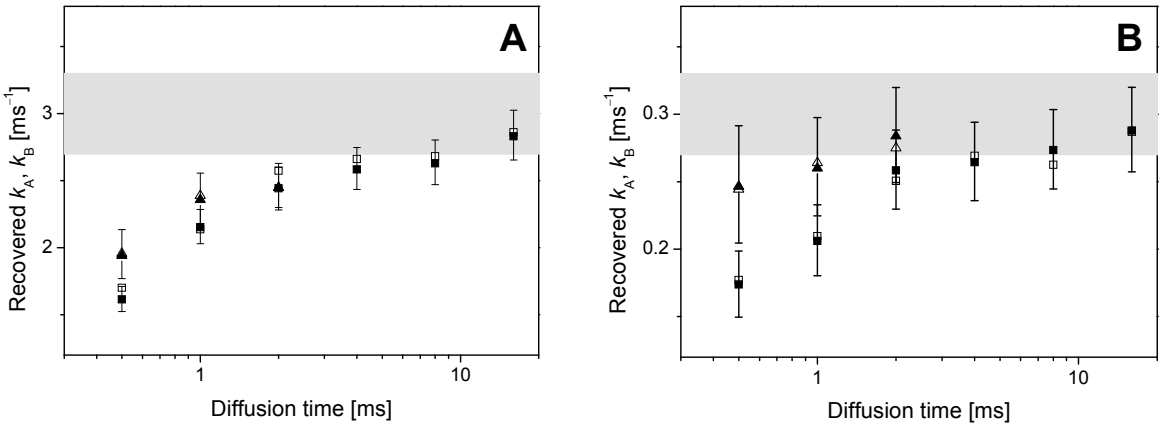

Figure 5. Underestimation of rate constants by dynamic-PDA as a consequence of diffusion on Δt-timescale (here Δt = 1 ms), which results in shortening of the observation time. Two series are simulated with $k_A = k_B = 3$ ms^{-1} (A) and $k_A = k_B = 0.3$ ms^{-1} (B), with the diffusion time varying from 0.5 to 16 ms. Triangles show the results of timewindow analysis within selected bursts. Full and empty symbols represent k_A and k_B values, respectively. Grey area indicates the range of rate constants which differ from their simulated values by no more than 10%. Solid lines show empirical correction described in the supplement. N_{FCS} = 0.002, ca 30000 useful 1 ms time windows.

4.5 Brightness effects

So far we have assumed that the total brightness (i.e. registered donor and acceptor emission) of states A and B is the same. In practice this would rarely be the case because of usually different quantum yields of the donor and the acceptor dyes and wavelength-dependent detection efficiency. This problem manifests itself in two related ways. At first, in this case the average FRET efficiency is not simply a time-weighted average (eq 1), but rather is shifted towards that of the brighter species. Thus, the weights of E_A and E_B become dependent on the corresponding brightness values Q_A and Q_B, leading to eq 2 replacing eq 1. Second,

one cannot use the same (overall) fluorescence intensity distribution $P(F)$ for all species, as discussed in details in ref (Kalinin, Felekyan et al. 2008).

Brightness variations can significantly bias dynamic-PDA if not taken into account, as illustrated in Fig 6. Unlike other artifacts which lead to under- or overestimation of both apparent rates by roughly the same factor (see Fig 5), brightness variations affect also the k_A/k_B ratio, i.e. the equilibrium constant (Fig 6). For a realistic difference in quantum yields (e.g. 0.8 and 0.3, as for the widely used FRET pair Alexa 488 – Cy5) errors in the range of 30 to 50% are expected.

Fortunately a combination of eq 2 and brightness correction methods [mixture-PDA] enables unbiased estimation of interconversion rates irrespective of brightness effects. Fig. 5 clearly shows that corrected k_A and k_B values (shown as circles in Fig 6) can be calculated with the same precision as in the absence of brightness variations (Fig. 4).

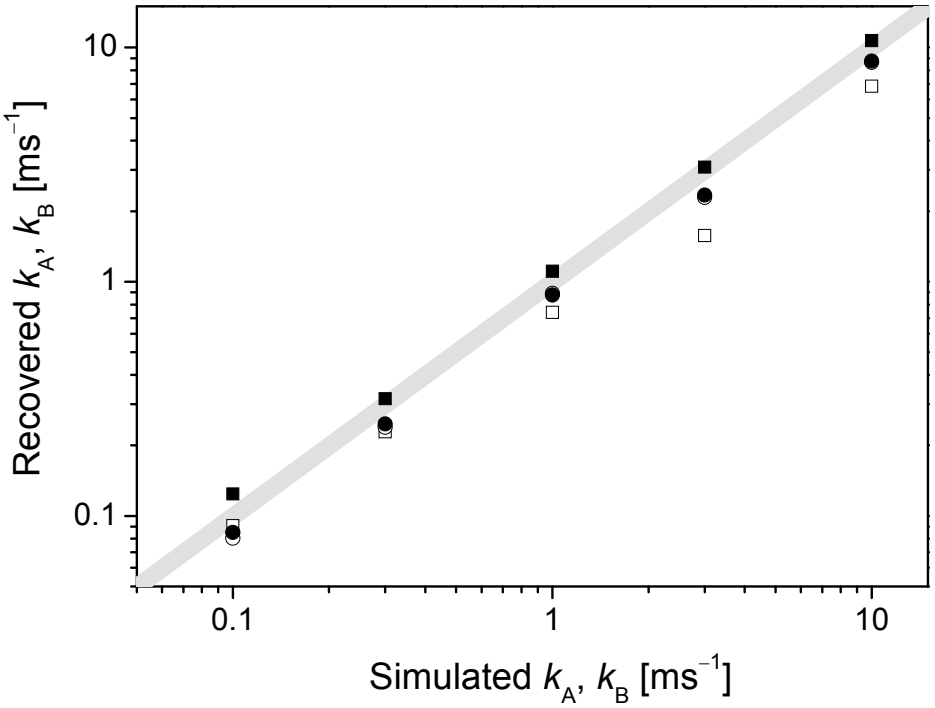

Figure 6. Brightness effects on dynamic-PDA. The brightness of the acceptor is taken to be 0.375 of that of the donor. $E_A = 0.25$, $E_B = 0.75$.

4.6 Multiple molecule events

It has been recently shown that the shape of FRET histograms can be affected by multi-molecular events even at relatively low concentrations, which may lead to severe misinterpretations [new Gopich paper, mix-PDA]. In the case of dynamic-PDA, multi-molecular events build histograms in between major peaks simulating higher rate constants, which makes it important to take these events into account. Clearly, multiple molecule events are expected to have the most pronounced effect on systems showing slow interconversion rates and distant peaks. To study the influence of multi-molecular events on dynamic-PDA, the behavior of such system has been simulated with $E_A = 0.1$, $E_B = 0.9$, $k_A = k_B = 0.1$ ms^{-1}, and varying total concentration.

Surprisingly, multi-molecular events might have a considerable (~ 20%) effect on the recovered rates already at a "typical single-molecule" concentration of $N_{FCS} = 0.01$ (Fig 7). At higher concentrations an overestimation of the rate constants by more than factor of 2 can be expected (Fig 7, squares).

To correct for multi-molecular events we applied the procedure described in [mixturePDA]. As shown in figure 6, this correction yields excellent results also in the case of dynamic states with recovered parameters in good agreement with the simulated ones. "Corrected" rates show no significant dependence on the concentration of the species at least up to $N_{FCS} = 0.1$ (see Fig 7, circles), extending the usable concentration range by an order of magnitude. The possibility to perform measurements at realistic concentrations could help to reduce unwanted contributions of impurities and hardware instabilities.

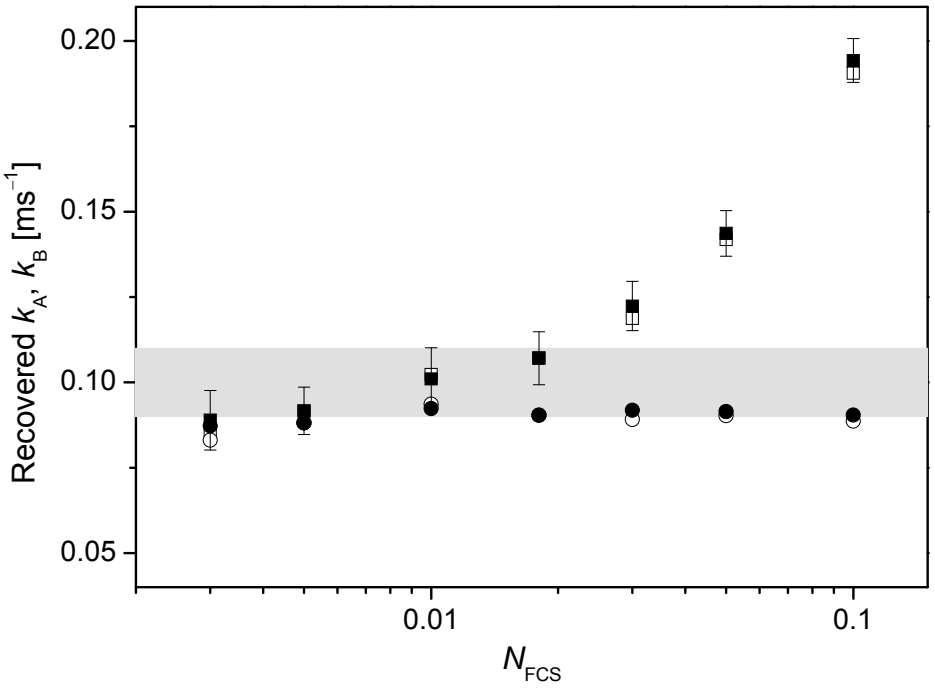

Figure 7. Multiple molecule events correction, the recovered rate constants are plotted as a function of N_{FCS}. Uncorrected rates are shown as squares while corrected ones are shown as circles. Full and empty symbols correspond to k_A and k_B values, respectively. Grey area indicates ± 10% region. $E_A = 0.1$; $E_B = 0.9$; $k_A = k_B = 0.1$ ms^{-1}, no D-only species.

5. Conclusions

With the present work we showed how PDA theory can be extended to dynamic cases. With the help of simulations we were able to identify the range of applicability of the method, that is dynamic processes with relaxation times 0.1 to 10 times the selected TW, where the time windows lower limit is defined by the photon statistic and the upper limit by the diffusion time. Furthermore in this work we presented correction methods to account for different brightness of the states and occurrence of multi-molecular events. Finally the results reported in this paper show how dynamic PDA complements FCS in all those cases in which the dynamic term would be superimposed to the diffusion time in the correlation.

6. References

Antonik, M., S. Felekyan, et al. (2006). "Separating structural heterogeneities from stochastic variations in fluorescence resonance energy transfer distributions via photon distribution analysis." Journal of Physical Chemistry B **110**(13): 6970-6978.

Fries, J. R., L. Brand, et al. (1998). "Quantitative identification of different single-molecules by selective time-resolved confocal fluorescence spectroscopy." Journal of Physical Chemistry A **102**: 6601-6613.

Gopich, I. and A. Szabo (2005). "Theory of photon statistics in single-molecule Förster resonance energy transfer." Journal of Chemical Physics(122): 014707.

Kalinin, S., S. Felekyan, et al. (2007). "Probability distribution analysis of single-molecule fluorescence anisotropy and resonance energy transfer." Journal of Physical Chemistry B **111**(34): 10253-10262.

Kalinin, S., S. Felekyan, et al. (2008). "Characterizing Multiple Molecular States in Single-Molecule Multiparameter Fluorescence Detection by Probability Distribution Analysis." Journal of Physical Chemistry B **112**(28): 8361-8374.

Lakowicz, J. R. (1999). Principles of Fluorescence Spectroscopy. New York, Kluwer Academic/ Plenum Publishers.

Magde, D., E. L. Elson, et al. (1972). "Thermodynamic fluctuations in a reacting system - measurement by fluorescence correlation spectroscopy." Physical Review Letters **29**: 705-708.

Nir, E., X. Michalet, et al. (2006). "Shot-noise limited single-molecule FRET histograms: Comparison between theory and experiments." Journal of Physical Chemistry B **110**(44): 22103-22124.

Widengren, J. and Ü. Mets (2002). Conceptual Basis of Fluorescence Correlation Spectroscopy and Related Techniques as Tools in Bioscience Single Molecule Detection in Solution: Methods and Applications. C. Zander, J. Enderlein and R. A. Keller**:** 69-120.

Appendix: Derivation of equation 3

There is a finite probability that the molecule spends the entire time window in state A or B, i.e. $T_A = \Delta t$ or $T_B = \Delta t$. This probability is given by a simple exponential decay. Otherwise, two cases can be described: one where the molecule ends the time window in the opposite state as which it began (i.e. beginning in A and ending in B), in which case there will be n occurrences of both states, and another case where the molecule ends the time window in same state as which it began, which implies (n + 1) occurrences of the start/end state and n occurrences of opposite state.

In order to describe these cases mathematically, use of the Erlang probability density function as described by eq A1 will be made.

$$P.D.F.(t) = \frac{k^n t^{n-1} e^{-kt}}{(n-1)!} \tag{A1}$$

Whereas the exponential function describes the likely wait until a single event occurs, the Erlang function describes the likely total wait until a number of events, n, occur, each event having the same rate constant k. By setting n = 1, eq A1 reduces to the exponential probability density function.

The probability $P(T_A,T_B)$ is based on the product of the Erlang density function for T_A and T_B. However the end state, i.e. the state which the molecule occupies as the time window comes to an end, must be treated differently. Including the end state in the Erlang density function would imply that the end state always terminates exactly at the end of the time window, when in fact it can only be said that it persists long enough to reach the end of the time window, but may be longer. Therefore, the end state, which is assumed to have a duration of t_e, is treated as a separate factor in the product and is described by an exponential decay. Assuming the molecule starts in state A and undergoes n switches from and to A, two probability density functions (P.D.F.) can be written:

$$P(T_A, T_B \mid \mathrm{A} \to \mathrm{B}, n) = \int \frac{k_B}{k_A + k_B} \cdot \frac{k_A^n T_A^{n-1} e^{-k_A T_A}}{(n-1)!} \cdot \frac{k_B^{n-1} (T_B - t_e)^{n-2} e^{-k_B (T_B - t_e)}}{(n-2)!} \cdot e^{-k_B t_e} dt_e \tag{A2a}$$

$$P(T_A, T_B \mid \mathrm{A} \to \mathrm{A}, n) = \int \frac{k_B}{k_A + k_B} \cdot \frac{k_A^n (T_A - t_e)^{n-1} e^{-k_A T_A}}{(n-1)!} \cdot \frac{k_B^n T_B^{n-1} e^{-k_B (T_B - t_e)}}{(n-1)!} \cdot e^{-k_A t_e} dt_e \tag{A2b}$$

The first term in the integral describes the probability of a molecule starting the window in state A. In eq A2a, the final state is B, and the duration of the end state, t_e, is a part of T_B. In eq A2b, t_e is a part of T_A. Integrating t_e over the range 0 to T_B or 0 to T_A respectively results in the distributions given in eq A3

$$P(T_A, T_B \mid A \to B, n) = \frac{k_B}{k_A + k_B} \cdot \frac{k_A^n T_A^{n-1} e^{-k_A T_A}}{(n-1)!} \cdot \frac{k_B^{n-1} T_B^{n-1} e^{-k_B T_B}}{(n-1)!} \tag{A3a}$$

$$P(T_A, T_B \mid A \to A, n) = \frac{k_B}{k_A + k_B} \cdot \frac{k_A^n T_A^n e^{-k_A T_A}}{n!} \cdot \frac{k_B^n T_B^{n-1} e^{-k_B T_B}}{(n-1)!} \tag{A3b}$$

Similar equations describing a molecule which begins the window in state B are obtained by switching the A's and B's of eq A3. Summing these four components provides $P(T_A, T_B)$, given that it has switched between the two states n times.

$$P(T_A, T_B \mid n) = \left[\frac{2k_B k_A}{k_A + k_B} \cdot \frac{k_A^{n-1} T_A^{n-1}}{(n-1)!} \cdot \frac{k_B^{n-1} T_B^{n-1}}{(n-1)!} + k_A k_B \cdot \frac{k_B T_A + k_A T_B}{k_A + k_B} \cdot \frac{k_A^n T_A^n}{n!} \cdot \frac{k_B^n T_B^{n-1}}{(n-1)!} \right] e^{-k_A T_A - k_B T_B} \tag{A4}$$

In eq A4, n ranges from 1 to ∞. By replacing n in eq A4 with (n+1) and summing over the range 0 to ∞, eq A4 can be put into the form of a Bessel function of order α (eq A5) with $x = 2\sqrt{k_A k_B T_A T_B}$, leading to the final form of eq A6 (eq 3 in the main text)

$$I_\alpha(x) = \sum_{n=0}^{\infty} \frac{(x/2)^{2n+\alpha}}{n!(n+\alpha)!} \tag{A5}$$

$$P(T_A, T_B) = \left[\frac{2k_B k_A}{k_A + k_B} I_0\left(2\sqrt{k_A k_B T_A T_B}\right) + \frac{k_B T_A + k_A T_B}{k_A + k_B} \cdot \frac{\sqrt{k_A k_B}}{\sqrt{T_A T_B}} I_1\left(2\sqrt{k_A k_B T_A T_B}\right) \right] e^{-k_A T_A - k_B T_B} \tag{A6}$$

Probability Distribution Analysis of a Two-State Interconverting FRET System

Stanislav Kalinin[1], Alessandro Valeri[1], Matthew Antonik,[1,†] Suren Felekyan and Claus A. M. Seidel*

Institut für Physikalische Chemie, Lehrstuhl für Molekulare Physikalische Chemie, Heinrich-Heine-Universität, Universitätsstraße 1, Geb 26.32, 40225 Düsseldorf, Germany

* To whom correspondence should be addressed.
E-mail: cseidel@gwdg.de

† Present address: Department of Physics & Astronomy, The University of Kansas, 1082 Malott Hall, 1251 Wescoe Hall Drive, Lawrence, KS 66045-7582; USA

[1] Contributed equally to this work

S1. Data shown in Fig 3.

Δt = 1 ms

rates, ms^{-1}	E_A	k_A, ms^{-1}	E_B	k_B , ms^{-1}	χ_r^2
0.03	0.749	0.04 ± 0.02	0.250	0.04 ± 0.02	1.02
0.1	0.749	0.09 ± 0.02	0.248	0.08 ± 0.02	0.84
0.3	0.748	0.25 ± 0.03	0.251	0.25 ± 0.03	0.73
1	0.745	0.85 ± 0.06	0.253	0.83 ± 0.06	1.08
3	0.732	2.19 ± 0.14	0.257	2.27 ± 0.15	0.95
10	0.860	18.6 ± 1.7	0.071	22.3 ± 2.0	1.48
30	0.737	31 ± 6	0.103	52 ± 10	0.89

Δt = 0.3 ms

rates, ms^{-1}	E_A	k_A, ms^{-1}	E_B	k_B , ms^{-1}	χ_r^2
0.033	0.749	0.01 ± 0.01	0.251	0.01 ± 0.01	1.08
0.11	0.751	0.11 ± 0.06	0.249	0.10 ± 0.06	1.06
0.33	0.748	0.34 ± 0.07	0.249	0.35 ± 0.07	1.01
1.1	0.748	1.08 ± 0.10	0.248	1.06 ± 0.10	1.07
3.3	0.745	2.97 ± 0.17	0.249	2.94 ± 0.17	0.90
11	0.737	9.2 ± 0.6	0.262	9.2 ± 0.6	0.76
33	0.940	83 ± 9	0.213	54 ± 6	0.86

Δt = 3 ms

rates, ms^{-1}	E_A	k_A, ms^{-1}	E_B	k_B , ms^{-1}	χ_r^2
0.027	0.750	0.02 ± 0.01	0.250	0.02 ± 0.01	1.05
0.09	0.749	0.06 ± 0.01	0.252	0.06 ± 0.01	1.22
0.27	0.748	0.19 ± 0.02	0.254	0.19 ± 0.02	1.35
0.9	0.739	0.55 ± 0.04	0.257	0.56 ± 0.05	1.42
2.7	0.728	1.47 ± 0.12	0.241	1.68 ± 0.13	0.84
9	0.781	9.8 ± 1.5	0.045	15.9 ± 2.4	1.38
27	0.955	59 ± 17	0.062	57 ± 16	1.01

S2. Approximate correction for fast diffusion

We propose a simple approximate correction procedure, which can to some extend reduce systematic errors due to the above mentioned effect, but still extracts all necessary information from measurable parameters. The main idea of this correction is to find a shorter "effective" time window $\Delta t'$, representing the mean observation time, for which the fluorescence intensity is constant and eqs *** are exact. The derivation given below should not be taken too seriously because it involves clear oversimplifications and a few assumptions that are certainly violated. The obtained result can be considered as empirical and used when simulations are impractical.

We consider a step-like fluorescence intensity $F'(t)$, which has the same mean and variance as the normalized experimental fluorescence intensity $F(t)$. $F'(t)$ can be expressed as

$$F'(t) = \Delta t / \Delta t', \qquad 0 \le t \le \Delta t' \tag{S1a}$$

$$F'(t) = 0, \qquad \Delta t' < t \le \Delta t \tag{S1b}$$

It is clear that $\langle F'(t)\rangle = 1$, and the variance of $F'(t)$ is

$$\left\langle F'^2(t)\right\rangle - 1 = \Delta t / \Delta t' - 1 = \left\langle F^2(t)\right\rangle - 1 \tag{S2}$$

Next, we will try to find an approximate expression for $\left\langle F^2(t)\right\rangle$. Let us consider a linear change of the fluorescence intensity with time, for which

$$F(t) = 1 - f + 2ft/\Delta t \qquad (0 \le t \le \Delta t) \tag{S3},$$

where f is a constant, and $\langle F(t)\rangle = 1$. The corresponding variance of the fluorescence intensity is a function of f, given by

$$\left\langle F^2(t)\right\rangle - \left\langle F(t)\right\rangle^2 = \left\langle F^2(t)\right\rangle - 1 = f^2/3 \tag{S4}$$

Now we have to estimate the value of f from measurable parameters. The mean change of fluorescence intensity during the time window can be accessed by FCS. Formal substitution of eq (S3) into the definition of correlation function for $t = \Delta t$ yields

$$G(\Delta t) \equiv \frac{\left\langle F(t)F(t+\Delta t)\right\rangle}{\left\langle F(t)\right\rangle^2} = 1 - f^2 \tag{S5}$$

Assuming that the change of the fluorescence intensity in eq (S3) is solely due to diffusion, only the diffusion term $G_D(\Delta t)$ of the correlation function is relevant. It is given by [ref]

$$G(\Delta t) = G_D(\Delta t) = \left(1 + \frac{\Delta t}{t_D}\right)^{-1}\left(1 + \frac{\omega_0^2}{z_0^2}\frac{\Delta t}{t_D}\right)^{-1/2} \tag{S6}$$

where $1/e^2$ radii of the laser focus in *xy*- and in *z*-direction are denoted by ω_0 and z_0, respectively, and t_D is the diffusion time. By combining eqs S2, S4 and S5 we finally obtain

$$\Delta t'/\Delta t = \left\langle F^2(t) \right\rangle^{-1} = (1 + f^2/3)^{-1} = \frac{3}{4 - G_D(\Delta t)} \qquad \text{(S7)}$$

$G_D(\Delta t)$ is measurable in an FCS experiment.

Correction is achieved simply by multiplying the values of interconversion rates by $\Delta t\ /\Delta t'$, which is equivalent to using the value of $\Delta t'$ (instead of Δt) in eqs ***. As we will show in Section *.* this simple correction works satisfactory at least for $\Delta t\ /t_D < 0.5$ provided that N_{min} is sufficiently high.

For a more general case (or if a better accuracy is required) corrections can be obtained by simulations.

IV

Nucleosome disassembly intermediates characterized by single-molecule FRET

Alexander Gansen*[1], Alessandro Valeri*[2], Florian Hauger[1], Suren Felekyan[2], Stanislav Kalinin[2], Katalin Tóth[1], Jörg Langowski+[1], Claus A: M. Seidel+[2]

1: Abteilung Biophysik der Makromoleküle, Deutsches Krebsforschungszentrum, Im Neuenheimer Feld 580, D-69120 Heidelberg, Germany
2: Lehrstuhl für Molekulare Physikalische Chemie, Heinrich-Heine-Universität, Universitätsstrasse 1, Geb. 26.32, 40225 Düsseldorf, Germany.

+Corresponding authors: J. Langowski: jl@dkfz.de; C. A. M. Seidel: cseidel@gwdg.de

* contributed equally

Abstract

The nucleosome has a central role in the compaction of genomic DNA and the control of DNA accessibility for transcription and replication. To help understanding the mechanism of nucleosome opening and closing in these processes, we studied the disassembly of mononucleosomes by quantitative single-molecule FRET with high spatial resolution, using the SELEX-generated "Widom 601" positioning sequence labeled with donor and acceptor fluorophores. Reversible dissociation was induced by increasing NaCl concentration. At least three species with different FRET were identified: the most stable high-FRET species corresponding to the intact nucleosome, a less stable mid-FRET species which we attribute to a first intermediate with a partially unwrapped DNA, and a low-FRET species characterized by a very broad FRET distribution, representing a highly unwrapped structure formed at the expense of the other two species. Selective FCS analysis indicates that even in the low-FRET state, some histones are still bound to the DNA. The interdye distance of 54.0 Å measured for the high-FRET species is consistent with the known crystallographic structure. A geometric model of the nucleosome disassembly predicts exactly the presence of the observed FRET species and confirms their assignment to two populations in the unwrapping pathway.

1. Introduction

The nucleosome is the basic unit of genome compaction [1,2]. It consists of an octamer of histone proteins around which about two turns of double-stranded DNA are wound. Its detailed structure has been elucidated in crystallographic studies [3-5] down to a resolution of 1.9 Å [6]. Sequence and chemical modifications of the DNA, histone content and posttranslational modifications are responsible for changes in gene activity and exert their action through the structure of the nucleosome.

Central to nucleosomal function is its restructuring during processes that act on DNA, e.g. transcription or replication. Various mechanisms for nucleosome unfolding, unwrapping or repositioning have been proposed[7,8], but so far no direct physical evidence (e.g. detection of intermediate states) exists for any particular one. Here we use Förster resonance energy transfer (FRET) [9] on the single molecule level to collect quantitative structural information that will allow us to elucidate such mechanisms.

FRET between fluorophores attached to sites on the nucleosomal DNA, DNA and histone, or only histone proteins, has been used to quantify nucleosome dynamics [10-13]. Earlier measurements in bulk fluorimetry, e.g., suggested that mononucleosome linker DNA arms s diverge slightly as they leave the histone core [14], which has been confirmed by the crystal structure of the tetranucleosome [5].

While bulk solution FRET is a proven tool for measuring average distances in biomolecules, much more detailed information on the diversity is obtained by analyzing FRET signals from single molecules [15-20]. FRET on surface-tethered nucleosomes was used to unravel spontaneous structure fluctuations [21,22]. Confocal spFRET experiments [23-25] on freely diffusing single nucleosomes established optimum conditions and showed the existence of structural subpopulations.

Beyond the simple determination of FRET efficiencies, many more parameters, such as fluorescence lifetime, anisotropy or burst duration, can be collected simultaneously from a single passage of a molecule through the laser focus. This 'multiparameter fluorescence detection' (MFD) technique together with a quantitative data analysis allows characterizing heterogeneous populations and structural substates in molecules [20,26-29].

Here we have applied MFD to FRET data from mononucleosomes reconstituted from recombinant histones on a 170 bp DNA fragment containing the 601 positioning sequence [30]. Using population-filtered fluorescence correlation analysis, modeling of possible dye positions, and an analysis of salt-dependent nucleosome dissociation, we can unravel intermediates in the dissociation pathway of nucleosomes.

2. Results and Discussion

2.1 Multiparameter analysis detects multiple nucleosomal species. On the DNA used here in nucleosome reconstitution, no energy transfer is expected due to the separation between the donor Alexa488 and the acceptor Alexa594, if the DNA is in the fully extended conformation with a donor-acceptor distance R_{DA}= 306 Å as shown in Fig. 1A. Within intact nucleosomes, when the DNA is wound around the histones, the fluorophores approach each other to less than 70 Å (Fig. 1B), enabling efficient FRET.

For single-molecule experiments, mononucleosome solutions less than 50 pM were made by diluting a 50 nM stock solution into the measurement buffer with NaCl concentrations as denoted. After mixing, data were taken for more than 1 hour at each buffer condition for analyzing the sample by single-molecule counting. Labeled molecules diffusing through a confocal detection volume generate brief bursts of fluorescence during the diffusion time (approx. 3.5 ms). These single-molecule events, which were selected from the signal trace using defined threshold criteria (see SI section 2.1), were used to determine signal intensities

(S), lifetimes (τ), and anisotropies (r) of both the donor (D) and acceptor (A) probes. Two-dimensional frequency histograms of the ratio of the donor and acceptor signal intensities (S_G/S_R), against donor lifetime in the presence of acceptor ($\tau_{D(A)}$) are presented in the left panel of Fig. 2A and B. The number of molecules (fluorescent bursts) in each bin is grey scale colored from white (lowest) to black (highest). The corresponding one-dimensional parameter histograms are given as projections. To check the stability of the sample, S_G/S_R is plotted against measurement time in the right panel of Fig. 2A and B.

Three populations with distinct fluorescence properties are immediately distinguishable in Fig. 2A. One small population is characterized by signal ratio, S_G/S_R, and donor lifetime, $\tau_{D(A)}$ similar to those of free donor dye ($S_G/S_R > 3$ and $\tau_{D(A)} \approx 4$ ns). It displays little or no FRET and will be referred to in the text as Low-FRET and D-Only (*LF+DOnly*) (for details see section 2.2). The other two major populations overlap and display higher fluorescence of the acceptor (i.e. smaller S_G/S_R), and shortening of the donor lifetime. These species are FRET-active and will be referred to as Mid-FRET (*MF*) ($S_G/S_R \approx 1.2$ and $\tau_{D(A)} \approx 2.9$ ns) and High-FRET (*HF*) ($S_G/S_R \approx 0.6$ and $\tau_{D(A)} \approx 2.2$ ns). On the basis of the structure in Fig. 1B we may assign *MF* and *HF* to conformations in which the DNA is wrapped around the histones and *LF* to species where the DNA fragment is more extended.

At low salt concentration (Fig. 2A), the majority of detected events showed FRET and the populations remained stable during the experiment, demonstrating good sample integrity and negligible photobleaching. Sample adsorption on the cover slip was insignificant over the whole period of 1 hour as indicated by a constant detection rate of individual nucleosomes. However at 50 mM NaCl (Fig. 2B), a large fraction of the FRET population converts into *LF* (see below).

For a more detailed FRET analysis the efficiency E must be calculated from the measured signal (S), which has to be corrected for mean background signal, spectral crosstalk,

direct acceptor excitation and detection efficiencies (see supplementary information (S.I.),section 2.1). For a direct proof that the observed signal changes are due to differences in E and not due to random local quenching interactions, more than only the fluorescence intensities are needed. Therefore a 2D frequency histogram of E is plotted against donor fluorescence lifetime in the presence of acceptor ($\tau_{D(A)}$) for 5 mM NaCl (Fig. 2C, upper panel) to demonstrate that the experimental data follow the theoretical relationship between $\tau_{D(A)}$ and E (red line) expected for purely FRET-related D quenching. Moreover, this analysis shows that the two species of interest (*MF* and *HF*), both centered on the red line, differ in their FRET value, because any non-FRET related influence on the D and A fluorescence would result in shifts from this line (see S.I, section 2.2).

FRET efficiencies are also affected by the relative orientation factor (κ^2) between the two fluorophores, which is included in the Förster radius (R_0). To justify dynamic isotropic averaging of donor and acceptor dipole moments, which results in a mean orientation factor $\kappa^2 = 2/3$ [31], the anisotropies of the fluorophores were analyzed. The lower panel of Fig. 2C shows the anisotropy (r_D) of the donor against $\tau_{D(A)}$. All donor populations are centered along the red line calculated from the Perrin equation for a mean donor rotational correlation time (ρ_D) of 1.16 ns. Compared to free DNA with $\rho_D = 0.63$ ns [31] this increase is small. The assumption that κ^2 equals 2/3 is also supported by the model for the sterically allowed positions of the donor and acceptor fluorophores obtained by MD simulations (Fig. 1B) [31] of free DNA. We estimated that 7.4 % of all donor and 39 % of all acceptor dye positions - accessible in free DNA - are blocked by the proximity of the histones. With the transition dipole moments of the remaining dye positions we computed $\kappa^2 = 0.65$, a value close to that of mobile dyes attached to free DNA ($\kappa^2 = 0.67 \pm 0.01$) which justifies to assume an isotropic FRET average ($\kappa^2 = 0.67$). The corresponding analysis of acceptor anisotropy also reveals a single dye population (see S.I; S.Fig. 8). To conclude, the multiparameter analysis proves that

the differences in E are due to distinct DA-distances and are not caused by any orientation or quenching artifact.

2.2 Nucleosomes show subpopulations with distinct dissociation properties at low salt concentration and pM dilution. Previous work showed that nucleosome complexes tend to dissociate both at higher salt concentration and at small nucleosome concentrations. While this fact is documented [21,24,25,32], so far no analysis exists describing potential conformational changes and intermediates upon nucleosome destabilization. To address this question in detail we performed Ångström-resolution FRET analysis by probability distribution analysis (PDA) of the photon counts as described earlier [33-35].

The statistical properties of the FRET efficiency histogram are affected by shot noise due to the statistical nature of photon detection, and by other sources of dynamic or static heterogeneity. Using the single-molecule advantage with a minimal mixing of species and a unique exact description for the theoretical shot noise distribution, PDA describes the shot noise free, "true" fluorescence signal distribution, which allows us to fit FRET efficiency histograms without prior assumptions even for complex biomolecular samples such as mononucleosomes.

As a first step we analyze the nucleosome dissociation at 25 mM NaCl concentration. To minimize statistical uncertainty we combine all bursts of a one-hour measurement in a single PDA analysis (Fig. 3A). Judging the quality of the fit by the reduced chi square χ_r^2 and weighted residuals (for more details see supplementary information, section 2.3), PDA showed unambiguously that actually four species are needed to describe the data properly. Moreover, a fixed DA distance for each FRET species is not sufficient, so that Gaussian distance distributions had to be used to fit the data. This deconvolution yielded a mean interdye distance (R_{DA}) and a distribution half-width for each species. Statistical uncertainties were calculated from χ_r^2 surfaces (Fig. 3E) and are given as 1σ standard deviation. At 25 mM NaCl the R_{DA} values and standard deviations were 54.0 ± 0.4 Å and 63.1 ± 0.4 Å for the *HF*-

(red) and the *MF*-species (orange), respectively. The half-widths (HW) and standard deviations of 3.0 ± 0.3 Å are essentially identical for both species.

Moreover, PDA clearly shows that the broad population close to zero FRET efficiency consists of two species: (I) a very broad distribution of molecules with donor and acceptor showing low to very low FRET (referred to as Low-FRET (*LF*), blue line), and (II) molecules labeled only with a donor (*DOnly*, green line). The two are easily distinguishable, because *LF* had direct acceptor excitation of 3.5% and a mean FRET efficiency ⟨E⟩ = 0.047 whereas *DOnly* had no acceptor signal. For all measurement conditions PDA gave stable *DOnly* fractions with an average fraction $\langle x_{DOnly} \rangle = 0.09 \pm 0.015$ that did not change with time (see below). In contrast, the fraction of *LF* molecules (blue) increased significantly with time at the expense of the FRET species (especially *MF*) as shown for the first and last subset of the one-hour measurement (Fig. 3C, D). However, the DA distances did not change and were also conserved for all NaCl concentrations (see S.I; S.Table 9). To further understand the nature of *LF* molecules, we compared it with free nucleosomal DNA in Fig. 3B. In PDA also a very broad Gaussian distribution with a mean R_{DA} = 103 Å and HW = 18 Å is needed for an appropriate description of free DNA. The shaded area represents the region with high uncertainties for distances $R_{DA} > 2R_0$. Therefore the only relevant contribution to the mean FRET efficiency ⟨E⟩ of 0.047 originates from the tail of the Gaussian distribution towards higher E (up to E = 0.5) (see S.I; S.eq. 13 and S.Table 10).

Approximating DNA by the worm-like chain model (see S.I., section 3.3 with S.eq. 20) a single average FRET efficiency of only $\langle E \rangle \cong 0.01$ would be expected due to fast bending motions in the micro- to millisecond range [36]. However, our FRET analysis shows the existence of broadly distributed nucleosomal DNA species which are at least stable for the millisecond dwell time in the confocal observation volume. Even if the majority of DA-distances of nucleosomal DNA is larger than 100 Å, a significant fraction of smaller DA-distances exist which we attribute to preexisting sequence dependent bending or higher

bendability in the nucleosomal DNA [37]. The fact, that the same *LF* species are also formed by disassembly of nucleosomes, indicates extensive histone dissociation under the single molecule conditions of higher salt concentration (for more experimental results see section 2.5).

Finally we checked whether the broadening of the FRET distribution was due to dynamical changes between substates during the passage of the nucleosome through the observation volume. Therefore we performed PDA with time windows of different length of 1 and 3 ms (see S.I; S.Fig. 2) using a model consisting of only static distributions. Independent of the time window used, we obtained the same fit results, implying that the four populations did not change during the millisecond dwell time.

2.3 The relative stability of nucleosome subspecies depends on NaCl concentration. The time course of the relative occupancy of the three double labeled DA populations for different NaCl concentrations is plotted in Fig. 4A. At 5 mM NaCl both *HF* and *MF* populations remained stable over time, but at higher salt their proportions dropped significantly, most pronounced for the *MF* species. This implies that the *HF* species is considerably more stable. The full lines describe the interconversion using a model with first order decays for the *HF* and *MF* species linked to a growth term for the *LF* species. A global fit to all time points yields apparent relaxation times for *HF* and *MF* FRET subpopulations of the order of 700 to 1000 seconds for all conditions (for details on the procedure and results see S.I, section 3.4 S,eq. 21 and S.tables 11 and 12). NaCl concentrations above 100 mM NaCl destabilized the samples such that single molecule experiments became impossible.. A similar dissociation occurred when we added 2 mM $MgCl_2$ to the buffer solution (data not shown).

The extrapolation to time zero gave stable average fractions of 0.29 ± 0.05, 0.42 ± 0.09, 0.21 ± 0.07 and 0.08 ± 0.02, respectively, for the *HF*, *MF*, *LF* and *DOnly* species, consistent with the fact that the same nucleosome stock solution was used for all salt concentrations.

We note that at medium NaCl concentrations the FRET populations did not drop to zero even during one hour, suggesting that these species approached a reversible equilibrium with *LF*. Fig. 4B summarizes the equilibrium fractions for all three DA species (obtained from global fit as a function of NaCl concentration). While at low salt concentrations destabilization is observed preferentially for the *MF* species, above 25 mM an additional dissociation of the *HF* species takes place.

2.4 The high FRET species represents the intact nucleosome. To obtain a structural model of the FRET subpopulations, we determined all possible positions that donor and acceptor dye may occupy when they are attached to the nucleosomal DNA via a flexible C6-linker. For the nucleosome the crystal structure 1KX5 was used as a model (only the histone core is considered while lateral chains extending over the DNA were cut). The sterically allowed positions of the donor and acceptor fluorophore on B-DNA were taken from Wozniak et al [31]. The aligned dye clouds were further adapted to the sterically allowed space by excluding all dye positions within a 4 Å thick surface layer on the histone core. Fig. 1B shows different views of the nucleosome with green and red clouds defining the accessible space of the fluorophores. The distance between the mean dye positions R_{mp} in the structural model is 58.6 Å with mean position FRET efficiency E_{mp} = 0.42. According to section 2.1 our FRET experiments yield an isotropic average FRET efficiency $\langle E \rangle_{iso}$ (see S.I, S.eq. 6), from which an apparent distance $\langle R_{DA} \rangle_{iso}^{exp}$ is obtained. To compare the model with the experiment, we have to use the dye coordinates in our structural model to calculate the mean $\langle E \rangle_{iso}^{model} = 0.41$ with corresponding apparent distance $\langle R_{DA} \rangle_{iso}^{model}$ = 59 Å, which for this special case is very close to R_{mp}. For the *HF* species the PDA derived $\langle E \rangle_{iso}^{exp}$ is 0.55 with a corresponding mean distance $\langle R_{DA} \rangle_{iso}^{exp}$ of 54.0 ± 0.4 Å. We assign the *HF* species to the intact nucleosome, because it has the most compact structure and the highest stability. Considering the *MF*

species the larger interdye distance of 63.1 ± 0.4 Å ($\langle E \rangle_{iso}^{exp}$ = 0.31) and the reduced stability suggest a less compact conformation. Further evidence for this assignment comes from other observations: (1) the stability of the nucleosome species depends also on the absolute nucleosome concentration; (2) modeling of nucleosome disassembly (see section 2.7).

2.5 Nucleosome dissociation does not completely proceed to free DNA. We further analyzed the properties of the *LF* species. It has been postulated that transcription can proceed through a nucleosome without complete histone dissociation [38]. Using FRET alone it is difficult to distinguish between complete and partial dissociation, since in either case the fluorophore separation exceeds the FRET range (> 120 Å). In order to obtain an additional parameter for the analysis, we computed FCS autocorrelation functions on the photon data from the nucleosome experiments and compared them to pure labeled DNA fragments. To remove contributions from scattered light and to separate the FRET species from the *LF+DOnly* population, we extended the theory of Enderlein [39] and applied spectrally resolved fluorescence lifetime filters (S.I. section 2.5, S.Fig. 5A,B) to all photon data. The computed subensemble filtered FCS curves for the nucleosome species are compared to free DNA in Fig. 5A. The FRET subensemble includes the *MF* and *HF* species. The *LF+DOnly* subensemble consists of *LF*, *DOnly* and fluorescent impurities similar to the free donor dye. First of all, we see that at 25 mM NaCl the three species displayed slightly different diffusion times increasing in the order *FRET* (*HF+MF*), *LF+DOnly* and free DNA. In contrast to free DNA, the nucleosomal species display a high-amplitude correlation term on the microsecond timescale. Even though we cannot assign this term to any particular process, we considered it as a signature that indicates that the *LF* species is distinct from free DNA, thus probably still associated with remaining histones.

Studying the NaCl dependence of the diffusion times in Fig.5B, we could refine our view about the different species (zoomed views are shown in S.Fig. 10). The diffusion times of the FRET species (mixture of *HF* and *MF*) stayed constant at all NaCl concentrations suggesting

that the structural features did not change significantly before disassembly. Moreover, the fact that the diffusion times were independent of the relative fractions of *HF* and *MF* (see Fig. 4B) indicated that *MF* has a hydrodynamic shape similar to a complete *HF* nucleosome even though the DNA is more loosely bound. We associated this species with an incomplete nucleosome.

At 5 mM NaCl the *LF+DOnly* subensemble diffuses faster than all other species, including the compact nucleosome. This finding is inconsistent with the notion of an extended DNA structure: due to its larger hydrodynamic radius, a very open 170 bp DNA should diffuse more *slowly* than the nucleosome. Since *LF* becomes the dominant species with increasing NaCl concentration (Fig. 4B), we must conclude that the fast-diffusing contribution at low salt is caused by minor *DOnly* like contaminations that are masked at higher salt by the dissociated nucleosomal DNA. Since the diffusion time of the *LF+DOnly* subensemble approaches that of free DNA for medium salt and slightly exceeds it at high salt, we consequently propose a subspecies lacking histones referred to as broken nucleosome (Fig. 7). At high salt concentrations it is likely that the *LF* populations include also a large fraction of free DNA as the amplitude of the µs bunching term in the autocorrelation function drops continuously.

2.6 A geometric model for nucleosome disassembly explains the broad distribution of FRET species. Nucleosome destabilization at higher salt concentrations and high dilution can be suppressed by adding an excess of unlabeled mononucleosomes (Fig. 6A). At higher nucleosome concentrations the most abundant species is the compact nucleosome which corresponds to the *HF* species (red line in Fig. 6B right histogram); dilution causes an increase of the *MF* species (orange line in Fig. 6B left histogram) without changing the DA distances. A similar redistribution between more closed and opened nucleosome structures as a function of concentration was observed earlier, measuring the distances between dyes positioned at the ends of the same DNA [24]. This confirms the observation in Fig. 4 that a

dynamic equilibrium between different nucleosome species exists where the DNA dissociates stepwise.

Therefore, we established a geometric model based on the crystal structure and the dye positions in Fig 1B to describe the FRET species during nucleosome disassembly (see caption of Fig. 6C, for further details see S.I., section 2.7). In order to compare theory and experiment, FRET efficiency histograms were computed. In the model of the nucleosome with an effective R = 40 Å the nucleosomal DNA (black line) is wrapped around a cylindrical histone core. The discrete model accounts for the fact that DNA dissociates stepwise at defined "contact points" (crossed spheres in Fig. 6) from either end. The nucleotide bases that form contact points are selected according to their proximity to the core. From the X-ray structure 12 contact points C were identified within 4 Å shell from the core (as summarized in S.Table 6). DNA is therefore assumed to dissociate in steps of 10 to 11 basepairs. Detached part(s) of DNA are assumed to be straight and tangential to the nucleosome core at the detachment point(s). For simplicity, all combinations of dissociated contacts of the donor and acceptor arm are considered to be equally probable. There is no doubt that in reality this assumption may be violated. However, this will change only amplitudes but not the positions of the FRET peaks in the histograms. Fig. 6D shows the computed FRET histogram for nucleosome intermediates with partly dissociated DNA, where one to eight contact points are broken; these intermediates are also listed in S.Table 8. Three peaks are clearly visible, for which the predicted FRET efficiencies nicely agree with those values measured for the *LF*, *MF* and *HF* species. If one distinguishes between different numbers of broken contact points, it is evident that for small numbers mainly two narrow distributions of FRET species are expected (Fig. 6E). For a larger number of broken contact points ($C_{broken} > 4$) a broad E distribution is expected ranging from *LF* to *HF* (Fig. 6F). Fig. 7 shows a cartoon of all possible disassembly intermediates based on the geometric model. It turns out that not only the level of FRET efficiency is characteristic but also the width of the individual FRET

distributions. Depending on the progress of disassembly the width of the corresponding FRET efficiency distributions of the species *LF*, *MF* and *HF* can be either narrow (n) or broad (b), i.e. a *HF* signal is not per-se indicative for an intact nucleosome. Thus, the width of the FRET peak, the presence of other FRET species and the measurement conditions are essential to identify the nucleosome species.

Finally it is important to note, that a geometric model with quasi-continuous dissociation steps of one-base size can not reproduce the characteristic E peaks of *LF* and *MF* (see S.Fig. 6).

2.7 The incomplete and broken nucleosome. Besides the prediction of the geometric model there is also multiple experimental evidence that the *MF* species (R_{DA} ~ 63 Å, $\langle E \rangle$ = 0.31) represents an intermediate during the dissociation process, based on the following observations: (I) The increased dissociation rate at higher salt concentration indicates a less stable conformation, (II) under quasibulk conditions this population is only a minor species as compared to the intact nucleosome while at pM concentrations it compries the majority of nucleosomes, (III) the structure is still quite compact with hydrodynamic properties similar to the intact nucleosome (Fig. 5B).

Our data agree with the idea that nucleosome dissociation is initiated by release of an H2A/H2B dimer, probably facilitated by transient unwrapping from one DNA end, a process shown to occur in nucleosomes with apparent lifetimes of the unwrapped state of 100-250 ms [21,22,40]. If during this time the dimer (partially) dissociated from the histone core, a rewrapping of the DNA may be prevented, leaving several tens of basepairs exposed. Assuming that the DNA stays fully attached to the remaining hexamer, the geometric model predicts an average FRET efficiency $\langle E \rangle \cong 0.32$ which is in very good agreement with experimental $\langle E \rangle \cong 0.31$.

A distance change of 9 Å could also result from a simple twist motion of the DNA along the intact octamer by 1 or 2 bp while still forming a closed conformation. Such twist defects are currently discussed as a potential mechanism for mobilization of nucleosomes [41,42]. Such a twisted but closed conformation is likely to have a similar stability w.r.t. salt concentration

and would not account for the observed increased rate of dissociation of the *MF* state. Thus, the reduction of DNA bending due to partial dissociation from the histones is the only feasible way for a limited increase of the DA distance (Fig. 5C).

One possible species of the broken nucleosome may be a tetrasome, where both H2A/H2B are dissociated; the $(H3H4)_2$ tetramer remains attached to the DNA, most likely at the innermost 20-30 bp centered around the dyad axis. Crystallographic data [6] and force rupture experiments [43] showed these sites to harbor the most intense DNA-histone interactions.

Conclusion

By FRET in confocal single molecule detection, we show that mononucleosome populations contain four separable molecular subspecies differing in FRET efficiency (*HF, MF, LF* and D*Only*). An analysis of the salt-dependent stability of the subpopulations allows us to identify these subspecies with steps on the pathway of nucleosome disassembly, which might occur by partial dissociation after opening from one of the linker DNA ends. Such transient opening is also suggested by recent simulations of nucleosome dynamics on a ten-microsecond time scale, using a coarse-grained model developed by one of the authors [44]. While the single-molecule FRET experiments shown here reveal details on the structure of nucleosomes in free solution that could not be achieved by other means so far, these experiments have just opened the route for a much more detailed mapping of nucleosome and chromatin structures, which will be done by labeling histone proteins and systematic variation of label positions.

Materials and Methods

Preparation of labeled nucleosomes. Mononucleosomes were reconstituted by salt dialysis from a fluorescently double labelled 170 bp long DNA fragment containing a positioning

sequence (Selex 601) and recombinant *X.laevis* histones. The labels are positioned at 33 bp (Alexa 594) and 45 bp (Alexa 488) from the both ends: far enough from each other to avoid FRET signal in free DNA and close to each other wound around the histone core in the nucleosome to give a measurable FRET signal. Only samples yielding more than 80% nucleosome were accepted. Details of the preparation and controls can be found in [23] and in the S.I. section1.1

Single-molecule fluorescence spectroscopy. All measurements were performed at 20 °C in TE buffer (10 mM Tris, 0.1 mM EDTA pH=7.5) supplemented with 0.1 g/l BSA, 1 mM ascorbic acid with NaCl concentrations as indicated. Experiments were essentially performed as in [29,45](for details see S.I. section 1.2).

Acknowledgments:

JL and CAMS thank the German Science foundation (DFG) in the priority program "Optical analysis of the structure and dynamics of supra-molecular biological complexes" grant SE 843/9-3 and SFB 590 for funding during this work. The authors also thank Paul Rothwell and Evangelos Sisamakis for helpful discussions and suggestions.

References

1. Olins, A.L. & Olins, D.E. Spheroid chromatin units (v bodies). *Science* **183**, 330-2 (1974).
2. Kornberg, R.D. Chromatin structure: a repeating unit of histones and DNA. *Science* **184**, 868-71 (1974).
3. Richmond, T.J., Finch, J.T., Rushton, B., Rhodes, D. & Klug, A. Structure of the nucleosome core particle at 7 A resolution. *Nature* **311**, 532-537 (1984).
4. Luger, K., Mäder, A.W., Richmond, R.K., Sargent, D.F. & Richmond, T.J. Crystal structure of the nucleosome core particle at 2.8 Å resolution. *Nature* **389**, 251-260 (1997).
5. Schalch, T., Duda, S., Sargent, D.F. & Richmond, T.J. X-ray structure of a tetranucleosome and its implications for the chromatin fibre. *Nature* **436**, 138-41 (2005).
6. Davey, C.A., Sargent, D.F., Luger, K., Maeder, A.W. & Richmond, T.J. Solvent mediated interactions in the structure of the nucleosome core particle at 1.9 a resolution. *J Mol Biol* **319**, 1097-113. (2002).
7. Schiessel, H., Widom, J., Bruinsma, R.F. & Gelbart, W.M. Polymer Reptation and Nucleosome Repositioning. *Phys Rev Lett* **86**, 4414-4417 (2001).
8. Kulic, I.M. & Schiessel, H. Nucleosome repositioning via loop formation. *Biophys J* **84**, 3197-211 (2003).
9. van der Meer, B.W., Coker, G. & Chen, S.Y.S. *Resonance Energy Transfer: Theory and Data*, (VCH, New York, 1994).
10. Lovullo, D., Daniel, D., Yodh, J., Lohr, D. & Woodbury, N.W. A fluorescence resonance energy transfer-based probe to monitor nucleosome structure. *Anal Biochem* **341**, 165-72 (2005).
11. Tóth, K., Brun, N. & Langowski, J. Chromatin Compaction at the Mononucleosome Level. *BIOCHEMISTRY* **45**, 1591-8 (2006).
12. Yang, J.G. & Narlikar, G.J. FRET-based methods to study ATP-dependent changes in chromatin structure. *Methods* **41**, 291-5 (2007).
13. Hoch, D.A., Stratton, J.J. & Gloss, L.M. Protein-Protein Förster Resonance Energy Transfer Analysis of Nucleosome Core Particles Containing H2A and H2A.Z. *J Mol Biol* **371**, 971-988 (2007).
14. Tóth, K., Brun, N. & Langowski, J. Trajectory of nucleosomal linker DNA studied by fluorescence resonance energy transfer. *BIOCHEMISTRY* **40**, 6921-6928. (2001).
15. Ha, T. et al. Probing the interaction between two single molecules: fluorescence resonance energy transfer between a single donor and a single acceptor. *Proc Natl Acad Sci U S A* **93**, 6264-8 (1996).
16. Jia, Y. et al. Nonexponential kinetics of a single tRNAPhe molecule under physiological conditions. *Proc Natl Acad Sci U S A* **94**, 7932-6 (1997).
17. Deniz, A.A. et al. Single-pair fluorescence resonance energy transfer on freely diffusing molecules: observation of Forster distance dependence and subpopulations. *Proc Natl Acad Sci U S A* **96**, 3670-5 (1999).
18. Talaga, D.S. et al. Dynamics and folding of single two-stranded coiled-coil peptides studied by fluorescent energy transfer confocal microscopy. *Proc Natl Acad Sci U S A* **97**, 13021-6 (2000).
19. Schuler, B., Lipman, E.A. & Eaton, W.A. Probing the free-energy surface for protein folding with single-molecule fluorescence spectroscopy. *Nature* **419**, 743-7 (2002).

20. Margittai, M. et al. Single-molecule fluorescence resonance energy transfer reveals a dynamic equilibrium between closed and open conformations of syntaxin 1. *Proc Natl Acad Sci U S A* **100**, 15516-21 (2003).
21. Koopmans, W.J., Brehm, A., Logie, C., Schmidt, T. & van Noort, J. Single-Pair FRET Microscopy Reveals Mononucleosome Dynamics. *J Fluoresc* **17**, 785-95 (2007).
22. Tomschik, M., Zheng, H., van Holde, K., Zlatanova, J. & Leuba, S.H. Fast, long-range, reversible conformational fluctuations in nucleosomes revealed by single-pair fluorescence resonance energy transfer. *Proc Natl Acad Sci U S A* **102**, 3278-83 (2005).
23. Gansen, A., Hauger, F., Toth, K. & Langowski, J. Single-pair fluorescence resonance energy transfer of nucleosomes in free diffusion: optimizing stability and resolution of subpopulations. *Anal Biochem* **368**, 193-204 (2007).
24. Gansen, A., Toth, K., Schwarz, N. & Langowski, J. Structural Variability of Nucleosomes Detected by Single-Pair Forster Resonance Energy Transfer: Histone Acetylation, Sequence Variation, and Salt Effects. *J Phys Chem B* (2008).
25. Kelbauskas, L. et al. Sequence-Dependent Variations Associated with H2A/H2B Depletion of Nucleosomes. *Biophys J* (2007).
26. Eggeling, C., Fries, J.R., Brand, L., Gunther, R. & Seidel, C.A. Monitoring conformational dynamics of a single molecule by selective fluorescence spectroscopy. *Proc Natl Acad Sci U S A* **95**, 1556-61. (1998).
27. Schaffer, J. et al. Identification of Single Molecules in Aqueous Solution by Time-Resolved Flourescence Anisotropy. *Journal of Physical Chemistry A* **103**, 331-336 (1999).
28. Eggeling, C. et al. Data registration and selective single-molecule analysis using multi- parameter fluorescence detection. *J Biotechnol* **86**, 163-80. (2001).
29. Rothwell, P.J. et al. Multiparameter single-molecule fluorescence spectroscopy reveals heterogeneity of HIV-1 reverse transcriptase:primer/template complexes. *Proc Natl Acad Sci U S A* **100**, 1655-60 (2003).
30. Thastrom, A. et al. Sequence motifs and free energies of selected natural and non-natural nucleosome positioning DNA sequences. *J Mol Biol* **288**, 213-29. (1999).
31. Wozniak, A.K., Schroder, G.F., Grubmuller, H., Seidel, C.A. & Oesterhelt, F. Single-molecule FRET measures bends and kinks in DNA. *Proc Natl Acad Sci U S A* **105**, 18337-42 (2008).
32. Claudet, C., Angelov, D., Bouvet, P., Dimitrov, S. & Bednar, J. Histone octamer instability under single molecule experiment conditions. *J Biol Chem* **280**, 19958-65 (2005).
33. Antonik, M., Felekyan, S., Gaiduk, A. & Seidel, C.A. Separating structural heterogeneities from stochastic variations in fluorescence resonance energy transfer distributions via photon distribution analysis. *J Phys Chem B Condens Matter Mater Surf Interfaces Biophys* **110**, 6970-8 (2006).
34. Kalinin, S., Felekyan, S., Antonik, M. & Seidel, C.A. Probability distribution analysis of single-molecule fluorescence anisotropy and resonance energy transfer. *J Phys Chem B* **111**, 10253-10262 (2007).
35. Kalinin, S., Felekyan, S., Valeri, A. & Seidel, C.A. Characterizing multiple molecular States in single-molecule multiparameter fluorescence detection by probability distribution analysis. *J Phys Chem B* **112**, 8361-8374 (2008).
36. Merlitz, H., Rippe, K., Klenin, K.V. & Langowski, J. Looping dynamics of linear DNA molecules and the effect of DNA curvature: a study by Brownian dynamics simulation. *Biophysical Journal* **74**, 773-779 (1998).
37. Ruscio, J.Z. & Onufriev, A. A computational study of nucleosomal DNA flexibility. *Biophysical Journal* **91**, 4121-4132 (2006).

38. Clark, D.J. & Felsenfeld, G. A nucleosome core is transferred out of the path of a transcribing polymerase. *Cell* **71**, 11-22 (1992).
39. Enderlein, J. & Gregor, I. Using fluorescence lifetime for discriminating detector afterpulsing in fluorescence-correlation spectroscopy. *Review of Scientific Instruments* **76**(2005).
40. Li, G., Levitus, M., Bustamante, C. & Widom, J. Rapid spontaneous accessibility of nucleosomal DNA. *Nat Struct Mol Biol* **12**, 46-53 (2005).
41. Flaus, A., Luger, K., Tan, S. & Richmond, T.J. Mapping nucleosome position at single base-pair resolution by using site-directed hydroxyl radicals. *Proc Natl Acad Sci U S A* **93**, 1370-5 (1996).
42. Kulic, I.M. & Schiessel, H. Chromatin dynamics: nucleosomes go mobile through twist defects. *Phys Rev Lett* **91**, 148103 (2003).
43. Brower-Toland, B. et al. Specific contributions of histone tails and their acetylation to the mechanical stability of nucleosomes. *J Mol Biol* **346**, 135-46 (2005).
44. Voltz, K. et al. Coarse-grained force field for the nucleosome from self-consistent multiscaling. *J Comput Chem* (2008).
45. Widengren, J. et al. Single-molecule detection and identification of multiple species by multiparameter fluorescence detection. *Analytical Chemistry* **78**, 2039-2050 (2006).

Figure 1.

(**A**) Nucleosomal DNA in extended conformation. The conformational space of the D and A dyes obtained by MD simulations is shown in green and red respectively. (**B**) Structure of a nucleosome. The first three structures from the left show different views of the nucleosome (crystal structure 1KX5 from the RCSB protein Data Bank, only the histone core is considered while lateral chains extending over the DNA were cut)[6]. The histone octamere is depicted in pink while the nucleosomal DNA duplex is represented in blue colours. The fourth structure of **1B** is an alternative representation of the third view where the dye distributions are replaced by their centers of mass with the corresponding interdye distance. The planes of the nucleotide bases linked to the dyes are depicted in white.

Figure 2.

MFD plots of single nucleosomes at different NaCl concentrations. **(A-B)** Nucleosomes at 5 mM NaCl and 50 mM NaCl. The ratio of the signal in the green channel, S_G, to the signal in the red channel, S_R, is plotted versus lifetime of the donor in presence of the acceptor, $\tau_{D(A)}$, in the left panel, and versus the measurement time in the right panel. **(C)** Nucleosomes at 5 mM NaCl. In the upper panel, FRET efficiency is plotted versus lifetime of the donor in presence of the acceptor, $\tau_{D(A)}$. FRET efficiencies obtained from raw signals S by correcting for green and red background (B_G = 2.3 kHz, B_R = 1.2 kHz), spectral crosstalk (α = 0.07), detection efficiencies (g_G / g_R = 0.58), direct excitation of the acceptor (DE = 1.35 kHz), quantum yield of the donor in the absence of the acceptor ($\Phi_{FD(0)}$ = 0.70) and quantum yield of the acceptor (Φ_{FA} = 0.70) (see supplementary information, Eq.6b). The red overlaid line is calculated from the empirical equation $E = 1-(0.00479+0.4813\tau_{D(A)}+0.26694\tau^2_{D(A)}-0.03435\tau^3_{D(A)}) / \tau_{D(0)}$, where $\tau_{D(0)}$ = 4.1 ns is the donor lifetime in absence of acceptor, the equation is a modification of the theoretical equation $E = 1- \tau_{D(A)} / \tau_{D(0)}$ and is needed to take into account the dye movement due to the flexible alkylchains in the linkers (SI section 2.2). In the lower panel, donor

anisotropy, r_D, is plotted versus donor lifetime, $\tau_{D(A)}$, together with an overlaid curve computed from the Perrin equation $r_D = r_0 / (1+\tau_{D(A)} / \rho_D)$, using a value for fundamental anisotropy of $r_0 = 0.37$ and a mean rotational correlation time, ρ_D, of 1.16 ns.

Figure 3. Stability of *HF* and *MF* species. PDA of the FRET efficiency of nucleosomes at 25 mM NaCl (**A**, complete measurement of 3840 seconds, **C**, first 306 seconds, **D** last 206 seconds) and free DNA in 5 mM NaCl **(B)** with the data histogram (grey) obtained using time intervals of 3 ms. The black bold line is the fit to a four state model accounting for *HF*, *MF*, *LF, DOnly* (red, orange, blue and green line, respectively). The fit includes also corrections for the simultaneous transit of more than one molecule in the detection volume (contribution not shown, for details see supplemental Fig. 2). Weighted residuals of the fit are displayed on top of each *E* histogram. One-σ standard deviations were determined by reduced chi-square surfaces. Using Gaussian distributions for the FRET species the following mean distances R_{DA}, half widths HW and fractions x_i have been obtained. The corresponding DA distance distributions of the *HF* and *MF* populations are displayed in the right sub-panel.
(A): *HF* (R_{DA} = 54.0 ± 0.4 Å, HW = 3.0 ± 0.3 Å, x_{HF} = 0.26 ± 0.03), *MF* (R_{DA} = 63.1 ± 0.4 Å, HW = 3.2 ± 0.3 Å, x_{MF} = 0.19 ± 0.03) and *LF* (R_{DA} = 119 ± 2 Å, HW = 31± 2 Å, x_{LF} = 0.47 ± 0.04). The *DOnly* species is described by E = 0 and x_{DOnly} = 0.08 ± 0.01. The residuals of the fit to a 3 and 4 state model are shown for comparison. **(B):** Free DNA was fitted with a simple two-state model consisting of *D-only* and *LF*: *LF* (R_{DA} = 103 Å, HW = 18 Å, x_{LF} = 0.89). The *DOnly* species is described by E = 0 and x_{DOnly} = 0.11. In panel B the shaded area represent the distances $R_{DA}>2R_0$. **(C and D):** For the fit of time segments mean distances and half widths were fixed to the values obtained for the complete measurement and only the fractions were allowed to vary: (C) x_{HF} = 0.29, x_{MF} = 0.35, x_{LF} = 0.27, x_{DOnly} = 0.09, (D) x_{HF} = 0.24, x_{MF} = 0.15, x_{LF} = 0.56, x_{DOnly} = 0.05. **(E)** Reduced chi-square surfaces for the PDA fit in panel A. In these plots reduced chi-square is plotted as a function of two fit parameters at the

time. The red lines delimit 68 % confidence intervals (corresponding to 1σ), that is, where χ_r^2 is lower than 1.45 (for further details see supplementary information 2.4.1).

Figure 4.

(A) Time evolution of three different species (*HF, MF, LF*) present in solution as obtained by PDA (e.g. Fig. 3A, B) for different NaCl concentrations. The solid lines are fits using Eq. 19 (supplementary information, section 2.5.3) with the results listed in supplementary tables 11 and 12 (supplementary information section 3.4). **(B)** Plot of the equilibrium fractions of *HF*, *MF* and *LF* (D*Only* not shown) as a function of NaCl concentration.

Figure 5.

Subensemble-filtered FCS. **(A)** FCS curves for free DNA (black), *LF+DOnly* (green) and *HF+MF* (red) species at 5, 12.5, 25 and 100mM NaCl. **(B)** Characteristic FCS diffusion times, t_{Diff}, of free DNA (black), *HF+MF* (red) and *LF+DOnly* (green), as a function of NaCl concentration obtained by fitting the curves by Eq. 19 (supplementary information section 2.5).

Figure 6.

Unfolding of nucleosomes. **(A)** Concentration dependent stability of mononucleosomes at 100 mM NaCl as a function of total nucleosome concentration. For each data point 50 pM of labeled nucleosomes were mixed with unlabeled 601 nucleosomes to obtain the final concentration [24]. The fractions of the different nucleosomal species were computed through PDA fit. The red line is the fit to a single exponential growth term: y = 0.98786-0.26216exp(-x/1.08284). **(B)** Three representative FRET efficiency distributions are shown for 60 min measurement time: 0.05, 0.7 and 3 nM nucleosomes. The fit (black line) of the experimental

FRET efficiency distributions (grey histograms) is decomposed in its components, *HF* (red line), *MF* (orange line) and Free DNA (blue line). PDA fit of free DNA (data not shown) showed that FRET efficiency distribution is the sum of two populations, *DOnly*, corresponding to a single distance with $R_{DA} \rightarrow \infty$, and *LF*, corresponding to Gaussian distribution of distances with R_{LF} = 75.1 Å and HW_{LF} = 10.3 Å. *DOnly* and *LF* distance and HW were fixed in the PDA fit of nucleosomes and only the fractions were allowed to vary. *HF* FRET efficiency distribution was estimated from the measurement at 3 nM nucelosomes and corresponds to a gaussian distribution of distances with R_{HF} = 54.5 Å and HW_{HF} = 3.02 Å, these values were kept fixed for the other concentrations and only the *HF* fraction was allowed to vary. The results for the fits reposted in 2B are: **0.05 nM)** R_{MF} = 57.3 Å, HW_{MF} = 12 Å, x_{MF} = 0.61, x_{HF} = 0.05, x_{LF} = 0.24, x_{DOnly} = 0.10; **0.7 nM)** R_{MF} = 53.6 Å, HW_{MF} = 9.4 Å, x_{MF} = 0.47, x_{HF} = 0.25, x_{LF} = 0.20, x_{DOnly} = 0.08; **3 nM)** R_{MF} = 52.5 Å, HW_{MF} = 8.7 Å, x_{MF} = 0.27, x_{HF} = 0.61, x_{LF} = 0.07, x_{DOnly} = 0.04 **(C)** Geometric model for the unfolding of a nucleosome, top and side view. DNA is represented in black, histones in pink, contact points with circled crosses, donor and acceptor dye in green and red respectively. In the top view, the semi-transparent red circle represents the position in which the acceptor dye would be in the case that DNA is completely wound around the histone core. Model parameters: Effective nucleosome radius R = 40 Å, rise per turn Δz = 45 Å, 80 base pairs per nucleosome turn, DNA length of 170 base pairs, donor dye position at 46.5 base pairs, acceptor dye position 136.5 base pairs, scaled Förster radius $ß R_0$ = 61.2 Å with ß = 1.1 (for further details see supplementary information, section 2.7). Unfolding of nucleosomes. **(D - F)** Possible FRET efficiency values as calculated from the geometrical model of the nucleosome unfolding: **(D)** all possible values, **(E)** values obtained for the loss of up to 4 contact points, **(F)** values obtained for the loss of at least 4 contact points.

Figure 7.

Sketches of the possible nucleosomal species. Nucleosomes lacking one H2A/H2B unit are indicated as *Incomplete*, while nucleosomes lacking more than one H2A/H2B units are indicated as *Broken*. Depending on the progress of disassembly the width of the corresponding FRET efficiency distributions of the species *LF*, *MF* and *HF* can be either narrow (n) or broad (b).

Figure 1

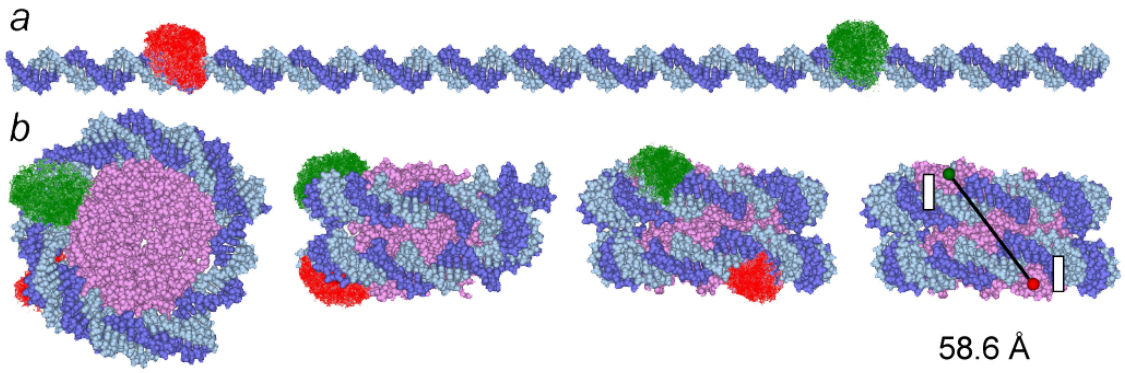

Figure 2

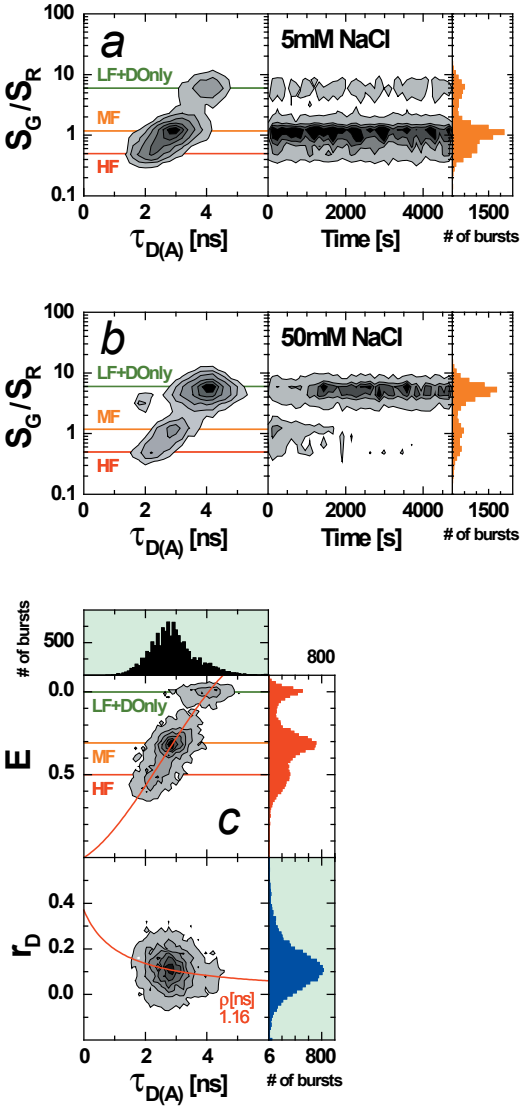
a
5mM NaCl
LF+DOnly
MF
HF
S_G/S_R
100
10
1
0.1
0
2
4
$\tau_{D(A)}$ [ns]
0
2000
4000
Time [s]
1500
# of bursts
b
50mM NaCl
LF+DOnly
MF
HF
S_G/S_R
$\tau_{D(A)}$ [ns]
Time [s]
# of bursts
# of bursts
500
800
E
0.0
0.5
LF+DOnly
MF
HF
c
r_D
0.4
0.2
0.0
ρ[ns]
1.16
6
800
# of bursts
$\tau_{D(A)}$ [ns]

Figure 3

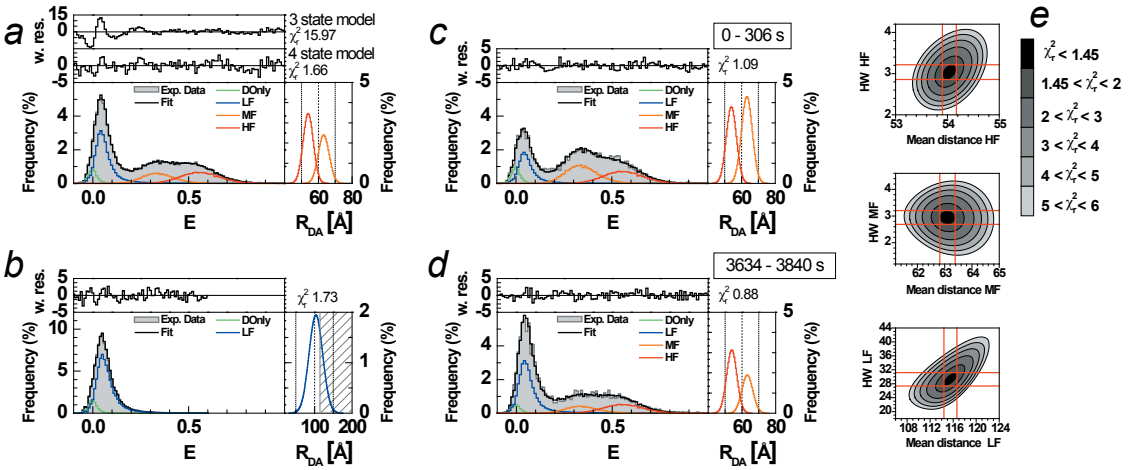
a
w. res.
3 state model
χ_r^2 15.97
4 state model
χ_r^2 1.66
Exp. Data
Fit
DOnly
LF
MF
HF
Frequency (%)
E
R_{DA} [Å]
b
χ_r^2 1.73
c
0 - 306 s
χ_r^2 1.09
d
3634 - 3840 s
χ_r^2 0.88
e
HW HF
Mean distance HF
HW MF
Mean distance MF
HW LF
Mean distance LF
χ_r^2 < 1.45
1.45 < χ_r^2 < 2
2 < χ_r^2 < 3
3 < χ_r^2 < 4
4 < χ_r^2 < 5
5 < χ_r^2 < 6

Figure 4

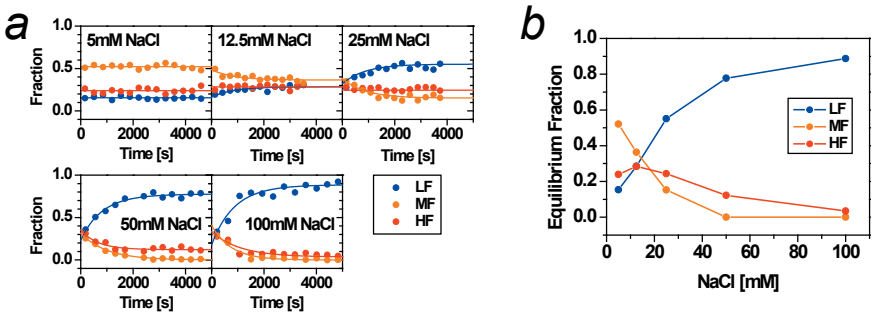
a
5mM NaCl
12.5mM NaCl
25mM NaCl
50mM NaCl
100mM NaCl
Fraction
Time [s]
LF
MF
HF
b
Equilibrium Fraction
NaCl [mM]

Figure 5

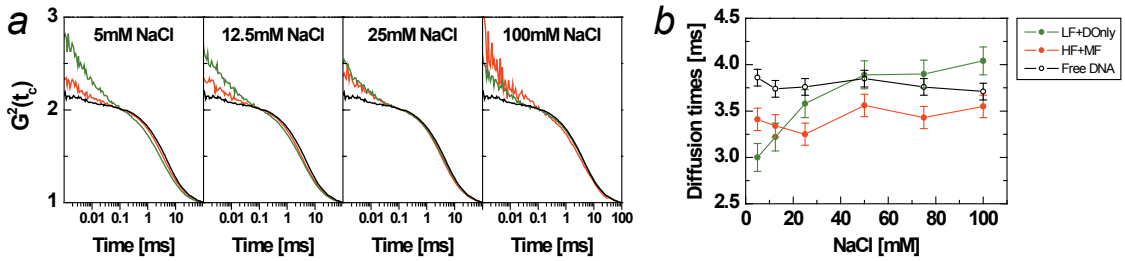
a
5mM NaCl
12.5mM NaCl
25mM NaCl
100mM NaCl
G²(t_c)
Time [ms]
b
Diffusion times [ms]
NaCl [mM]
LF+DOnly
HF+MF
Free DNA

Figure 6

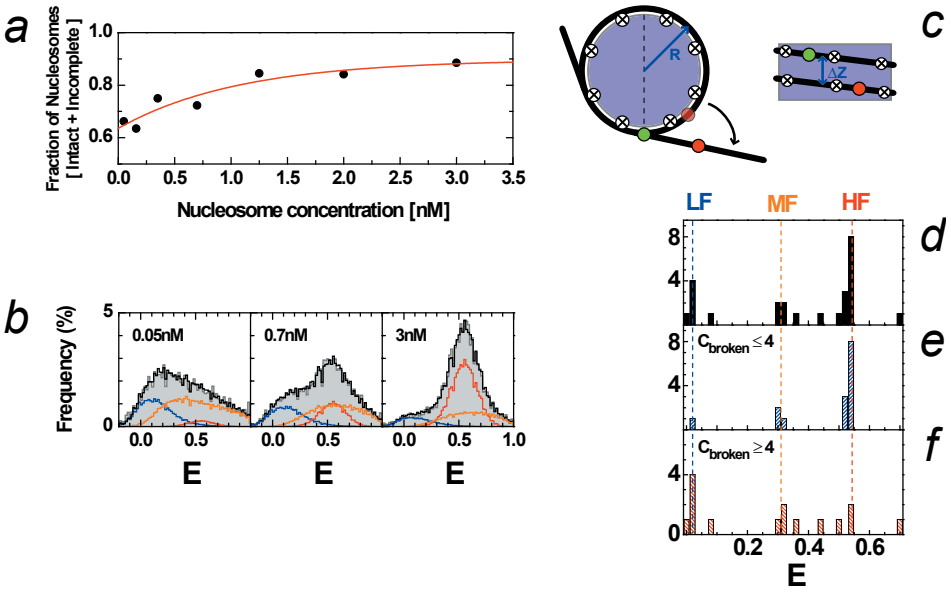
a
Fraction of Nucleosomes [Intact + Incomplete]
1.0
0.8
0.6
0.0
0.5
1.0
1.5
2.0
2.5
3.0
3.5
Nucleosome concentration [nM]
b
Frequency (%)
5
0
0.05nM
0.7nM
3nM
0.0
0.5
0.0
0.5
0.0
0.5
1.0
E
E
E
c
R
ΔZ
LF
MF
HF
d
8
4
e
8
4
C broken ≤ 4
f
C broken ≥ 4
4
0
0.2
0.4
0.6
E

Figure 7

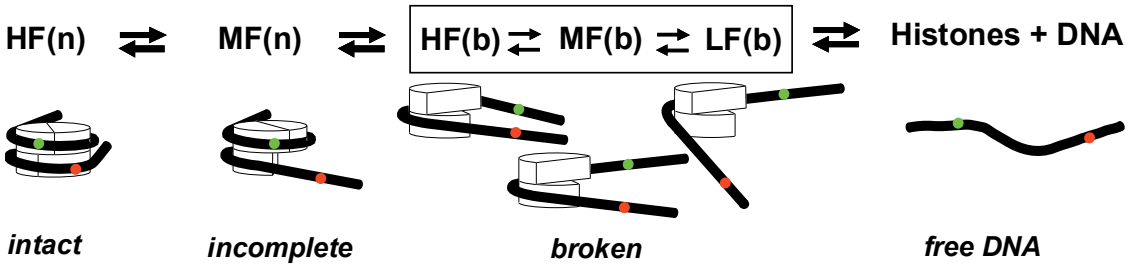
HF(n)
MF(n)
HF(b)
MF(b)
LF(b)
Histones + DNA
intact
incomplete
broken
free DNA

Nucleosome disassembly intermediates characterized by single-molecule FRET

Alexander Gansen*[1], Alessandro Valeri*[2], Florian Hauger[1], Suren Felekyan[2], Stanislav Kalinin[2], Katalin Tóth[1], Jörg Langowski+[1], Claus A: M. Seidel+[2]

1: Abteilung Biophysik der Makromoleküle, Deutsches Krebsforschungszentrum, Im Neuenheimer Feld 580, D-69120 Heidelberg, Germany

2: Lehrstuhl für Molekulare Physikalische Chemie, Heinrich-Heine-Universität, Universitätsstrasse 1, Geb. 26.32, 40225 Düsseldorf, Germany.

+Corresponding authors: J. Langowski: jl@dkfz.de; C. A. M. Seidel: cseidel@gwdg.de

* contributed equally

Supplementary information

1. Supplementary Materials and Methods.

1.1 Samples.

Mononucleosomes were reconstituted on a 170 bp long DNA fragment containing the SELEX 601 positioning sequence [1] and unmodified recombinant *X. laevis* histones. The details of the preparation can be found in[2]. DNA fragments were prepared by PCR using primers labeled with Alexa488 and Alexa594 (Purimex, Grebenstein, Germany) and the PCR Master Kit from Promega (Madison, WI, USA). The template pgem3z601 was kindly provided by Jon Widom from Northwestern University. The primers were:

5'-catgcacaggatgtatatatctgacacgtgcct(Alexa594)ggagac-3' and

5'-accctatacgcggccgccctggagaatcccggtgccgaggccgct(Alexa488)caattg-3'.

Both fluorophores were attached via aminolink-c6 linkers. In the intact nucleosome both fluorophores are located on opposite turns of the two superhelical DNA gyres (see Fig. 1A). The complete sequence can be found in our previous work [3].

After PCR DNA was purified by isopropanol precipitation and gel filtration with NAP-5 columns (Pharmacia), concentrated to 0.1-0.5 mg/ml in TE (10 mM Tris, 0.1 mM EDTA, pH 7.5) in a vacuum centrifuge and checked on an 8 % polyacrylamide gel and with absorption spectroscopy.

Preparation of recombinant *X. laevis* histone octamers followed the procedure described in [4,5]. Nucleosomes were reconstituted by mixing labeled DNA and histone octamer at a molar ratio of 1:1.4 in TE, pH 7.5 and 2 M NaCl. Salt step dialysis was carried out at 4° C with steps of 1.8 M, 1.4 M, 1 M, 0.8 M, 0.6 M, 0.4 M, 0.2 M, 0.1 M for 50 minutes each. Nucleosomes were finally dialysed against 5 mM NaCl over night. Reconstitution efficiency were checked by quantitative agarose gel electrophoresis to measure bound to free DNA ratio and yielded typically >80 % intact nucleosomes. Nucleosome positioning properties were checked on a native polyacrylamide gel and with restriction analysis as described in [3].

1.2 Measurement conditions of single-molecule multiparameter fluorescence detection.

The experiments were carried out with a confocal epi-illuminated set-up [6]. The fluorescently labelled complexes were excited by a linearly polarized, active-mode-locked Argon-ion laser (476 nm, 73 MHz, 150 ps). The laser was focused into the dilute solution (< 50 pM) of labelled nucleosome complexes by a 60x water immersion objective. Each molecule generates a brief burst of fluorescence photons as it traverses the detection volume. This photon-train is divided initially into its parallel and perpendicular components via a polarizing beamsplitter and then into a wavelength ranges below and above 595 nm. Additionally, red (HQ 630/60 nm) and green (HQ 520/66 nm) filters were in front of the detectors ensure that only fluorescence photons coming from the acceptor (Alexa 594) and donor (Alexa 488) dyes are

registered. Correction factors $l_1 = 0.0308$ and $l_2 = 0.0368$ are used to account for the mixing of polarization by the microscope objective and *G*-factors ($G_{Green} = 0.989$ for the green channels and $G_{Red} = 1.120$ for the red channels) are applied to compensate for the slightly different detection efficiency of the two polarization components. Detection is performed using four avalanche photodiodes (SPCM-AQR-14, Laser Components, Germany, for the red channels, and PDM050CTC, MPD, Italy, for the green channels). The signals from all detectors are passed through a passive delay unit and two routers to two synchronized time-correlated single photon counting boards (SPC 132, Becker and Hickl, Germany) which are connected to a PC. Fluorescence bursts are distinguished from the background of 3-3.5 kHz by applying certain threshold intensity criteria (0.1 ms interphoton time, 150 photons minimum per burst [6].)

2. Supplementary Theory for FRET Analysis.

2.1 Calculation for FRET Parameters.

FRET occurs between two fluorophores when the emission spectrum of an excited donor (D) fluorophore overlaps with the absorption spectrum of a nearby acceptor (A) fluorophore. The efficiency, *E*, of FRET depends strongly on the interdye distance R_{DA} and the Förster radius, R_0 (eq. 1)[7].

$$E = \left[1 + \left(\frac{R_{DA}}{R_0}\right)^{1/6}\right]^{-1} \qquad \text{(eq.1)}$$

Each fluorophore pair has a characteristic Förster radius, R_0, which accounts for the system properties. It is calculated in [Å] by $R_0 = \left(c_{FT}\, J(\lambda)\, \kappa^2\, \Phi_{FD(0)}\, n^{-4}\right)^{1/6}$. $J(\lambda)$ is the overlap integral of the donor emission with the acceptor absorption spectrum with the units [M^{-1} cm^{-1} nm^4], κ^2 accounts for the relative orientation of the donor and acceptor (usually assumed to be 2/3), $\Phi_{FD(0)}$ is the donor fluorescence quantum yield in absence of transfer, and the *n* refractive

index of the medium (n = 1.33). For the given units the constant c_{FT} equals 8.79 10^{-5} mol. For the Alexa488-Alexa594 pair in water we estimated R_0 = 55.6 Å.

The efficiency of energy transfer is related to fluorescence lifetimes through [8,9]

$$E = 1 - \frac{\tau_{D(A)}}{\tau_{D(0)}} \qquad \text{(eq.2)}$$

Energy transfer efficiency is experimentally calculated from the fluorescence intensity of the donor, F_D, and acceptor, F_A, (eq.3)

$$E = \frac{F_A \Phi_{FD(0)}}{F_D \Phi_{FA} + F_A \Phi_{FD(0)}} \qquad \text{(eq.3)}$$

where $\Phi_{FD(0)}$ is the donor fluorescence quantum yield without acceptor and Φ_{FA} is the acceptor fluorescence quantum yield.

To obtain fluorescence intensity of donor and acceptor, the signal intensities (S_G and S_R) were corrected for mean background counts (typically between 2-2.3 kHz for the green channels, $\langle B_G \rangle$ (donor), and 1-1.2 kHz for the red channels, $\langle B_R \rangle$ (acceptor)), spectral crosstalk, α (0.07), direct excitation of the acceptor, DE (1.35kHz) and the ratio of the detection efficiencies, g, between the green and red channels (g_G/g_R = 0.58) (eq. 4).

$$F_D = \frac{S_G - \langle B_G \rangle}{g_G} = \frac{F_G}{g_G}$$

$$F_A = \frac{S_R - (\langle B_R \rangle + DE) - \alpha (S_G - \langle B_G \rangle)}{g_R} = \frac{F_R}{g_R} \qquad \text{(eq.4)}$$

Fluorescence lifetime is determined for each burst in two steps: (i) by generating a histogram of photon arrival times, and (ii) by fitting the histograms to a single exponential using a maximum likelihood estimator and iterative convolutions to account for the scatter contribution [6]. The lifetime of the donor dye ($\tau_{D(0)}$) coupled to the nucleosomal DNA in absence of the acceptor was determined to be 4.1 ns.

2.1.1. Calculation of expected FRET efficiency by using MD simulations

Molecular dynamics (MD) simulations provide "clouds" of possible positions of the dyes[10], see also Section 2.6. From these data it is possible to calculate the mean position FRET efficiency, E_{mp}, as:

$$E_{mp} = \frac{R_0^6}{R_0^6 + R_{mp}^6} \qquad \text{(eq.5)}$$

However, due to the flexibility of the fluorophore linker R_{mp} is not directly accessible in FRET experiments. What is measured in the experiment is the isotropic average FRET efficiency [10], $\langle E \rangle_{iso}$, that is the average over all FRET efficiencies calculated from all the possible donor-acceptor distances R_i. Using the the Förster radius R_0 $\langle E \rangle_{iso}$ is calculated as:

$$\langle E \rangle_{iso} = \left\langle \frac{R_0^6}{R_0^6 + R_i^6} \right\rangle \qquad \text{(eq.6)}$$

2.2 Dye linker flexibility.

In the case of a dynamic system, in which a molecule during the transit in the focus can switch between different states, each characterized by a transfer efficiency E, the lifetime calculated by the Maximum Likelihood Estimator (MLE) [11] is a fluorescence intensity weighted average lifetime:

$$\tau_{ave,a} = \sum_i a_i \tau_i \qquad \text{with} \qquad a_i = \frac{x_i \tau_i}{\sum_i x_i \tau_i} \qquad \text{(eq.7)}$$

In equation 7, τ_i is the fluorescence lifetime of the i-th state and x_i the fraction of time the molecule spends in the i-th state. On the other hand E is a species weighted average:

$$E_{ave,x} = \sum_i x_i E_i \qquad \text{(eq.8)}$$

where E_i is the FRET efficiency of the i-th species.

For this reason, in presence of dynamic processes equation 2 does not hold anymore and a correction must be performed. In our nucleosome measurements we observed a deviation from the behaviour of equation 2 that could be easily explained with a dynamic fluctuation of distances. We interpreted this fluctuation as the effect of dye linker flexibility. To test this hypothesis we first considered that each mean distance R_{DA} appears in reality as two distances $R_{DA} \pm \sigma$, where σ (= 6Å) is the displacement due to the linker flexibility. The value of σ = 6Å is consistent with the results of bulk TCSPC measurements on shorter DNA fragments (unpublished results). Then from the two distances we calculated the fluorescence weighted average and the species weighted average, $\tau_{ave,x} = \sum_i x_i \tau_i$ (that would satisfy equation 2). Finally we plotted the species weighted average as a function of the fluorescence weighted average (Supplementary Figure 1).

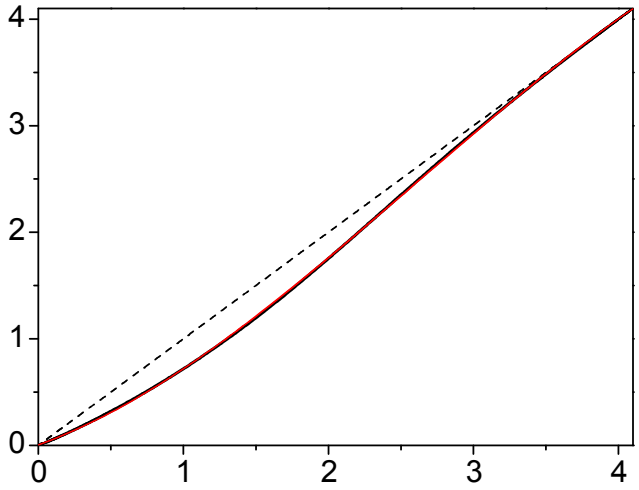

Supplementary Figure 1. Fluorescence lifetime correction. Species-averaged lifetime is plotted as a function of fluorescence-averaged lifetime, black line. The red line represents the fit to a third order polynomial. The dashed line, $\tau_{ave,\,a} = \tau_{ave,\,x,}$ is used to show the zone where the two lifetime averages differ the most.

By a polynomial fitting we obtained an equation that would *convert* one average into the other (eq.7)

$$\tau_{ave,x} = 0.00479 + 0.4813\tau_{ave,a} + 0.26694\tau_{ave,a}^2 - 0.03435\tau_{ave,a}^3 \qquad \text{(eq.9)}$$

and substituted it into equation 2

$$E = 1 - \frac{0.00479 + 0.4813\tau_{ave,a} + 0.26694\tau_{ave,a}^2 - 0.03435\tau_{ave,a}^3}{\tau_{D(0)}} \qquad \text{(eq.10)}$$

2.3 Probability distribution analysis (PDA).

As shown by Antonik et al.[12], PDA can be simplified if each fluorescence burst is first divided into bins of equal length, i.e., time windows. Working with such time windows allows us to study the probability distribution without taking into account the distribution of observation times that arise due to the diffusion of the molecule through the focus. In order to handle properly multi-molecular events [13], we analysed the entire photon stream without applying any burst selection beforehand. In addition, each data set was studied by globally fitting time windows of two different lengths, 1ms and 3ms.

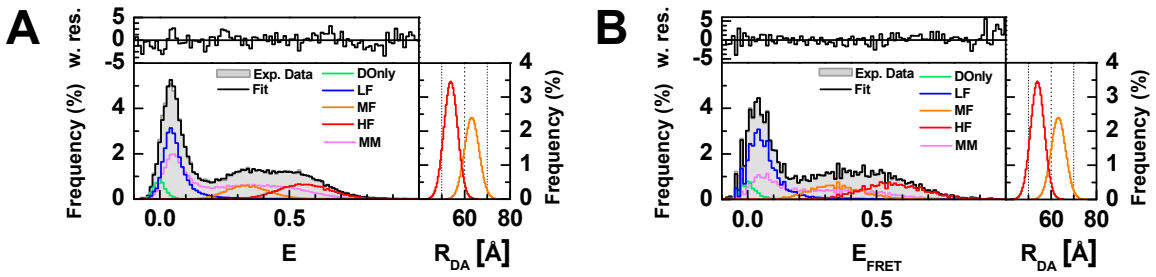

Supplementary Figure 2. Global PDA fit. FRET efficiency histograms for nucleosomes at 25 mM NaCl are displayed for time windows of 3ms (A) and 1ms (B). The two datasets are fit with the same parameters. The black bold line is the fit to a four state model accounting for *HF, MF, LF* and *DOnly* (red, orange, blue and green line, respectively). The fit includes also the simultaneous transit of more than one molecule in the detection volume, multi-molecular events MM (light magenta line). Using Gaussian distributions for the FRET species the following mean distances R_{DA}, half widths HW and fractions x_i have been obtained: *HF* (R_{DA}

= 54.0 Å, HW = 3.0 Å, x_{HF} = 0.26), *MF* (R_{DA} = 63.1 Å, HW = 3.2 Å, x_{MF} = 0.19) and *LF* (R_{DA} = 119, HW = 31 Å, x_{LF} = 0.47). The *DOnly* species is described by E = 0 and x_{DOnly} = 0.08. The *HF* and *MF* populations are displayed in the right sub-panel. Weighted residuals of the fit are displayed on top of each *E* histogram.

Both time windows are fitted equally well using the same set of parameters, therefore we can exclude the presence of dynamical processes with timescale comparable to the dwell time of the nucleosome in the focus.

Histograms of donor-acceptor distances, R_{DA}, and FRET efficiencies, *E*, were calculated from experimental data sets according to equations 3 and 11 [14]

$$R_{DA} = R_0 \left(\frac{\Phi_{FA} F_D}{\Phi_{FD(0)} F_A} \right)^{1/6} \qquad \text{(eq.11)}$$

Fits to experimental histograms were generated by applying equations 3, 4 and 11 to theoretical distributions $P(S_G, S_R)$ which were calculated using the reported PDA theory [12,15]. The use of R_{DA} histograms allows for visual comparison of deconvoluted distance distributions and original shot-noise broadened data. In terms of accuracy of the analysis the choice of 1-D histogram parameter (e.g. S_G/S_R ratio, FRET efficiency or apparent donor-acceptor distance) has only a negligible effect [15].

The experimental histograms were fitted using software developed in-house, using a four-state model to account for donor only species and the three FRET species (*LF, MF* and *HF*). A single-distance model was not sufficient to describe the FRET states; this could be due to numerous experimental artefacts [12,16] and/or complex acceptor dye photophysics. Thus, each FRET state was fitted using an (apparent) Gaussian distribution of distances, with a mean of R_{DA} (center of the Gaussian distribution) and a half-width of HW.

2.3.1 Correction of PDA model functions for the presence of direct excitation

Let us assume that the direct excitation probability is p_{DE} as shown in Supplementary Figure 3

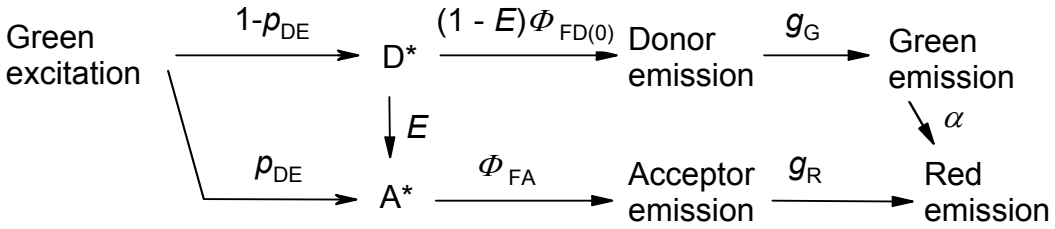

Supplementary Figure 3. Excitation and emission pathways entering the PDA model function, eq. 12

Supplementary Figure 3 shows all processes considered in PDA together with their probabilities. It follows directly from Supplementary Figure 3 that a probability of a detected photon being green is

$$\begin{aligned} p_G &= \frac{(1-p_{DE})(1-E)\Phi_{FD(0)}g_G}{(1+\alpha)(1-p_{DE})(1-E)\Phi_{FD(0)}g_G + (p_{DE}+(1-p_{DE})E)\Phi_{FA}g_R} \\ &= \left(1+\alpha+\frac{(p_{DE}(1-p_{DE})^{-1}+E)\Phi_{FA}}{(1-E)G\Phi_{FD(0)}}\right)^{-1} \end{aligned} \qquad \text{(eq.12)}$$

Equation 12 replaces equation 3 in ref [13].

2.4 Confidence intervals estimation in PDA.

2.4.1 Chi-squared surfaces.

χ_r^2 – surfaces represent 2D plots of the reduced chi-squared values χ_r^2) against any two fit parameters while keeping other parameters fixed at their optimal values [17]. Assuming no or little correlation between the two plotted and remaining fit parameters (which might not be the case, see next subsection), χ_r^2 – surfaces allow for estimation of error intervals [17].

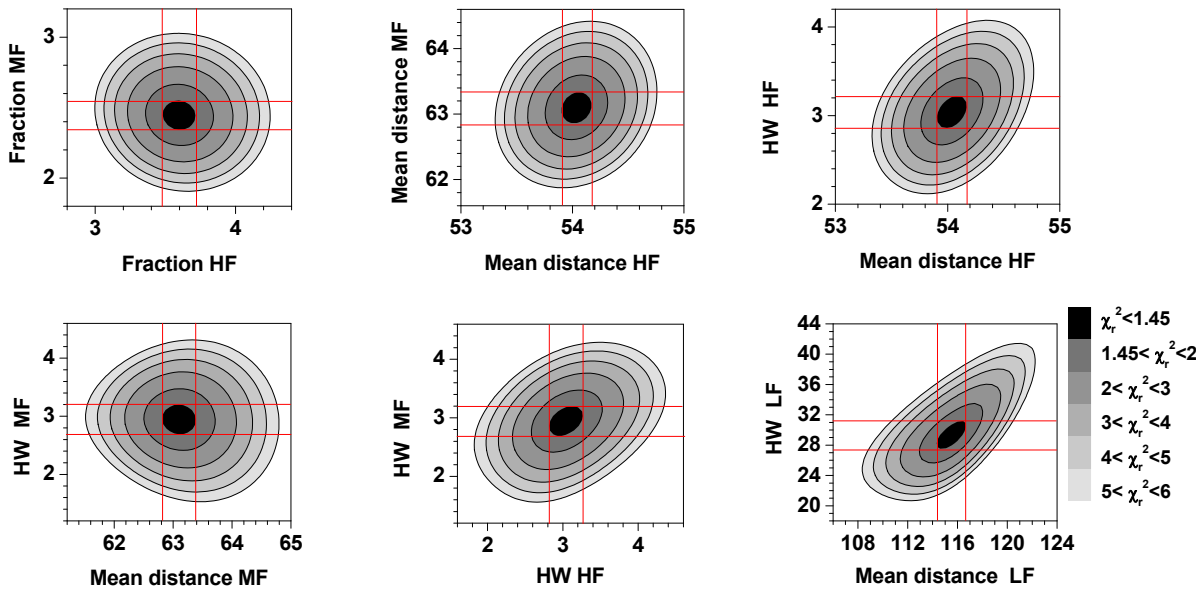

Supplementary Figure 4. χ_r^2 – surfaces. χ_r^2 – surfaces calculated for nucleosomes at 25 mM NaCl. In these plots reduced chi-square is plotted as a function of two fit parameters at a time. The red lines delimit 68 % confidence intervals (corresponding to 1σ), that is, where $\chi_r^2 < \chi_{r,\,fit}^2 + (2/N_{bins})^{1/2} = 1.28 + 0.17 = 1.45$, where $\chi_{r,\,fit}^2$ is the reduced chi-square obtained by the fit and N_{bins} is the number of fitted histogram bins ($N_{bins} = 71$ and $\chi_{r,\,fit}^2 = 1.28$).

2.4.2 Error limits for multiple parameters.

Alternatively, we varied all free fit parameters of the fit in a random manner. The χ_r^2-value was calculated at 10000 to 50000 random points yielding 20-1000 points with χ_r^2-values within $\pm(2/N_{bins})^{1/2}$ of that of the optimal fit [18]. Parameter intervals where such fits were possible were assigned as confidence intervals, as presented in Supplementary Table 1 for the case of 25 mM NaCl. Other data sets discussed in the main text were of comparable data quality and there was therefore no reason to expect significantly different error limits. In most of cases the presented error limits are consistent with those obtained from χ_r^2 – surfaces.

Supplementary Table 1. Confidence intervals calculated for nucleosomes at 25 mM NaCl, as described in Section 2.4.2

Parameter	Mean	1σ standard deviation	Relative Error [%]
Species: HF			
R_{DA} [Å]	54.0	0.4	0.7
HW [Å]	3.0	0.3	10
x	0.26	0.03	12
Species: MF			
R_{DA} [Å]	63.1	0.5	0.8
HW [Å]	3.2	0.3	9
x	0.19	0.03	12
Species: LF			
R_{DA} [Å]	119	2	1.7
HW [Å]	31	2	6.5
x	0.47	0.04	8
Species: DOnly			
x	0.08	0.01	13

2.4.3 Systematic errors due to crosstalk and direct excitation.

The spectral crosstalk (eq. 12) and the direct excitation (eq. 12 and Supplementary Figure 3) significantly contribute to the red signal. To investigate the influence of these parameters on fit results, we fixed the values of crosstalk and direct excitation probability at "wrong" values (Supplementary Tables 2 and 3) and fitted the data as usually. Supplementary Tables 2 and 3 make it clear, that a 10 % relative systematic error in crosstalk and direct excitation would result in approximately 6 Å and 4 Å errors in the longer distance R_{DA} (i.e., that of *LF* species), respectively. The effect of crosstalk and direct excitation on the parameters of *HF*- and *MF*-states is much less pronounced.

Supplementary Table 2. Systematic errors due to direct excitation.

Direct excitation probability p_{DE}	0.0315	0.035 (used in fits)	0.0385
R_{DA} (Å)	115	119	126
HW (Å)	28.4	30.8	33.8

Supplementary Table 3. Systematic errors due to crosstalk.

Crosstalk α	0.063	0.07 (used in fits)	0.077
R_{DA} (Å)	116	119	123
HW (Å)	29.1	30.8	32.4

2.4.4 Distances beyond the FRET range.

In some cases, PDA fits produce mean distances well beyond the maximum distance measurable by FRET. The error analysis suggests however relatively high accuracy of a few angstrom (Supplementary Table 1). Intuitively this seems to be conflicting with the well-known conception of the distance range accessible to FRET being roughly within $0.5R_0$ to $2R_0$ [19].

To explain this fact one should notice that the modelled distance distributions are so broad that the mean FRET efficiency is actually measurable. Supplementary Tables 4 and 5 illustrate this effect for R_{DA} = 120 Å and half width HW = 30 Å. It is clear that, despite a very large absolute value of R_{DA}, small changes in either mean or width of the distance can change the average FRET efficiency $\langle E \rangle$ by 1-2 %, which is easily detected by PDA[12].

Supplementary Table 4. Mean FRET efficiencies calculated for constant R_{DA} = 120 Å and various distribution half-widths (HW).

HW [Å]	$\langle E \rangle$
20	0.019
25	0.029
30	0.043
35	0.060
40	0.081

Supplementary Table 5. Mean FRET efficiencies calculated for constant HW =30 Å and various R_{DA}.

R_{DA} [Å]	$\langle E \rangle$
110	0.071
115	0.055
120	0.043
125	0.033
130	0.025

Considering a Gaussian distribution of distances $P(r_{DA})$ with a mean (centre) distance R_{DA} and a half width HW, the mean FRET efficiencies $\langle E \rangle$ in Supplementary Tables 4 and 5 were calculated according to equation 13

$$\langle E \rangle = \int_0^{+\infty} P(r_{DA}) E(r_{DA}) dr_{DA} = \int_0^{+\infty} \frac{1}{\mathrm{HW}\sqrt{2\pi}} \exp\left(\frac{-(r_{DA} - R_{DA})^2}{2(\mathrm{HW})^2} \right) \frac{1}{1 + (r_{DA}/R_0)^6} dr_{DA} \qquad \text{(eq.13)}$$

2.5 Species selective filtered fluorescence correlation spectroscopy (fFCS).

Fluorescence correlation spectroscopy, FCS, is a powerful method to determine the diffusion time of a fluorescently labelled molecule and study all those processes that lead to a fluctuation in the fluorescence signal. In the absence of interactions between the fluorophore and the molecule to which it is attached, Alexa488 and Alexa594 dyes have a correlation curve that can be explained only in term of translational diffusion and triplet formation:

$$G(t_C) = 1 + \frac{1}{N} \cdot \left(1 + \frac{t_C}{t_{Diff}}\right)^{-1} \cdot \left(1 + \left(\frac{\omega_0}{z_0}\right)^2 \cdot \frac{t_C}{t_{Diff}}\right)^{-\frac{1}{2}} \cdot \left(1 + \frac{T}{(1-T)} \cdot \exp(-t_C/t_T)\right) \qquad \text{(eq.14)}$$

where N is the average number of molecules in the detection volume, t_{Diff} the diffusion time, z_0 and ω_0 the $1/e^2$ radii in the axial and radial direction respectively, T the amplitude of the triplet, t_T the characteristic time of the triplet.

Knowing the shape and size of the focal volume, it is possible to calculate the diffusion coefficient, D, as:

$$D = \frac{\omega_0^2}{4 \cdot t_D} \qquad \text{(eq.15)}$$

By fitting equation 14 it is possible to know the average number of molecules present in the focal volume, however, in the case FCS performed at single molecule concentration, the presence of scatter photons influences the amplitude of the correlation curve leading to an incorrect evaluation of N [6].

When more than one FRET species are simultaneously present in solution, equation 14 does not hold anymore. For a mixture of species, in fact, the correlation function becomes:

$$G(t_C) = 1 + \frac{1}{N} \cdot \frac{\sum_i^n x_i \cdot Q_i^2 \cdot G_i^2(t_C)}{\left(\sum_i^n x_i \cdot Q_i\right)^2} \qquad \text{(eq.15)}$$

where x_i is the fraction of the ith species, Q_i is its brightness, and $G_i^2(t_C)$ its normalised correlation function. In this case, even knowing exactly the brightness of each species, it will be very difficult to sort them correctly if their diffusion times do not differ significantly.

To solve this problem Enderlein and co-workers [20-22] have suggested using the fluorescence lifetime decay pattern of the different species to build filters that will attribute to each photon a certain likelihood, even negative, that said photon belongs to a determined species. By applying the filters only those photons will be correlated that belong to the same species; and by using the instrumental response function as an additional pattern it is possible to eliminate the contribution of scattered photons and compute the correct correlation amplitudes even at single molecule concentrations.

2.5.1 Building the filters.

For simplicity, we consider the mixture of two molecular species measured with a confocal microscope set-up as the one used for this work (as described in section 1.2). If ${}^{\parallel}p_j^{(i)}$ and ${}^{\perp}p_j^{(i)}$ are the normalized probabilities of measuring a photon of the ith species within the jth TCSPC-channel in the parallel and perpendicular polarizations relative to the linearly polarized excitation light respectively, then any measured TCSPC decay histogram ${}^{\parallel}H_j$ and ${}^{\perp}H_j$ of the mixture can be expressed as a linear combination of the decay patterns of the two species

$$\begin{cases} {}^{\parallel}H_j = \sum_{i=1}^{n(=2)} w^{(i)} \cdot {}^{\parallel}p_j^{(i)} = w^{(1)} \cdot {}^{\parallel}p_j^{(1)} + w^{(2)} \cdot {}^{\parallel}p_j^{(2)} \\ {}^{\perp}H_j = \sum_{i=1}^{n(=2)} w^{(i)} \cdot {}^{\perp}p_j^{(i)} = w^{(1)} \cdot {}^{\perp}p_j^{(1)} + w^{(2)} \cdot {}^{\perp}p_j^{(2)} \end{cases} \qquad \text{(eq.16)}$$

where $w^{(i)}$ is the amplitude of the photon count contribution (in photons number) of the ith species. Now, as described by Enderlein and co-workers it is possible to build two filter sets ${}^{\parallel}f_j^{(i)}$ and ${}^{\perp}f_j^{(i)}$, so that

$$\left\langle \sum_{j=1}^{L} {}^{\parallel}f_j^{(i)} \cdot {}^{\parallel}H_j \right\rangle = {}^{\parallel}w^{(i)}, \quad \left\langle \sum_{j=1}^{L} {}^{\perp}f_j^{(i)} \cdot {}^{\perp}H_j \right\rangle = {}^{\perp}w^{(i)} \qquad \text{(eq.17)}$$

where ${}^{\parallel}w^{(i)}$ and ${}^{\perp}w^{(i)}$ are the photon count contributions of the *i*th species in the parallel and perpendicular detection channels respectively (${}^{\parallel}w^{(i)} + {}^{\perp}w^{(i)} = w^{(i)}$), L the total number of TCSPC channels, and the brackets denote averaging over an infinite number of measurements. The correlation between the different polarisations of the same spectral range of the *i*th species, auto-cross correlation $G_{\perp,\parallel}^{(i)}(t_c)$, can be then calculated as

$$G_{\perp,\parallel}^{(i)}(t_c) = \frac{\left\langle \left(\sum_{j=1}^{L} {}^{\perp}f_j^{(i)} \cdot {}^{\perp}S_j(t) \right) \cdot \left(\sum_{j=1}^{L} {}^{\parallel}f_j^{(i)} \cdot {}^{\parallel}S_j(t+t_c) \right) \right\rangle}{\left\langle \sum_{j=1}^{L} {}^{\perp}f_j^{(i)} \cdot {}^{\perp}S_j(t) \right\rangle \cdot \left\langle \sum_{j=1}^{L} {}^{\parallel}f_j^{(i)} \cdot {}^{\parallel}S_j(t+t_c) \right\rangle} \qquad \text{(eq.18)}$$

where ${}^{\perp}S_j(t)$ is the fluorescence signal in the *j*th TCSPC channel of total perpendicular signal at measurement time *t* and ${}^{\parallel}S_j(t+t_c)$ is the fluorescence signal in the *j*th TCSPC channel of total parallel signal at measurement time.

The fluorescence lifetime filters can be devised not only for two different polarisations of the same spectral range, but also for any combination of polarisation and spectral range. For this work the filters were built using the lifetime pattern of both green and red channels, and the correlation was computed only for the parallel polarisation, $G_{(G_{\parallel}+R_{\parallel})(G_{\parallel}+R_{\parallel})}^{(i)}(t_c)$.

2.5.2 Selecting the species.

To obtain the decay pattern of the different species we performed sub-ensemble analysis [23] by selecting the fluorescence bursts in the $\tau_{D(A)}$ versus S_G/S_R 2D plot as the ones in figures 2A and 2B of the main text. Due to the close similarity between the decay patterns, Donor-only and *LF* are grouped together, and the *HF* and *MF* species are grouped in the FRET species. The instrument response function was used as additional species to get rid of scatter photons. As

an example, in the Supplementary Figure 5 are reported the fluorescence decay filters obtained for 5 mM NaCl.

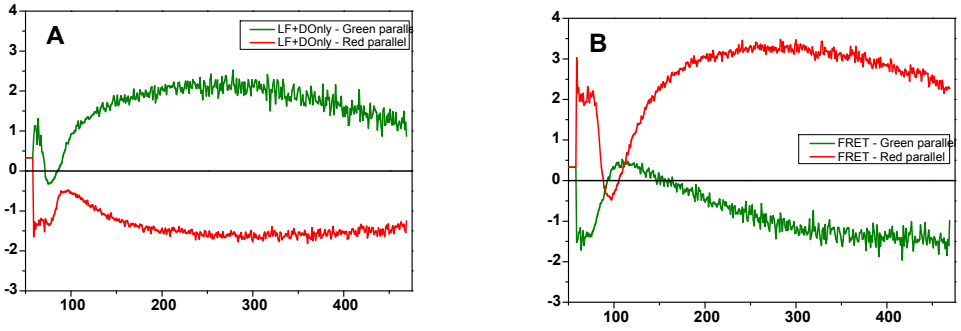

Supplementary Figure 5. **Fluorescence decay filters.** Filter sets for nucleosomes at 5 mM NaCl. **(A)** *LF+DOnly* species. **(B)** FRET species.

2.5.3 Fit model.

The correlation curves obtained were fitted with a model taking into account, translational diffusion, triplet formation and an additional correlation term, bunching term, whose nature we did not investigate in this work:

$$G(t_C) = 1 + \frac{1}{N} \cdot \left(1 + \frac{t_C}{t_{Diff}}\right)^{-1} \cdot \left(1 + \left(\frac{\omega_0}{z_0}\right)^2 \cdot \frac{t_C}{t_{Diff}}\right)^{-\frac{1}{2}} \cdot \left(1 + \frac{T}{(1-T)} \cdot \exp(-t_C/t_T)\right) \cdot \left(1 + \frac{B}{(1-B)} \cdot \exp(-t_C/t_B)\right)$$

(eq.19)

where N is the average number of molecules in the detection volume, t_{Diff} the diffusion time, z_0 and ω_0 the $1/e^2$ radii in the axial and radial direction respectively, T the amplitude of the triplet, t_T the characteristic time of the triplet, B the amplitude (fraction) of the second bunching term and t_B the characteristic time of the second bunching term.

2.6 Modelling

2.6.1 Modelling the fluorophore position cloud obtained from MD simulations to the nucleosomal DNA structure.

In order to compare the nucleosome structure with our data, we modelled the fluorophore position clouds obtained from the MD simulation of a straight B-DNA [10] to the respective bases in the nucleosomal DNA. On a local view, the backbone of the nucleosomal DNA shows significant deviation from that of the straight DNA. Thus we aligned the positional clouds together with the straight DNA to the nucleosomal DNA by superposing the thymine where the fluorophores are bound. After alignment, some of the dye positions fell in the space between the DNA and the histone core of the nucleosome and had to be discarded because sterically forbidden. The removal of the hindered positions was automated and performed by discarding all donor position within 2 Å of the histones and all acceptor positions within 4 Å of the histone core. This procedure left 93 % of the original donor cloud and 61 % of the original acceptor cloud. Even though the restriction on the acceptor cloud may seem severe, the impact on the average orientation of the dye was minimal, and a $\kappa^2 = 0.65$ was calculated. Mean FRET efficiency was calculated by equation 6.

2.7 Geometric model description of nucleosomes

2.7.1 Continuous model

We assume that both ends of DNA can partly dissociate from the core as shown in Figure 6. The number of dissociated bases from donor and acceptor sides (N_D and N_A, respectively) can be arbitrary provided at least one basepair remains bound. Internal detachment is not considered. Detached part(s) of DNA are assumed to be straight and tangential to the nucleosome core at the detachment point(s) (see Figure 6, main text). There can be an additional constant separation between the DNA loops along the z-axis, Δz (Figure 6).

For simplicity, all combinations of N_D and N_A are considered to be equally probable. There is no doubt that in reality this assumption is violated. However, this will change only amplitudes but not the positions of the peaks.

Unlike the "discrete" model (see next section and main text), the continuous model does not produce any MF peak (Supplementary Figure 6), which is clearly inconsistent with our experimental data.

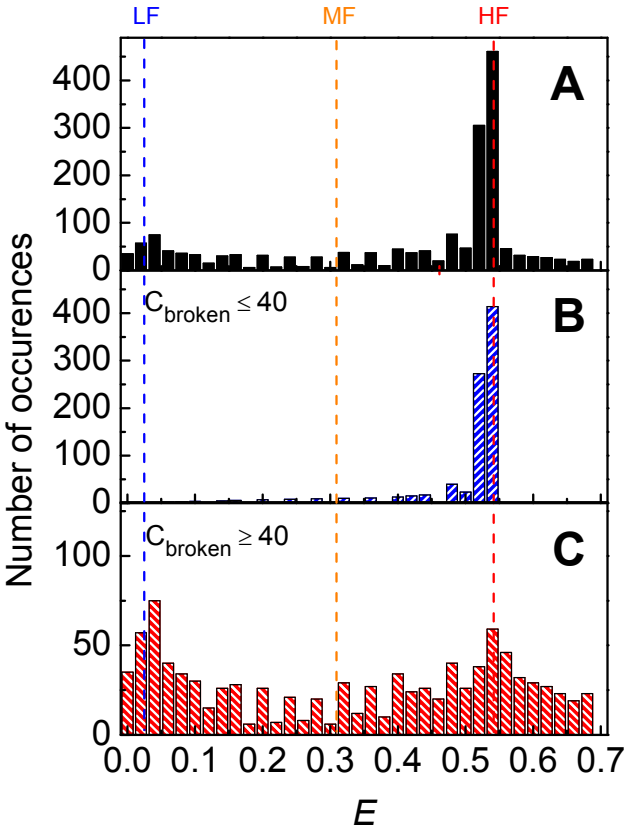

Supplementary Figure 6. Possible FRET efficiency values calculated by using continuous dissociation model (Section 2.7.1, Supplementary Table 7). (A) all possible values, **(B)** values obtained for unwinding of up to 40 nucleic bases, **(C)** values obtained for unwinding of at least 40 nucleic bases.

2.7.2 Discrete (contact point) model

The discrete model accounts for the fact that DNA dissociates stepwise at defined "contact points" (see Fig. 6). The bases that form contact points are selected according to their proximity to the core. From the X-ray structure 12 contact points have been identified within 4 Å shell from the core, as summarized in Supplementary Table 6. DNA is therefore assumed to dissociate in steps of 10-11 basepairs (cf. Supplementary Table 6).

Supplementary Table 6. Contact points as obtained from the X-ray structure.

I-strand ID	J-strand ID	mean (I- and J-strands)	relative to D dye	relative to A dye	Absolute bp# D side	Absolute bp# A side
66						
55	59	57	-16		29	
44	49	46.5	-5.5		39.5	
34	38.5	36.25	4.75		49.75	
23.5	27.5	25.5	15.5		60.5	
13	17.5	15.25	25.75		70.75	
2.5	8	5.25	35.75		80.75	
8	2.5	5.25		46.75		91.25
17.5	13	15.25		36.75		101.25
27.5	23.5	25.5		26.5		111.5
38.5	34	36.25		15.75		122.25
49	44	46.5		5.5		132.5
59	55	57		-5		143
	66					

2.7.3 Model parameters

We need also to calculate *xy*- and *z*-components of the DA-distance vector and the effective radius *R*, which is the distance from the centre of the core to the dye cloud's centre of mass (Fig. 7). From the X-ray structure we estimate the effective radius of about 39-44 Å (40 Å are assumed in the simulation) and Δz of about 45 Å. Assuming another radius R = 45 Å does not significantly change the FRET efficiency pattern shown in Figure 6 in the main text. In addition, the shifts between the centre of mass of the dye clouds and their respective attachment points are taken into account. These shifts are approximately equivalent to a displacement of 1.5 basepairs. Other model parameters are summarized in Supplementary Table 7. A scaling factor ß = 1.1 for the Förster radius R_0 = 55.6 Å is used in the geometric model to normalize the experimental FRET efficiency of the compact nucleosome to the theoretical one.

Supplementary Table 7. Geometric model parameters.

Effective radius *R,* Å	40
Basepairs per turn	80
DNA length, basepairs	170
D dye position, basepairs	46.5
A dye position, basepairs	136.5
Δz (per turn), Å	45
scaled Förster radius ßR_0, Å	61.2
Scaling factor ß	1.1

Supplementary Table 8. FRET efficiency levels and corresponding numbers of broken contact points (C_{broken}).

E	C_{broken} A side	C_{broken} D side	C_{broken} total
0.7116	2	3	5
0.55	0	0; 1	0; 1
0.5497	1	3	4
0.546	0	2	2
0.5446	1	0; 1	1; 2
0.5443	2	2	4
0.5415	1	2	3
0.536	0	3	3
0.5353	2	0; 1	2; 3
0.5024	2	4	6
0.4495	3	3	6
0.3628	1	4	5
0.3374	0	4	4
0.3238	3	2	5
0.308	3	0; 1	3; 4
0.0852	3	4	7
0.0368	4	2	6
0.036	4	0	4
0.036	4	1	5
0.0249	4	3	7
0.0038	4	4	8

To easily distinguish the FRET Efficiency groups represented in figure 6, panel E from the groups in figure 6, panel F, color coding has been introduced in Supplementary Table 8: yellow rows are relative to the *MF* part of panel E while green rows are relative to the *HF* one.

3. Supplementary Results

3.1 Acceptor anisotropies

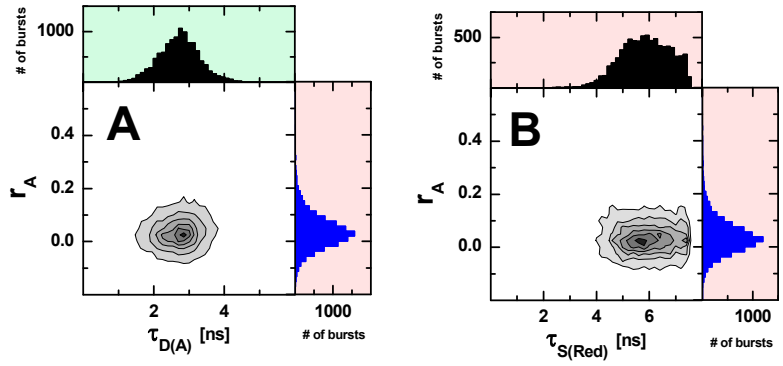

Supplementary Figure 8. Acceptor anisotropy of nucleosmes at 5 mM NaCl. (A): Anisotropy of the acceptor r_A is plotted against lifetime of the donor in presence of the acceptor $\tau_{D(A)}$. (B): Anisotropy of the acceptor r_A is plotted against signal decay time in the red detection channel $\tau_{S(Red)}$.

3.2 PDA fit.

The results of the PDA fits for nucleosomes at different salt concentrations (see main text section 2.2) are reported in the supplementary table 9.

Supplementary Table 9. PDA fit.

Condition	HF			MF			LF			DOnly	χ^2
	R_{DA}	HW	x_{HF}	R_{DA}	HW	x_{MF}	R_{DA}	HW	x_{LF}	x_{DOnly}	
5mM NaCl	53.4	2.6	0.24	63.1	3.2	0.52	113	39	0.15	0.09	3.18
12.5mM NaCl	54.3	3.0	0.28	63.7	2.4	0.40	116	34	0.24	0.08	2.42
25mM NaCl	54.0	3.0	0.26	63.2	1.7	0.19	119	31	0.47	0.08	1.66
50mM NaCl	55.0	4.7	0.17	64.5	2.0	0.06	115	28	0.66	0.11	2.02
100mM NaCl	54.4	3.5	0.10	63.2	1.5	0.06	114	29	0.75	0.09	1.46
Free DNA 5mM NaCl	---	---	---	---	---	---	103	18	0.89	0.11	3.99

Average R_{HF} = 54.2 Å

Average R_{MF} = 63.5 Å

From the values tabled in Supplementary Table 9 it was possible to calculate (eq. 13) for each species the mean FRET efficiency. The values are reported in Supplementary table 10.

Supplementary Table 10. Mean FRET efficiencies of populations presented in Supplementary Table 9, calculated by using eq. 13.

Condition	HF	MF	LF
	$\langle E \rangle$	$\langle E \rangle$	$\langle E \rangle$
5mM NaCl	0.56	0.32	0.10
12.5mM NaCl	0.54	0.31	0.069
25mM NaCl	0.55	0.32	0.047
50mM NaCl	0.52	0.29	0.048
100mM NaCl	0.53	0.32	0.053
average $\langle E \rangle$	0.54	0.31	0.063
Free DNA 5mM NaCl			0.047

3.3 Free DNA and Worm-like Chain Model

In free DNA, the dyes are separated by 92 basepairs, that is, approximately 300 Å. DNA is not fully rigid; a quantitative dependence of DNA looping probability on the DNA length has

been given in [24] where also the effect of this flexibility on transcriptional activation has been discussed. Later, a more thorough analysis gave an expression for the end-to-end distance distribution in DNA[25,26]. We applied this expression to estimate the DA distance distribution $P(r_{DA})$ and concomitantly the mean FRET efficiency expected for the free DNA. In combination with equation 13 we used eq. 2 from ref [25], which reads

$$P(r_{DA}) = a\, r_{DA} \frac{\exp(-R_s / 8L_p\left[1-(r_{DA}/R_s)^2\right])}{\left[1-(r_{DA}/R_s)^2\right]\left[2-(r_{DA}/R_s)^2\right]^2} \qquad \text{(eq.20)}$$

where R_s is the length of fully stretched DNA segment, L_p stands for the DNA persistence length, and a is a normalisation factor. Assuming the persistence length of DNA of 530 Å, one obtains $\langle E \rangle \cong 0.01$, which is significantly lower than the measured $\langle E \rangle$ of 0.047 (Supplementary Table 10).

3.4 Time evolution of FRET species.

In order to study the evolution of the species with time, the measurement time of each salt condition was divided in time segments (200-300 s), and each segment was fit with PDA using the four state model described in the main text. At first, the whole joint data set was analyzed to determine the properties of the individual species, which are compiled in supplementary table 9. To obtain the individual species fractions x_{HF}, x_{MF}, x_{LF}, x_{DOnly} in the small time segments, we fixed the structural parameters and varied only the individual fractions. The obtained fractions are shown in Fig. 4A.

To characterize the characteristic times of the evolution of *LF, HF* and *MF* species, the fractions obtained from the PDA fit of each NaCl concentration were fit separately with a global system of equations:

$$\begin{cases} N_{DOnly} = const. \\ N_{HF}(t) = N_{HF}(0) + N_{HF}(\infty)\exp\left[-\dfrac{t}{\tau_{HF}}\right] \\ N_{MF}(t) = N_{MF}(0) + N_{MF}(\infty)\exp\left[-\dfrac{t}{\tau_{MF}}\right] \\ N_{LF}(t) = \left(1 - N_{HF}(0) - N_{MF}(0) - N_{DOnly}\right) + \\ \qquad N_{HF}(\infty)\left(1 - \exp\left[-\dfrac{t}{\tau_{HF}}\right]\right) + N_{MF}(\infty)\left(1 - \exp\left[-\dfrac{t}{\tau_{MF}}\right]\right) \end{cases} \qquad \text{(eq.21)}$$

where N_{DOnly} is the fraction of *DOnly*, $N_{HF}(0)$ the fraction of *HF* at time zero, $N_{HF}(\infty)$ the fraction of *HF* lost when equilibrium is reached, τ_{HF} the characteristic time of *HF* fraction decay, $N_{MF}(0)$ the fraction of *MF* at time zero, $N_{MF}(\infty)$ the fraction of *MF* lost when equilibrium is reached, τ_{MF} the characteristic time of *MF* fraction decay. The results of the fits are reported in the Supplementary Tables 11 and 12.

Supplementary Table 11. Fit results for *HF* and *MF*.

Condition	HF			MF		
	Time zero fraction	Equilibrium fraction	Characteristic time [s]	Time zero fraction	Equilibrium fraction	Characteristic time [s]
5mM NaCl	0.24	0.24	---[a]	0.52	0.52	---[a]
12.5mM NaCl	0.28	0.28	---[a]	0.49	0.36	848
25mM NaCl	0.24	0.24	---[a]	0.38	0.15	866
50mM NaCl	0.35	0.12	655	0.31	0.00	991
100mM NaCl	0.33	0.04	1097	0.41	0.00	745
average ± σ	0.29 ± 0.05			0.42 ± 0.09		

[a]: the fractions of *HF* and *MF* at 5 mM NaCl and the fraction of *HF* at 12.5 mM and 25 mM are constant.

Supplementary Table 12. Fit results for *LF* and *DOnly*.

Condition	LF		DOnly	
	Time zero fraction	Equilibrium fraction	Time zero fraction	Equilibrium fraction
5mM NaCl	0.15	0.15	0.08	0.08
12.5mM NaCl	0.16	0.29	0.07	0.07
25mM NaCl	0.32	0.55	0.05	0.05
50mM NaCl	0.23	0.78	0.10	0.10
100mM NaCl	0.18	0.89	0.08	0.08
average ± σ	0.21 ± 0.07		0.08 ± 0.02	

3.5 FCS Salt dependence

Nucleosome samples and free DNA samples were measured on different days, with the exception of free DNA at 5 mM NaCl that was measured on both sessions. Because characteristic diffusion times scale with the detection volume, see equation 15, due to the slightly different set-up alignment the characteristic diffusion times cannot be directly compared. To overcome this problem we scaled the results of free DNA so that the diffusion times at 5 mM NaCl from the different days would coincide. The results from the fit are reported in Supplementary Table 13.

Supplementary Table 13. Characteristic diffusion times.

Condition	LF+ DOnly [ms]	HF+MF [ms]	Free DNA [ms]
5mM NaCl	3.00 ± 0.15	3.41 ± 0.12	3.86 ± 0.09
12.5mM NaCl	3.22 ± 0.15	3.34 ± 0.12	3.74 ± 0.09
25mM NaCl	3.58 ± 0.15	3.25 ± 0.12	3.76 ± 0.09
50mM NaCl	3.89 ± 0.15	3.56 ± 0.12	3.85 ± 0.09
75mM NaCl	3.90 ± 0.15	3.43 ± 0.12	3.76 ± 0.09
100mM NaCl	4.04 ± 0.15	3.55 ± 0.12	3.71 ± 0.09

Each dataset was divided in two parts and fitted separately. For some salt conditions more than one measurement was available. From the fit results were calculated average diffusion times, shown in Supplementary Table 13, and standard deviations. The errors of *LF+DOnly, HF+MF* and free DNA reported are the averages of the standard deviations obtained for that species at the different NaCl concentrations.

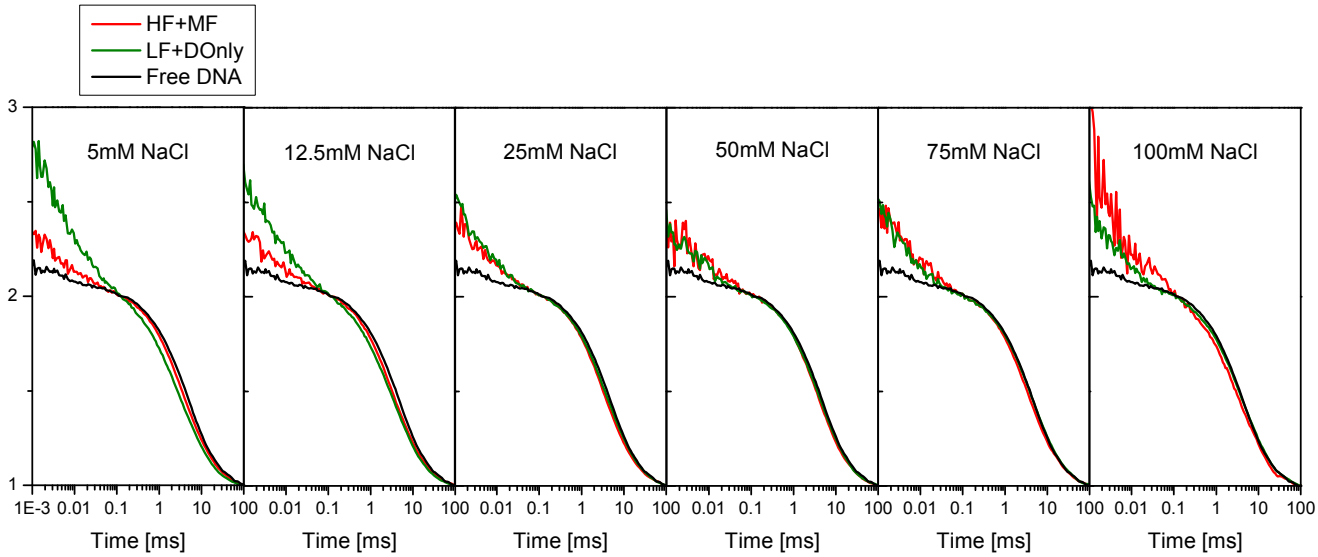

Supplementary Figure 9. Salt dependence of filtered fluorescence correlation curves. For each salt condition are plotted, free DNA (black), *LF+DOnly* species (green) and *HF+MF* species (red). Free DNA curves are rescaled as described in this section.

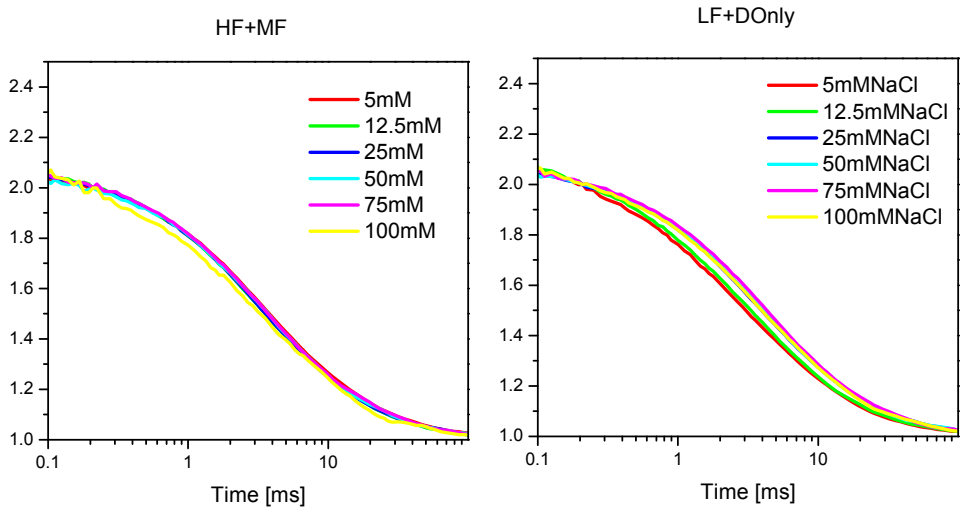

Supplementary Figure 10. Salt dependence of *HF+MF* and *LF+DOnly* fluorescence correlation curves.

3.6 Nucleosome titration

Nucleosome titration experiments were performed on a single molecule setup described in [2]. 50 pM of labeled nucleosomes were diluted in TE buffer (10 mM Tris, 0.1 mM EDTA pH=7.5) supplemented with 100 mM NaCl, 1 mM ascorbic acid, 0.1 g/l BSA and an excess of unlabeled nucleosomes. Samples were carefully mixed and data were taken for 1 hour. The resulting donor-acceptor distance distributions were analysed with PDA using 4 subspecies, *HF*, *MF*, *LF* and *Donly* as described above. The results of the PDA fit are reported in Supplementary Table 14. Here, R_{HF} and R_{MF} are the center positions of the *HF* and *MF* population with corresponding half widths HW_{HF} and HW_{MF}. x_{HF}, x_{MF}, X_{LF} and X_{Donly} denote the fractions of the individual subspecies. At nucleosome concentrations in the nM range the *HF* population was the dominating species, whereas *LF* and in particular *MF* growed substantially as the total nucleosome concentration is lowered indicating an increased unwrapping under these conditions.

Supplementary Table 14. Titration of nucleosomes at 100 mM NaCl.

	R_{HF}	HW_{HF}	x_{HF}	R_{MF}	HW_{MF}	x_{MF}	x_{LF}	x_{DOnly}
0.05nM	54.5	3.0	0.05	57.3	12	0.61	0.24	0.10
0.16nM	54.5	3.0	0.03	55.6	9.8	0.61	0.26	0.10
0.35nM	54.5	3.0	0.10	53.6	8.1	0.65	0.19	0.06
0.7nM	54.5	3.0	0.25	53.6	9.4	0.47	0.20	0.08
1.25nM	54.5	3.0	0.34	53.3	7.6	0.51	0.11	0.05
2mM	54.5	3.0	0.47	52.7	9.7	0.37	0.09	0.07
3nM	54.5	3.0	0.61	52.5	8.7	0.27	0.07	0.04
Free DNA (LF)	75.1	10.3	0.95	---	---	---	---	0.05

References

1. Thastrom, A. et al. Sequence motifs and free energies of selected natural and non-natural nucleosome positioning DNA sequences. *J Mol Biol* **288**, 213-29. (1999).
2. Gansen, A., Toth, K., Schwarz, N. & Langowski, J. Structural Variability of Nucleosomes Detected by Single-Pair Forster Resonance Energy Transfer: Histone Acetylation, Sequence Variation, and Salt Effects. *J Phys Chem B* (2008).
3. Gansen, A., Hauger, F., Toth, K. & Langowski, J. Single-pair fluorescence resonance energy transfer of nucleosomes in free diffusion: optimizing stability and resolution of subpopulations. *Anal Biochem* **368**, 193-204 (2007).
4. Luger, K., Rechsteiner, T.J. & Richmond, T.J. Preparation of nucleosome core particle from recombinant histones. *Methods in Enzymology* **304**, 3-19 (1999).
5. Tóth, K., Brun, N. & Langowski, J. Chromatin Compaction at the Mononucleosome Level. *BIOCHEMISTRY* **45**, 1591-8 (2006).
6. Eggeling, C. et al. Data registration and selective single-molecule analysis using multi- parameter fluorescence detection. *J Biotechnol* **86**, 163-80. (2001).
7. Cheung, H.C. Resonance Energy Transfer. in *Topics in Fluorescence Spectroscopy*, Vol. 2 (ed. Lakowicz, J.R.) 127-176 (Plenum Press, New York, 1991).
8. Clegg, R.M. Fluorescence resonance energy transfer and nucleic acids. *Methods in Enzymology* **211**, 353-388 (1992).
9. Selvin, P.R. Fluorescence Resonance Energy Transfer. *Methods in Enzymology* **246**, 300-34 (1995).
10. Wozniak, A.K., Schroder, G.F., Grubmuller, H., Seidel, C.A. & Oesterhelt, F. Single-molecule FRET measures bends and kinks in DNA. *Proc Natl Acad Sci U S A* **105**, 18337-42 (2008).
11. Maus, M. et al. An experimental comparison of the maximum likelihood estimation and nonlinear least-squares fluorescence lifetime analysis of single molecules. *Anal Chem* **73**, 2078-86 (2001).
12. Antonik, M., Felekyan, S., Gaiduk, A. & Seidel, C.A. Separating structural heterogeneities from stochastic variations in fluorescence resonance energy transfer distributions via photon distribution analysis. *J Phys Chem B Condens Matter Mater Surf Interfaces Biophys* **110**, 6970-8 (2006).
13. Kalinin, S., Felekyan, S., Valeri, A. & Seidel, C.A. Characterizing multiple molecular States in single-molecule multiparameter fluorescence detection by probability distribution analysis. *J Phys Chem B* **112**, 8361-8374 (2008).
14. Rothwell, P.J. et al. Multiparameter single-molecule fluorescence spectroscopy reveals heterogeneity of HIV-1 reverse transcriptase:primer/template complexes. *Proc Natl Acad Sci U S A* **100**, 1655-60 (2003).
15. Kalinin, S., Felekyan, S., Antonik, M. & Seidel, C.A. Probability distribution analysis of single-molecule fluorescence anisotropy and resonance energy transfer. *J Phys Chem B* **111**, 10253-10262 (2007).
16. Nir, E. et al. Shot-noise limited single-molecule FRET histograms: comparison between theory and experiments. *J Phys Chem B* **110**, 22103-24 (2006).
17. Bevington, P.R. *Data Reduction and Error Analysis for the Physical Sciences*, (McGraw-Hill, New York, 1969).
18. Soong, T.T. *Fundamentals of probability and statistics for engineers*, (John Wiley & Sons, West Sussex, England, 2004).
19. Valeur, B. *Molecular Fluorescence: Principles and Applications*, (Wiley-VCH Verlag Weinheim, 2002).
20. Böhmer, M., Wahl, M., Rahn, H.-J., Erdmann, R. & Enderlein, J. Time-resolved fluorescence correlation spectroscopy. *Chemical Physics Letters* **353**, 439-445 (2002).

21. Enderlein, J. & Gregor, I. Using fluorescence lifetime for discriminating detector afterpulsing in fluorescence-correlation spectroscopy. *Review of Scientific Instruments* **76**(2005).
22. Kapusta, P., Wahl, M., Benda, A., Hof, M. & Enderlein, J. Fluorescence lifetime correlation spectroscopy. *J Fluoresc* **17**, 43-8 (2007).
23. Neubauer, H. et al. Orientational and dynamical heterogeneity of rhodamine 6G terminally attached to a DNA helix revealed by NMR and single-molecule fluorescence spectroscopy. *J Am Chem Soc* **129**, 12746-55 (2007).
24. Rippe, K., von Hippel, P.H. & Langowski, J. Action at a distance: DNA-looping and initiation of transcription. *Trends in Biochemical Sciences* **20**, 500-506 (1995).
25. Valle, F., Favre, M., De Los Rios, P., Rosa, A. & Dietler, G. Scaling exponents and probability distributions of DNA end-to-end distance. *Phys Rev Lett* **95**, 158105 (2005).
26. Winkler, R.G. Deformation of semiflexible chains. *Journal of Chemical Physics* **118**, 2919-2928 (2003).

Declaration

I declare that the following thesis has been completed independently, without illegitimate help and has not been submitted previously for a degree.

Alessandro Valeri,

Düsseldorf, 02.02.2009